TECHNICAL TRANSACTIONS
ELECTRICAL ENGINEERING

CZASOPISMO TECHNICZNE
ELEKTROTECHNIKA

ISSUE 2-E (13)

YEAR 2015 (112)

ZESZYT 2-E (13)

ROK 2015 (112)

WYDAWNICTWO POLITECHNIKI KRAKOWSKIEJ

TECHNICAL TRANSACTIONS
ELECTRICAL ENGINEERING

CZASOPISMO TECHNICZNE
ELEKTROTECHNIKA

ISSUE 2-E (13)
YEAR 2015 (112)

ZESZYT 2-E (13)
ROK 2015 (112)

Basic version of each Technical Transactions magazine is its online version
Pierwotną wersją każdego zeszytu Czasopisma Technicznego jest jego wersja online
www.ejournals.eu/Czasopismo-Techniczne www.technicaltransactions.com www.czasopismotechniczne.pl

Series: Electrical Engineering
2-E/2015

ELECTROTECHNICS

ELEKTROTECHNIKA

TECHNICAL TRANSACTIONS | **CZASOPISMO TECHNICZNE**
ELECTRICAL ENGINEERING | ELEKTROTECHNIKA
2-E/2015

AGNIESZKA BANACH*, MACIEJ SUŁOWICZ**

MULTI-CRITERION FAULT DIAGNOSIS OF ROLLING BEARINGS

MULTIKRYTERIALNA DIAGNOSTYKA USZKODZEŃ ŁOŻYSK TOCZNYCH

A b s t r a c t

In this paper, the possibilities of rolling bearing diagnostics, according to the PN and ISO standards, utilising the dimensionless discriminants of vibroacoustic processes, CPB frequency analysis and envelope detection methods are presented. The test bench, the measuring system, as well as the obtained results are described in detail. The authors' own algorithm for the course of action during the process of detecting damage torolling bearings, involving the multi--criterion diagnostic utilising the afore methods is also described.

Keywords: *bearings damage*, *CPB frequency analysis method*, *envelope detection*, *PN ISO standards*, *discriminants of vibroacoustic processes*

S t r e s z c z e n i e

W artykule przedstawiono możliwości: diagnostyki łożysk tocznych z użyciem metod PN i ISO, wykorzystania amplitudowych dyskryminant bezwymiarowych procesów wibroakustycznych, analizy częstotliwościowej CPB i analizy obwiedni. Opisano szczegółowo stanowisko pomiarowe, na którym przeprowadzono badania, układ pomiarowy oraz uzyskane wyniki analizy. Zaprezentowano też autorski algorytm postępowania podczas wykrywania uszkodzeń łożysk tocznych obejmujący diagnostykę multikryterialną z zastosowaniem powyższych metod.

Słowa kluczowe: *uszkodzenie łożysk*, *metoda analizy częstotliwościowej CPB*, *detekcja obwiedni*, *normy PN ISO*, *dyskryminanty procesów wibroakustycznych*

DOI: 10.4467/2353737XCT.15.084.3916

* M.Sc. Eng. Agnieszka Banach, Institute of Industrial Electrical Engineering and Technical Computer Science, Cracow University of Technology.

** Ph.D. Eng. Maciej Sułowicz, Institute of Electromechanical Energy Conversion, Faculty of Electrical and Computer Engineering, Cracow University of Technology.

1. Introduction

The non-invasive diagnosis of electrical machines and devices functioning in various technological processes is a very important issue in the process of maintaining proper functioning of these elements. The purpose of the diagnostic of these objects is to detect their impermissible states and to prevent damage in order to assure longevity and trouble--free work of industrial drive systems [3, 4, 10].The bearings are very important elements of electrical machines working in drive systems. Independent statistical data, published by the American sources [5] EPRI and IEEE, state that over 40% of mechanical damage stems from damage to rolling bearings [9].

Detecting defects of rolling bearings at an early stage is a very important element of monitoring the technical condition of electrical machines [3]. Currently in the industry, the dominant methods in the diagnosis of rolling bearings involve the analysis of signals in time and frequency domains [4], and the basic quantities are mechanical vibrations and phase currents. Simultaneous occurrence of several types of damage can give identical symptoms in the analysed diagnostic signals, which as a consequence can make the proper assessment of the condition of rolling bearings difficult [10].

In this paper, the selected methods, which can be applied jointly to the diagnosis of the condition of rolling bearings in selected electrical machines, are shown and discussed. The application of several independent diagnostic methods provides an increase in the precision and the reliability of the diagnosis of the condition of rolling bearings.

In further sections, the comparative analysis and the assessment of the effectiveness of detecting faults in rolling bearings using the following methods is presented: procedures determined in the PN and ISO standards [6, 7]; utilising the dimensionless discriminants of vibroacoustic process [2, 12]; CPB (Constant Percentage Bandwidth) frequency analysis method [8, 12]; the envelope detection method [8, 12, 13].

The simultaneous application of these methods and combining them into one as a multi--criterion indicator of the bearing diagnosis will improve the reliability of the assessment of the technical condition of the diagnosed bearings in the supervised machine. One method is not always sufficient to assure the increasing reliability requirements applicable to the technical condition of rolling bearings in electrical machines.

2. Construction of the test bench

The test bench (Fig. 1) for testing damage to bearings was equipped with an induction motor and connected to the DC machine by the means of an elastic shaft. The analysed induction motor: Sg112M4 (P_N = 4 kW, U_N = 400 V, ΔI_N = 8.1 A, n_N = 1445 rpm) is a typical, general purpose, low voltage, low power machine, which is used in industry. To be able to test the induction motor at various loads, the shaft of the induction motor was connected to the PZM5545DC machine (P_N = 4.5 kW, U_N = 230 V, I_N = 19.6 A, n_N = 1450 rpm, I_w = 0.86 A), working as a generator. This solution allowed achieving a fluid regulation of the applied load. The torque measuring device (DataFlex 22 series) was installed on the shaft of the machine; this allowed the rotational speed and torque on the machine's shaft

to be measured. Two accelerometers were installed on the bearing end shield, in the pre--determined positions, in the *OX* and *OY* axes. The signals from the accelerometers and the PA-3000 signal conditioner were connected to the DAQ NI-USB 6259 BNC data acquisition card; whereas signals from the torque measuring device were delivered directly to the data acquisition card.

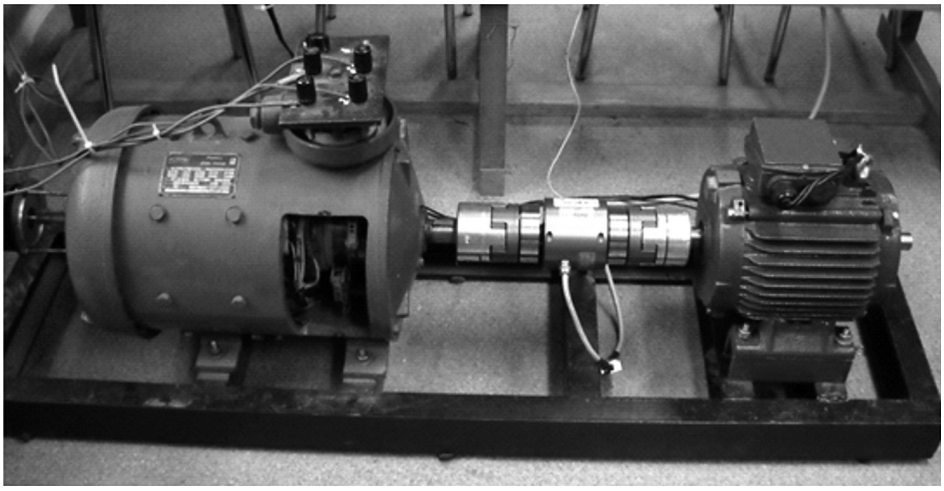

Fig. 1. Connection of the electrical machines

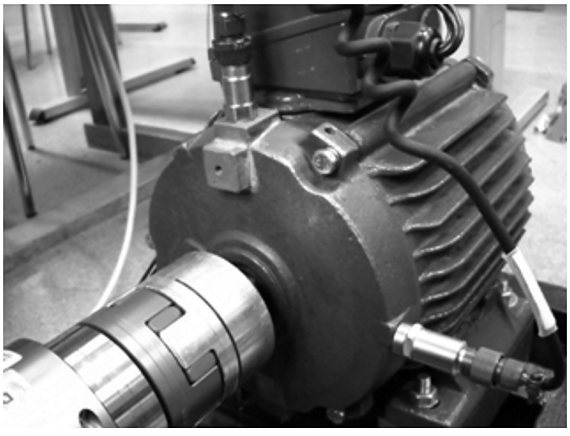

Fig. 2. Location where the vibration acceleration measurements were taken

In the analysed induction motor, the FAG 6306 2R bearings were installed, one after another. The bearings were pre-conditioned and damaged in a specific way. The types of bearings damage are presented in Table 1.

Bearings damaged differently were analysed during the normal work of the motor, at idling motor and during normal work of the machine under various, pre-determined loads.

Table 1

Categories of analysed bearings

Name	Technical condition of the rolling bearing
Bearing 1	Symmetrical (healthy)
Bearing 2	One ball defect
Bearing 3	Two ball defects
Bearing 4	An inner bearing race defect
Bearing 5	An outer bearing race defect
Bearing 6	An outer bearing race defect – external incision
Bearing 7	An inner and outer bearing race defect

For each of the bearing categories, several measuring series were arranged for each of the bearings, for changes in the load current of the analysed machine between 0.5 A and 3.5 A, with 0.25 A increments. Such a measurement procedure allowed us to obtain a family of characteristics, for which it was possible to determine the damage during normal exploitation of the bearings.

3. Methods of diagnosing the technical condition of rolling bearings

Diagnosing the condition of rolling bearings in electric machines is usually based on utilising the information obtained from the machine during its normal work, i.e. vibroacoustic signals [5, 11, 12]. Those signals are generated during every exploitation and manufacturing process. They are a source of information regarding the dynamic processes in the machine and pertain to acoustic phenomena and vibrations. While analysing the vibrations of an electrical machine, particular attention is paid to vibrations generated by each element of the system, beginning with the rolling bearing and ending with the coupling elements. The bearing is one of the most important elements of electrical motors and correctly diagnosing their technical condition can significantly influence the prolonged exploitation of the machine.

The vibration standards recommend the measurement of the RMS value of the effective vibration velocity for frequencies from 10 to 1000 Hz in bearing nodes in V, H, A directions [6, 7]. This value is calculated in accordance to the dependency:

$$V_{\mathrm{RMS}} = \sqrt{\frac{1}{T}\int_0^T V(t)^2\,dt} \tag{1}$$

where:

V_{RMS} – value of the effective vibration velocity for the specified frequency limits,
T – period of time, for which the V_{RMS} is determined, integration time,
$V(t)$ – vibration velocity, signal of the vibration velocity.

The vibration signal measured at the measurement points indicated by the standard does not react clearly enough to the damage of the rolling bearings at the initial phase of the

damage (noise phase, beginning of the vibration phase). One can only expect a reaction during the vibration phase and thermal phase.

The important factor influencing the assessment performed using this method is the rotational speed. The obtained results suggest that in the *OY* axis, the vibrations increase as the rotational speed decreases, that is when the load applied to the machine increases (Fig. 3).

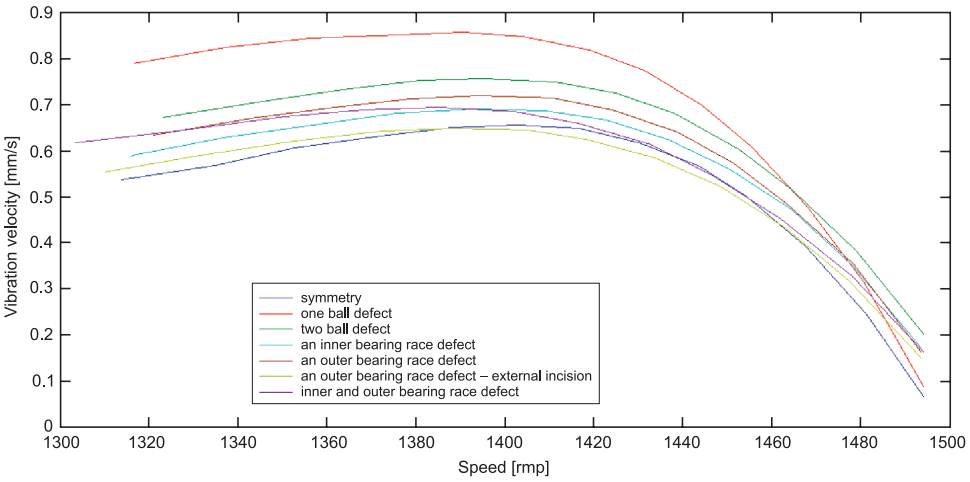

Fig. 3. Graphical representation of vibration velocity, with reference to the rotational speed for the accelerometer of the *OY* axis

The loaded machine is subjected to a larger mechanical moment, this is visible in the machine vibration velocity. The representation of the bearing defects on the graph shows planes, these can be used for assessing the technical condition of the bearings. Due to taking repeated measurements of the condition of the rolling bearings in the drive system, it is possible to accumulate the defect model database. Every machine has its own vibrations resulting from the work of the machine system or its reaction to the stimuli from the surrounding area. The prepared defect model database will be designed only for one, selected machine set. In this situation, it is impossible to develop a universal model, which would be used for determining defects in any machine. Further regular measurements will give a picture of the defects of the rolling bearings in the particular analysed machine.

Another, useful diagnostic method involves the utilisation of amplitude discriminants of dimensionless vibroacoustic processes. This method is based on measurements of vibration acceleration [11, 13], and the important factor here is the change of the peak coefficient during the electric machine exploitation time. Those measurements are made with the use of a measuring device able to determine the actual effective value and the peak value.

The method of measuring the peak coefficient only assesses the technical condition of the rolling bearing, but it does not determine the cause of the change of state. The advantage of this method is a fast and easy measurement taking process. The effectiveness of this

method decreases when other sources of impulse signals are located in the vicinity of the analysed system [12].

Also, the $K(t)$ parameter, determining the rolling bearing exploitation time, expressed in the manner described below, can be used for diagnosing the technical condition of the rolling bearings [10]:

$$K(t) = \frac{a_{\mathrm{RMS}}(0)a_{\mathrm{PEAK}}(0)}{a_{\mathrm{RMS}}(t)a_{\mathrm{PEAK}}(t)} \tag{2}$$

where:

$a_{\mathrm{RMS}}(0)$, $a_{\mathrm{RMS}}(t)$ – effective values of the bearing node vibrations acceleration for the time $t = 0$ – start of the observation procedure (first start of the machine) and for time t – any moment in time during the period of bearing exploitation,

$a_{\mathrm{PEAK}}(0)$, $a_{\mathrm{PEAK}}(t)$ – peak values of the bearing node vibrations acceleration for the time $t = 0$ – start of the observation procedure (first start of the machine) and for time t – any moment in time during the period of bearing exploitation.

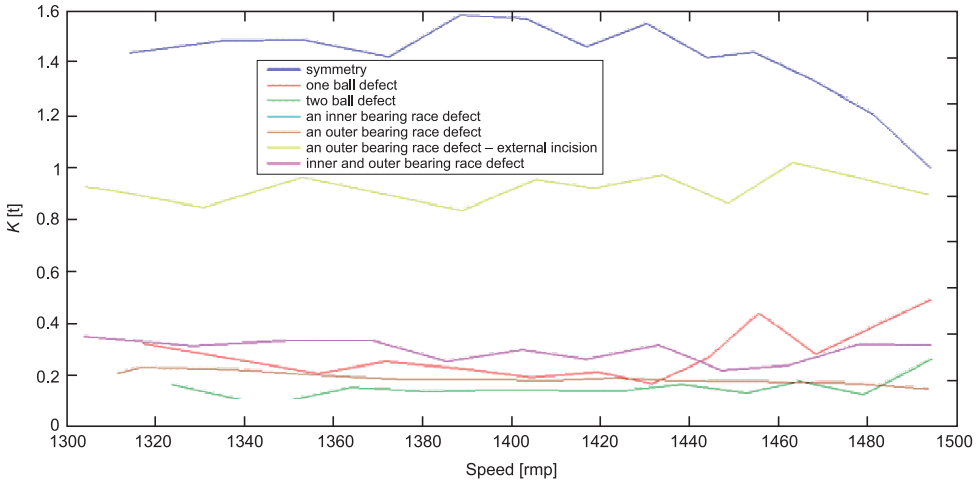

Fig. 4. Graphic representation of the K parameter, in relation to the rotational speed for accelerometer of the OY axis

This method was not designed to analyse a specific type of damage, as all values of the exploitation factor remain at comparatively the same level. We are not able to unequivocally determine the plane which corresponds with one, specific type of bearing damage. Thus, the method of measuring the shape coefficient is not suitable for a detailed analysis, but can only be used to determine that the bearings are damaged, but without indicating the specific element which has become worn during the normal exploitation process.

The CPB frequency analysis method is based on the frequency distribution of the vibration spectrum, this is used for seeking the characteristic frequencies and is responsible for the damage of the specific component of the rolling bearing [1, 8, 12].

Fundamental Train Frequency (frequency of the cage), FTF:

$$f_K = \frac{1}{2} f_r \left(1 - \frac{BD}{PD}\cos\beta\right) \tag{3}$$

Ball Defect Frequency, BDF:

$$f_{ET} = f_r \frac{PD}{BD}\left[1 - \left(\frac{BD}{PD}\cos\beta\right)^2\right] \tag{4}$$

Ball Pass Frequency of the Outer Race, BPFO:

$$f_{BZ} = f_r \frac{n_k}{2}\left(1 - \frac{BD}{PD}\cos\beta\right) \tag{5}$$

Ball Pass Frequency of the InnerRace, BPFI:

$$f_{BW} = f_r \frac{n_k}{2}\left(1 + \frac{BD}{PD}\cos\beta\right) \tag{6}$$

Table 2

Specification of the frequency of damage for the selected loads applied to the machine [Hz]

Machine status	Rotational speed [rotations/min^{-1}]	Outer bearing race	Inner bearing race	Ball defect	Fundamental train	Rotational frequency
Idle	1493	73.95	125.15	45.19	9.24	24.88
Under load	1289	63.84	108.03	39.01	7.98	21.48

Characteristic frequencies calculated for the outer bearing race, the inner bearing race, the ball, the fundamental train and for the first rotational frequency were presented in Table 2. The frequencies were determined using formulas 3–6 for catalogue sizes of the analysed, FAG 6306 rolling bearing. By analysing the aforementioned table, one can notice that the characteristic frequencies are strongly dependent on the current rotational velocity of the machine.

The CPB frequency analysis method is very difficult to interpret, but it is possible to precisely determine which components were damaged. The conducted research proved the validity of the measurement of vibration acceleration in the node of the bearing and suggest the vertical axis of measurement for the analysed machine setup.

The conducted research proved that interpretation of the defects associated with the damage of the inner and outer race is relatively easy (Fig. 5), whereas damage from defects of the rolling elements proved to be difficult to interpret (Fig. 6).

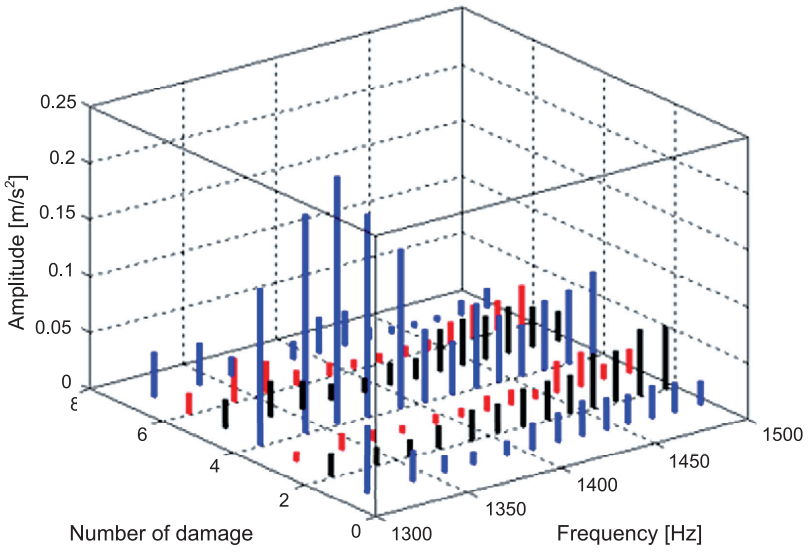

Fig. 5. Attrition, erosion of the outer ring and outer race

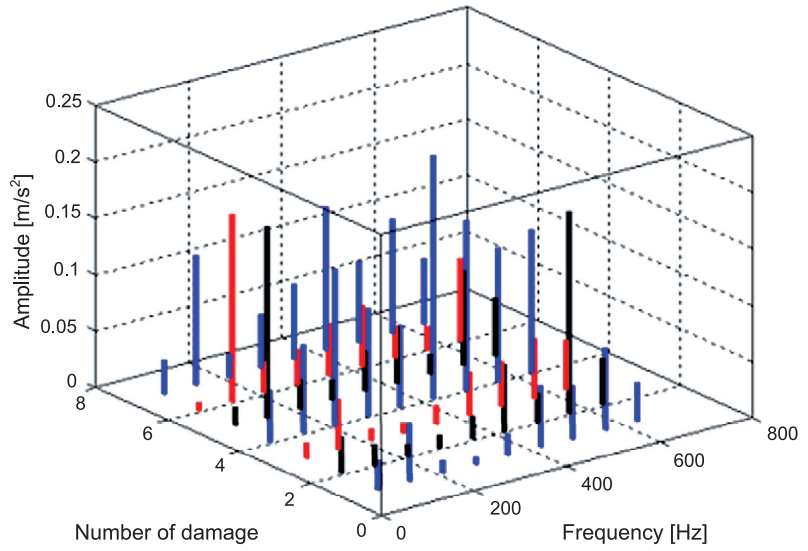

Fig. 6. Indentations and cracks on the outer ring of outer race – under full load

Another diagnostic method effective at assessing the condition of the rolling bearings is the envelope detection method. The envelope detection method is one of the most popular methods of vibroacoustic diagnosis of rolling bearings. This is the most reliable method, and in addition, it allows us to precisely determine the type and degree of damage, as well as allowing the detection of damage at an early stage [8, 12, 13].

The envelope detection method involves the specific analysis of the resonance vibrations of the machine. The vibration signal from the sensor, after filtration, utilises the sensor's own resonance, which is subjected to demodulation and next, on this basis, the signal envelope spectrum is determined. The spectrum of the vibration signal envelope contains components, characterised by vibration frequencies is consistent with the defects of the particular components of the rolling bearing [1, 12].

The envelope detection method is used for analysing slowly changing signals. During the conducted research, the defect of the outer race was most significant (Fig. 7).

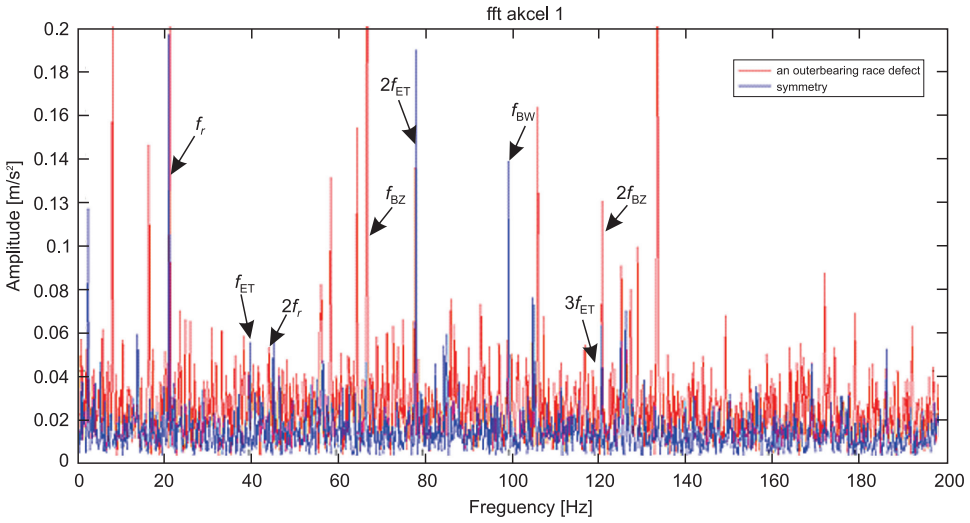

Fig. 7. Damaged outer bearing race and the symmetry state – for the *OY* axis

The modified envelope detection method can be used as an initial method of transforming the vibration signal for the CPB method. Determining the envelope from the vibration signal and subsequently completing the spectrum analysis using the FFT method allows us to improve the differentiation of the particular frequency lines. The CPB method itself is used to determine the specific defects of the analysed rolling bearing on the basis of the characteristic frequency symptoms selected from the vibration spectra.

4. Work algorithm for determining the defects of rolling bearings using multi-criteria diagnostics

The assessment of the technical condition of the bearing is conducted over several stages. The development of the algorithm aims at systematising the measurement process, so the person, who is involved in diagnostic measurements for the first time, would be able to knowingly complete the analysis, without analysing in detail the specific character of the particular method and to ensure that the entire process of assessing the technical condition of the bearing could be performed intuitively (Fig. 8).

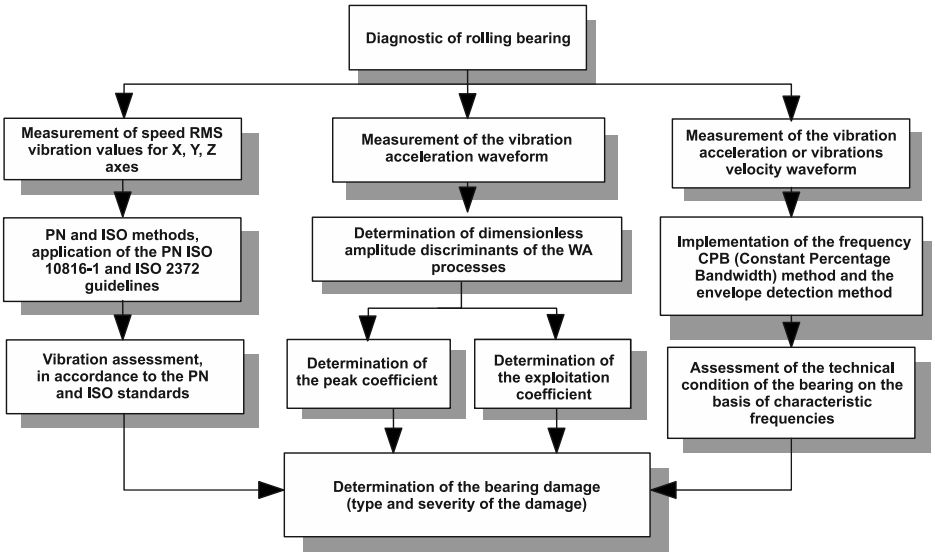

Fig. 8. Algorithm for determining the defects of rolling bearings

Using the PN and ISO methods, it is important to firstly notice that the measurements are taken along three axes (*OX*, *OY*, *OZ*), in accordance to the instructions specified in the PN-ISO 10816-1 standard [6]. The *OX* and *OY* axes are used for measuring the vibrations, whereas the *OZ* axis is used for detecting defects in the machine foundation. The standard classifies the machines with regard to their power and the method of attaching the machine to the foundation. The analysis of the obtained measurement results are done on the basis of the vibrations acceleration for the particular machine. It is clearly visible that the PN and ISO method, based on the ISO 2372 and PN-ISO 10816-1 standards, is a general method, used only for detecting the occurrence of the bearing damage, without the possibility of determining the type of the defect.

Another method is utilising the dimensionless discriminants of the vibroacoustic process. Particular attention is paid to the two following aspects – the peak coefficient and the exploitation coefficient of the rolling bearing. Long lasting work involving the systematic analysis of bearings might lead to the development of a pattern for determining the peak coefficient [9]. In addition, the analysis of the exploitation coefficient alone, which is conducted systematically, can be demonstrated by the exploitation curve for the specific type of bearing defect and can indicate the machine's utility threshold without knowledge regarding the damaged element.

The two aforementioned methods are very easy to implement in industry. They do not require extensive knowledge or the ability to interpret the measurement data. The damage of the rolling bearings can be observed only on the basis of the analysis of diagrams presented in form of trends.

The CPB frequency analysis method, used in conjunction with the envelope detection method, is one of the most advanced methods of analysing the defects of the rolling bearings.

It is suggested that it should be used at the end of the machine's exploitation process [12]. Due to this method, it is possible to differentiate the types of defects. In industry, the defects of the bearings occur during the exploitation process, but it is possible to determine cases of bearing damage during installation. On the basis of the frequency analysis of the machine, it is possible to ascertain that the defects occurred early in the exploitation process. The spectrum of the vibration signal allows us to assess the amplitudes and to derive conclusions pertaining to the damaged bearing component. The increase of the characteristic frequencies amplitudes, responsible for the selected types of defects, e.g. for the damage of the rolling element. Each type of defect is illustrated by the characteristic line in the vibrations frequency spectrum. By putting the amplitude diagrams side by side it is possible to notice that the dispersion of the characteristic frequencies changes during the exploitation time of the bearing. By observing the characteristic frequencies, it is possible to notice the first symptoms of damage at the early stage of machine exploitation. It allows a more effective utilisation of the machine, downtime planning, and preventing the defects of the entire machine assembly.

5. Conclusions

Vibroacoustic signals are associated with the work of each electrical machine and they reflect the most important physical phenomena occurring in the machines, e.g. the interaction between the particular components of the assembly, the imminent failure condition, mechanical stresses, and others. The course of those processes determines the correct functioning of the machine. The measurement of vibrations in the bearing nodes is a common and widely used practice used for assessing the technical condition of the machine. Diagnosis of the state of rolling bearings is mostly associated with the vibration diagnostics. The development of electronics and the increasing database of diagnostic information turn the vibroacoustic diagnostic into an effective tool for detecting defects of rolling bearings.

In this paper, the important problems of diagnosing the rolling bearings were presented. In addition, frequently occurring defects of the rolling elements were described and the selected defects were characterised and presented in a graphical form. Numerous problems associated with the diagnostics of rolling bearings and the correct determination of the particular components of the exploited system was discussed.

Neither of the diagnostic methods give unambiguous results of the assessment of the technical condition of the bearings. The analyses conducted with the use of the proposed methods can help to develop the exploitation curve of the machine and plant the assembly overhaul and change of the rolling bearings. The completion of the diagnostic process will allow for minimising the costs associated with the defects of the exploited machines.

References

[1] Barkow A.W., Barkowa N.A., Azowcew A.J., *Monitoring i diagnostyka rotornych maszyn po wibracji*, Izd. Centr. SPbGMTU, Sankt-Peterburg 2000.

[2] Cempel C., *Diagnostyka wibroakustyczna maszyn*, PWN, Warszawa 1989.

[3] Dwojak J., Szymaniec S., *Diagnostyka eksploatacyjna zespołów maszynowych w energetyce*, Oficyna Wydawnicza Politechniki Opolskiej, Opole 2013.

[4] Dwojak J., Rzepiela M., *Diagnostyka i obsługa techniczna łożysk tocznych*, Poradnik, Diagnostyka Techniczna, Warszawa 2003.
[5] Dzwonkowski A., *Metoda diagnostyki łożysk na podstawie analizy przebiegów prądu i napięcia zasilającego silnik indukcyjny*, Politechnika Gdańska, Gdańsk 2011.
[6] ISO 2372. Mechanical vibration of machines with operating speeds from 10 to 200 rev/s – Basis for specifying evaluation standards.
[7] Klimowski M., *Diagnostyka wibroakustyczna w oparciu o uregulowania normatywne PN i ISO*, Zeszyty Problemowe – Maszyny Elektryczne, 2013, Nr 2(99), 115-120.
[8] Klimowski M., *Diagnostyka łożysk tocznychsilników elektrycznych przy wykorzystaniu metody analizy czętotliwościowej oraz metody detekcji obwiedni*, Zeszyty Problemowe – Maszyny Elektryczne, 2014, Nr 2(103), 157-163.
[9] Kowalski Cz.T., *Monitorowanie i diagnostyka uszkodzeń silników indukcyjnych z wykorzystaniem sieci neuronowych*, Prace Naukowe Instytutu Maszyn, Napędów i Pomiarów Elektrycznych Politechnik Wrocławskiej Nr 57, Seria: Monografie Nr 18, Wrocław 2005.
[10] Łączkowski R., *Wibroakustyka maszyn i urządzeń*, WNT, Warszawa 1983.
[11] Swędrowski L., *Nowa metoda diagnostyki łożysk silnika indukcyjnego oparta na pomiarze i analizie widmowej prądu zasilającego*, Politechnika Gdańska, Gdańsk 2005.
[12] Szymaniec S., *Diagnostyka stanu izolacji uzwojeń i stanu łożysk silników indukcyjnych klatkowych w warunkach przemysłowej eksploatacji*, Politechnika Opolska, Opole 2006.
[13] Brüel & Kjær: http://www.bruel.com.pl/.

TECHNICAL TRANSACTIONS | **CZASOPISMO TECHNICZNE**
ELECTRICAL ENGINEERING | ELEKTROTECHNIKA
2-E/2015

VASYL I. HUDYM*, PIOTR DROZDOWSKI**, VOLODYMYR HUDYM***,
ANDRZEJ POSTOLIUK****, DOMINIK MAMCARZ*****

ANALYSIS OF THE WORK STATES OF A PULSE CURRENT ELECTRIC ARC FURNACE

ANALIZA STANÓW PRACY PIECA ŁUKOWEGO PRĄDU IMPULSOWEGO

A b s t r a c t

This article presents the results of the analysis of a six-electrode pulse current electric arc furnace (EAF). The characteristics of a power supply system for an EAF are presented for symmetrical states and the most probable asymmetrical states.

Keywords: *electric arc furnace*, *EAF*, *pulse current*, *six-electrode arc furnace*

S t r e s z c z e n i e

W artykule przedstawiono wyniki badań pracy sześcioelektrodowego pieca łukowego prądu impulsowego. Charakterystyki energetyczne układu zasilania pieca łukowego zostały przedstawione dla stanów symetrycznych oraz najbardziej prawdopodobnych stanów niesymetrycznych.

Słowa kluczowe: *elektryczny piec łukowy*, *prąd impulsowy*, *sześcioelektrodowy piec łukowy*

DOI: 10.4467/2353737XCT.15.085.3917

* Prof. Ph.D. D.Sc. Eng. Vasyl I. Hudym, Institute of Electromechanical Energy Conversion, Faculty of Electrical and Computer Engineering, Cracow University of Technology, Lwowski Państwowy Uniwersytet Bezpieczeństwa Życia.

** Ph.D. D.Sc. Eng. Piotr Drozdowski, Institute of Electromechanical Energy Conversion, Faculty of Electrical and Computer Engineering, Cracow University of Technology.

*** Ph.D. Eng. Volodymyr Hudym, Politechnika Lwowska.

**** M.Sc. Eng. Andrzej Postoliuk, Inżynier pierwszej kategorii sektora obliczeń stanów pracy systemów elektroenergetycznych, Zakład Zachodniej Sieci Magistralnej, Lwów, Ukraina.

***** M.Sc. Eng. Dominik Mamcarz, Institute of Electromechanical Energy Conversion, Faculty of Electrical and Computer Engineering, Cracow University of Technology.

1. Introduction

In recent years, direct-current EAFs have been competing within the steelmaking industry with three-phase alternating current EAFs in terms of their effect on power supply systems. However, the use of high-power direct-current EAFs is limited by certain factors, the most important of which are multiple overvoltages caused by dips in high-value technological current [1]. Short-term technological shutdowns of direct-current EAFs have to be performed while the EAF is under load. This creates additional requirements for circuit breakers installed on the side of the primary winding of the furnace transformer. Frequent shutdowns of furnace transformers directly under load reduce the technological viability of circuit breakers, sometimes even damaging them and prematurely excluding them from use [2, 3].

2. Analysis of the results

In order to partially solve the aforementioned issues in EAFs used in steelmaking, a design of a six-electrode pulse current EAF was developed in which the arc can be interrupted by raising the electrodes, and the furnace transformer was disconnected from the electrical power supply during the no-load state of the EAF. Figure 1 shows a schematic of the power supply system for the pulse current EAF [4]. An equivalent system was presented with a voltage of 230 kV and an equivalent reactance of 8 Ω. The power transformer was supplied with 230 kV via an overhead line, of length 7 km and cross-section 3×500 mm^2. The parameters of the power transformer are summarized in Table 1. The three--phase cable line of a length of 520 m, constructed of four cables 1×240 mm^2 was used to supply the furnace transformer (parameters summarized in Table 1). Rectifier diodes were modeled as resistance. When the diode was ON, resistance equaled R_{ON} $5 \cdot 10^{-3}\Omega$, when OFF, $R_{OFF} = 10^6\Omega$.

In order to analyze the power system shown in Fig. 1, a mathematical model implemented in an DELPHI 6 environment was used. Developed software package based on the minimum input information (graph data and branch of graph parameters) forming in an automatic cycle of the system of equations.

Table 1

The parameters of the power and furnace transformers

Parameter	Power transformer	Furnace transformer
S_n	160 MVA	12.5 MVA
U_1/U_2	230 kV/35 kV	35 kV/0.2–0.4 kV
$u_{k\%}$	10%	11.5%
ΔP_{Fe}	450 kW	22 kW
ΔP_{Cu}	167 kW	90 kW
I_0	0.6%	0.5%

This solution enables much longer commutation breaks in circuit breakers and improves working conditions for the insulation of the EAF basic device. The technological operation involves six arcs with overlapping currents between individual electrodes. This requires estimating the power of each arc and the conditions for the transition to a continuous arc, and burning the arcs under the electrodes. These factors need to be taken into account when using EAFs of this type. In addition, the EAF energy conversion efficiency, the power factor, and the relationship between arc active power and the voltage between the electrode and charge need to be determined to help select the optimal method for regulating active power in the EAF.

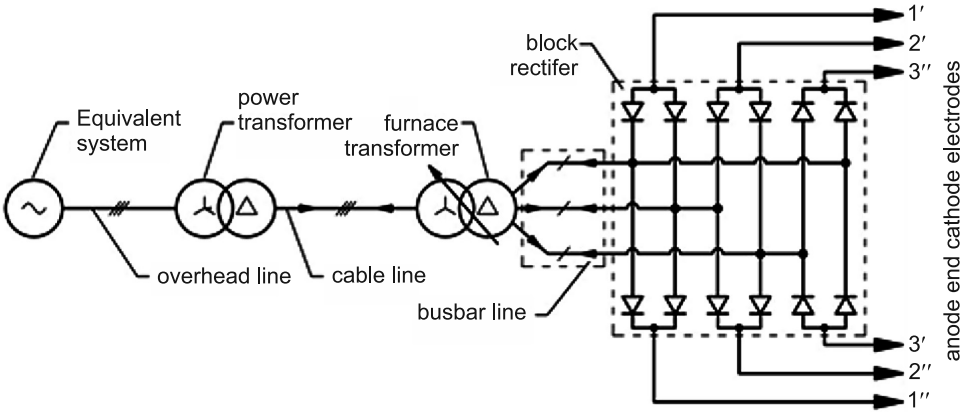

Fig. 1. Concept schematic of the power supply system for the pulse current EAF

In this case, the task involves testing the proposed six-electrode pulse current EAF, shown in Fig. 1. The testing should primarily concern steady states of the EAF in order to arrive at its operating characteristics. This will allow the effect on the power supply system and the most probable asymmetrical states to be determined from the viewpoint of the electrical power quality (higher harmonics generation [5, 6]), and will allow the conditions for continuous arc burning under electrodes to be obtained. The values of currents and voltages obtained based on model testing will help assess whether the choice of the electrical device and individual semiconductor elements is correct.

Research involved assessing the effect of a six-electrode pulse current EAF working in different states on the power supply system, it aimed to determine the distribution of the higher harmonics of current in the power network and assess the asymmetry of active power and passive power in phase wires. The obtained information will help select the methods and means of improving the quality of electrical power in the power network and improve the compatibility between the EAF and the power network.

To this end, research was proposed on the symmetrical states of EAF operation and the asymmetrical states with the greatest effect on the power network, i.e.:

– Interruption of an arc.
– Short-circuit between an electrode and charge.

– Interruption of one arc under the cathode and another arc under the anode.
– Simultaneous interruption of one arc and short-circuit between another electrode and charge.

Research on electromagnetic waveforms during an accidental change to the dynamic characteristics of an electrical arc haven't been performed. In a symmetrical state, instantaneous values of arc currents and voltages are identical (Fig. 2).

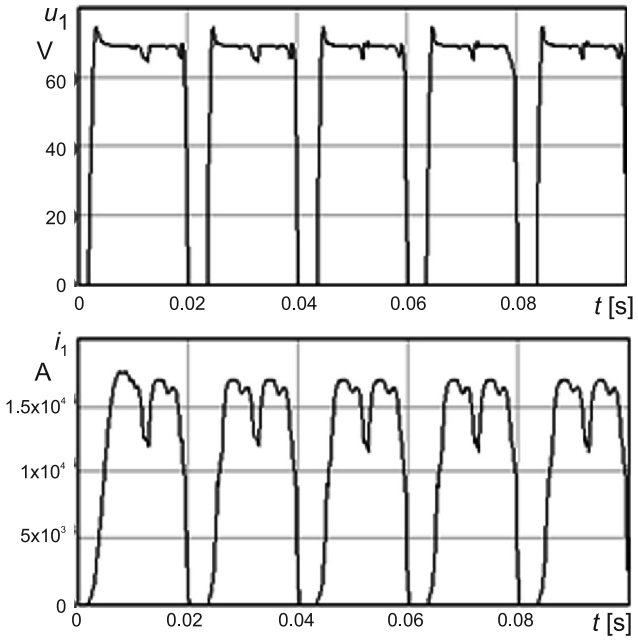

Fig. 2. Instantaneous values of arc currents (flowing through electrode 2', 1") and voltages (electrode 1") in the symmetrical state

As Figure 2 shows, each zero-current break in a single 50 Hz period lasts 3.3 μs, and the arc under each electrode last for 16.7 μs, which constitutes 83.55% of the entire period. This means that each electrode is highly efficient. The deformation of electrical arc currents and voltages depends on the R and L parameters of the power network. Once a choke is connected via a series circuit with the furnace transformer, the zero-current break shortens, and may even be eliminated completely. Figure 3 shows a graphical representation of the relationship between the zero-current break and a time constant, given by $\tau = L/R$. As can be seen in the figure, the value of the break decreases with an increase in L.

If the arc voltage reaches 110 V and the arc current in this state amounts to approx. 15 kA, the mean values of voltage and the current during each period amounts to approx. 75 V and 9 kA, respectively, which corresponds to 700 kW of power in each arc and to over 4 MW of total EAF power. Research showed that maximal power under each arc is 926 kW, which corresponds to approx. 6 MW of total power. If the arc voltage corresponding to maximal power increases or decreases, the power of the EAF slowly decreases.

Fig. 3. Zero-current break duration as a function of the time constant

Figure 4a shows the power characteristics of an arc depending on its voltage (arc length). As can be seen in the figure, arc power depends parabolically on arc voltage. Therefore, arc electrical power can be adjusted by changing the arc length or transformer turns ratio (arc voltage), which is easily achievable in practice.

Note that in a symmetrical state, the EAF generates the fifth and seventh current harmonics into the power network. Figure 4b shows the relationship between the value of the fifth and seventh current harmonics and arc voltage. As can be seen in the figure, the value of the total harmonic distortion increases with an increase in arc voltage due to a decrease in the amplitude of the first harmonic and an increase in the amplitude of the fifth harmonic. The largest increase in the fifth current harmonic occurs when changes in arc voltage correspond to arc power of no less than 80% of maximal power. Further increase in arc voltage is accompanied by a slow increase in the relative value of the fifth harmonic and a decrease in the absolute value of the fifth harmonic. In a symetrical state the power factor of EAF falls between 0.75–0.8.

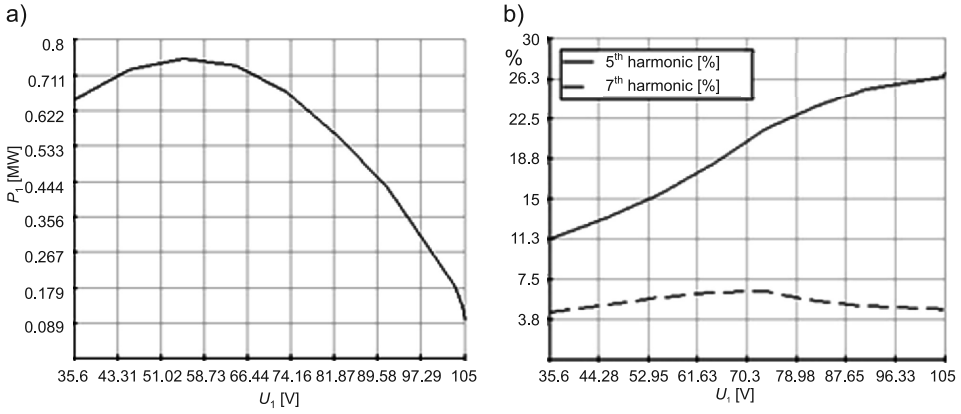

Fig. 4. Relationship between arc power and voltage and between current harmonics and voltage

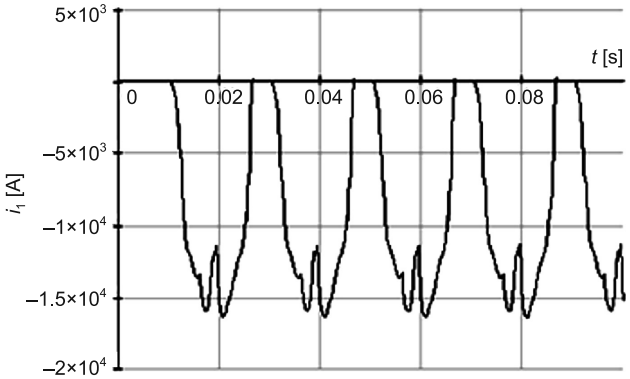

Fig. 5a. Oscillograms of currents in the case of the interrupt arc under the electrode 1' (currents of electrode 1' and 1")

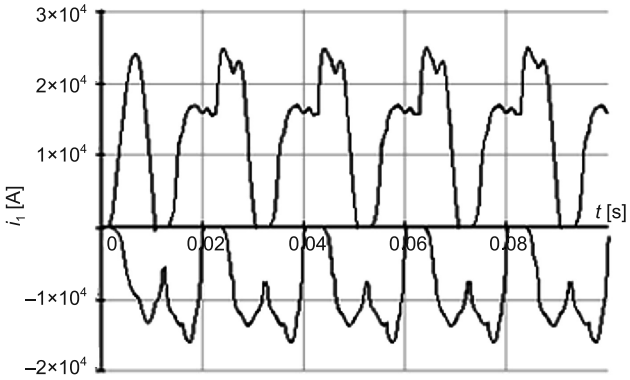

Fig. 5b. Oscillograms of currents in the case of the interrupt arc under the electrode 1' (currents of electrode 2' and 2")

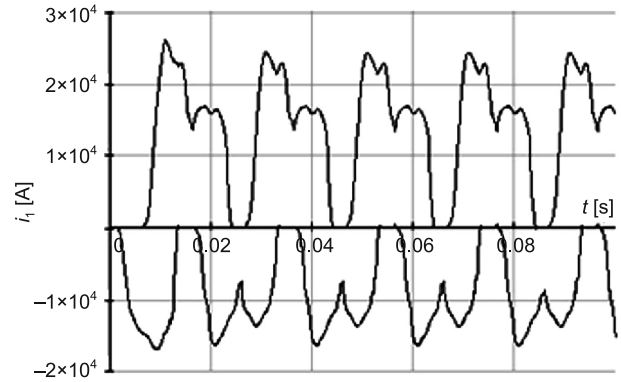

Fig. 5c. Oscillograms of currents in the case of the interrupt arc under the electrode 1' (currents of electrode 3' and 3")

If an arc is interrupted (in this case, under Electrode 1'), an asymmetric state occurs. Figure 5 shows oscillograms of currents in each electrode (in the following order: 1'/1"; 2'/2"; 3'/3") with current amplitudes in working arcs (1", 2" and 3"). The current of Electrode 1' equals zero, while current amplitudes in Electrodes 2' and 3' increase 1.7 times compared to the symmetrical state.

In this case, the voltage amplitudes of the arcs change. This affects the power of appropriate arcs, as shown in Table 2.

Table 2

Active power in each EAF arc (interrupt arc under the electrode 1')

Number of electrode	Active power [kW]
1'	0
2'	604
3'	627
1"	930
2"	601
3"	910
Total power EAF [kW]	3672

A short-circuit between an EAF electrode and charge (in this case, 1') causes the current of the electrode to nearly double compared to the symmetrical state, as shown in Fig. 6a (top). Other current amplitudes increase by 10% to 25% compared to current amplitudes during the symmetrical state.

Current harmonics in the power network in this state differ from the symmetrical state in that the second harmonic appears in addition to the fifth and seventh harmonics, albeit the fifth harmonic remains the highest. Moreover, it was noted that voltage amplitude between

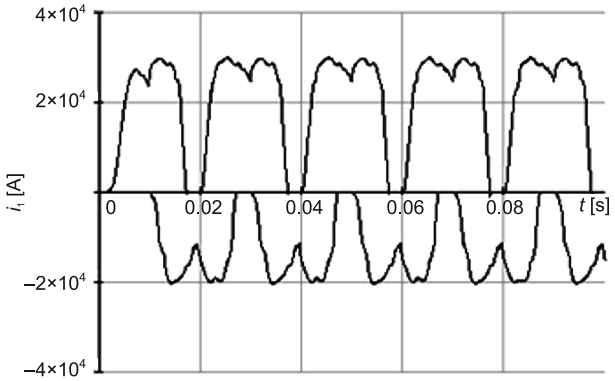

Fig. 6a. Current oscillograms after a short-circuit between Electrode 1' and charge (currents of electrode 1' and 1")

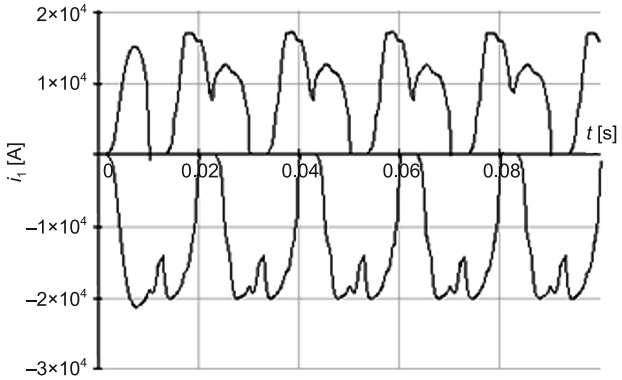

Fig. 6b. Current oscillograms after a short-circuit between Electrode 1' and charge (currents of electrode 2' and 2")

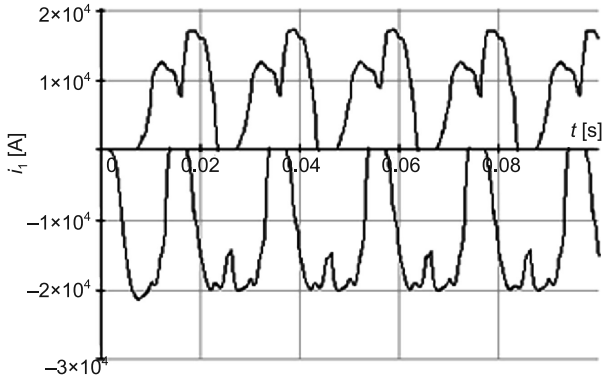

Fig. 6c. Current oscillograms after a short-circuit between Electrode 1' and charge (currents of electrode 3' and 3")

the electrode with the interrupted arc and charge increased 1.84 times, and mean value increased 1.76 times compared to the symmetrical state. Voltages under other electrodes do not change.

A short-circuit between an electrode and charge leads to considerable asymmetry in the currents of other arcs and currents in the power network. Figure 6 shows the instantaneous values of arc currents. It was noted that the circuit current of an electrode connected to a charge increased by only 2 times compared to the arc current of a given electrode in the symmetrical state when the circuit current in the three-phase EAF reaches a value 3 to 3.5 times greater than the normal value. In this case, the value of the circuit's current can be limited by arc resistance under the second electrode of the rectifier.

During a short-circuit in an EAF electrode, the apparent power input is 1.15 times lower than the apparent power input of the furnace after an arc is interrupted and amounts to 4.6 MVA, which is 1.3 times lower than in the symmetrical state. Active power and passive

power decrease accordingly, and the range of changes in the apparent power of the furnace during a short-circuit between an electrode and charge falls between 1.7 MVA and 6.0 MVA. In this state, the EAF generates considerably more harmonics. The third, fourth, and sixth harmonics appear in addition to the second, fifth, and seventh harmonics, with the relative values of the fifth and seventh harmonics lower than in the symmetrical state due to an increase in the value of the first harmonic. In this case, the power factor of EAF falls between 0.45–0.6. In the other cases the power factor included in the range 0.55–0.75, depending of asymmetry type.

Table 3

Active power in each EAF arc (short circuit electrode 1' with charge material)

Number of electrode	Active power [kW]
1'	0
2'	603
3'	628
1"	931
2"	600
3"	911
Total power EAF [kW]	3673

If the arcs between an anode and charge, and between a cathode and charge are interrupted, an asymmetrical state occurs. As a result, the current amplitudes of other arcs decrease by approx. 1.5 times compared to the symmetrical state. Moreover, currents in the power network include the second, third, fourth, fifth, seventh, tenth, and eleventh harmonics, with the fifth harmonic of the phase current showing the highest value. Analysis of the instantaneous values of the currents of other arcs shows that the break interval between current pulses in individual electrodes does not change, i.e., the breaks do not depend on the states of the arcs of other rectifiers.

Table 4

Active power in each EAF arc (interruption of two arcs)

Number of electrode	Active power [kW]
1'	0
2'	772
3'	0
1"	771
2"	749
3"	748
Total power EAF [kW]	3040

The maximal voltage value under the electrode with the interrupted arc increases by 1.8 times, the mean value increases by 1.6 times, and the voltages of other arcs do not change. Because active power, passive power, and apparent power increase proportionally to the increase in the currents of other arcs, the total apparent power decreases by approx. 1.2 times compared to the symmetrical state.

Lastly, let us consider the working state of an EAF when two electrodes (one anode and one cathode, each from a different rectifier) short-circuit. In this state, the values of currents flowing through the short-circuited electrodes are 2.27 times greater than those in the symmetrical state. While the values of currents in other electrodes of the same rectifiers do not change, currents flowing through the third rectifier practically double.

Table 5 shows an overview of power values. As can be seen in the table, apparent power, and active power of the EAF decrease by two times compared to the symmetrical state. Because total passive power practically corresponds to the symmetrical state, the power factor decreases considerably, and must, therefore, be increased by compensating the reactive power.

Table 5

Active power in each EAF arc (short circuit of two arcs witch charge material)

Number of electrode	Active power [kW]
1'	0
2'	484
3'	0
1"	1002
2"	495
3"	1000
Total power EAF [kW]	2981

Figure 7 shows histograms of the total active power taken by the EAF to enable comparison between power inputs. As the figure indicates, active power depends on the work state of the EAF, while passive power remains almost constant.

Fig. 7. Active power in different arc work states

3. Conclusions

Analysis of results obtained by simulating different work states of a pulse current EAF with a furnace transformer of 12.5 MVA power leads to the following conclusions:

1. Results concerning steady states indicate that the fifth and seventh harmonics have the highest power in the power supply system, and that the share of other harmonics (third, sixth, ninth, eleventh, and thirteenth) does not exceed 1%. The amplitude of the seventh harmonic is practically independent from the arc voltage and reaches approx. 6%, while the amplitude of the fifth harmonic increases with an increase in the arc voltage and reaches 15% compared to the amplitude of the first harmonic.
2. The EAF arc power depends on the arc length and reaches its maximum voltage at which the arc resistance approaches the impedance of the EAF power supply system.
3. Interruptions in arc currents and short-circuits between electrodes and charge decrease the active power input of the EAF by 25–30% due to asymmetry between voltages and currents in the EAF power supply system. At the same time, a short-circuit between electrodes and charge increases the current in the components of the rectifier to 30%, and an interruption in the arc increases voltage on non-active semiconductors. All this should be taken into account when selecting rectifiers.
4. An increase in time constants in the arc profile decreases zero-current breaks under each electrode. This relationship is nearly linear. During operation, the time constant is adjusted by changing the arc length (arc resistance). This should be taken into account when selecting a method for automatically adjusting the position of electrodes, as it affects the power characteristics of the EAF.

References

[1] *Влияние дуговых электропечей па системы электроснабжения*, под ред. Смелянского М.Я. и Минеева Р.В., Энергия, 1975, 184 с. [eng. *Influence on power supply systems by EAF*, Ed. By Smielanski M.J. and Minjejew F.Ch., Energy, 1975, 184 p.].

[2] Гиндулин Ф.Х., Гольдштейн В.Г., Дульзон А.А., Халилов Ф.Х., *Перенапряжения в сетях 6–35 кВ*, Энергоатомиздат, 1989, 212 с. [eng. Gindulin F.H., Goldstein V.G., Dulzon A.A., Khalilov F.H., *Overvoltages in 6–35 kV networks*, Elektroatomizdat, Moscow 1989, 212 p.].

[3] Перхач В.С., Гудым В.И., *Переходные процессы включения трансформаторов дуговых сталеплавильных печей*, Техническая электродинамика, № 1/1989, с. 27-31 [eng. Perchacz V.S., Hudym V.I., *Transients states after switching EAF transformers*, Technical Electrodynamics, No 1/1989, p. 27-31].

[4] Гудим В.І., Постолюк А.Я., Дроздовський П., Карбовнічек М., *Система електропостачання дугової електропечі імпульсного струму*, Патент № 101412. UA. МПК H02J 3/18. від. 25.03.2013 [eng. Hudym V.I., Postoliuk A.J., Drozdowski P., Karbowniczek M., *The power supply system for the pulse current EAF*, Patent No 101412 UA. MPK H02J 3/18, Publication date 25.03.2013].

[5] Arrillaga J., Bradley D.A., Bodger P.S., *Power System Harmonics*, John Wiley & Sons, New York 1985.

[6] Жежеленко И.В., *Высшие гармоники в системах электроснабжения промышленных предрприятий, 4-е изд*., перераб. и доп., Энергоатомиздат, 2000, 331 с. [eng. Żeżelenko I.V., *Higher harmonics in industrial power systems*, Elektroatomizdat, Moscow 2000, 331 p.].

TECHNICAL TRANSACTIONS | **CZASOPISMO TECHNICZNE**
ELECTRICAL ENGINEERING | ELEKTROTECHNIKA
2-E/2015

KRZYSZTOF LUDWINEK*

SOME ASPECTS OF INDUCTANCE DISTRIBUTIONS MODELING IN *dq*0-AXES AND DAMPING CIRCUITS ON THE ROTOR OF A SALIENT POLE SYNCHRONOUS GENERATOR

WYBRANE PROBLEMY MODELOWANIA ROZKŁADU INDUKCYJNOŚCI W OSI *dq*0 I OBWODÓW TŁUMIĄCYCH WIRNIKA GENERATORA SYNCHRONICZNEGO JAWNOBIEGUNOWEGO

Abstract

This paper concerns a salient pole synchronous generator with damping bars on the rotor, and presents a comparison of the distribution of self and mutual inductances in the stator natural reference frame *abc* for a linear and a nonlinear circuital model, as well as in the rotor reference frame *dq*0. Moreover, this paper shows a proposed method of modeling the damping circuits on the rotor of a salient pole synchronous generator. An experimental verification of the registered induced voltage in the damping bars on the rotor is presented.

Keywords: *synchronous generator*, *inductance distributions*, *damping circuits*

Streszczenie

W niniejszym artykule przedstawiono – dla liniowego i nieliniowego modelu obwodowego generatora synchronicznego jawnobiegunowego z prętami tłumiącymi na wirniku – porównanie rozkładów indukcyjności własnych i wzajemnych w naturalnym układzie odniesienia *abc* związanym ze stojanem oraz w układzie odniesienia *dq*0 związanym z wirnikiem. Ponadto artykuł zawiera propozycję modelowania obwodów klatki tłumiącej wirnika generatora synchronicznego jawnobiegunowego. Opisane w nim też badanie eksperymentalne zarejestrowanych indukowanych napięć w prętach tłumiących wirnika.

Słowa kluczowe: *generator synchroniczny*, *rozkłady indukcyjności*, *obwody tłumiące*

DOI: 10.4467/2353737XCT.15.086.3918

* Ph.D. Eng. Krzysztof Ludwinek, Department of Industrial Electrical Engineering and Automatics, Kielce University of Technology.

1. Introduction

The most important aspect in simulations of electromagnetic properties of a synchronous generator and a squirrel cage induction motor using a circuital model are choosing suitable reference frames and the presence of damping bars (the most frequently on the rotor) [1–7]. If the self and mutual inductances of the stator windings contain only the constant component and the same magnitude of the 2nd harmonic, the simulation studies of synchronous generators using circuital models in the rotor reference frame $dq0$ are very popular due to constant self and mutual inductance distributions [1, 7]. The circuital models in $dq0$-axes are obtained using Park's transformation of the models in the stator natural reference frame. The inductance distributions in the $dq0$-axes for the magnetic core linearity can be expressed as [8]:

$$\mathbf{L}_{dq}(\theta) = \mathbf{B}(\theta)\mathbf{L}_{s}(\theta)\mathbf{B}^{-1}(\theta) \tag{1}$$

where:

$d, q, 0$ – the winding in dices in the dq-axes and zero-sequence,
θ – electrical angle of the rotor position,
$\mathbf{L}_{dq0}$ – the matrix of self and mutual inductance distributions in the $dq0$-axes,
$\mathbf{L}_{s}$ – the matrix of self and mutual inductance distributions of stator winding,
$\mathbf{B}, \mathbf{B}^{-1}$ – matrixes of transformation and inverse transformation.

In expression (1) the inductance matrix $\mathbf{L}_{dq0}(\theta)$ in the $dq0$-axes can be formulated as [7]:

$$\mathbf{L}_{dq0}(\theta) = \begin{bmatrix} L_{d}(\theta) & L_{dq}(\theta) & L_{d0}(\theta) \\ L_{qd}(\theta) & L_{q}(\theta) & L_{q0}(\theta) \\ L_{0d}(\theta) & L_{0q}(\theta) & L_{0}(\theta) \end{bmatrix} \tag{2}$$

where:

L_{d}, L_{q}, L_{0} – self inductances in the $dq0$-axes,
$L_{dq}, L_{qd}, L_{d0}, L_{0d}, L_{q0}, L_{0q}$ – mutual inductances in the $dq0$-axes.

Generally, in the stator and the rotor natural reference frame, the matrix of self and mutual inductances of synchronous generators $\mathbf{L}_{sfr}(\theta)$ (for magnetic core linearity) as a function of the electrical angle of the rotor position θ can be defined as [1–4, 7]:

$$\mathbf{L}_{sfr}(\theta) = \left[\begin{array}{c|c} \mathbf{L}_{s}(\theta) & \mathbf{L}_{sr}(\theta) \\ \hline \mathbf{L}_{rs}(\theta) & \mathbf{L}_{r}(\theta) \end{array}\right] \tag{3}$$

where:

θ – electrical angle of the rotor position $\theta = \theta_{m} p$,
θ_{m} – mechanical angle of the rotor position,
p – the number of pole pairs,
$\mathbf{L}_{s}$ – matrix of self and mutual inductance distributions of stator windings,
$\mathbf{L}_{sr}, \mathbf{L}_{rs}$ – matrixes of mutual inductance distributions of stator and rotor windings,
$\mathbf{L}_{r}$ – matrix of self and mutual inductance distribution of rotor windings.

Most often, the inductances in expression (3) can be calculated as follows:

- In an experimental way, e.g. Standstill Frequency Response Test (SSFR), Pseudo--Random Binary Sequence (PRBS) [9, 10] etc.,
- With the use of programs based on the finite element method using commercial software, such as Maxwell, Flux, Opera etc, or using widely available Finite Element Method Magnetics (FEMM) software, or using the edge element method [11–16],
- By means of one's own programs developed in LabView, Matlab/Simulink, etc. [3, 10],
- By the combination of electromagnetic field equations and differential equations using the commercial software (Maxwell, Flux, Opera etc.) [12],
- In ananalytical way [1, 17, 18].

Generally, for a non-uniform air gap on the stator and rotor side (for linear cases), the self and mutual inductances $L_{mn(v)}$ in relationship (1) are a function of the electrical rotor position angle θ, and for the *v*-th spatial harmonic inductance they can be described by means of a triple Fourier series [1]:

$$L_{mn(v)} = \sum_{v}\sum_{r}\sum_{s} L_{sr(v)}^{mn} e^{jv(\alpha_m - \alpha_n)} e^{jr\alpha_m} e^{js\theta} \tag{4}$$

where:

- m, n – the index of arbitrary stator and rotor windings,
- α_m – the angle between the individual stator winding magnetic axes and the stator reference axis,
- α_n – the angle between the individual rotor winding magnetic axis and the rotor reference axis,
- r, s – indices depending on the harmonic orders of the permeance function, representing the geometry of a rotor and stator air gap sides.

In this paper, the self and mutual inductances for the distributed stator windings and rotor damping bars are determined using the FEMM program in 2D [16]. In the case of 2D programs, the end leakage inductance should be calculated using, for example, the analytical technique [19–20].

Moreover, in this paper, for the linear circuit model, the influence of the higher harmonic contents of the $\mathbf{L}_s(\theta)$ in the stator natural reference frame *abc*, as well as $\mathbf{L}_{dq0}(\theta)$ in the rotor reference frame *dq*0 are presented. The $\mathbf{L}_{sr}(\theta)$, $\mathbf{L}_{rs}(\theta)$ and $\mathbf{L}_r(\theta)$ matrices (3) are not taken into account in this paper.

In the circuital modeling of a synchronous generator, apart from choosing suitable reference frames, another serious problem is the presence of the damping circuits [4, 5, 8, 11, 21, 22]. As shown in [23, 24] due to the presence of the damping circuits on the rotor, the *THDu* (total harmonic distortion) in induced stator voltage in the no-load state is higher than in the case of the rotor without the damping circuits. This is due to the components $\mathbf{L}_{sr}\mathrm{d}\mathbf{i}_r/\mathrm{d}t$ in a circuital model, where, the current derivative $\mathrm{d}\mathbf{i}_r/\mathrm{d}t$ in some damping bars of the examined 5.5 kVA salient pole synchronous generator has a value of almost 20 kA/s [23]. The most important aspect of computing the damper circuit in a synchronous and a squirrel cage motor is to obtain the current distribution in damping bars. Classical calculation of current distribution in damping bars on the rotor is usually performed analytically [1, 3–6,

8, 24]. This paper shows a proposed method of modeling the damping circuits on the rotor of a salient pole synchronous generator on the example of 10 damping bars on the rotor.

In this paper, the self and mutual inductances $\mathbf{L}_s(\theta)$ in expression (3) and $\mathbf{L}_{dq0}(\theta)$ in expression (2) are carried out on the basis of the real construction data of a salient pole synchronous generator rated: S_N = 5.5 kVA; U_N = 400 V (*Y*); n_N = 3000 rpm; I_N = 7.9 A; $\cos\varphi_N$ = 0.8; Q_s = 24 (number of stator slots) factory single-layer winding; 10-damping bars shorted by two ring segments. Moreover, the number of pole pairs p = 1, a rotor with and without the skew is taken into account (the factory rotor skew α_q is equal to 15° and is equal to stator slot pitch). Calculating the self and mutual inductance distributions (as a function of the stator currents and electrical rotor position angle θ) are carried out in the FEMM 2D software and a linear and nonlinear magnetic circuit are taken into account. In the FEMM 2D software, the skew effect is obtained by subdividing the active rotor length into 5 skewed axial slides along the axial length. An inductance distribution with the rotor skew L_{mns} is calculated as [7]:

$$L_{mns} = \frac{1}{\alpha_q} \int_{\theta-\frac{\alpha_q}{2}}^{\theta+\frac{\alpha_q}{2}} L_{mn} \partial\theta \tag{5}$$

where:

α_q – an electrical rotor skew,

L_{mns}, L_{mn} – the inductance with and without a rotor skew, respectively.

A method of determining the self and mutual inductance distributions in the 2D FEMM program is detailed presented in [23, 25].

2. Stator winding self and mutual inductances

Figure 1 presents magnetic flux distribution lines of the examined 5.5 kVA nonlinear salient pole synchronous generator with 10 damping bars (5 bars per pole). In Figure 1, an example of slot leakage flux which penetrates the rotor pole pieces is shown. In Figure 1,

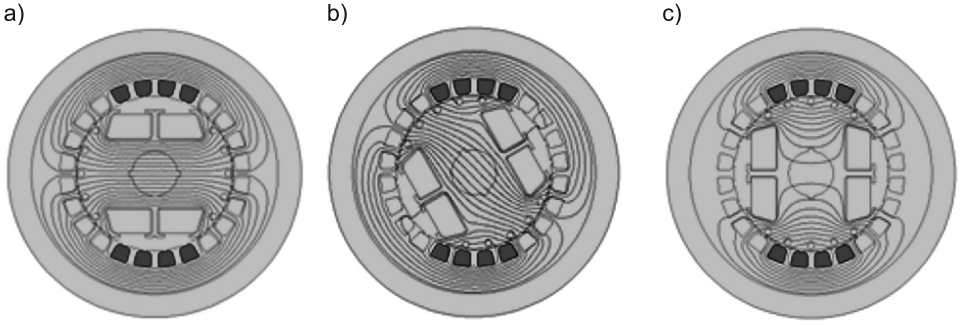

Fig. 1. Influence of the rotor position on magnetic field distribution and slot leakage flux: a) θ = 0 deg, b) θ = 55 deg, c) θ = 90 deg

the total field on the rotor position is presented. At θ = 90°, the total field can also be observed, but in *q* axis.

The magnetic field distribution, shown in Fig. 1, is obtained from stator current flowing in the phase winding *a* (in Fig. 1– four upper and four lower slots). Figure 2a–d shows the distributed stator winding self and mutual inductances for the linear and nonlinear model L_a, L_{an} (without the skew), L_{as}, L_{asn} (with the skew) and L_{ab}, L_{abn} (without the skew), L_{abs}, L_{absn} (with the skew) versus the electrical angular position of the rotor for the nominal stator current I_N = 7.9 A.

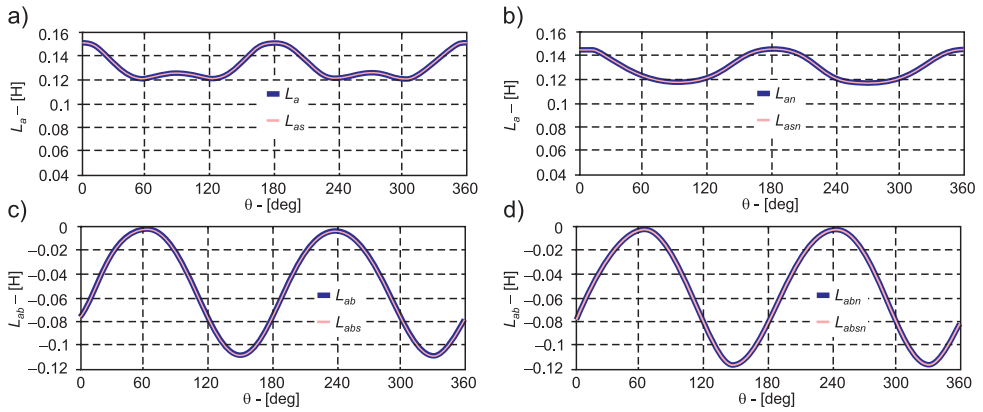

Fig. 2. Comparison of distribution of the stator winding self and mutual inductances versus the angular position of the rotor with the skew (index s) and without the skew for linear and nonlinear model: a) L_{as}, L_a, b) L_{asn}, L_{an}, c) L_{abs}, L_{ab}, d) L_{absn}, L_{abn}

In Figure 3, the comparison of distribution of the stator winding self and mutual inductances (Fig. 2) due to Fourier analysis is presented.

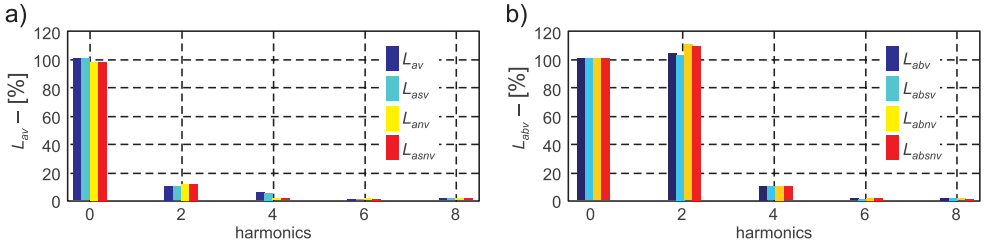

Fig. 3. Comparison of distribution of the stator winding self and mutualinductances with and without the rotor skew: a) L_{as}, L_a for linear model, L_{asn}, L_{an} for nonlinear model, b) L_{abs}, L_{ab} for linear model, L_{absn}, L_{abn} for nonlinear model

From presented the self and mutual stator inductance distributions (Fig. 2) and the higher harmonic contents (Fig. 3), it can be concluded that one rotation of the rotor makes the two--fold change of the magnetic permeability in the *d* and *q* axes and introduces a significant

inductance variation in each stator winding. Moreover, the value of the leakage flux varies depending on the electrical angular position of the rotor. This results in the largest participation of even harmonics in the distribution of the mutual stator inductances, among which, the most significant is the 2nd harmonic significantly greater than the second harmonic magnitude of the self-inductance (of the stator winding). A large participation of the second harmonic magnitude is the result of the participation of the slot leakage flux which even penetrates the rotor pole pieces [19]. The amplitudes of the higher harmonic components lying near the fundamental component due to the rotor skew (α_q = 15 deg) and are only reduced to a small extent. The reduction of spatial harmonic distribution of the self and mutual inductances by the skew of the rotor for the examined synchronous generator is presented in detail in [25].

3. A distribution of the self and mutual stator inductances in the *dq*0-axes

Figure 4 shows a comparison of the distribution of the self and mutual inductances in *dq*0-axes for the linear and nonlinear model with and without the rotor skew versus the electrical angular rotor position. The distributions are calculated on the basis of relationships (1) and (3) whilst taking into account the self and mutual stator inductances (Fig. 2). The self and mutual inductances in the *dq*0-axes after Park's transformation of the matrix $\mathbf{L}_s(\theta,\mathbf{i}_s)$ (3) are presented in detail in the paper [7].

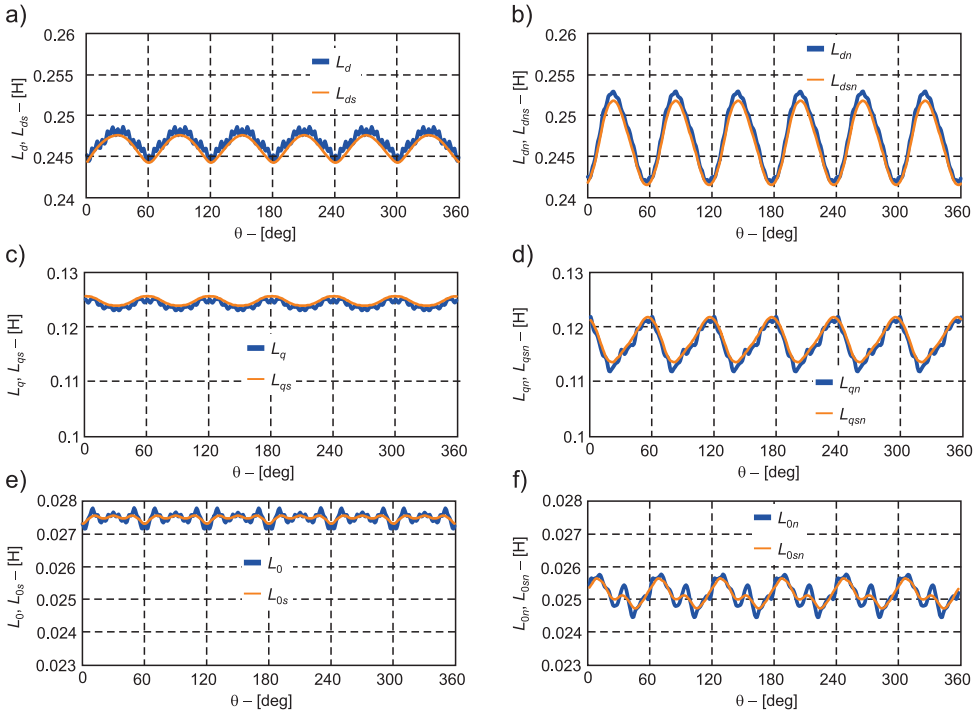

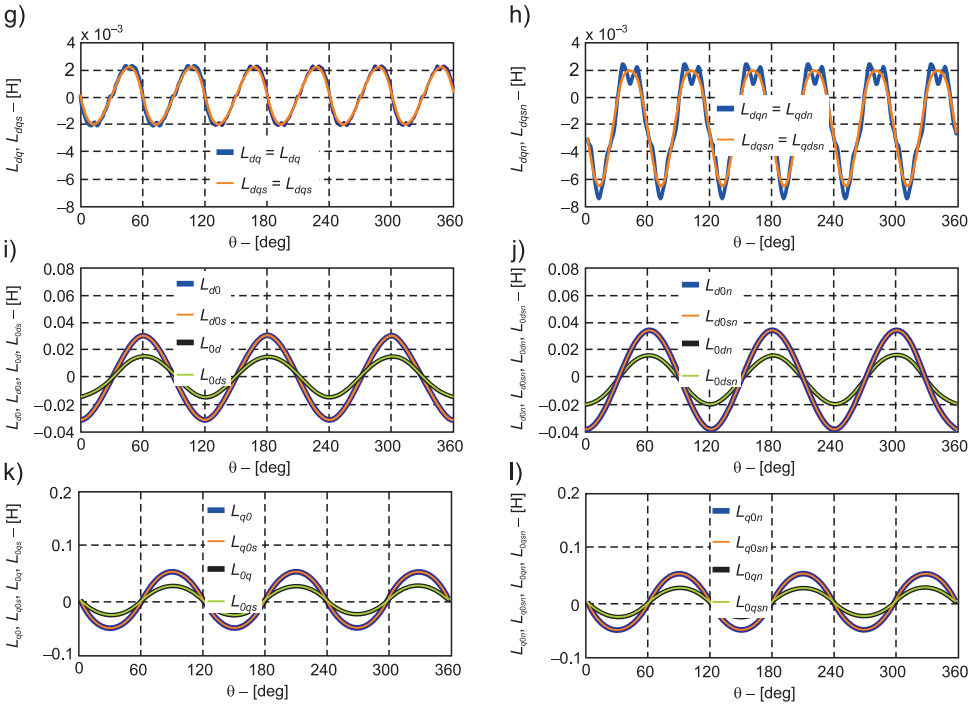

Fig. 4. Comparison of the self and mutual inductance distributions in the $dq0$-axes with and without the skew for linear and nonlinear model: a) L_d and L_{ds}, b) L_{dn} and L_{dsn}, c) L_q and L_{qs}, d) L_{qn} and L_{qsn}, e) L_0 and L_{0s}, f) L_{0n} and L_{0sn}, g) $L_{dq}(L_{qd})$ and $L_{dqs}(L_{qds})$, h) $L_{dqn}(L_{qdn})$ and $L_{dqsn}(L_{qdsn})$, i) L_{d0}, L_{0d} and L_{d0s}, L_{0ds}, j) L_{d0n}, L_{0dn} and L_{d0sn}, L_{0dsn}, k) L_{q0}, L_{0q} and L_{q0s}, L_{0qs}, l) L_{q0}, L_{0q} and L_{q0s}, L_{0qs}

If the self and mutual inductances of the stator windings contain the constant component, the 2nd and the higher harmonics, than the self and mutual inductances in the $dq0$-axes depend on the rotor position angle (Fig. 4). In the self inductance distributions, L_d, L_q, L_0 and in the mutual ones L_{dq} and L_{qd} dominate 6th harmonic. In other mutual inductance distributions, L_{d0}, L_{0d} and L_{q0}, L_{0q} dominate 3rd harmonic.

4. Modeling the damping circuits on the rotor

In dynamic states, the electromagnetic properties of a salient pole synchronous generator depend on the presence of the damping circuits [8, 11, 21, 22]. On the one hand, the damping circuits allow for shortening many transients' stages, e.g. the hunting, reducing higher harmonics in the field winding current [6, 22]. On the other hand, the damping circuits, due to higher harmonic currents, have an influence upon increasing higher harmonic contents in induced stator phase voltages (and armature currents in load states) in synchronous generator [6, 23]. The way of representation elements of damping circuits in circuital model has an

influence on the induced voltage waveforms in the stator windings, in the field winding and in the damping bars [11, 12, 21, 23]. There are many ways to obtain the parameters of the damping circuits, e.g. in an experimental and an analytical way or FEM methods [11, 12, 21]. The classical calculation of currents in the damping circuits on the rotor of a synchronous generator and an induction motor is usually performed analytically [1, 3, 21, 24]. In Figure 5, equivalent circuit parameters of damping circuits for the salient pole synchronous generator in the rotor natural reference frame is presented [5]. The damping circuit consists of ten damping bars and elements of end rings.

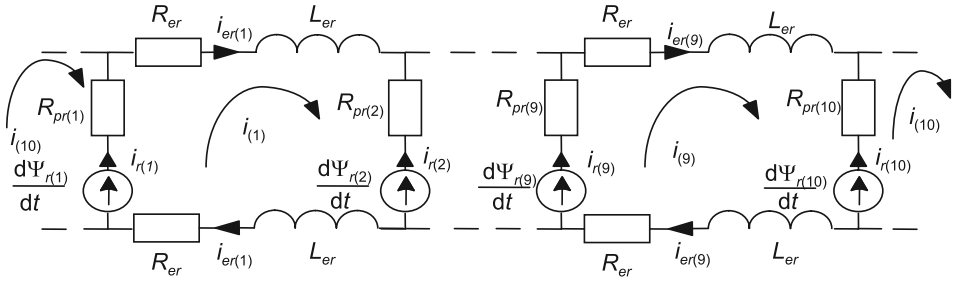

Fig. 5. Equivalent circuit parameters of ten damping circuits

Shown in Figure 1, each element in the circuits denotes [5]:

- in the k-th damping bar: R_{pr} resistive element and $e_{r(k)} = d\Psi_{r(k)}/dt$ induced voltage in the inductance lying in the pole piece in the area of the main flux,
- in the k-th segment of short circuital ring element: R_{er} resistive and L_{er} leakage inductance lying in the area outside the main flux. These elements for 2D models are calculated in an analytical way.

The inductances and resistances of the damping circuits (Fig. 5) can be described by means of the methods of circuit theory in the following forms [1, 3, 5, 24]:

$$\mathbf{R}_{rr} = \begin{bmatrix} 2(R_{pr}+R_{er}) & -R_{er} & 0 & 0 & \dots & -R_{er} \\ -R_{er} & 2(R_{pr}+R_{er}) & -R_{er} & 0 & \dots & 0 \\ 0 & -R_{er} & 2(R_{pr}+R_{er}) & -R_{er} & \dots & 0 \\ \dots & \dots & \dots & \dots & \dots & 0 \\ -R_{er} & 0 & 0 & 0 & -R_{er} & 2(R_{pr}+R_{er}) \end{bmatrix} \tag{6}$$

$$\mathbf{L}_{\sigma rr} = \begin{bmatrix} 2(L_{\sigma pr}+L_{er}) & -L_{er} & 0 & 0 & \dots & -L_{er} \\ -L_{\sigma er} & 2(L_{\sigma pr}+L_{er}) & -L_{er} & 0 & \dots & 0 \\ 0 & -L_{er} & 2(L_{\sigma pr}+L_{er}) & -L_{er} & \dots & 0 \\ \dots & \dots & \dots & \dots & \dots & 0 \\ -L_{er} & 0 & 0 & 0 & -L_{er} & 2(L_{\sigma pr}+L_{er}) \end{bmatrix} \tag{7}$$

$$\mathbf{L}_{rr}(\theta,\mathbf{i}_r)=\begin{bmatrix} L_{r(1)}(\theta,\mathbf{i}_r) & L_{r(1,2)}(\theta,\mathbf{i}_r) & L_{r(1,3)}(\theta,\mathbf{i}_r) & L_{r(1,4)}(\theta,\mathbf{i}_r) & \dots & L_{r(1,10)}(\theta,\mathbf{i}_r) \\ L_{r(2,1)}(\theta,\mathbf{i}_r) & L_{r(2)}(\theta,\mathbf{i}_r) & L_{r(2,3)}(\theta,\mathbf{i}_r) & L_{r(2,4)}(\theta,\mathbf{i}_r) & \dots & L_{r(2,10)}(\theta,\mathbf{i}_r) \\ L_{r(3,1)}(\theta,\mathbf{i}_r) & L_{r(3,2)}(\theta,\mathbf{i}_r) & L_{r(3)}(\theta,\mathbf{i}_r) & L_{r(3,4)}(\theta,\mathbf{i}_r) & \dots & L_{r(3,10)}(\theta,\mathbf{i}_r) \\ \dots & \dots & \dots & \dots & \dots & \dots \\ L_{r(10,1)}(\theta,\mathbf{i}_r) & L_{r(10,2)}(\theta,\mathbf{i}_r) & L_{r(10,3)}(\theta,\mathbf{i}_r) & L_{r(10,4)}(\theta,\mathbf{i}_r) & \dots & L_{r(1,10)}(\theta,\mathbf{i}_r) \end{bmatrix} \tag{8}$$

where:

$L_{r(k)}$, $L_{r(k,\,l)}$ – self and mutual inductances in the k-th damping circuits,
L_{er} – leakage inductance of end ring elements,
$L_{\sigma pr}$ – leakage inductance of damping circuits,
k,l – indexes in the k-th and l-th damping circuits,
$\mathbf{R}_{rr}$ – matrix of resistive of damping bars and shorted ring elements,
$\mathbf{L}_{\sigma rr}$ – matrix of leakage inductance,
$\mathbf{L}_{rr}$ – matrix of self and mutual inductances of damping circuits.
$\mathbf{i}_r$ – matrix of damping circuit currents $[i_{r(1)}, \dots, i_{r(k)}]^T$.

Elements R_{er} and L_{er} of the circuital ring segments (shown in Fig. 5) can be reduced to another form, creating a circuit diagram of the damping cage as shown in Fig. 6 [5]. As shown in the paper, the self and mutual inductance distributions in the $dq0$-axes are dependent on the angle position of the rotor. Moreover, the Park's transformation of the higher harmonics of the stator self and mutual inductance distributions to the $dq0$-axes does not eliminate the influence of the rotor position angle and, in simulations only, introduces additional unnecessary calculations [7]. Hence, in simulations of a salient pole synchronous

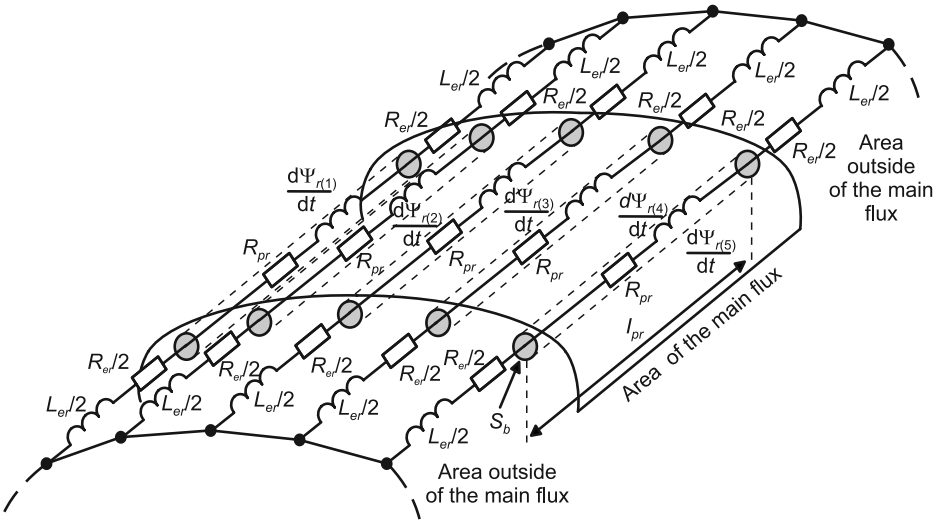

Fig. 6. Equivalent circuit parameters of damping circuits with elements lying with area of main flux and area outside of the main flux

generator, the induced phase stator voltages u_a, u_b and u_c and stator currents i_a, i_b and i_c are easier to carry out with a circuital model in the stator and rotor natural reference frame.

Figure 7 shows the equivalent circuit parameters of a synchronous generator in a no-load state in the stator and rotor natural reference frame. The equivalent circuit parameters represent the stator windings, the field winding and shorted equivalent 5-damping bars per pole. Equivalent resistances $R_{r(k)}$ for $k = \{1, 2, \ldots 10\}$ damping bars and equivalent leakage inductances L'_{er} can be expressed as [5]:

$$R_{r(k)} = R_{pr(k)} + \frac{R_{er(k)}}{2(\sin\alpha_{Q_{r(k)}})^2} = R_{pr}(k) + R'_{er(k)} \quad \text{and} \quad L'_{er(k)} = \frac{L_{er(k)}}{2(\sin\alpha_{Q_{r(k)}})^2} \tag{9}$$

where:

$\alpha_{Q_{r(k)}}$ – is the angle between the equivalent k-th rotor damping bar (with ring elements) and the rotor reference axis $\alpha_{Q_{r(k)}} = \pi p / Q_r$,

Q_r – number of damping bars per pole.

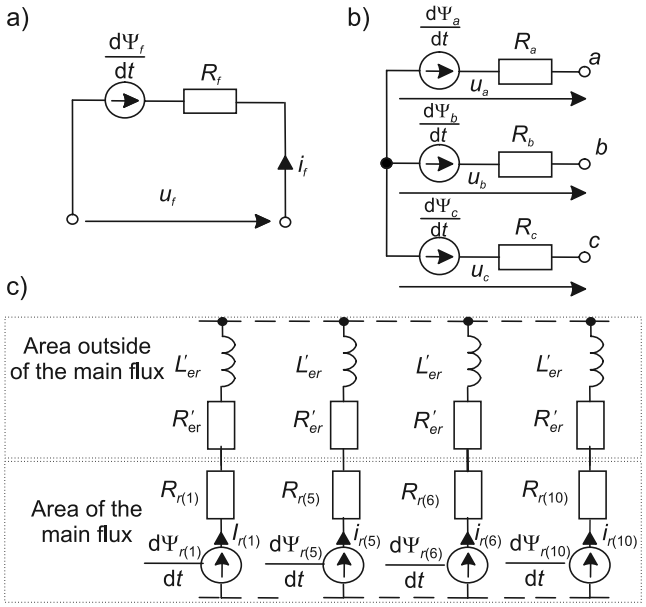

Fig. 7. Equivalent circuit parameters of a salient pole synchronous generator in the stator and rotor natural reference frame in the no-load state: a) field winding, b) stator windings, c) damping circuits reduced to single phases

As shown in [23] in the no-load steady state in the damping bars, the amplitude of higher harmonic currents $i_{r(k)v}$ are very small. So, for the non-linear model, the influence of the $i_{r(k)v}$ currents on the self and mutual inductance distributions and the field winding ampere conductors can be omitted. In the no-load steady state, it can be assumed that the self and mutual inductance distributions are dependent only on the electrical angle of the

rotor position θ and field current i_f. From the equivalent circuit of a salient pole synchronous generator (Fig. 7), the voltage u_a, u_b and u_c of induced in the three-phase armature windings, the voltage $d\Psi_{r(k)}(\theta, i_f)/dt$ induced in the the *k*-th damping bar (taking into account the field winding and the electrical angle of the rotor position)can be derived from the equations in stator coordinates (for the stator windings – Fig. 7) and in rotor coordinates (for the field winding and damping bars – Fig. 7)

$$\frac{d\psi_a(\theta,i_f)}{dt} = u_a, \quad \frac{d\psi_b(\theta,i_f)}{dt} = u_b, \quad \frac{d\psi_c(\theta,i_f)}{dt} = u_c \tag{10}$$

$$\frac{d\psi_f(\theta,i_f)}{dt} + R_f i_f = u_f \tag{11}$$

$$\frac{d\psi_{r(k)}(\theta,i_f)}{dt} + R_{r(k)} i_{r(k)} + L_{er}\frac{i_{r(k)}}{dt} = 0 \tag{12}$$

$$\frac{d\theta}{dt} = p\omega \quad \text{and} \quad i_{r(1)} + i_{r(2)} + \ldots + i_{r(k)} = 0 \tag{13}$$

where:

- a, b, c, f – indexes of stator windings and field winding,
- $r(k)$ – index of *k*-th-damping bar,
- Ψ_a, Ψ_b, Ψ_c – stator linkage fluxes,
- u_a, u_b,u_c – stator phase voltages,
- i_f – field current,
- R_f – resistance of field winding,
- $\Psi_{r(k)}$ – *k*-th-damping bar linkage flux,
- $R_{r(k)}$ – resistance of the equivalent *k*-th-damping bars and ring elements,
- $i_{r(k)}$ – current in equivalent *k*-th damping bars and ring elements,
- θ – electrical angle of the rotor position,
- ω – electrical angular velocity.

In equations (10)–(12),the differential linkage fluxes in no-load steady state can be derived from the equations [5]:

$$\frac{d\boldsymbol{\Psi}_{sfr}(\theta,i_f)}{dt} = \frac{d\theta}{dt}\frac{\partial \mathbf{L}_{sfr}(\theta,i_f)}{\partial\theta}\mathbf{i}_{sfr} + \mathbf{L}_{sfr}(\theta,i_f)\frac{d\mathbf{i}_{sfr}}{dt} \tag{14}$$

where:

- $\mathbf{i}_{sfr}$ – matrix of stator currents (i_a, i_b, i_c are equal to 0), field current and currents in equivalent *k*-thdamping bars and ring elements $[i_a, i_b, i_c, i_f, i_{r(1)}, \ldots, i_{r(k)}]^T$,
- $\boldsymbol{\Psi}_{sfr}$ – matrix of linkage fluxes of stator windings, field winding, andequivalent *k*-th damping bars $[\Psi_a, \Psi_b, \Psi_c, \Psi_f, \Psi_{r(1)}, \ldots, \Psi_{r(k)}]^T$, $\boldsymbol{\Psi}_{sfr} = \mathbf{L}_{sfr}\mathbf{i}_{sfr}$,
- $\mathbf{L}_{sfr}$ – matrix of self and mutual inductances of stator-to-rotor windings and damping bars (and ring elements).

The matrix $\mathbf{L}_{sfr}$for $k = 10$ damping bars in no-load steady state can be expressed as [5]:

$$\mathbf{L}_{sfr}(\theta,i_f)=\begin{bmatrix} L_a+L_{es} & L_{ab} & L_{ac} & L_{af}(\theta,i_f) & L_{ar(1)}(\theta,i_f) & \dots & L_{ar(10)}(\theta,i_f) \\ L_{ba} & L_b+L_{es} & L_{bc} & L_{bf}(\theta,i_f) & L_{br(1)}(\theta,i_f) & \dots & L_{br(10)}(\theta,i_f) \\ L_{ca} & L_{cb} & L_c+L_{es} & L_{cf}(\theta,i_f) & L_{cr(1)}(\theta,i_f) & \dots & L_{cr(10)}(\theta,i_f) \\ L_{fa}(\theta,i_f) & L_{fb}(\theta,i_f) & L_{fc}(\theta,i_f) & L_f(\theta,i_f)+L_{ef} & L_{fr(1)}(\theta,i_f) & \dots & L_{fr(10)}(\theta,i_f) \\ L_{r(1)a}(\theta,i_f) & L_{r(1)b}(\theta,i_f) & L_{r(1)c}(\theta,i_f) & L_{r(1)f}(\theta,i_f) & L_{r(1)}(\theta,i_f)+L_{er} & \dots & L_{r(10)}(\theta,i_f) \\ \dots & \dots & \dots & \dots & \dots & \dots & \dots \\ L_{r(10)a}(\theta,i_f) & L_{r(10)b}(\theta,i_f) & L_{r(10)c}(\theta,i_f) & L_{r(10)f}(\theta,i_f) & L_{r(10,1)}(\theta,i_f) & \cdots & L_{r(10)}(\theta,i_f)+L_{er} \end{bmatrix} \tag{15}$$

The stator to damping bar mutual inductance distributions $L_{sr(k)}(\theta, i_f)$, $L_{r(k)s}(\theta, i_f)$, the field winding to damping bars mutual inductance distributions $L_{fr(k)}(\theta,i_f)$, $L_{r(k)f}(\theta,i_f)$, and the damping bar self inductance distributions $L_{r(k)}(\theta, i_f)$ are determined for the same core permeability which occurs in no-load state when the field winding constitutes the only magnetomotive force, whereas $s = \{a, b, c\}$. From expressions (10)–(15) and $\mathbf{L}_{sfr} = \mathbf{L}_{sfr}(\theta,i_f)$ the u_a, u_b and u_c can be expressed:

$$\begin{bmatrix} u_a \\ u_b \\ u_c \\ u_f \\ 0 \\ \dots \\ 0 \end{bmatrix} = \left\{ \omega\frac{\partial\mathbf{L}_{sfr}(\theta,i_f)}{\partial\theta} + \begin{bmatrix} R_a & 0 & 0 & 0 & 0 & \dots & 0 \\ 0 & R_b & 0 & 0 & 0 & \dots & 0 \\ 0 & 0 & R_c & 0 & 0 & \dots & 0 \\ 0 & 0 & 0 & R_f & 0 & \dots & 0 \\ 0 & 0 & 0 & 0 & R_{r(1)} & \cdots & 0 \\ 0 & 0 & 0 & 0 & 0 & \dots & 0 \\ 0 & 0 & 0 & 0 & 0 & \dots & R_{r(10)} \end{bmatrix} \right\} \begin{bmatrix} 0 \\ 0 \\ 0 \\ i_f \\ i_{r(1)} \\ \dots \\ i_{r(10)} \end{bmatrix} + \mathbf{L}_{sfr}(\theta,i_f)\frac{d}{dt}\begin{bmatrix} 0 \\ 0 \\ 0 \\ i_f \\ i_{r(1)} \\ \dots \\ i_{r(10)} \end{bmatrix} \tag{16}$$

From (16) results:

$$\mathbf{u}_{sfr} = \left(\omega\frac{\partial\mathbf{L}_{sfr}(\theta,i_f)}{\partial\theta} + \mathbf{R}_{sfr} \right)\mathbf{i}_{sfr} + \mathbf{L}_{sfr}(\theta,i_f)\frac{\mathrm{d}\mathbf{i}_{sfr}}{\mathrm{d}t} \tag{17}$$

where:

- $\mathbf{u}_{sfr}$ – matrix of induced stator phase voltages, field voltage and shorted damping bars voltages $[u_a, u_b, u_c, u_f, 0, \dots, 0]^T$,
- R_a, R_b, R_c – stator winding resistances,
- $\mathbf{R}_{sfr}$ – diagonal matrix of resistance of the stator windings, the field winding, the 10 damping bars and ring elements.

From expression (16) results, that in no-load state of the synchronous generator the circuit model of the field winding and the equivalent 10 damping bars (with the ring segments) can be expressed as [5]:

$$\begin{bmatrix} u_f \\ 0 \\ \dots \\ 0 \end{bmatrix} = \left\{ \omega \frac{\partial}{\partial \theta} \begin{bmatrix} L_f(\theta, i_f) + L_{ef} & L_{fr(1)}(\theta, i_f) & \dots & L_{fr(10)}(\theta, i_f) \\ L_{r(1)f}(\theta, i_f) & L_{r(1)}(\theta, i_f) + L_{er} & \dots & L_{r(1,10)}(\theta, i_f) \\ \dots & \dots & \dots & \dots \\ L_{r(10)f}(\theta, i_f) & L_{r(1,10)}(\theta, i_f) & \dots & L_{r(10)}(\theta, i_f) + L_{er} \end{bmatrix} + \begin{bmatrix} R_f & 0 & \dots & 0 \\ 0 & R_{r(1)} & \dots & 0 \\ \dots & \dots & \dots & \dots \\ 0 & 0 & \dots & R_{r(10)} \end{bmatrix} \right\} \times$$

$$\times \begin{bmatrix} i_f \\ i_{r(1)} \\ \dots \\ i_{r(10)} \end{bmatrix} + \left[\begin{bmatrix} L_f(\theta, i_f) + L_{ef} & L_{fr(1)}(\theta, i_f) & \dots & L_{fr(10)}(\theta, i_f) \\ L_{r(1)f}(\theta, i_f) & L_{r(1)}(\theta, i_f) + L_{er} & \dots & L_{r(1,10)}(\theta, i_f) \\ \dots & \dots & \dots & \dots \\ L_{r(10)f}(\theta, i_f) & L_{r(1,10)}(\theta, i_f) & \dots & L_{r(10)}(\theta, i_f) + L_{er} \end{bmatrix} \right] \frac{\mathrm{d}}{\mathrm{d}t} \begin{bmatrix} i_f \\ i_{r(1)} \\ \dots \\ i_{r(10)} \end{bmatrix} \tag{18}$$

A method of determining the self and mutual inductance distributions of stator-to-rotor windings and damping bars (with ring elements) in (15)–(18) is detailed presented in [5, 7, 16, 23, 25]. Figure 8 presents the mutual inductance distributions of field winding to damping bars $L_{r(1)f} - L_{r(5)f}$ and $L_{r(1n)f} - L_{r(5n)f}$ and the derivative distributions $\partial L_{r(1)f}/\partial\theta - \partial L_{r(3)f}/\partial\theta$ and $\partial L_{r(1n)f}/\partial\theta - \partial L_{r(3n)f}/\partial\theta$ for a linear and a nonlinear magnetic circuit of the examined 5.5 kVA with the rotor without skew. The initial length of the air gap of the pole piece in the longitudinal axis of the rotor is equal to $\delta_0 = 0.55$ mm. The simulations are carried out in the FEMM program under no-load in a steady state (I_f = const.).

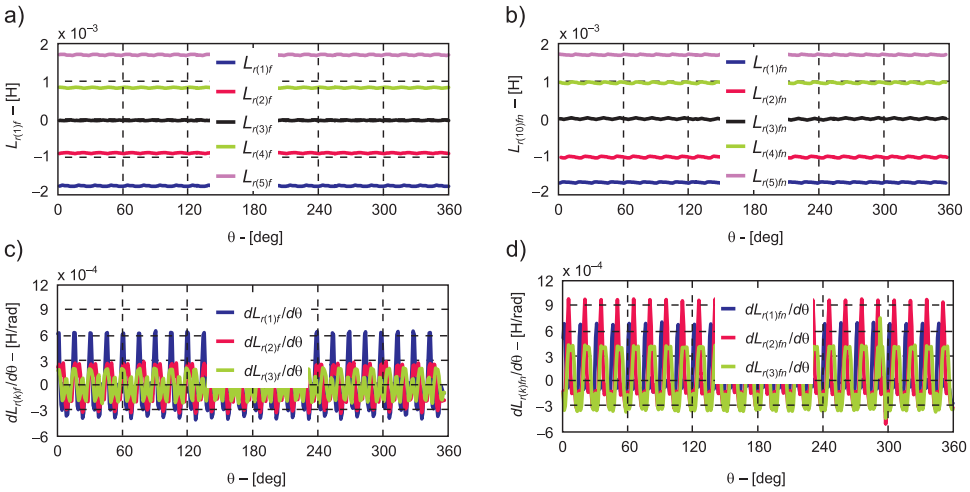

Fig. 8. Comparison of the field winding to damping bar mutual distributions without the rotor skew for linear and nonlinear model of: a) inductances $L_{r(1)f} - L_{r(5)f}$ ($L_{r(6)f} - L_{r(10)f}$), b) inductances $L_{r(1)fn} - L_{r(5)fn}$ ($L_{r(6)fn} - L_{r(10)fn}$), c) derivatives $\partial L_{r(1)f}/\partial\theta - \partial L_{r(3)f}/\partial\theta$, d) derivatives $\partial L_{r(1)fn}/\partial\theta - \partial L_{r(3)fn}/\partial\theta$

5. Experimental verification

Figure 9 shows a measurement set for the investigation of the 5.5 kVA salient pole synchronous generator with the special construction of the rotor(the additional two sets of rings connected to the 5 damping bars per pole). Experimental verification of the induced voltages in the damping bars without the rotor skew are performed under no-load of the 5.5 kVA salient pole synchronous generators. During the investigations, the damping bars were opened ($i_{r(1)} - i_{r(5)}$ were equal to zero) and the field winding was powered by a DC voltage source. The voltages in the 4 damping bars were registered using a four-channel digital oscilloscope. From (18) results that $u_{r(1)} = \omega\partial L_{r(1)fn}/\partial\theta$, $u_{r(2)} = \omega\partial L_{r(2)fn}/\partial\theta$, $u_{r(3)} = = \omega\partial L_{r(3)fn}/\partial\theta$, $u_{r(4)} = \omega\partial L_{r(4)fn}/\partial\theta$ and $u_{r(5)} = \omega\partial L_{r(5)fn}/\partial\theta$. In Figure 10, registered waveforms of $u_{r(1)}$ (Channel 1), $u_{r(2)}$ (Channel 2), $u_{r(3)}$ (Channel 3) and $u_{r(4)}$ (Channel 4) are presented.

Fig. 9. Measurement set for investigation of the induced voltages in the 5 damping bars of the 5.5 kVA salient pole synchronous generator with the special construction of the rotor

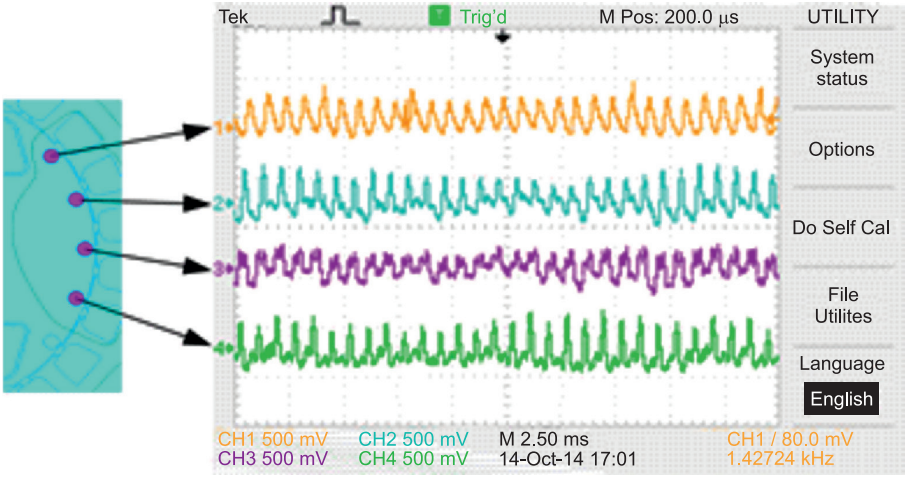

Fig. 10. Registered waveforms of the induced voltages in four damping bars under no-load conditions for the 5.5 kVA salient pole synchronous generator without the rotor skew

Registered waveforms of the induced voltages in four damping bars (Fig. 10) are very similar to the derivatives shown in Fig. 8. Deformations of the induced voltage in each damping bar result from vibrations of the rotor and the used measurement method (the induced voltages are registered between two brushes and two slip-rings).

6. Conclusion

This article presents two problems. The first is the analysis of the constant component and higher harmonic contents in the self and mutual inductance distributions in the stator natural reference frame *abc* and in the *dq*0-axes (in the rotor reference frame) for the linear and nonlinear (field) model of the salient pole synchronous generator-rated 5.5 kVA. The second problem is modeling the damping circuits on the rotor of a salient pole synchronous generator.

As shown in the paper, for the tested salient pole synchronous generator 5.5 kVA within the self and mutual stator inductance distributions, the most significant are the 2nd and 4th harmonics which are only influenced by the rotor skew to a small extent. Hence, the rotor skew on the inductance distributions in the stator natural reference frame *abc* and in the *dq*0--axes for linear and nonlinear model have little effect.

From comparison of the linear and nonlinear model, it results that the nonlinearity slightly increases the magnitudes of 2nd harmonic. The 2nd harmonic is six times greater in mutual inductance then in the self inductance distributions. For this reason, the 2nd harmonic of the slot leakage flux introduces an alternate component that is present in the L_{d0}, L_{0d}, L_{q0} and L_{0q} mutual inductances in *dq*0-axes with and without a rotor skew.

In the second problem, this article presents the experimental verification of the proposed method of modeling the resistance and self and mutual inductance distributions of damping bars, which is detailed presented in [5]. An important advantage of this method is:

- diagonal matrix of damping bar resistances in circuital models (written as the diagonal matrix of the stator winding resistances),
- a simple way of determining the self and mutual inductance distributions both for the stator windings, field winding and *k*-th damping bars (having an even or an odd number),
- the fact that the damping bars can be treated as a single phase winding.

References

[1] Sobczyk T.J., *Methodology of mathematical modeling of induction machines* (in Polish), WNT, Warsaw 2004.

[2] Sobczyk T.J., *Extreme possibilities of circuital models of electric machines*, Electrical Power Quality and Utilisation, 2006, Vol. 7, No. 2, 103-110.

[3] Staszak J., *Modeling the electromechanical characteristics of three-phase squirrel-cage induction motor by selection the stator windings and the power supply system* (in Polish), Wydawnictwo Politechniki Świętokrzyskiej, Monograph M31, Kielce 2012.

[4] Vicol L., Banyai A., Viorel I.A., Simond J.J., *On the damper cage bars' currents calculation for salient pole large synchronous machines*, Optimization of Electrical and Electronic Equipment, 11th International Conference on 22–24 May 2008, 9-14.
[5] Ludwinek K., *Proposed way of modeling the damping circuits on the rotor of a salient pole synchronous generator* (in Polish), Zeszyty Problemowe – Maszyny Elektryczne, 2014, No. 104, Komel, Katowice, 179-186.
[6] Ludwinek K., *Model of synchronous machine for co-operation with distorted and asymmetrical electric power system* (in Polish), Zeszyty Naukowe Politechniki Świętokrzyskiej, Elektryka, 2005, No. 42, Kielce, 239-250.
[7] Ludwinek K., *Some aspects of representation of inductance distributions in dq0-axes in a salient pole synchronous generator*, Zeszyty Problemowe – Maszyny Elektryczne, 2014, No. 104, Komel, Katowice, 187-184.
[8] Zajczyk R., *Mathematical models of power system for examination of electro-mechanical unsteady states and control processes* (in Polish), Gdańsk University of Technology, Gdańsk 2003.
[9] Vermeulen H.J., Strauss J.M., Shikoana V., *Online estimation of synchronous generator parameters using PRBS perturbations*, IEEE Transactions on Power Systems, 2002, Vol. 17, No. 3, 674-700.
[10] Ludwinek K., Staszak J., *Possibility of graphical environment applications for evaluating of equivalent circuit parameters and time constants*, Przegląd Elektrotechniczny, 2011, No. 12a, 195-200.
[11] Berhausen S., Boboń A., Paszek S., *A methodology for determining electromagnetic parameters of a synchronous machine based on analysis of transient waveforms obtained by the finite element method under no-load conditions*, Zeszyty Problemowe – Maszyny Elektryczne, no. 84, 2009, published by Komel Katowice, Poland, 29-32.
[12] Berhausen S., Boboń A., *A field method for determining parameters and characteristics of a synchronous machine* (in Polish), Zeszyty Problemowe – Maszyny Elektryczne, 2011, No. 91, Komel, Katowice, 43-49.
[13] Danhong Z., *Finite element analysis of synchronous machines*, Doctor's Thesis, Pennsylvania State University, 2009.
[14] Demenko A., Pietrowski W., Stachowiak D., *Flux density calculation in permanent magnet machine using edge element method*, Przegląd Elektrotechniczny, 2005, No. 10, 2-7.
[15] Burlikowski W., *Comparison of different implementations of reluctance motor simulational model*, Proceedings of XLIII International Symposium on Electrical Machines, Poland, Poznań, 2–5 Juny, 2007, 147-150.
[16] http://www.femm.info/wiki/HomePage.
[17] Skwarczyński J., *Salient poles inner asymmetries* (in Polish), Scientific Bulletins of Stanisław Staszic Academy of Mining and Metallurgy, Electrotechnics, Bulletin 16, 1990.
[18] Tessarolo A., *Accurate Computation of Multiphase Synchronous Machine Inductances Based on Winding Function Theory*, IEEE Transactions on Energy Conversion, 2012, vol. 27, 895-904.
[19] Dąbrowski M., *Design of alternating current electrical machines* (in Polish), WNT, Warsaw 1994.
[20] Freese M., Kulig S., *Influence of constructional turbo-generator end region design on end winding inductances*, Archives of Electrical Engineering, 2012, Vol. 61, No. 2, 199-210.
[21] Paszek S., Berhausen S., Boboń A., Majka Ł., Nocoń A., Pasko M., Pruski P., Kraszewski T., *Mesurement Estimation of Dynamic Parameters of Synchronous Generators and Excitation Systems Working in the National Power System*, Monograph, Wydawnictwo Politechniki Ślaskiej, Gliwice 2013.

[22] Nadolski R., Staszak J., Harbaoui L., *Consideration of solid rotor damping circuit in natural hunting of turbogenerator*, Archives of Electrical Engineering, 1998, Vol. 47, No. 2, 233-243.
[23] Ludwinek K., *Influence of Representation of the Stator to Rotor Mutual Inductances on the Induced Phase Voltage Waveforms in a Salient Pole Synchronous Generator*, Zeszyty Problemowe – Maszyny Elektryczne, 2014, No. 104, Komel, Katowice, 147-154.
[24] Skwarczyński J., Weinreb K., *Method of Analysis of Slot Harmonics in the Salient-Pole Synchronous Generators*, International Conference on Electrical Machines (ICEM), Boston, MA, August 13–15, 1990, 1165-1170.
[25] Ludwinek K., *Representation of the stator to rotor self- and mutual inductances in a salient pole synchronous generator in the no-load state*, Zeszyty Problemowe – Maszyny Elektryczne, 2014, No. 104, Komel, Katowice, 147-154.

TECHNICAL TRANSACTIONS | **CZASOPISMO TECHNICZNE**
ELECTRICAL ENGINEERING | ELEKTROTECHNIKA
2-E/2015

WITOLD MAZGAJ*, BARTOSZ ROZEGNAŁ*, ZBIGNIEW SZULAR*

SWITCHING LOSSES IN THREE-PHASE VOLTAGE SOURCE INVERTERS

STRATY PRZEŁĄCZANIA W TRÓJFAZOWYCH FALOWNIKACH NAPIĘCIA

A b s t r a c t

The efficiency of three-phase voltage source inverters depends mainly on power losses that occur in semi-conductor elements. Total losses in these elements are a sum of conduction losses and switching losses. The switching losses are dependent on the supply voltage, load current, operating frequency and on the dynamic parameters of the switching elements; these losses can be limited with the use of soft switching methods. This paper discusses the switching loss dependence on the above mentioned factors. An analysis was carried out on power losses in voltage source inverters which generate the output voltage in the form of a rectangular wave and losses in these inverters operating with pulse width modulation. A comparison of switching losses was performed for two voltage source inverters with different nominal power ratings.

Keywords: *pulse width modulation*, *switching losses*, *voltage source inverter*

S t r e s z c z e n i e

Sprawność trójfazowch falowników napięcia zależy głównie od strat mocy występujących w elementach półprzewodnikowych. Straty w tych elementach są sumą strat przewodzenia i strat przełączania. Straty przełączania zależą od napięcia zasilania, prądu odbiornika, częstotliwości pracy oraz od parametrów dynamicznych tranzystorów IGBT; straty te mogą być ograniczone przez zastosowanie układów wspomagających przełączanie elementów. W artykule omówiono zależność strat przełączania od wymienionych czynników. Przeprowadzono analizę strat w falowniku generującym na wyjściu napięcie w postaci fali prostokątnej oraz analizę strat przełączania w falowniku pracującym z modulacją szerokości impulsów. Porównania strat przełączania dokonano dla dwóch falowników napięcia o różnych mocach znamionowych.

Słowa kluczowe: *falownik napięcia*, *modulacja szerokości impulsów*, *straty przełączania*

DOI: 10.4467/2353737XCT.15.087.3919

* Ph.D. D.Sc. Eng. Witold Mazgaj, M.Sc. Eng. Bartosz Rozegnał, Ph.D. Eng. Zbigniew Szular, Institute of Electromechanical Energy Conversion, Faculty of Electrical and Computer Engineering, Cracow University of Technology.

1. Introduction

The efficiency of power electronics devices is very high and is in the range from 97 to 99 percent. Despite this fact, many scientific centers still conduct studies which tend to improve this efficiency. This problem is significant, first of all, in three-phase voltage source inverters (VSI), which frequently operate with relatively high frequencies. Partially, this issue also concerns DC-DC converters, however, their application is much smaller than the use of the VSIs. Power losses in these inverters occur mainly in semi-conductor elements, first of all, in insulated gate bipolar transistors (IGBTs) and in their freewheeling diodes. Total power losses in semi-conductor elements are a sum of the conduction losses and the switching losses [1, 2]. The first kind of power losses depend mainly on a collector current and on the collector-emitter voltage of the given transistor. However, we do not have any influence on these losses because their reduction requires decreasing the collector-emitter voltage during a conduction state; this is only possible by technological procedures during the manufacture of IGBTs. It is worth underlining that the junction temperature can have a significant influence on the value of these losses.

The switching losses occur during both the transistor turn-on and turn-off processes and they depend on the following parameters: the voltage supplying the given three-phase VSI, the load current, and the dynamic parameters of the given IGBT; these parameters depend in varying degrees on the junction temperature and on the resistance in the gate-driver circuit. The switching losses can be reduced by use of soft switching methods [3, 4]. In these methods, the transistor current or the collector-emitter voltage should be close to zero during the turn-on and turn-off processes.

On the one hand, the pursuit of the reduced losses is to increase the efficiency of power electronic inverters; on the other hand, less switching losses should lead to an improvement of cooling conditions of IGBTs. Fulfillment of the second requirement is often more important than improvement of the efficiency, especially in medium and high power inverters – this has significant meaning when inverters operate with pulse width modulation (PWM). The determination of a transistor cooling method requires calculations, among others, the switching losses, which are one of the components of the heat source in any transistor thermal model.

2. Switching losses in insulated gate bipolar transistors

Total power losses in IGBTs are the sum of the conduction losses P_{con} and the switching losses P_{sw}. The first loss component is frequently described as follows:

$$P_{con} = \frac{1}{T_p} \int_0^{t_{con}} i_C(t)\, u_{CEsat}(t)\, dt \tag{1}$$

where:

T_p – switching period,
$i_C(t)$ – collector current,

$u_{CEsat}(t)$ – collector-emitter voltage during transistor conduction,
t_{con} – transistor conduction time.

The transistor conduction time t_{con} depends on the applied control method of the given electronic power device. The collector-emitter voltage during transistor conduction is a non--linear function of the transistor current. On average, this voltage is within the range of 1.5 V to 2.5 V. Scientific research and technological attempts tend to decrease the collector--emitter voltage during transistor conduction. In recent years, constructing injection--enhanced gate transistors has succeeded in significantly reducing this voltage to 1.3 V. It is worth underlining that in some cases, integrated gate commutated thyristors (IGCTs) are used instead of the IGBTs [5]. The conduction losses occurring in the freewheeling diodes can be estimated similarly to the transistor losses, but in this case, the diode conduction time depends on the switching moments of the IGBTs. The diode voltage during conduction intervals is higher than the voltage of typical silicon diodes, and it can even be equal to 2.0 V.

Quite often, the problem of switching losses in IGBTs is considered on the basis of different test circuits without taking into account a specific power electronics device [6–8]. However, estimation of total switching losses in electronic power converters, especially in voltage source inverters, should be carried out whilst taking into account an applied circuit of overvoltage protection. Most frequently, this protection circuit consists of a capacitor, resistor, and fast diode, but these elements can be connected in two ways; both versions of the overvoltage protection circuit (RDC snubber) are shown in Figs. 1 and 2 [9–11]. It is necessary to stress that the chosen protection circuit can significantly influence the switching processes of the IGBTs and thereby affects the switching losses. Total switching losses in VSIs also depend on losses in resistors of the gate-driver circuits, and on losses relating to the occurrence of parasitic inductances in the DC supply circuit.

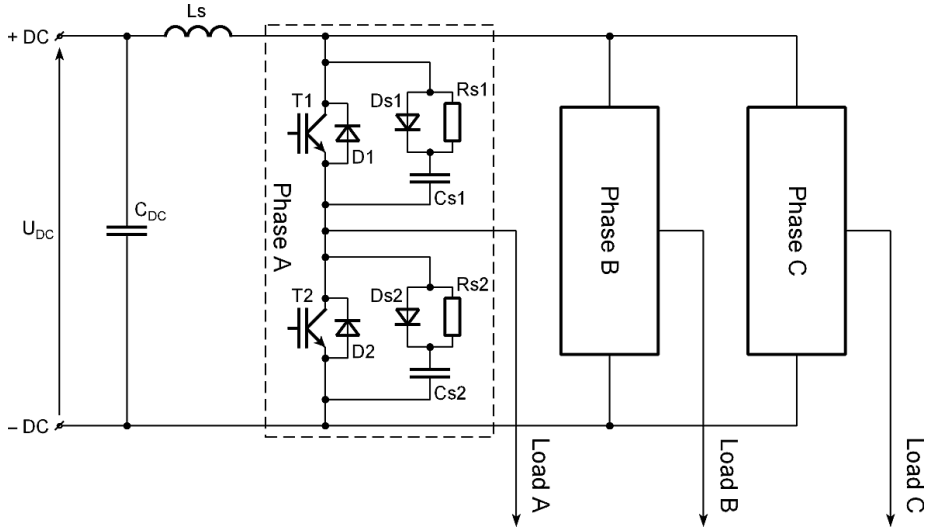

Fig. 1. The first type of RDC snubber in the three-phase VSI

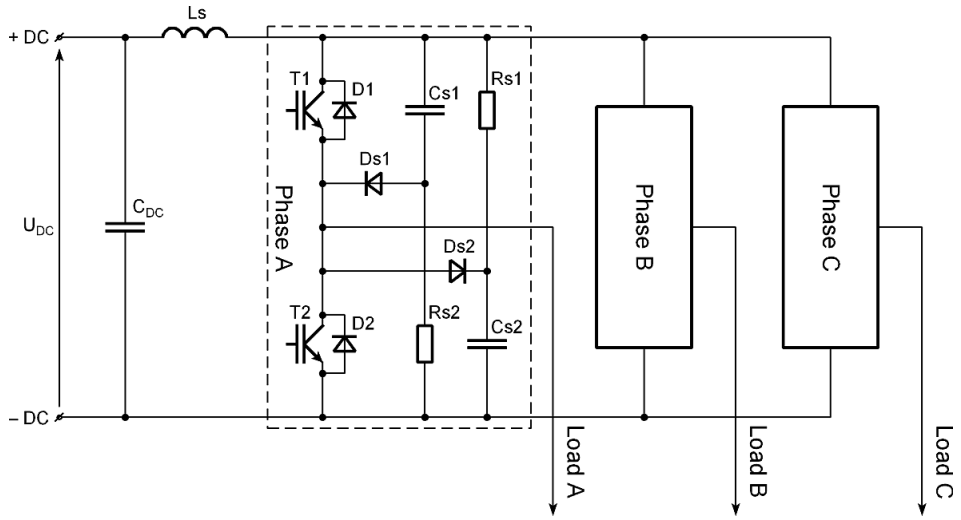

Fig. 2. The second type of RDC snubber in the three-phase VSI

The switching losses depend not only on the collector current and supplying voltage, but their value significantly depends on the change time of the transistor current and voltage during the turn-on and turn-off processes. In order to estimate switching losses, real waveforms of the transistor voltage and current should be approximated by appropriate time functions. In some papers [8, 12], these waveforms are heavily idealized, and the switching processes are considered in several time intervals. However, datasheets do not usually contain all of the required parameters, e.g. duration of individual intervals, values of currents or voltages in the border between some individual time intervals etc. In the presented paper, we assume that the simplified waveforms of transistor currents and voltages have shapes as is shown in Fig. 3. In this Figure, t_r denotes the so-called rise time – this is the time when the collector current rises to 10% of the maximum value at the IGBT turn-on process and when the collector-emitter voltage drops to 10% of the maximum value. The fall time t_f is the time when the collector current drops from 90% to 10% of the maximum value during the turn-off process. These times vary significantly with respect to the turn-on and turn-off times, denoted as t_{on}, and t_{off}, respectively.

It is necessary to stress that the rise time t_r depends significantly on the collector current, and this time increases as the collector current increases. In turn, we can assume that the fall time t_f has very little dependence upon the collector current. It is worth underlining that the resistance of the gate-driver circuit strongly influences the value of the rise time t_r, so the value of this resistance should be taken into account in the determination of this time.

As is shown in Fig. 3, a certain current overshoot appears during the transistor turn-on process. This overshoot is caused by the reverse recovery current of the freewheeling diode of the transistor T2 (Figs. 1 and 2) in the given phase branch [12]. This type of current overshoot also occurs when the overvoltage protection (snubber) presented in Fig. 1 is applied

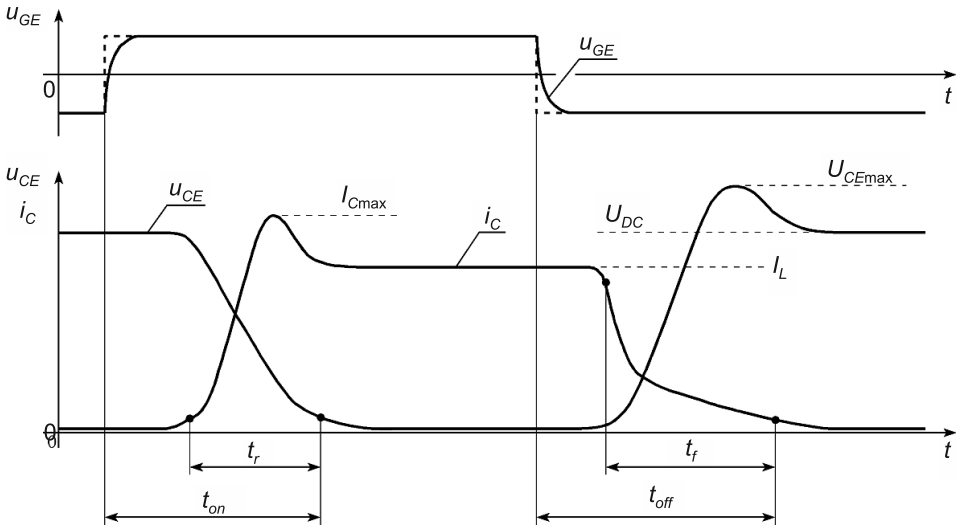

Fig. 3. Simplified waveforms of the transistor current i_C, the collector-emitter voltage u_{CE} during the turn-on and turn-off processes; u_{GE} denotes the gate-emitter voltage

in the given VSI. When the transistor T1 is turned-on, the capacitor Cs1 discharges by the resistor Rs1 and by the conducting transistor T1. Therefore, the current of this transistor during the turn-on process is the sum of the load current, the reverse recovery current of the second freewheeling diode D2, and the discharging current of the capacitor Cs1. In the turn-off process, a voltage overshoot occurs which is caused by occurring a certain parasitic inductance Ls in the DC supply circuit (Figs. 1 and 2) – this is further described in section 3.

The transistor current and voltage do not abruptly change their values during switching processes. Therefore, in these processes, average power losses can be determined as an integral of the product of these values. Both the current and the voltage of the given transistor can vary differently during the switching processes. Therefore, switching losses in the turn-on process and losses in the turn-off process per one switching period should be determined separately:

$$P_{sw} = \frac{1}{T_p}\left(\int_0^{t_r} i_{Cr}(t)\, u_{CEr}(t)\, dt + \int_0^{t_f} i_{Cf}(t)\, u_{CEf}(t)\, dt \right) \tag{2}$$

where:

$u_{CEr}(t)$ – collector-emitter voltage during the turn-on process,
$u_{CEf}(t)$ – collector-emitter voltage during the turn-off process,
$i_{Cr}(t)$ – collector current during the turn-on process,
$i_{Cf}(t)$ – collector current during the turn-off process,
t_r – current rise time in the turn-on process,
t_f – current fall time in the turn-off process.

Switching losses in one period of the output voltage are the sum of the switching losses in the individual switching intervals. In most cases of turn-on processes, it can be assumed that the transistor current and voltage are linear time functions:

$$i_{Cr}(t) = \frac{I_{C\max}}{t_r} t, \quad u_{CEr}(t) = -\frac{U_{DC}}{t_r} t + U_{DC} \tag{3}$$

where:

$I_{C\max}$ – maximum value of the collector current,
U_{DC} – voltage of a power supply source.

The maximum value $I_{C\max}$ of the collector current in the turn-on process is the sum of the load current I_L and the reverse recovery current $I_{rr\max}$ of the freewheeling diode when the second transistor in the given phase of the VSI is turning-off. It is necessary to stress that the load current I_L is different in each switching interval. The discharge current of the snubber capacitor has a certain influence on the maximum value of the collector current, but it refers only to the case in which the snubber shown in Fig. 1 is applied. After integration, we obtain the last relationship describing the average losses in the turn-on process:

$$P_{\text{on}} = \frac{1}{6} f_p U_{DC} I_{C\max} t_r \tag{4}$$

where:

f_p – switching frequency.

In waveforms of the collector current in the turn-off process, we can observe two characteristic intervals [13, 14]. In the first, the collector current decreases quite rapidly. When this current reaches a value of about 30 percent of the initial current value, the collector current decreases to zero much slower. The most common datasheets do not contain the time value at which the collector current changes its derivative. Therefore, we propose to approximate the collector current changes by means of the exponential function in the form:

$$i_{Cf}(t) = I_L e^{-\frac{t}{\tau_f}} \tag{5}$$

where:

τ_f – time constant of the collector current decrease during the turn-off process.

On the basis of the definition of the fall time t_f, we can write the following relationship:

$$0.1 I_L = 0.9 I_L e^{-\frac{t_f}{\tau_f}} \tag{6}$$

hence the time constant τ_f is equal to 0.46 t_f.

The maximum value of the collector-emitter voltage $U_{CE\max}$ in the turn-off process is equal to the voltage of the snubber capacitor Cs1 (Figs. 1 and 2), thus, the voltage $U_{CE\max}$ can be written as the sum $U_{DC} + U_{ad}$, wherein the latter voltage is approximately equal to $I_L \sqrt{\text{Ls} / \text{Cs1}}$. When we take into account formula (5) and we assume that the collector--emitter voltage is a linear time function in the turn-off process, the switching losses can be estimated with the use of the formula:

$$P_{\text{off}} = 0.135 f_p I_L U_{CE\max} t_f \tag{7}$$

Relationships (4) and (7) allow us to estimate the switching losses of one transistor in one switching period.

3. Other switching losses in three-phase voltage source inverters

The total switching losses in VSIs also include losses relating to the turn-off process of the freewheeling diodes, losses occurring in the resistors of the gate-drive circuits and losses which concern magnetic energy related to the parasitic inductances of the DC supply circuit.

Switching losses which occur in the freewheeling diodes during their turn-off processes cannot be neglected in estimation of the total switching losses in VSIs. When the collector current of the turning-on transistor (T1 in Fig. 1 or in Fig. 2) reaches the value of the loads current, the turn-off process of the freewheeling diode D2 begins. The reverse recovery current of the diode D2 flows though the transistor T1; additionally, it increases the switching losses in this transistor. Simplified waveforms of the current and voltage of the freewheeling diode are shown in Fig. 4 [1, 12, 13].

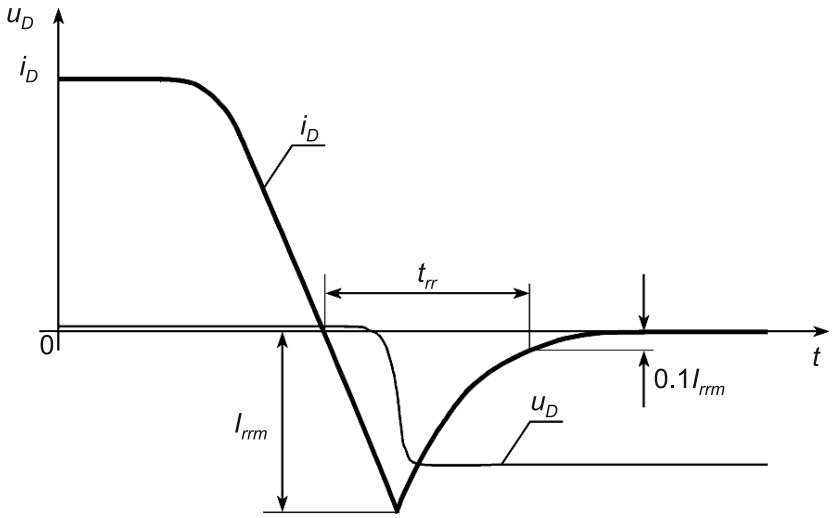

Fig. 4. Simplified waveforms of the current and voltage of the freewheeling diode

Manufacturers of IGBTs do not specify time intervals when the reverse recovery current decreases from the maximum value I_{rrm} to zero. Assuming that this time interval is approximately equal to half of the time t_{rr}, the switching losses in the freewheeling diode can be estimated with the use of the formula:

$$P_{Drr} = \frac{1}{4} f_P I_{rrm} U_{DC} t_{rr} \tag{8}$$

where:

I_{rrm} – maximum value of the reverse recovery current,
t_{rr} – reverse recovery time.

When any transistor, e.g. T1, is turning-off, the magnetic energy related to the parasitic inductance Ls of the DC supply circuit is stored in the snubber capacitor C1, and its voltage rises above the DC voltage. Next, this capacitor discharges through the snubber resistance Rs1 and the DC source to the DC voltage. A certain part of the energy stored in the capacitor C1 is returned to the DC source, and a certain energy part is dissipated in the snubber resistance Rs1. Estimation of the energy stored in the snubber capacitor is not easy because the accurate determination of the parasitic inductance is a quite difficult task. Some authors have assumed that this inductance, which depends strongly on the construction of the given converter, is equal to a few dozen of nH [1, 8], but this value can be even equal to a few hundred of nH. Approximate calculations carried out for the parasitic inductance 100 nH have shown that the switching losses related to the parasitic inductance of the DC circuit are less than 0.2% with respect to the total switching losses.

Power losses related to the switching processes also occur in resistances of the transistor gate-drive circuits. Due to the existence of the parasitic capacitances in IGBTs, especially the capacitance between the transistor gate and its emitter, short current pulses occur during transistor switching processes. The current in the gate-drive circuit decreases aperiodic to zero due to the resistive-capacitive character of this circuit, so the switching losses in the gate resistance can be estimated by using the following formula (two switching processes occur in one switching period):

$$P_{RG} = 4 f_P U_G^2 C_{GE} \tag{9}$$

where:

U_G – output voltage of IGBT drivers (usually ± 15 V),
C_{GE} – gate-emitter parasitic capacitance.

4. Switching losses in three-phase voltage source inverters

The character of switching process depends, first of all, on the inverter control method and on the additional circuit which protects IGBTs against overvoltages. When the snubber presented in Figure 1 is applied in the VSI, then the capacitor voltage is equal to zero when the given transistor is in the conduction state. Therefore, the turn-off process has a soft character because the capacitor voltage cannot change its value abruptly. Thus, this process occurs at almost zero voltage. In cases when the second RDC snubber is applied, the capacitor voltage is always higher than zero.

4.1. Losses in inverters generating output voltage in the form of a rectangular wave

When the given VSI operates with the use of the so-called six-step modulation, each transistor is controlled for the conduction state through one half of the period of the output voltage. In this case, the phase-to-phase output voltage has a rectangular shape. After the

turn-off process of the transistor T2, the turn-on process of the T1 transistor occurs. At the same time, a discharging process of the C1 capacitor begins. The load current of phase A flows through the diode D1 in a certain time interval. If the capacitor discharging the current is less than the load current in phase A, then the discharging current flows through the D1 diode, the resultant current of which is the difference of the load current and the capacitor discharging current. When the load current reaches a value of zero, the transistor T1 begins to conduct the load current of phase A – this means that the turn-on process of the transistor T1 has a soft character because this process occurs with the zero current of this transistor.

In three-phase VSIs with the first type of protection circuit, both switching processes have a soft character. Thus, the switching losses in IGBTs can be neglected. Losses associated with the switching processes refer to dissipation of the capacitor energy in the snubber resistance R_s, and they can be described by the following relationship:

$$P_{Rs} = \frac{1}{2} f_{\text{out}} C_s U_{DC}^2 \tag{10}$$

where:

C_s – capacitance of the snubber capacitor,
f_{out} – frequency of the output voltage.

In some VSIs, the overvoltage protection circuit has the form as is presented in Fig. 2. The capacitor voltages are equal to the supplying voltage, independently on the transistor operation state. As previously, the turn-on process has a soft character, but due to the capacitor voltage, the transistor turn-off process is hard. In this case, power losses in the transistor depend on the current value $I_{C\text{off}}$ at the beginning of the turn-off process and they can be estimated with the use of the formula:

$$P_{\text{off}} = \frac{1}{6} f_{\text{out}} U_{DC} I_{C_{\max}} t_f \tag{11}$$

The power losses calculated for the whole VSI should be multiplied by 6. It is necessary to underline that in this control method, each transistor is turned-on and turned-off only once in the period of the VSI output voltage. Therefore, switching losses are relatively small in respect to the conduction losses, so the switching losses can be neglected in the calculation of the inverter efficiency. For example, power losses were calculated for two chosen VSIs with the assumption that these inverters generated an output voltage in the form of the rectangular wave and that they have the first type of RDC snubber (Fig. 1). Nominal parameters of these inverters are presented in Table 1 – I_{LRMS} denotes the root mean square value of the load current.

Table 1

Parameters of two chosen voltage source inverters

P_N [kW]	U_{DC} [V]	$I_{C\max}$ [A]	I_{LRMS} [A]	R_G [Ω]	t_{on} [µs]	t_r [µs]	t_{off} [µs]	t_f [µs]	t_{rr} [µs]	I_{rr} [A]	C_{GE} [nF]
11.0	490	24.0	9.90	6.30	0.073	0.023	0.71	0.50	0.12	4	10
100	480	600	106	0.52	0.60	0.17	1.20	0.11	0.20	300	41
				5	1.00	0.50	1.60	0.11	0.19	260	

The capacitances of the RDC snubbers of these inverters were respectively equal to 86, and 68 nF. In the considered case of the inverter control method, power losses occurred mainly in the resistance of the snubber, and for a frequency of 50 Hz, these losses were about 0.03 W for the first inverter and 0.78 W for the second.

4.2. Switching losses in VSIs with the Pulse Width Modulation

The switching losses have a significant value in VSIs, which are controlled with the use of pulse width modulation (PWM), especially when the switching frequency equals a dozen or so kHz. It is understood that the greater the inverter nominal power is, the lower the switching frequency, but the inverter nominal current rises. This case occurs, first of all, in inverters of medium and high nominal power. As previously, the switching losses strongly depend on the type of RDC snubber. When the given VSI is protected by means of the snubber presented in Fig. 1, the transistor turn-off process has a soft character, but keeping in mind that the snubber capacitor should itself discharge to zero before the next transistor turn-off process begins. Figure 5 shows, for example, the waveforms of the transistor voltage, transistor current, and actual value of the power losses which were measured in a laboratory voltage source inverter.

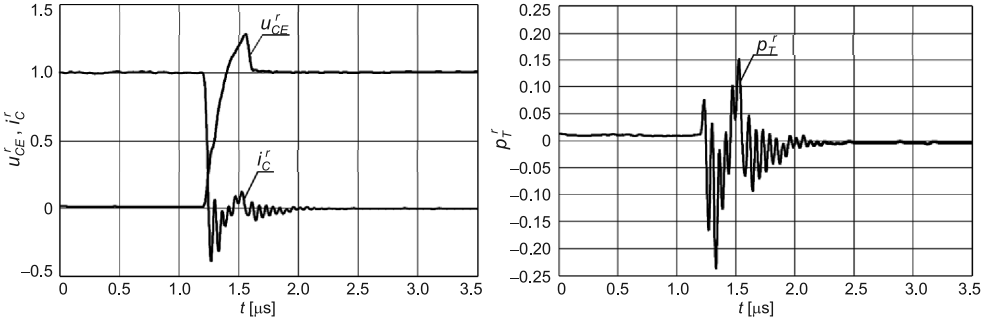

Fig. 5. Waveforms of relative values of transistor voltage, the transistor current and power losses during the turn-off process; reference voltage – 150 V; reference current – 16 A; and reference power – 2.5 kW

The turn-on processes of the IGBTs in inverters have a hard character. In turn, Figure 6 shows waveforms of the transistor voltage, the transistor current and power losses during the turn-on process. When the transistor is turning-on, then its current is equal to the sum of the load current, the current of the capacitor discharging, and of the freewheeling diode reverse recovery current of the second transistor in the given phase of the VSI.

Power losses occurring in the turn-on process depend strongly on the load current. For simplicity, it was assumed that the load current has a sinusoidal shape. Assuming that switching moments occur at equal time intervals, the value of the transistor switching current in the *k*-th switching interval can be determined as follows:

$$i_L(k) = I_{L\max} \sin\left(k\frac{2\pi}{m_f}\right) \tag{12}$$

where:

k – switching number in a half period of the output voltage,

$I_{L\max}$ – amplitude of the first harmonic of the load current.

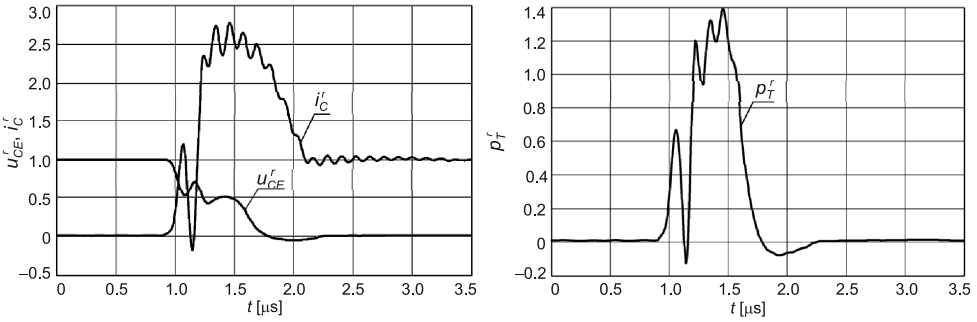

Fig. 6. Waveforms of relative values of the transistor voltage, the transistor current and power losses during turn-on process: reference voltage – 150 V; reference current – 16 A; reference power – 2.5 kW

Thus, the turn-on losses in IGBTs which are caused by the load current can be estimated with the use of the formula:

$$P_{\text{on}} = \frac{1}{6} f_{\text{out}} U_{DC} t_r I_{L\max} \sum_{k=1}^{\frac{m_f}{2}} \sin\left(k \frac{2\pi}{m_f}\right) \tag{13}$$

In the case when the snubber shown in Fig. 1 is applied in the given VSI, these losses are a little higher due to the capacitor discharge current flowing through turning-on transistor.

The turn-off losses in IGBTs depend on the type of snubber. These losses are close to zero when the snubber presented in Fig. 1 is applied. In the case when the second snubber is applied, the turn-off losses in IGBTs can be estimated by means of the following relationship (using the formula (7) and (12)):

$$P_{\text{off}} = 0.135 f_{\text{out}} t_f I_{L\max} \sum_{k=1}^{\frac{m_f}{2}} \left[\sin\left(k \frac{2\pi}{m_f}\right) \left(U_{DC} + \sqrt{\frac{L_S}{C_S}} I_{L\max} \sin\left(k \frac{2\pi}{m_f}\right) \right) \right] \tag{14}$$

A comparison of the switching losses was carried out for two previously selected voltage source inverters. Calculations of switching losses were performed for two switching frequencies which were equal to 3 kHz and 6 kHz. It was assumed that the parasitic inductance of the DC supply circuit was equal to 100 nH. Individual types of switching power losses are presented in Table 2 and in Table 3. In the first case, the switching losses in IGBTs are equal to the losses occurring in the turn-on process because the turn-off losses are close to zero due to the applying of the snubber which is shown in Fig. 1. The switching losses related to the parasitic inductance of the DC circuit are less than 0.002 W and 0.25 W for the 11 kW and 100 kW VSI, respectively.

Table 2

Switching power losses in voltage source inverters in W Snubber shown in Fig. 1

Switching frequency	3 kHz			6 kHz		
VSI nominal power	11 kW	100 kW		11 kW	100 kW	
Gate resistance	6.3	0.52	5	6.3	0.52	5
Total switching losses in IGBTs	0.19	35.03	93.88	0.39	70.11	187.89
Total switching losses in freewheeling diodes	1.06	129.6	106.70	2.11	259.2	213.41
Total losses in all snubbers	64.82	62.20	62.20	129.66	124.42	124.42
Losses in resistances of gate-driver circuits	0.162	0.66	0.66	0.32	1.33	1.33
Total other losses in inverter	66.05	192.57	169.68	132.10	385.15	339.36
Total switching losses in inverter	66.24	227.61	263.56	132.49	455.27	527.25

Table 3

Switching power losses in voltage source inverters in W Snubber shown in Fig. 2

Switching frequency	3 kHz			6 kHz		
VSI nominal power	11 kW	100 kW		11 kW	100 kW	
Gate resistance	6.3	0.52	5	6.3	0.52	5
Turn-on losses in all IGBTs	0.19	35.03	93.88	0.39	70.11	187.89
Turn-off losses in all IGBTs	2.57	8.29	8.29	5.01	16.13	16.13
Total switching losses in IGBTs	2.73	43.32	102.17	5.40	86.25	204.02
Total switching losses in freewheeling diodes	1.06	129.60	106.70	2.12	259.20	213.41
Total losses in all snubbers	0.047	5.40	5.40	0.0911	10.46	10.46
Losses in resistances of gate-driver circuits	0.162	0.66	0.66	0.32	1.33	1.33
Total other losses in inverter	1.27	135.77	112.88	2.53	271.20	225.41
Total switching losses in inverter	4.03	179.09	215.04	7.93	357.45	429.42

5. Conclusions

In total switching losses in VSIs, the switching losses occurring in IGBTs have a significant share, but the amount of these losses depends strongly on the applied type of the overvoltage protection circuit. However, the influence of this circuit on the switching losses in IGBTs decreases with increases in the VSI nominal power. When the first type of overvoltage protection is applied, the switching losses in IGBTs are less than in the case

when the second type of the protection circuit is used, especially for VSIs of relatively small nominal power ratings.

It is necessary to stress that power losses occurring in freewheeling diodes should be taken into consideration, because the reverse recovery time of these diodes is comparable to the switching times of IGBTs and the amount of these losses is comparable to losses in IGBTs. On the other hand, the switching losses occurring in gate resistances and losses related to the parasitic inductance of the DC supply circuit can be neglected because their share in the total switching losses are less than 1 per cent.

Switching losses in inverters generating output voltage in the form of the rectangular wave depend directly proportional on the frequency of the output voltage; in this case, the output voltage frequency is the same as the switching frequency of IGBTs. When inverters operate with the pulse width modulation, the total switching losses do not practically depend on the frequency of the output voltage and these losses depend directly on the switching frequency (usually frequency of a saw-tooth wave), which should be many times higher than the output voltage frequency.

References

[1] Feix G., Dieckerhoff S., Allmeling J., Schonberger J., *Simple Methods to Calculate IGBT and Diode Conduction and Switching Losses*, 13th European Conference on Power Electronics and Applications, EPE, Barcelona, Spain, 8–10 September, 2009, 1-8.

[2] Drofenik U., Kolar J.W., *A General Scheme for Calculating Switching- and Conduction-Losses of Power Semiconductors in Numerical Circuit Simulations of Power Electronic Systems*, 5th International Power Electronics Conference, IPEC-Niigata, Japan, 2005.

[3] Hiraki E., Tanaka T., Nakaoka M., *Zero-Voltage and Zero-Current Soft – Switching PWM Inverter*, 36th Power Electronics Specialists Conference PESC, Recife, Brazil, 12–16 June, 2005, 798-803.

[4] Martinez B., Li R., Ma K., Xu D., *Hard Switching and Soft Switching Inverters Efficiency Evaluation*, International Conference on Electrical Machines and Systems ICEMS, Wuhan, China, 17–20 October, 2008, 1752-1757.

[5] Bernet S., Lüscher M., Steimer P.K., *IGCTs in Soft Switching Power Converters*, 8th European Conference on Power Electronics and Applications, Lausanne, France, 7–9 September. 1999, 1-11.

[6] Jinrong Q., Khan A., Batarseh I., *Turn-off Switching Loss Model and Analysis of IGBT under Different Switching Operation Modes*, 21st International Conference on Industrial Electronics, Control, and Instrumentation IEEE IECON, Orlando, USA, 6–10 November, 1995, Vol. 1, 240-245.

[7] Cavalcanti M.C., da Silva E.R., Boroyevich D., Wei D., *A Feasible Loss Model for IGBT in Soft-Switching Inverters*, 34th IEEE Power Electronics Specialist Conference, PESC, de Campina Grande, Brazil, 15–19 June, 2003, Vol. 4, 1845-1850.

[8] Maswood A.I., *A switching loss study in SPWM igbt inverter*, 2nd IEEE International Conference on Power and Energy (PECon 08), Johor Baharu, Malaysia, 1–3 December, 2008, 609-613.

[9] Rashid M.H., *Power electronics handbook*, Academic Press, San Diego 2001.

[10] Skvarenina T.L., *The power electronics handbook, Industrial Electronics Series*, CRC Press, Boca Raton 2002.

[11] Peng F.Z., Gui-Jia S., Tolbert L.M., *A Passive Soft-Switching Snubber for PWM Inverters*, IEEE Transactions on Power Electronics, Vol. 19, Issue 2, March 2004, 363-370.

[12] Rajapakse A.D., Gole A.M., Wilson P.L., *Approximate Loss Formulae for Estimation of IGBT Switching Losses through EMTP-type Simulations*, International Conference on Power Systems Transients, IPST, Montreal, Canada, 19–23 June, 2005, Paper No. 184.

[13] Mori M., Kobayashi H., Saiki T., Nagasu M., Sakano J., Saitou R., *3.3 kV Punchthrough IGBTwith Low Loss and Fast Switching*, IEEE International Symposium on Power Semiconductor Devices and IC's, ISPSD, Weimar, Germany, 26–29 May, 1997, 229-232.

[14] Petterteig A., Lode J., Undeland T.M., *IGBT turn-off losses for hard switching and with capacitive snubbers*, IEEE Conference of Industry Applications Society Annual Meeting, Dearborn, USA, 28 September–4 October, 1991, Vol. 2, 1501-1507.

TECHNICAL TRANSACTIONS | **CZASOPISMO TECHNICZNE**
ELECTRICAL ENGINEERING | ELEKTROTECHNIKA
2-E/2015

ADRIAN MŁOT*, MARIUSZ KORKOSZ**, MARIAN ŁUKANISZYN*

ANALYSIS OF INTEGRAL PARAMETERS IN A SINGLE-PHASE SLOTLESS AXIAL-FLUX MACHINE USED IN SMALL WIND TURBINES

ANALIZA PARAMETRÓW FUNKCJONALNYCH W JEDNOFAZOWYM BEZŻŁOBKOWYM GENERATORZE WIATROWYM O STRUMIENIU OSIOWYM

Abstract

The design of a ferrite magnet generator with trapezoidal shaped permanent magnets and coils for a wind turbine is studied. Based on the 3-D finite element analysis (FEA), the electromagnetic performances of the two generator prototypes and a simple design modification for one of the axial-flux generator prototypes are analyzed. The best generator is chosen from a range of designs, where the goal is to increase the voltage generated by the 8/8 pole and a single-phase slotless machine. Experimental results from a small size prototype machine validate the 3-D FEA models presented, and hence give confidence in their use for design.

Keywords: *axial-flux generators*, *wind turbine generators*, *efficiency*, *finite-element analysis*

Streszczenie

W niniejszym artykule omówiono konstrukcje jednofazowych bezżłobkowych generatorów tarczowych o 8 biegunach stojana i wirnika przeznaczonych do małych elektrowni wiatrowych. W badanych generatorach zastosowano magnesy w kształcie trapezoidalnym, a także cewki trapezoidalne. W celu zobrazowania wpływu geometrii na parametry funkcjonalne generatora oraz uzyskanie wyższej wartości napięcia rotacji w uzwojeniu dokonano modyfikacji obwodu magnetycznego jednej z analizowanych konstrukcji. Do obliczeń pola magnetycznego wykorzystano program trójwymiarowy (3D) oparty na metodzie elementów skończonych (MES). Zaprezentowano wyniki obliczeń numerycznych i wybrane wyniki badań laboratoryjnych.

Słowa kluczowe: *maszyny ze strumieniem osiowym*, *małe turbiny wiatrowe*, *sprawność*, *metoda elementów skończonych*

DOI: 10.4467/2353737XCT.15.088.3920

* Ph.D. Eng. Adrian Młot, Prof. Ph.D. D.Sc. Eng. Marian Łukaniszyn, Faculty of Electrical Engineering, Automatic Control and Informatics, Opole University of Technology.

** Ph.D. D.Sc. Eng. Mariusz Korkosz, The Faculty of Electrical and Computer Engineering, Rzeszow University of Technology.

1. Introduction

Axial-flux machines (AFM) with magnets for wind generator applications can be built in many configurations [7–9, 12, 13, 15]. Machines with coreless stators can potentially operate at a higher efficiency than conventional ones because of the absence of core losses. AFM-based generators can be structured as: single-rotor, single-stator; double-rotor, single--stator; single-rotor, double-stator; multi-rotor, multi-stator machines. The stator disc can be slotted or slotless. The simplified structure of AFM is a slotless single-stator disk design with winding placed or wound on the stator disk. Small size AF generators for wind turbine applications offer a promising alternative for many remote electrical uses [1–6, 10]. Their high compactness and disk-shaped profile make the axial-flux machines suitable for mechanical integration with wind turbines.

The goal of this paper is to investigate the electromagnetic field and performance of the two presented prototypes. The prototypes of generators are chosen from a range of designs based on minimizing the material cost and energy loss [14]. To demonstrate the influence of the generator, geometry changes on the generator performance, and the modification of the stator and rotor was investigated and analyzed on prototype A. A wide range of generator characteristics modeling can be found in the literature [7–9, 12–15]. The presented generator should generate sufficient output DC voltage to charge up to 4–5 batteries of 12-volt each. This generator design should be suited for charging a 48-volt battery system. The small amount of energy produced by the generators can be stored by the battery charging station and that stored energy can sufficiently improve the quality of life for such areas, giving people access to electrical lighting, TV, radio, etc. In contrast to this, the 3-D FEA approach to calculating generator characteristics and electromagnetic modeling, that uses a professional software package, has been presented in [15]. The analytical methods and the finite-element (FE) methods are, in many instances, used to investigate certain design aspects and analyse the electromagnetic field. FE models give an excellent representation of the magnetic field inside the machine.

Calcualtion of the wind generator characteristics is mainly about power-speed, efficiency--speed or torque speed characteristics. The prediction of generator performance was verified with measurements. The comparison between the measured and simulated impact of generators for the wind turbine application during normal operation is in good agreement. Testing includes both generator prototypes, the testing focuses on the DC output voltage and DC output current at various speeds. It shows that the proposed prototype B with full pitch magnets can be applied successfully to generate up to 60 V at the open-circuit operation. Future research works will be concentrated on the generators efficiency, the flux distribution in the stator and rotor core and the magnetic force between the stator and rotor.

2. Description of the axial-flux generator

Axial-flux generators with magnets are one of the best solutions for small-scale wind generators. In this study, ferrite magnet generators with surface-magnet systems are studied and analyzed. A schematic drawing of the prototype axial-flux generators are shown in Fig. 1.

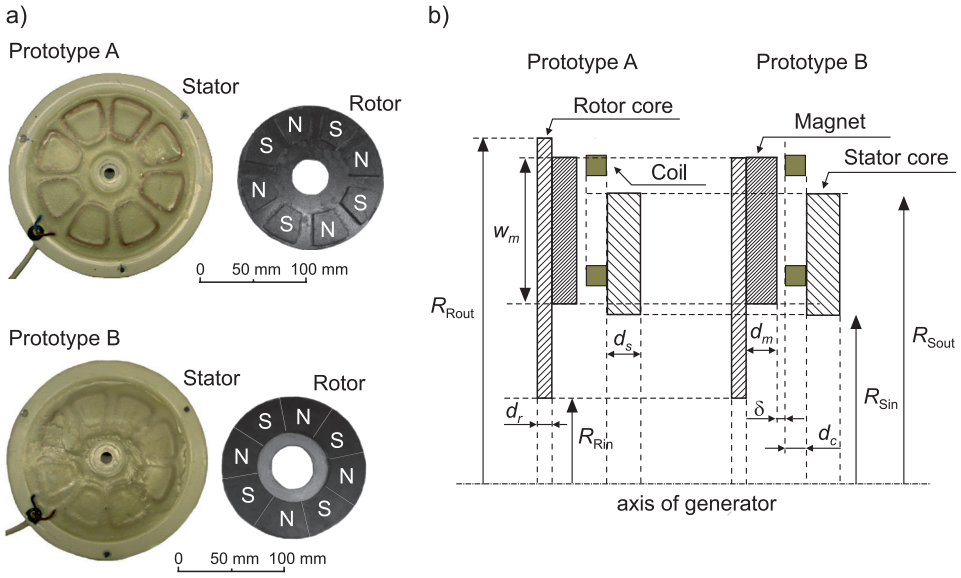

Fig. 1. Prototypes of 8-pole axial-flux generators (a) and one-stator one-rotor topology (b)

The rotors of prototype versions A and B are composed of a thin 3 mm thick steel plate, and 138.4 mm and 130.4 mm in outer diameter, respectively. Ferrite magnets are arranged in a radial pattern around the rotor plate. The initial design of prototype A of the generator includes 8 trapezoidal-shaped surface-mounted magnets with an arc of 30 mech. degrees. Prototype B consists of a rotor with 45 mech. degrees of trapezoidal-shaped magnet arc covering a full rotor pole pitch. Magnets with black epoxy coating were chosen specifically to protect them against scratching and corrosion. The slotless stator core disk for both prototypes with winding consists of a number of single-layer trapezoidal-shaped coils. These coils have the advantages of being easy to make and have a relatively short end-winding. The coils are held together and mounted on a stator disk surface by using a composite material of epoxy resin. The geometry parameters of prototypes are listed in Table 1.

Table 1

The main parameters of generator geometry and material specification

Data of generator	Version of generator prototype	
	A	B
Type of magnet	Ferrite	Ferrite
Thickness of magnet	5 mm	5 mm
High of magnet	29.5 mm	29.5 mm
Remanent magnetic flux	0.66 T	0.66 T
Outer radius of rotor core/magnet	69.2 mm	65.2 mm
Inner radius of rotor core/magnet	17.2 mm	17.2 mm
Outer radius of stator core	58 mm	58 mm

Inner radius of stator core	34 mm	34 mm
Thickness of stator core	7 mm	7 mm
Turn number per coil	124	124
Number of rotor/stator pole	8/8	8/8
Thickness of coil	4 mm	4 mm
Air-gap (stator-magnet)	1.5 mm	1.5 mm
Resistance of phase (in series)	26.9 Ω	26.9 Ω

The principal application of such wind turbines is battery charging, in which the generator is connected through a rectifier to a battery system. In order to convert the available wind power to mechanical power, the rotor should usually operate at optimal speed ratio, with its revolutions per minute varying in proportion to wind speed. In the small size wind turbine generator under study, the torque and speed control system does not need to be used regarding the application that the generators are used for.

3. Three dimensional FEA models of axial-flux generators

The three-dimensional magnetic field analysis was conducted during the investigation of the output voltage, efficiency and magnetic force. Two prototypes with single-phase winding are analyzed by the 3-D finite element method. Single-phase winding terminals of the generator are connected to a diode rectifier circuit with a resistive load. The 3-D FEA models of prototypes having a periodicity property (45° mech. degrees) are shown in Fig. 2.

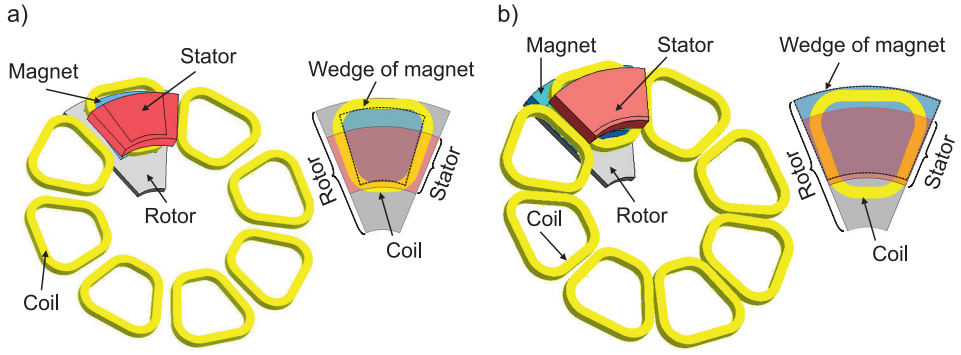

Fig. 2. 3-D FEA models of 8-pole axial-flux generator, prototype A (a), and prototype B (b)

The electrical and mechanical performance of the electric motor depend on its geometry and properties of magnetic materials. In the past, basic electromagnetic theory was used by industrial experience for preliminary motor design of the presented prototypes. 3-D FEA was used to verify the AF generators, and the results show the useful performance of the machines for wind turbine applications. However, performance of the motor can be enhanced by the modification design in terms of efficiency, torque etc. For prototype A, the geometry of the generator was redesined (Fig. 3).

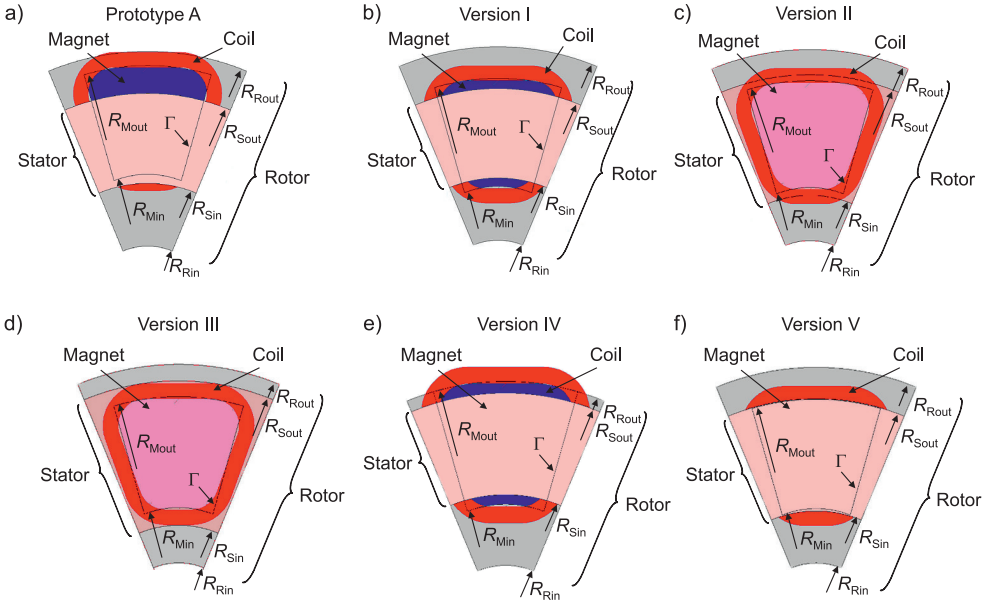

Fig. 3. The geometry of prototype A before modification (a), and several versions of prototype A after modification (b–f)

The modification process was performed with the following changes to stator, rotor, magnet and coil sizes: version I (Fig. 3b) consists of the coils moved about 4.8 mm to the center of the stator disc. Also, the magnets are placed to the center of the stator disk by changing the magnet inner and outer radius, magnet volume was then reduced about 0.3%. Those positions of coils and magnet are fixed in all further modifications (Fig. 3c–f). The contour profile of magnets are highlighed by the Γ symbol. Version II (Fig. 3c) concerns a modification of the stator disc width in a radial direction ($R_{Sout} - R_{Sin}$) in order to place the outer and inner edges of magnet in the middle of the coil thickness, thereby the width of stator disk is wider than the magnet width ($R_{PMout} - R_{PMin}$). The next version III (Fig. 3d) is based on further extension of the stator disc width in order to cover the whole coil. On version IV (Fig. 3e), the outer radius of the rotor disk was reduced and aligned to the outer

Table 2

Geometry parameters of generator version A after modification

Version of AFM	Parameter [mm]					
	R_{Sin}	R_{Sout}	R_{Rin}	R_{Rout}	R_{Min}	R_{Min}
Prototype A	34	58	17.2	69.2	35.8	65.2
I	34	58	17.2	69.2	31.3	60.7
II	31	62.4	17.2	69.2	31.3	60.7
III	27.1	64.9	17.2	69.2	31.3	60.7
IV	34	58	17.2	60.7	31.3	60.7
V	31	60.9	17.2	69.2	31.3	60.7

radius of magnet. After that modification, the external end-winding sticking out of the stator disc, and the rest of stator disc geometry dimentions are the same as in prototype A. The last modification (version V, Fig. 3f), is based on the same rotor disk and magnet geometry dimensions as in version I. The width of the stator disk was increased in order to cover the whole face of the magnet.

The stator, rotor, and magnet dimensions before and after the geometry modification are given in Table 2.

4. FEA results and experimental verification

Simulation and measurements of the axial-flux machine response to voltage at different speeds were performed. The machine was operated as a generator and the load level varied from no load to full load. The speed of the generator was changed from 1000 rpm down to 250 rpm. In the first stage of the experiment, the input mechanical energy was fed to the drive rotor of the proposed generators which can change mechanical energy into electrical energy. The prediction and measured voltages generated by phase caused by different speeds of the generator are presented in Fig. 4.

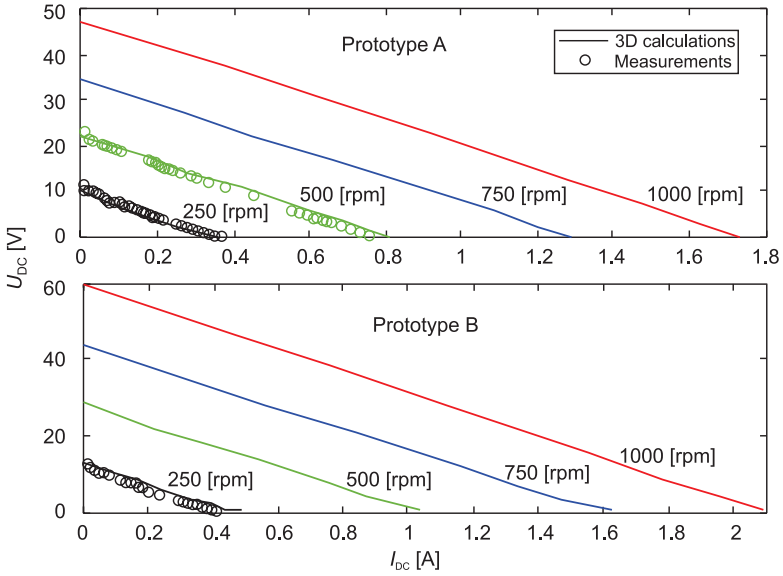

Fig. 4. DC output voltage at varied speed versus DC output current when connected to resistive load

If a higher DC load voltage is required to recharge 5 batteries of 12-volts each, the speed of operation must be high. For instance, if a DC load voltage of 60 V is required, the rotor speed has to be higher than 1000 rpm to generate this voltage within the range of peak efficiency. The prototype B seems a better solution to reach the high voltage to recharge 5 batteries than

prototype A – this generates DC output voltage about 10 V lower than prototype B at a speed above 500 rpm. The line voltage in the open-circuit condition is approx. 48 V and 60 V at 1000 rpm for prototypes A and B, respectively. The open-circuit and load characteristics for different rotational shaft speeds were measured. The computed results of the DC voltage vs. the DC output current at resistive loaded operation agree strongly with the experimentally measured values. The increase of the generated voltage is directly related to the increase of the power output, and the generated voltage is proportional to the strength of the magnetic field.

The speed range is limited by the maximum power that can be dissipated in the rotor resistances. The results presented in the following plots correspond to 250 rpm, 500 rpm, 750 rpm and 1000 rpm of the rotor speed at various generator loads. The efficiency of prototype A and B increases to about 58% and 64% at high speed, respectively (Fig. 5).

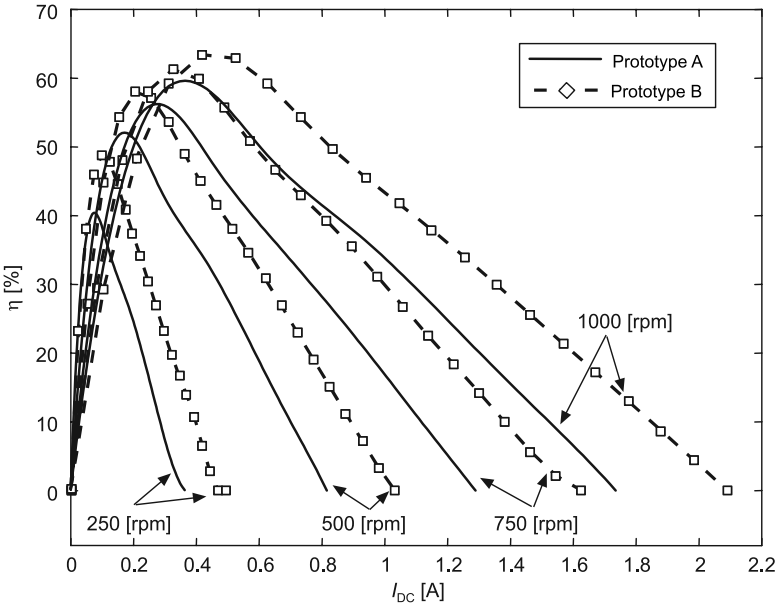

Fig. 5. Efficiency of AFM versus DC output current at varied speed when connected to resistive load

Figure 6 shows the magnetic flux distribution in the air-gap of the investigated machines obtained by FEA as a function of one mechanical period, during the open-circuit operation condition. It is clearly demonstrated that the prototype B of the generator has a higher volume of magnets realized by the use of a wider arc of the magnet as compared with prototype A, therefore, the strength of the magnetic field increased.

All the versions of modified prototype A have a lower saturation effect observed in the stator or rotor cores. Table 3 presents a list of peak values for the calculated flux density in the stator core under open-circuit operation conditions.

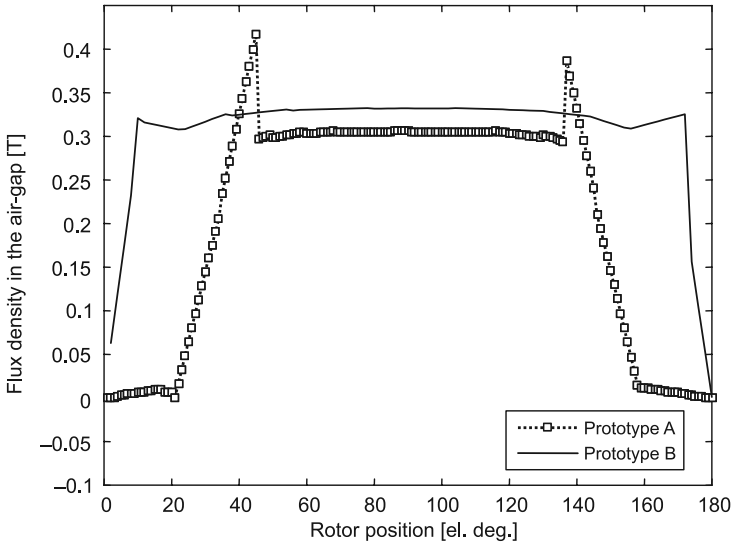

Fig. 6. Magnetic flux density distribution in the air-gap of prototype A and prototype B

The right choice of the ratio of the inner stator disc diameter to the outer diameter has a crucial influence on back-EMF voltage, which is the induced voltage when the current is zero. The results of the obtained DC output voltage after the modified stator/rotor geometry of prototype A are listed in Table 3. It clearly demonstrates that changing the diameter ratio of the stator disc has an influence on the induced voltage by the coils. Induced voltage (e) is a function of the flux-linkage of the winding ($d\psi/dt$).

Table 3

The maximum value of flux density and voltage generated at 1000 rpm observed in prototype A and its modified versions

Generator version	Open-circuit operation condition	
	B_{max} [T]	U_{DC} [V]
Prototype A	1.19	46.66
I	1.21	48.84
II	1.23	50.09
III	1.23	49.86
IV	1.38	48.19
V	1.23	50.13

Since we have postulated that there is no current, it is the flux-linkage produced in the winding by the magnet. The rotation magnet causes the flux-linkage of the winding to alternate and generate an alternating EMF. If the flux waveform in the air-gap is given by a sinusoidal function such as $\psi = \phi \cdot \sin(\theta)$ (where θ – angular position of the coil in electric degree) then the induced EMF voltage by the coil with the number of turn N_t can be expressed as:

$$e = -\frac{\mathrm{d}\psi}{\mathrm{d}t} = -N_t \phi \cos\left(\theta \frac{\mathrm{d}\theta}{\mathrm{d}t}\right) \tag{1}$$

where $\mathrm{d}\theta/\mathrm{d}t$ is the angular frequency of the coil (ω). The eq. (1) can be expressed as:

$$e = -N_t \phi \omega \cos(\omega \cdot t) = -N_t B S_{Fe} \cos(\omega \cdot t) \tag{2}$$

The maximum value of the induced voltage (U_{DC}) of one coil (one pole of the stator) for the maximum value of the flux density (B) in the air-gap is given by:

$$U_{\mathrm{DC}} = N_t \cdot \phi \cdot p \cdot \omega_m = N_t \cdot B \cdot S_{Fe} \cdot p \frac{2\pi}{60} n \tag{3}$$

where:

p – the number of rotor pole,
n – the speed of the rotor,
ω_m – angular velocity in mechanical degree.

Equation (3) shows that the induced voltage is a function of the angular velocity and cross-section of the stator disc (S_{Fe}). According to the results listed in Table 3, the maximum voltage induced by winding occurs at ratios 0.5, 0.42, 0.56 of the stator inner to outer diameter, respectively, for the generator versions II, III and V. According to literature [2, 12] the optimal ratio for the idealized axial-flux machine is 0.58.

In axial-flux magnet machines, there is an axial force between the rotor magnets and the stator disc. The period of force fluctuations is equal to the angular distance between two identical magnets. The average axial force from one period was calculated. Figure 7 shows the average axial force between stator and magnet vs. rotor speed at varied resistive load.

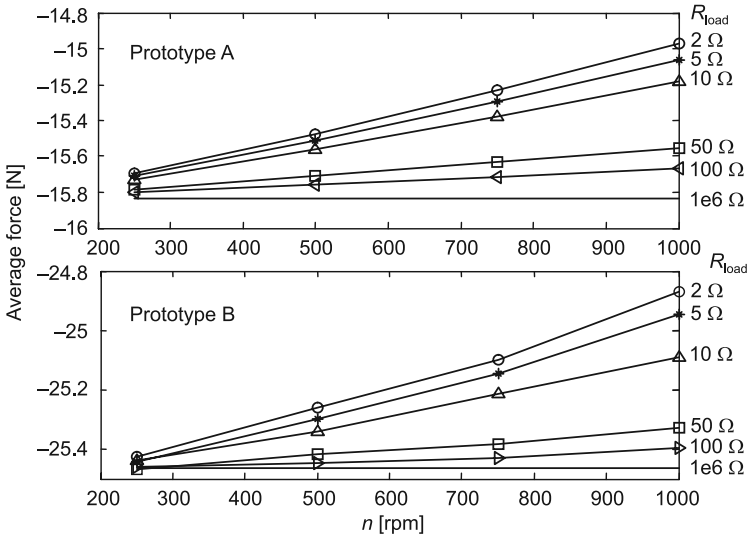

Fig. 7. Axial force between stator and rotor vs. rotor speed at varied load from open-circuit to 2 Ω

5. Conclusion

In this paper, we have presented the design of an axial-flux magnet generator which has the capability to be manufactured in a small workshop. Two prototype concepts of wind generator have been presented. The generators have been chosen from a range of designs based on minimizing the material cost and energy loss.

The main aim of this paper has been to design the wind generator producing the required DC output voltage at the resistance load operation. This generator design is suitable for charging a 3 to 5, 12 V battery system with the rectified generator output voltage. As FEA results show the generators are able to reach the required DC load voltage at speeds in the range of 750 to 1000 rpm. According to Fig. 4, prototype B generates approx. 10 V more than prototype A. Generator prototype B has a higher volume of magnets realized by use of a wider arc of magnet, therefore the strength of the magnetic field is increased (Fig. 6). There is a further possibility to increase the output DC voltage by decreasing the air-gap between the magnets and the stator core. The generated voltage is proportional to the strength of the magnetic field, which depends on the axial length between the stator and magnets.

The authors would like to express their gratitude to the Electrical Machine Laboratory, Department of Electrical & Electronic Engineering, University of Bristol, UK, for the support in accessing the experimental axial flux wind generator.

References

[1] Parviainen A., Pyrhonen J., Kontkanen P., *Axial flux PM generator with concentrated winding for small wind power applications*, Electric Machines and Drives, IEEE, 2005, 1187-1191.

[2] Vansompel H., Sergeant P., Dupre L., *Optimized design considering the mass influence of an axial flux permanent-magnet synchronous generator with concentrated pole windings*, IEEE Transactions on Magnetics, December 2010, Vol. 46(12), 4101-4107.

[3] Khan M.A., Pillay P., Batane N.R., Morrison D.J., *FPGA Prototyping a composite SMC/steel axial-flux PM wind generator*, Industry Applications Conference, 41st IAS Annual Meeting, IEEE, October 2006, Vol. 5, 2374-2381.

[4] Ani S.O., Polinder H., Ferreira J.A., *Energy yield of two generator system for small wind turbine application*, IEEE International Electric Machines and Drives Conference, IEMDC, May 2011, 735-740.

[5] Louie H., *Experiences in the construction of open source low technology off-grid wind turbines*, Power and Energy Society General Meeting, IEEE, July 2011, 1-7.

[6] Andriollo M., Bertoli M., Martinelli G., Morini A., Torella A., *Permanent magnet axial flux disc generator for small wind turbines*, Electrical Machines, ICEM, IEEE, September 2008, 1-6.

[7] Gerlando A., Foglia G., IacchettiM., Perini R., *Axial-flux PM machines with concentrated armature windings: Design analysis and test validation of wind energy generators*, IEEE Transactions on Industrial Electronics, September 2011, Vol. 58(9), 3795-3805.

[8] Yicheng C., Pragasen P., *Axial-flux PM wind generator with a soft magnetic composite core*, Industry Applications Conference, Fortieth IAS Annual Meeting, IEEE, October 2005, Vol. 1, 231-237.

[9] Javadi S., Mirsalim M., *Design and analysis of 42-V coreless axial-flux permanent-magnet generators for automotive applications*, IEEE Transactions on Magnetics, April 2010, Vol. 46(4), 1015-1023.
[10] Bumby J.R., Stannard N., Dominy J., McLeod N., *A permanent magnet generator for small scale wind and water turbines*, IEEE, September 2008, 1-6.
[11] Glinka T., Wolnik T., Król E., *Silnik tarczowy z wirnikiem wewnętrznym – obliczenia obwodu elektromagnetycznego*, Zeszyty Problemowe – Maszyny Elektryczne, 2011, Nr 92, 23-28.
[12] Glinka T., Jakubiec M., *Rozwiązania silników tarczowych*, Zeszyty Problemowe – Maszyny Elektryczne, 2007, Nr 77, 243-249.
[13] Glinka T., Król E., Białas A., Wolnik T., *Silniki tarczowe z magnesami trwałymi*, Zeszyty Problemowe – Maszyny Elektryczne, 2010, Nr 87, 63-68.
[14] Hosseini S.M., Agha-Mirsalim M., Mizaei M., *Design, prototyping and analysis of a low-cost disk permanent magnet generator with rectangular flat-shaped magnets*, Iranian Journal of Science and Technology, Transaction B, Engineering, 2008, No. B3, 191-203.
[15] Giangrande P., Cupertino F., Pellegrino G., Ronchetto D., Gerada C., Sumner M., *Analysis of two-part rotor, axial flux permanent magnet machines*, Energy Conversion Congress and Exposition (ECCE), IEEE, September 2011, 1576-1581.

TECHNICAL TRANSACTIONS | **CZASOPISMO TECHNICZNE**
ELECTRICAL ENGINEERING | ELEKTROTECHNIKA
2-E/2015

TADEUSZ SOBCZYK*, MICHAŁ RADZIK**

DIRECT DETERMINATION OF PERIODIC SOLUTION IN THE TIME DOMAIN FOR ELECTROMECHANICAL CONVERTERS

BEZPOŚREDNIE WYZNACZANIE ROZWIĄZAŃ OKRESOWYCH DLA PRZETWORNIKÓW ELEKTROMECHANICZNYCH W DZIEDZINIE CZASU

Abstract

The main aim of this paper is to identify relationships for direct determination in the time domain of periodic steady-state solutions for differential equations. A new discrete operator of differentiating has been defined. As a result, a set of algebraic equations has been written. Based on this, an algorithm for nonlinear differential equations has been proposed. Numerical tests have been carried out both for a new discrete operator and for steady-state analysis in a simple electromechanical converter.

Keywords: *analysis in time domain*, *discrete operator of differentiating*

Streszczenie

W niniejszej pracy przedstawiono rozważania prowadzące do równań umożliwiających obliczanie rozwiązań ustalonych bezpośrednio w dziedzinie czasu dla układów opisywanych równaniami różniczkowymi, o których wiadomo, że posiadają rozwiązania okresowe o znanym okresie. Zdefiniowano dyskretny operator różniczkowania określający chwilowe wartości pochodnej funkcji w wybranym zbiorze punktów na podstawie wartości funkcji w tym zbiorze oraz podano równania algebraiczne określające rozwiązania ustalone w tych punktach. Równania te uogólniono na układy nieliniowe posiadające rozwiązania okresowe z myślą o układach elektromechanicznych oraz energoelektronicznych. Dyskretny operator różniczkowania poddano testom dla najbardziej charakterystycznych funkcji. W artykule przedstawiono ponadto wyniki testowych obliczeń stanu ustalonego w prostym przetworniku elektromechanicznym.

Słowa kluczowe: *analiza w dziedzinie czasu*, *dyskretny operator różniczkowania*

DOI: 10.4467/2353737XCT.15.089.3921

* Prof. Ph.D. D.Sc. Eng. Tadeusz J. Sobczyk, Institute on Electromechanical Energy Conversion, Cracow University of Technology.

** Ph.D. Eng. Michał Radzik, Technical Institute, State Higher Vocational School in Nowy Sacz.

1. Introduction

Steady states in electrical circuits and in various types of electromagnetic objects are issues of great interest in electrical engineering because the technical parameters of devices are based on them. Steady states calculation methods are fundamental problems of electrical engineering and are basic tools for identifying the properties of electrical circuits, for example symbolic calculus which is used to analyse circuits with sinusoidal current waveform. This is a method which operates in the frequency domain. It allows the simple specification of parameters of set solutions on the basis of which one can clearly determine values of solutions in particular moments of time if necessary. The symbolic calculus in circuits with power electronic elements, even if it can be used, is not an effective method. Usually, simulation methods are used to determine steady states, increasing simulation time until the steady state is reached.

Specifying time performances on the basis of the Fourier spectra obtained with frequency methods can be insufficient in the case of deformed temporary solutions containing erratic changes of value, nothing that due to the Gibbs phenomenon. This paper presents an attempt to create an algorithm which allows the direct calculation of the temporary values of periodic steady waveforms where a circuit is described by a system of linear ordinary differential equation with temporary variable modulus which has periodic steady solutions.

2. Formulation of the problem

From a mathematical point of view, the particular solution is looking for to the system of differential equations in the form:

$$\frac{d\mathbf{x}}{dt} = \mathbf{A}(t) \cdot \mathbf{x} + \mathbf{b}(t) \tag{1}$$

in which both matrix $\mathbf{A}(t)$ and input vector $\mathbf{b}(t)$ are periodic and can be represented in the Fourier series:

$$\mathbf{A}(t) = \mathbf{A}(t+T) = \sum_{k=-\infty}^{\infty} \mathbf{A}_k \cdot \mathbf{e}^{jk\Omega t} \qquad \mathbf{b}(t) = \mathbf{b}(t+T) = \sum_{k=-\infty}^{\infty} \mathbf{B}_k \cdot \mathbf{e}^{jk\Omega t} \tag{2}$$

It can be proved that such a solution, known in engineering as steady-state, is also periodic and can be represented in form of the Fourier series:

$$\mathbf{x}(t) = \mathbf{x}(t+T) = \sum_{k=-\infty}^{\infty} \mathbf{X}_k \cdot \mathbf{e}^{jk\Omega t}, \quad \mathbf{\Omega} = 2\pi / T \tag{3}$$

The values of coefficients of this Fourier series comply with the infinite system of algebraic equations in the form [1, 2]:

$$j\boldsymbol{\Omega}\begin{bmatrix} \ddots & & & & \\ & \mathbf{E} & & & \\ & & \mathbf{0} & & \\ & & & -\mathbf{E} & \\ & & & & \ddots \end{bmatrix}\begin{bmatrix} \vdots \\ \mathbf{X}_1 \\ \mathbf{X}_0 \\ \mathbf{X}_{-1} \\ \vdots \end{bmatrix} = \begin{bmatrix} \ddots & \vdots & \vdots & \vdots & \\ \cdots & \mathbf{A}_0 & \mathbf{A}_1 & \mathbf{A}_2 & \cdots \\ \cdots & \mathbf{A}_{-1} & \mathbf{A}_0 & \mathbf{A}_1 & \cdots \\ \cdots & \mathbf{A}_{-2} & \mathbf{A}_{-1} & \mathbf{A}_0 & \cdots \\ & \vdots & \vdots & \vdots & \ddots \end{bmatrix}\begin{bmatrix} \vdots \\ \mathbf{X}_1 \\ \mathbf{X}_0 \\ \mathbf{X}_{-1} \\ \vdots \end{bmatrix} + \begin{bmatrix} \vdots \\ \mathbf{B}_1 \\ \mathbf{B}_0 \\ \mathbf{B}_{-1} \\ \vdots \end{bmatrix} \tag{4}$$

in which $\mathbf{A}_k$ and $\mathbf{B}_k$ are coefficients of the complex Fourier series (2). The equation set (4), limited to finite dimensions, allows us to calculate the spectra of solution in a given range of frequency. Therefore, it is a solution in the frequency domain, on the basis of which one can determine waveforms in time domain.

Equations (4) where used to formulate the equations directly determining values of the steady-state solutions in a selected set of points over the period of its variations, i.e. determining the solution in the time domain. For this purpose, a relation between values of a periodic function with period T and the coefficients of a Fourier series has been used. The relation between a set $2N$+1 of points evenly distributed over the period of a function, so, that $t_n = n \cdot T/(2N + 1)$ for $n = \{0, \pm1, \pm2, \ldots, \pm N\}$ and a set of $2N + 1$ the first successive harmonics $n = \{0, \pm1, \pm2, \ldots, \pm N\}$ of the complex Fourier series can be written in the form [3, 4]:

$$\mathbf{x}^N = \mathbf{C} \cdot \mathbf{X}^N \tag{5}$$

where:

$$\mathbf{x}^N = [x_N \quad \cdots \quad x_1 \quad x_0 \quad x_{-1} \quad \cdots \quad x_{-N}]^T$$

$$\mathbf{X}^N = [X_N \quad \cdots \quad X_1 \quad X_0 \quad X_{-1} \quad \cdots \quad X_{-N}]^T$$

Matrix **C** is in form:

$$\mathbf{C} = \begin{bmatrix} c^{N^2} & \cdots & c^N & 1 & c^{-N} & \cdots & c^{-N^2} \\ \vdots & & \vdots & \vdots & \vdots & & \vdots \\ c^N & \cdots & c^1 & 1 & c^{-1} & \cdots & c^{-N} \\ 1 & \cdots & 1 & 1 & 1 & \cdots & 1 \\ c^{-N} & \cdots & c^{-1} & 1 & c^1 & \cdots & c^N \\ \vdots & & \vdots & \vdots & \vdots & & \vdots \\ c^{-N^2} & & c^{-N} & 1 & c^N & & c^{N^2} \end{bmatrix} \tag{6}$$

where $c = e^{j(2\pi/(2N+1))}$.

We can demonstrate that matrix **C** complies with the relationship:

$$(\overset{*}{\mathbf{C}}^T) \cdot \mathbf{C} = (2N+1) \cdot \mathbf{E}_{2N+1} \tag{7}$$

Therefore relationships between the Fourier modules and values of function can be written down in the form

$$\mathbf{X}^N = \frac{1}{2N+1}(\overset{*}{\mathbf{C}}^T)\cdot\mathbf{x}^N \tag{8}$$

Equations (4) and relationships (5) and (8) will be used to formulate equations directly determining instantaneous values of periodic solutions.

3. Equations defining the solution in the time-domain for linear equations

To form of algebraic equations defining the periodic solutions in the time domain we should limit infinite harmonic balance equations (4) to dimensions, $(2N + 1) \times (2N + 1)$ from which we can calculate a Fourier spectra of the solution set to the N-th harmonic, inclusive. This system written down compactly has the form:

$$j\cdot\mathbf{\Omega}^N\cdot\mathbf{X}^N = \mathbf{A}^N\cdot\mathbf{X}^N + \mathbf{B}^N \tag{9}$$

Relationships between the momentary values of a solution and a Fourier series modulus for a vector solution $\mathbf{x}(t)$ can be, on the basis of (5) and (6), written in the form:

$$\mathbf{x}^N = \mathbf{C}\cdot\mathbf{X}^N;\quad \mathbf{X}^N = \frac{1}{2N+1}(\overset{*}{\mathbf{C}}^T)\cdot\mathbf{x}^N \tag{10}$$

Matrix $\mathbf{C}$ takes the form identical to matrix $\mathbf{C}$ given by formula (6), but each of its elements is constituted by a diagonal matrix of dimension of matrix $\mathbf{A}(t)$ of the system (1), comprising elements equal to the appropriate element in matrix $\mathbf{C}$.

The system of equations which determines the solution set in the time domain can be obtained after conducting the following mathematical calculations:

$$j\cdot\frac{1}{2N+1}(\mathbf{C}\cdot\mathbf{\Omega}^N\cdot(\overset{*}{\mathbf{C}}^T))\cdot\mathbf{x}^N = \frac{1}{2\mathrm{N}+1}(\mathbf{C}\cdot\mathbf{A}^N\cdot(\overset{*}{\mathbf{C}}^T))\cdot\mathbf{x}^N + \mathbf{C}\cdot\mathbf{B}^N \tag{11}$$

Designating:

$$j\cdot\frac{1}{2N+1}(\mathbf{C}\cdot\mathbf{\Omega}^N\cdot(\overset{*}{\mathbf{C}}^T)) = \mathbf{D}^N \tag{12}$$

$$\frac{1}{2N+1}(\mathbf{C}\cdot\mathbf{A}^N\cdot(\overset{*}{\mathbf{C}}^T)) = \mathbf{a}^N \tag{13}$$

$$\mathbf{b}^N = \mathbf{C}\cdot\mathbf{B}^N \tag{14}$$

we obtain a system of linear algebraic equations:

$$(\mathbf{D}^N - \mathbf{a}^N)\cdot\mathbf{x}^N = \mathbf{b}^N \tag{15}$$

Matrixes $\mathbf{D}^N$ and $\mathbf{a}^N$ obtained as a result of multiplying the matrix in brackets in relationships (12) and (13) are squared and have dimensions $(2\mathrm{N} + 1) \times (2\mathrm{N} + 1)$, and $\mathbf{b}^N$ is a vector with $(2N + 1)$ elements. These dimensions correspond to the number of points in which values of periodic solutions are calculated. Matrix $\mathbf{D}^N$ represents a differential operator, and matrix $\mathbf{A}^N$ and $\mathbf{b}^N$ represents values of matrix $\mathbf{A}(t)$ and the inlet vector $\mathbf{b}(t)$ at selected instances of time.

Matrix $\mathbf{D}^N$, which can be called a discrete differential operator for a periodic function, takes the form:

$$\mathbf{D}^N = \begin{bmatrix} \mathbf{0} & -\mathbf{d}_1 & -\mathbf{d}_2 & \cdots & -\mathbf{d}_N & \cdots & \cdots & \cdots & -\mathbf{d}_{2N} \\ \mathbf{d}_1 & \ddots & \ddots & \ddots & \vdots & \ddots & & & \vdots \\ \mathbf{d}_2 & \ddots & \mathbf{0} & -\mathbf{d}_1 & -\mathbf{d}_2 & & \ddots & & \vdots \\ \vdots & \ddots & \mathbf{d}_1 & \mathbf{0} & -\mathbf{d}_1 & -\mathbf{d}_2 & & \ddots & \vdots \\ \mathbf{d}_N & \cdots & \mathbf{d}_2 & \mathbf{d}_1 & \mathbf{0} & -\mathbf{d}_1 & -\mathbf{d}_2 & \cdots & -\mathbf{d}_N \\ \vdots & \ddots & & \mathbf{d}_2 & \mathbf{d}_1 & \mathbf{0} & -\mathbf{d}_1 & \ddots & \vdots \\ \vdots & & \ddots & & \mathbf{d}_2 & \mathbf{d}_1 & \mathbf{0} & \ddots & -\mathbf{d}_2 \\ \vdots & & & \ddots & \vdots & \ddots & \ddots & \ddots & -\mathbf{d}_1 \\ \mathbf{d}_{2N} & \cdots & \cdots & \cdots & \mathbf{d}_N & \cdots & \mathbf{d}_2 & \mathbf{d}_1 & \mathbf{0} \end{bmatrix} \tag{16}$$

whose elements are diagonal matrices $\mathbf{d}_n$ of dimensions of the system (1) with the values d_n on the diagonal:

$$\mathbf{d}_n = \begin{bmatrix} d_n & & & & \\ & \ddots & & & \\ & & d_n & & \\ & & & \ddots & \\ & & & & d_n \end{bmatrix}$$

These values are calculated from relationship:

$$d_n = \frac{\mathbf{\Omega}}{2N+1} \cdot \sum_{k=1}^{N} 2k \cdot \sin\left(k \cdot n \cdot \frac{2\pi}{2N+1} \right) \tag{17}$$

Matrix $\mathbf{D}^N$ is singular, which is quite obvious, because we cannot reproduce the constant periodic function on the basis of its derivative.

Execution of operations provided in (13) and (14) is not necessary, because they determine values of matrix vector $\mathbf{A}(t)$ and vector $\mathbf{b}(t)$ in selected time instances. They can be designated directly from these matrices, and not using their distribution in a Fourier series. Therefore we can write:

$$\mathbf{a}^N = \begin{bmatrix} \mathbf{A}(N) & & & & & & & \\ & \ddots & & & & & & \\ & & \mathbf{A}(1) & & & & & \\ & & & \mathbf{A}(0) & & & & \\ & & & & \mathbf{A}(-1) & & & \\ & & & & & \ddots & & \\ & & & & & & \mathbf{A}(-N) \end{bmatrix}$$

$$\mathbf{b}^N = [\mathbf{b}(N) \quad \cdots \quad \mathbf{b}(1) \quad \mathbf{b}(0) \quad \mathbf{b}(-1) \quad \cdots \quad \mathbf{b}(-N)]^T$$

where by matrices $\mathbf{A}(n)$ and vectors $\mathbf{b}(n)$ are denoted the matrix $\mathbf{A}(t)$ and the vector $\mathbf{b}(t)$, respectively, calculated for the time instances t_n. Then, the system of equations (15) takes the form:

$$\begin{bmatrix} -\mathbf{A}(N) & -\mathbf{d}_1 & \cdots & -\mathbf{d}_N & & \cdots & -\mathbf{d}_{2N} \\ \mathbf{d}_1 & \ddots & \ddots & \vdots & & & \vdots \\ \vdots & \ddots & -\mathbf{A}(1) & -\mathbf{d}_1 & -\mathbf{d}_2 & & \\ \mathbf{d}_N & \cdots & \mathbf{d}_1 & -\mathbf{A}(0) & -\mathbf{d}_1 & \cdots & -\mathbf{d}_N \\ & & \mathbf{d}_2 & \mathbf{d}_1 & -\mathbf{A}(-1) & \ddots & \\ \vdots & & & \vdots & \ddots & \ddots & -\mathbf{d}_1 \\ \mathbf{d}_2 & \cdots & & \mathbf{d}_N & & \mathbf{d}_1 & -\mathbf{A}(-N) \end{bmatrix} \begin{bmatrix} \mathbf{x}_N \\ \vdots \\ \mathbf{x}_1 \\ \mathbf{x}_0 \\ \mathbf{x}_{-1} \\ \vdots \\ \mathbf{x}_{-N} \end{bmatrix} = \begin{bmatrix} \mathbf{b}(N) \\ \vdots \\ \mathbf{b}(1) \\ \mathbf{b}(0) \\ \mathbf{b}(-1) \\ \vdots \\ \mathbf{b}(-N) \end{bmatrix} \tag{18}$$

It is the system of algebraic equations which was sought, from which one can directly calculate the values of periodic solution in a selected set of $2N + 1$ points.

The above considerations can be generalized to the non-linear system of differential equations of the form:

$$\frac{\mathrm{d}\mathbf{x}}{\mathrm{d}t} = \mathbf{f}(\mathbf{x}, t) \tag{19}$$

in cases where it is known that there is a solution to the given equation and this solution is periodic $\mathbf{x}(t) = \mathbf{x}(t + T)$. In order to do this, we must write down the system (19) in the form:

$$\frac{\mathrm{d}\mathbf{x}}{\mathrm{d}t} = \mathbf{A}(\mathbf{x}, t)\mathbf{x} + \mathbf{b}(t) \tag{20}$$

For this equation, we can create an iterative algorithm for seeking a periodic solution based on equations (15) and (19). Such an algorithm requires an iterative solving of equations of the form (in a compact notation):

$$(\mathbf{D}^N - \mathbf{a}_i^N) \cdot \mathbf{x}_{i+1}^N = \mathbf{b}^N \tag{21}$$

in which $\mathbf{x}_{i+1}^N$ is a vector of seeking solutions in iteration $i + 1$. Matrix $\mathbf{a}_i^N$ has form:

$$\mathbf{a}_i^N = \begin{bmatrix} \mathbf{A}_i(N) & & & & & & \\ & \ddots & & & & & \\ & & \mathbf{A}_i(1) & & & & \\ & & & \mathbf{A}_i(0) & & & \\ & & & & \mathbf{A}_i(-1) & & \\ & & & & & \ddots & \\ & & & & & & \mathbf{A}_i(-N) \end{bmatrix}$$

and contains matrixes $\mathbf{A}_i(n)$ calculated for the solution obtained in the i-th iteration for subsequent time instants. Such an algorithm requires the determination of the value of the starting solution.

4. Study of discrete differentiation operator

In order to check the correctness of the operation of the differentiation operator $\mathbf{D}^N$, the following calculation were performed:

– the correctness of calculating the derivative of a constant function was checked. As a result of the derivative because the values of matrix elements $\mathbf{D}^N$ comply to condition:

$$d_n = -d_{2N+1-n} \quad \text{for} \quad n = (1, 2, \ldots, N) \tag{22}$$

– correctness of calculating derivative of a function $\cos x$ was checked. The calculation results for $N = 100$ were shown in Fig. 1. Accuracy of function reconstruction $-\sin x$ is of the order of 10^{-12}.

– correctness of calculating derivative of a discontinuous function was checked. The derivative is not quite correctly reconstructed because there are effects similar to the Gibbs effect when calculating the value of discontinuous function on the basis of a Fourier series. This is illustrated in Fig. 2 with $N = 100$.

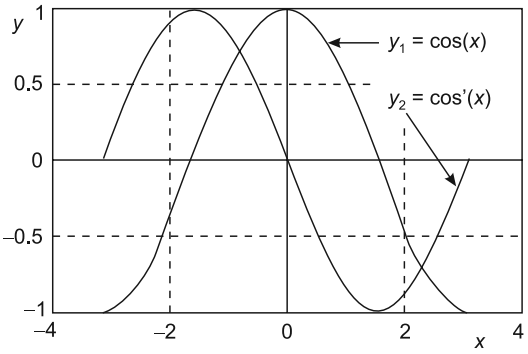

Fig. 1. Reconstruction of derivative of the function $\cos x$ by the operator of differentiation $\mathbf{D}^N$

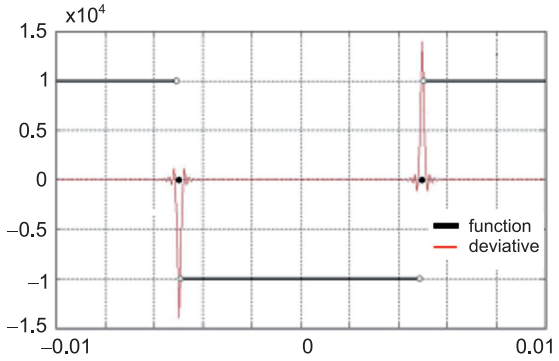

Fig. 2. Reconstruction of derivative of the discontinuous function by the operator of differentiation $\mathbf{D}^N$

5. Example of designating the solution for an electromechanical transducer

In order to illustrate the proposed approach, the steady-state analysis of the simplest electromechanical converter described by the equation is presented:

$$\frac{d}{dt}(L_0 + L_1 \cdot \cos(2\varphi)) \cdot i + R \cdot i = u(t) \tag{23}$$

The steady-state conditions are supplying voltage that is mono-harmonic:

$$u(t) = \sqrt{2}U \cdot \cos(\Omega \cdot t) \tag{24}$$

at constant angular velocity $\varphi = \Omega \cdot t + \varphi_0$. In these conditions, it can be envisaged that the solution in steady state will be periodic. The equation of the converter has been written in the normal form, corresponding to the equation (1):

$$\frac{d\psi}{dt} = \frac{R}{L(t)} \cdot \psi + u(t) \tag{25}$$

making use of the formula $\psi = L(t) \cdot i$.

The calculations were performed for the following parameters: L_0 = 3 H; L_1 = 2 H; $\varphi_0 = \pi/2$; U = 230 V; $\Omega = 2 \cdot \pi \cdot 50$ 1/sek. Also, for three resistance values: R = 100 Ω; R = 1000 Ω; R = 2000 Ω. It was assumed that N = 100, i.e. 201 equally distributed points were chosen in the range of voltage variation ($-T/2$, $T/2$). On the basis of equation (21), a system of equations (18) of dimensions (201×201) were set up, obtaining from its solution, the value of the linkage flux in the selected set of points. Values of current in these points were determined from the relationship $i = \psi/L(t)$.

The calculation results in the form of variability diagram $i(t)$ and $\psi(t)$ were shown in the following figures – for R = 100 Ω on Fig. 3, for R = 1000 Ω in Fig. 4 and R = 2000 Ω for Fig. 5. In Figure 3a, the waveform of flux is practically an integral of the voltage because the value of drop in voltage across the resistance is relatively small. The current is distorted due to the variable inductance. As the resistance is being increased, the flux deforms more and more, and consequently, the current deforms as well. Waveforms were determined directly in time. A small modification also allows the direct determination of current.

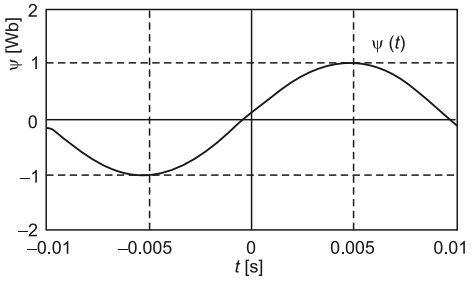

Fig. 3a. Flux waveform $\psi(t)$ (R = 100 Ω)

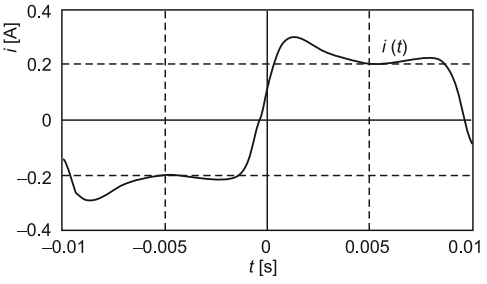

Fig. 3b. Current waveform $i(t)$ (R = 100 Ω)

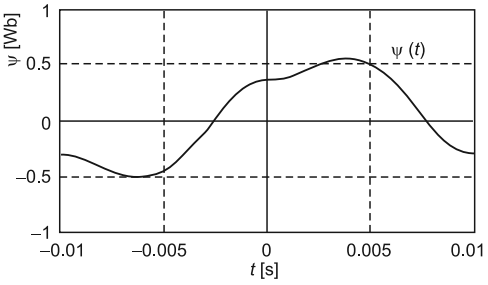

Fig. 4a. Flux waveform $\psi(t)$ ($R = 1000\ \Omega$)

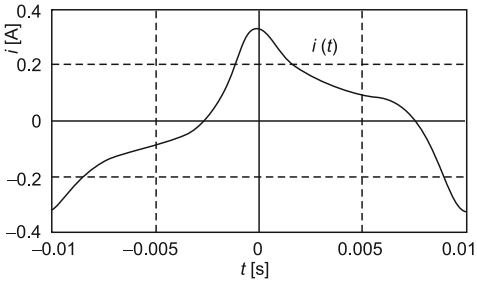

Fig. 4b. Current waveform $i(t)$ ($R = 1000\ \Omega$)

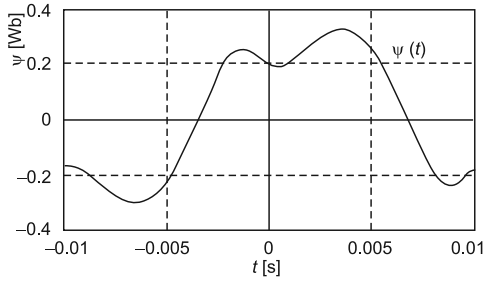

Fig. 5a. Flux waveform $\psi(t)$ ($R = 2000\ \Omega$)

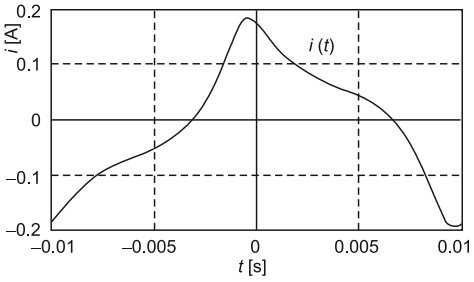

Fig. 5b. Current waveform $i(t)$ ($R = 1000\ \Omega$)

6. Conclusions

In this paper, equations for the direct determination of the instantaneous values for the periodic steady-state solution of linear differential equations with periodically variable parameters were evaluated. The obtained equations take the form of a set of linear algebraic equations and eliminate the need to use the Fourier series. The new discrete differential operator is an important element of this system.

Numerical tests of the discrete differential operator confirmed its correctness for calculation of derivatives for differentiable functions and its usefulness for the steady-state analysis of electromechanical converters.

References

[1] Boyce W.E., DiPrima R.C., *Elementary Differential equations*, John Wiley & Sons, New York 1969.

[2] Sobczyk T., *A reinterpretation of the Floquet solution of the ordinary differential equation system with periodic coefficients as a problem of infinite matrix*, Compel, Boole Press Ltd, Vol. 5, No. 1, Dublin 1986, 1-22.

[3] Burden R.L., Faires J.D., *Numerical analysis*, PWS-KENT Pub. Comp., Boston 1985.

[4] Sobczyk T., *Direct determination of two-periodic solution for nonlinear dynamic systems*, Compel, James & James Science Pub. Ltd., Vol. 13, No. 3, 1994, 509-529.

[5] Sobczyk T., *Bezpośrednie wyznaczanie w dziedzinie czasu okresowych rozwiązań ustalonych dla równań różniczkowych*, Materiały Konferencji PTETiS „Wybrane Zagadnienia Elektrotechniki i Elektroniki", CD, Rzeszów–Czarna 2013.

[6] Sobczyk T.J., Radzik M., *Bezpośrednie wyznaczanie rozwiązań okresowych dla przetworników elektromechanicznych w dziedzinie czasu*, Zeszyty Problemowe – Maszyny Elektryczne, Wydawnictwo Instytut Maszyn i Napędów Elektrycznych (KOMEL), Nr 103, 3/2014, 223-228 (SME 2014).

TECHNICAL TRANSACTIONS | **CZASOPISMO TECHNICZNE**
ELECTRICAL ENGINEERING | ELEKTROTECHNIKA
2-E/2015

JERZY SZCZEPANIK*, BARTOSZ ROZEGNAŁ*

THE DEVELOPMENT OF THE REAL LIFE MODEL OF THE FIVE NODE POWER SYSTEM

STRUKTURA I ANALIZA PRACY PIĘCIOWĘZŁOWEGO SYSTEMU ELEKTROENERGETYCZNEGO

Abstract

This paper presents the process of the development of the real life laboratory model of the five node power system of closed loop structure. The model was built using 'power' scaling and taking into consideration the parameters of the 400 kV lines built in the Polish National Power system. After the three-year development of the model, the parameters of the elements of this model were gained or obtained using classic identification procedures. During this part of the research, some differences between the parameter values given by the manufacturers and those obtained through identification procedures were reported and analyzed. The Matlab/Simulink model of the laboratory setup was then built to emulate the system behavior during dynamic states. The comparison of the currents, voltages and generator speeds proved to be simple tasks since the shape of the short-circuit current waveforms, for example, depends not only on parameter values but also on the time of the fault occurrence with respect to system voltages. Thus, the time responses of the laboratory and Simulink models were compared to evaluate time constants of the post fault processes.

Keywords: *close loop power system*, *short circuits in transmission line*, *models of HV transmission line*, *power system dynamics*

Streszczenie

W niniejszym artykule opisano proces budowy laboratoryjnego pięciowęzłowego modelu systemu elektroenergetycznego o zamkniętej strukturze. Model wybudowany został z użyciem skalowania „mocowego", gdzie parametry poszczególnych urządzeń (linii) odpowiadają polskiemu systemowi 400 kV. Po zaprojektowaniu oraz wybudowaniu systemu, co trwało trzy lata, parametry elektryczne i mechaniczne modelu systemu zostały albo uzyskane od producentów elementów, albo zidentyfikowane za pomocą klasycznych procedur. W trakcie tej części badań zaobserwowano znaczące różnice pomiędzy identyfikowanymi parametrami oraz parametrami otrzymanymi od producentów, pomimo zastosowania różnych metod identyfikacyjnych. Następnym krokiem było stworzenie modelu systemu laboratoryjnego w programie Matlab/Simulink w celu emulacji dynamiki rzeczywistego systemu. Porównanie parametrów zwarciowych okazało się trudnym przedsięwzięciem, gdyż odpowiedź systemu zależy nie tylko od wartości jego parametrów, ale także od momentu wystąpienia zakłócenia w stosunku do przebiegu napięcia. Tak więc porównanie dotyczyło głównie czasów zaniku procesów pozakłóceniowych, co pozwoliło na oszacowanie i porównanie stałych czasowych układu laboratoryjnego oraz modelu komputerowego.

Słowa kluczowe: *system elektroenergetyczny*, *zwarcia w linii elektroenergetycznej*, *modele linii NN*, *dynamika i stabilność systemu*

DOI: 10.4467/2353737XCT.15.090.3922

* Ph.D. Eng. Jerzy Szczepanik, M.Sc. Eng. Bartosz Rozegnał, Institute of Electromechanical Energy Conversion, Faculty of Electrical and Computer Engineering, Cracow University of Technology.

1. Introduction

The research work described in this paper includes the development of the multi-node, closed loop structure power system model, the process of the identification of its parameters and comparison of results obtained from simulations with real life system response. The purpose of the model development and construction are for studies of system stability, observability, its dynamic behavior for different conditions of work as well as studies associated with power flow control and cooperation of renewable energy sources with the power system model. The structure of the model resembles the IEEE five node benchmark structure (Fig. 1). However, the parameters of the system elements were calculated on the basis of the Polish National 400 kV network [1, 2]. The model of the system works using a voltage of 400 V and is assumed to be an equivalent of a 400 kV network.

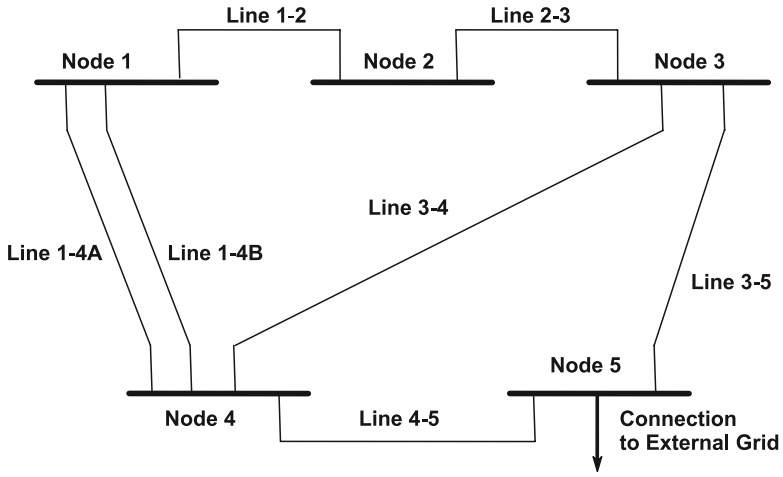

Fig. 1. Structure of the laboratory system model

The voltage ratio is 1:1000, thus calculation of the values of real elements using classic scaling based upon the energy conservation principle, where values of the real life elements are multiplied by the square of model and real life system voltage ratio $\left(\frac{V_1}{V_2}\right)^2$ is not possible. The model has to then be built using ratio of powers, i.e. downscaling real life power. The maximum power of all system elements was limited by the capabilities of the lab supply system to a range of 50–60 kVA. The model resembles 1–2 GVA real life system and the following ratios were applied to calculate the model elements [3–5].

Power ratio:

$$\eta_P = 25\,000 \div 1 \quad \text{(real life system 500 [MVA] = 20 [KVA] model)}$$

Voltage ratio:

$$\eta_U = 1000 \div 1 \text{ (Grid HV 400 [KV] = 400 [V] model)}$$

calculated from voltage and power ratios, current ratio [3, 5]:

$$\eta_I = \frac{\eta_P}{\eta_U} = \frac{25\,000}{1000} = 25$$

The assumed ratios were used to estimate and calculate the values of system parameters. The power of the generators (4 pieces for 4 nodes) was assumed as 20, 16 and 2 × 10 kVA equivalent to 500, 400 and 2 × 250 MVA, the line model continuous current rating was assumed to be 30 A (power rating $S = \sqrt{3} \times V_N \cdot I_N \approx 20.8$ kVA).

2. Detailed structure of the laboratory model

The laboratory model was built in the Power System Laboratory at the Faculty of Electrical and Computer Science Engineering. It consists of five nodes – each node in fact resembling the system switchyard. Nodes 1, 3, 4, and 5 (Fig. 2) include generation sets, which consist of a generator propelled by a DC machine driven via a two quadrant converter. The generator sets are connected to the model of the grid using transformers in a similar way to the way in which real life generators are connected to the grid via block transformers [2, 3, 6].

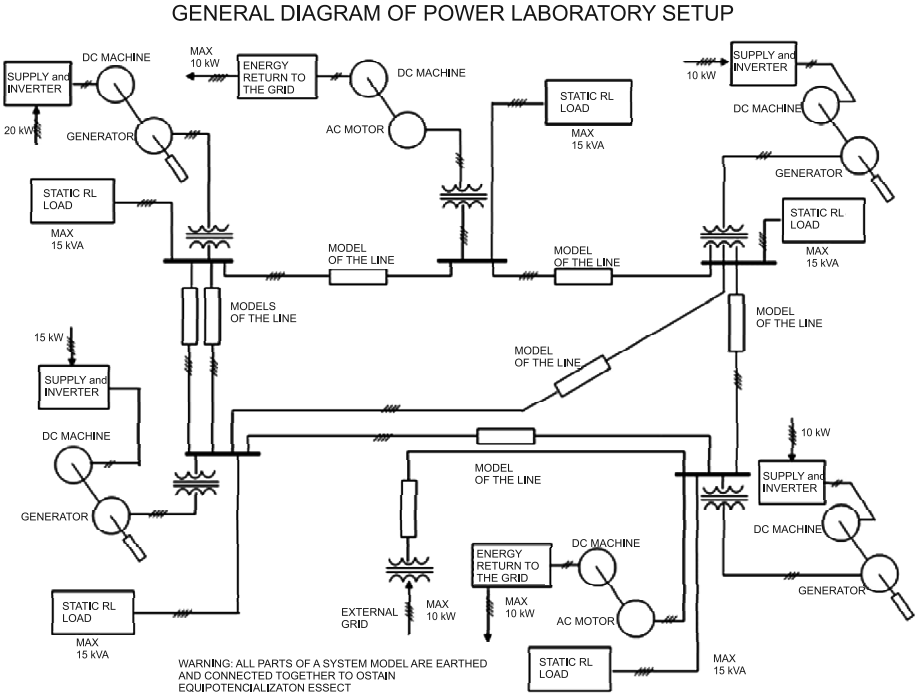

Fig. 2. General diagram of power laboratory setup

One of the nodes (node 5) is connected to the external supply grid via a 10 kVA transformer. Of course, it is impossible to connect a grid to an already working system without synchronization, thus, the blockade disabling the possibility of grid connection in case of voltage presence on switchyard bus was introduced. The generators and line models are connected to the switchyard busses using vacuum based switches, able to connect or disconnect currents up to 1600 A.

All system nodes include loads – passive and/or active ones. Passive loads were built using adjustable resistances and reactances. The active loads consist of the AC machine driven from the system rails via a soft start device. The AC machine propels the DC generator, which returns energy to the grid via a four quadrant converter.

Each node is equipped with sophisticated measurement equipment able to measure currents, active and reactive powers for all lines, generators and loads connected to node's bus for steady state measurements as well as fast response current to current transducers to measure currents during disturbances.

3. The development of elements of the laboratory model

3.1. System generating units

System generating units were built using separately excited DC motors propelling synchronous generator with separate excitation input. The field regulator for each generator was built using a programmable controller with an analog data acquisition module for generator voltage and a custom designed PWM power module for field winding supply. The generator was also equipped with a field current limiter as a protection against generator overcurrent for standalone work [7, 8].

The DC machine control is executed using a dedicated controller able to work in two or four quadrant arrangements. Basic control possibilities include the control of speed or torque of the motor in both directions of the rotation. Also, the slope of the speed and torque ramps can be adjusted, which is very helpful for limiting time of controller response during disturbances. The features of the converter include the possibility to set up different regimes of work – work for constant speed and work for given output torque (given load of the generator working with the system). When generator is working with a certain given torque at 3000 rpm, it delivers to the system a given active power. The generator working with the constant speed control is then used as a swing bus control to balance system loads. Such an approach enables keeping a constant generator speed (constant system frequency) at the required level [9].

3.2. Models of the lines

The power lines in Poland (even 400 kV lines) are too short for wave phenomena to occur. However, if distorted waveforms of currents and voltages are taken into consideration, the classic lumped parameter model (PI type model) may not be sufficient to exhibit the expected line behavior. Thus, chain type models were designed, each consisting of several PI sections. The sections of the lines are identical for every model, and the length of the line is varied by connecting different numbers of sections in series [10, 11].

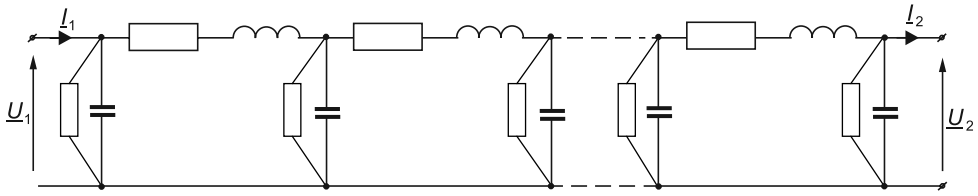

Fig. 3. Scheme of electrical line (transmission line) consisted of *n* two-port networks [11]

The model of the single power line π-section was built using assumed ratios and taking into consideration parameters of standard 30 km 400 kV as a basic length. The lines were built using 2×3, 2×4, 1×5, 1×6 and 1×8 sections.

3.3. Loads

The passive load includes resistive load banks of 9 kW (for 400 V voltage) divided into 4 steps: 600 W; 1.2 kW; 2.4 kW; 4.8 kW – inductive load 9 kvar controlled via a three phase autotransformer. This setup allows for composing an active load from 0 to 9 kW every 600 W (16 steps of control) and from continuously controlled reactive power. However, the control of the load inductances is not linear, since the inductance connected to the secondary side of the autotransformer is visible from the grid as multiplied by the square of autotransformer adjustable winding ratio [12].

The machine load block (active load) includes 10 kW AC induction motor driven from node bus via transformer, soft-start and propelling DC machine. The DC machine returns energy to the lab supplying grid via the four quadrant converter. The converter is able to vary the power returned to the grid, thus varying the AC machine load [1, 2].

3.4. Measurement arrangements

The system was equipped with state of the art measurement systems. Each input to the node's bus was fitted with current, active and reactive power measurements as well as current to current fast response transducers used to capture current waveform during dynamic processes. Other measured parameters include bus voltages, generator speeds and torque for two chosen generators [2, 3]. The results of the measurements are acquired using computers and D/A cards. Cards are 16 bit, 16 differential input channel devices with maximum sampling up to 1 Mb per channel.

3.5. Short circuit Module

A special module was built to simulate the system response to a short circuit. The module can provide any type of short circuit (any configuration) and the duration of this short circuit can be adjusted from 50 to 2000 ms, by 1 ms [11, 13]. Additional features of the module include triggering signal to the cards (4 cards with 64 channels), which can be connected to measure the required quantities in different nodes.

4. Identification of system parameters for modelling purposes

The model based on the described concept was built in power lab and the properties of the model were tested. These properties include static power flow distribution as well as system response to the disturbances such as short circuits for a chosen system states in several locations, line disconnection, generator shut down or rapid change in generator load and/or generators excitation currents.

The static condition of work and dynamic response of the system were investigated during real life model tests. Additionally, the Matlab/Simulink model was built to emulate a real life laboratory system and to test the possibility of real life dynamic behavior prediction.

The adequacy of the model is strongly dependent on parameter values and the complexity of used single element models. The values of the parameters had to be approximated from the real life lab model. Some of parameters required to perform the simulation can be obtained from the manufacturers of the system components (generators, transformers) or found using advanced parameter identification techniques.

4.1. Parameters of the lines

The parameters of single pi-section of the line corresponding to the 30 km of real 400 kV line (R_L, X_L –longitude resistance and reactance; G_L, B_L – parallel conductance and susceptance of line) were measured using technical methods. The measurements were performed several times, using different measuring devices and then the average value was calculated for each element. The measurements of the mutual inductance between phases were done for a series connections of two phases of 8 segments line. After the first measurement, the connection of phases was reversed and then the mutual inductance M was calculated in following way [10, 11, 14]:

$$M = \frac{L1_{zg} - L1_{re}}{4} \tag{1}$$

where:

$L1_{zg}$ – average inductance of one section for initial connection,
$L1_{re}$ – average inductance of one section for reverse connection.

The parameters derived from the model were multiplied by assumed ratios for the system model and compared to the real life 400 kV line [11].

The Matlab model used during dynamic states requires not only values of the elements for positive and negative sequences, but also the values of the elements for the ‘0’ sequence [15]. These values of parameters for the zero sequence, used in the simulation, were estimated on the basis of the parameter estimation for the real line and transformation to the model scale.

Phase *L*1		Phase *L*2		Phase *L*3	
Resistance					
R_8 =	0.3186 Ω	R_8 =	0.3189 Ω	R_8 =	0.3178 Ω
R_1 =	0.0398 Ω	R_1 =	0.0399 Ω	R_1 =	0.0397 Ω
Inductance					
Z_8 =	1.863491	Z_8 =	1.880975	Z_8 =	1.885867
Z_1 =	0.232936	Z_1 =	0.235122	Z_1 =	0.235733
X_1 =	0.229629	X_1 =	0.231846	X_1 =	0.232466
L_{11} =	0.000731	L_{12} =	0.000738	L_{13} =	0.000740
Phase *L*1-*L*3 consistently coupled		**Phase *L*1-*L*2 consistently coupled**		**Phase *L*2-*L*3 consistently coupled**	
Z_{16p} =	3.758951407	Z_{16z} =	3.817120623	Z_{16z} =	3.82364404
X_{16p} =	3.758135813	X_{16z} =	3.81631746	X_{16z} =	3.822842248
L_{16p} =	0.01196249	L_{16z} =	0.012147687	L_{16z} =	0.012168456
Phase *L*1-*L*3 oppositely coupled		**Phase *L*1-*L*2 oppositely coupled**		**Phase *L*2-*L*3 oppositely coupled**	
Z_{16p} =	3.758951407	Z_{16p} =	3.736507937	Z_{16p} =	3.778454633
X_{16p} =	3.758135813	X_{16p} =	3.735687443	X_{16p} =	3.77764325
L_{16p} =	0.01196249	L_{16p} =	0.011891035	L_{16p} =	0.012024584
M_{1-3} =	5.86369E-06	M_{1-2} =	8.0204E-06	M_{1-2} =	4.49602E-06

4.2. Parameters of the transformer model

The transformer model used for simulation is the simplest linear model with standard elements. The parameter estimation was performed using basic measurements for short circuit and no load at the secondary side of the transformer $U_{Z\%}$, ΔP_{Cu}, I_0 and ΔP_{Fe} for the stated conditions [12] (Fig. 4).

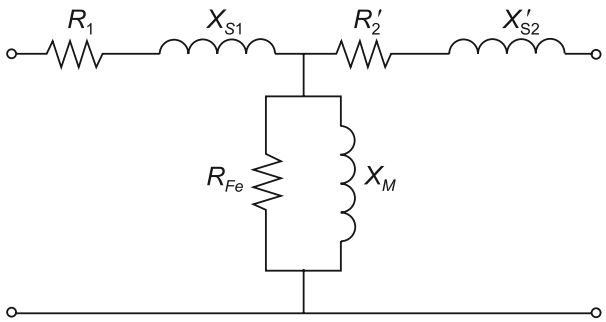

Fig. 4. Basic diagram of the transformer equivalent circuit [12]

Additionally, the resistances of the primary and secondary side were measured using Wheatstone bridge and using DC source, volt and amp meters as for small transformers, winding resistances can be comparable to the leakage reactances [16].

Tap Transformer 10 kVA					
Resistance R_1, R_2' and reactance X_{S1}, X_{S2}'					
Tap 440 V		Tap 400 V		Tap 360 V	
R_1 =	0.173 Ω	R_1 =	0.173 Ω	R_1 =	0.173 Ω
R_2' =	0.127 Ω	R_2' =	0.115 Ω	R_2' =	0.102 Ω
X_{S1} =	0.156 Ω	X_{S1} =	0.158 Ω	X_{S1} =	0.174 Ω
X_{S2} =	0.156 Ω	X_{S2} =	0.158 Ω	X_{S2} =	0.174 Ω
Z =	0.432 Ω	Z =	0.428 Ω	Z =	0.444 Ω
Vertical impedance (no load condition)					
Z_P =	259.0991 Ω	R_{Fe} =	580.501 Ω	X_M =	295.560 Ω

Transformer 10 kVA		Transformer 20 kVA	
Resistance R_1, R_2' and reactance X_{S1}, X_{S2}'			
R_1 =	0.155 Ω	R_1 =	0.050 Ω
R_2' =	0.113 Ω	R_2' =	0.034 Ω
X_{S1} =	0.150 Ω	X_{S1} =	0.063 Ω
X_{S2} =	0.150 Ω	X_{S2} =	0.063 Ω
Z =	0.403 Ω	Z =	0.152 Ω
Vertical Impedance (no load condition)			
Z_P =	249.3506 Ω	Z_P =	115.935 Ω
R_{Fe} =	572.1854 Ω	R_{Fe} =	592.5047 Ω
X_M =	277.041 Ω	X_M =	118.220 Ω

The measurements were done for three types of transformers with windings arranged star/delta used in lab system model: 10 kVA 400/400 V, 20 kVA 400/400 V and transformer with taps 10 kVA 400/360-400-440 V used for grid connection.

The most difficult cases in this research were the mechanical parameters identification procedures for generator – DC motor units, which were used to model the generator-turbine setup. The shaft of the generator is connected to the DC machine shaft using coupling, thus the mechanical data such as friction and moments of inertia have to be estimated for the whole unit.

Unit mechanical losses for nominal speed were estimated by measurement of the difference of DC machine input power and calculated machine electrical losses. Of course, this approach required measurements of the resistances of the DC machine and its currents for nominal speed and no load (generator was disconnected from the bus). Then, the moment of inertia for every generating unit was calculated in the following way, using the speed deceleration curve and known mechanical losses [17]:

$$J = \left(\frac{30}{\pi}\right)^2 \frac{P_{\text{mech}} \cdot \Delta t}{n_n \cdot \Delta n} = \frac{P_{\text{mech}} \cdot \Delta t}{\omega_n \cdot \Delta \omega} \,[\text{kg} \cdot \text{m}^2] \tag{2}$$

where:

P_{mech} – mechanical losses close to nominal speed,
ω_n – nominal speed [18].

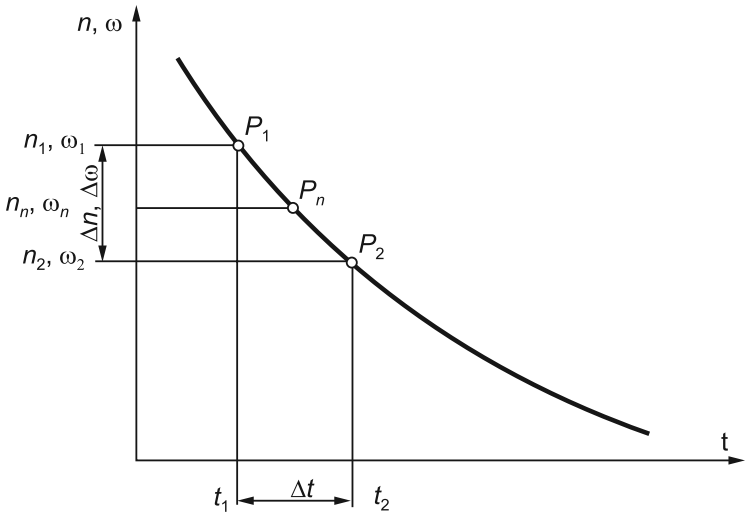

Fig. 5. Example of speed versus time curve [17]

Knowledge of the nominal speed losses also allows the calculation of the friction coefficient which is necessary to form the rotor movement equation in the Matlab model.

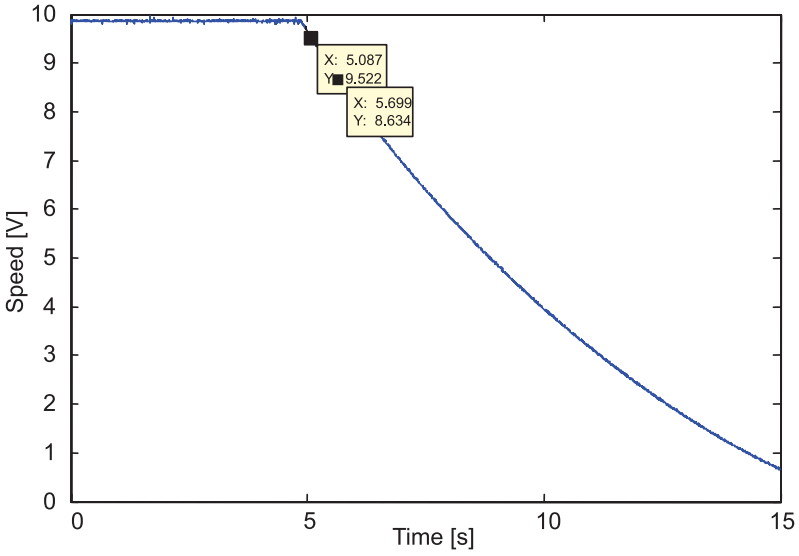

Fig. 6. Received speed versus time curve for 20 kVA generating unit

4.3. Identification of the generator electrical parameters

The resistances of the stator and field were measured using an ohmmeter and Thomson bridge, while synchronous reactances X_d and X_q of the generator were measured using a limited slip method [16, 18]. Figure 7 shows the obtained waveforms and dependencies 3 and 4 explain the calculation concept.

$$X_d = \frac{U_{s\max}}{\sqrt{3} I_{s\min}} \tag{3}$$

$$X_q = \frac{U_{s\min}}{\sqrt{3} I_{s\max}} \tag{4}$$

The calculations of the generator subtransied reactances X_d'', X_q''.

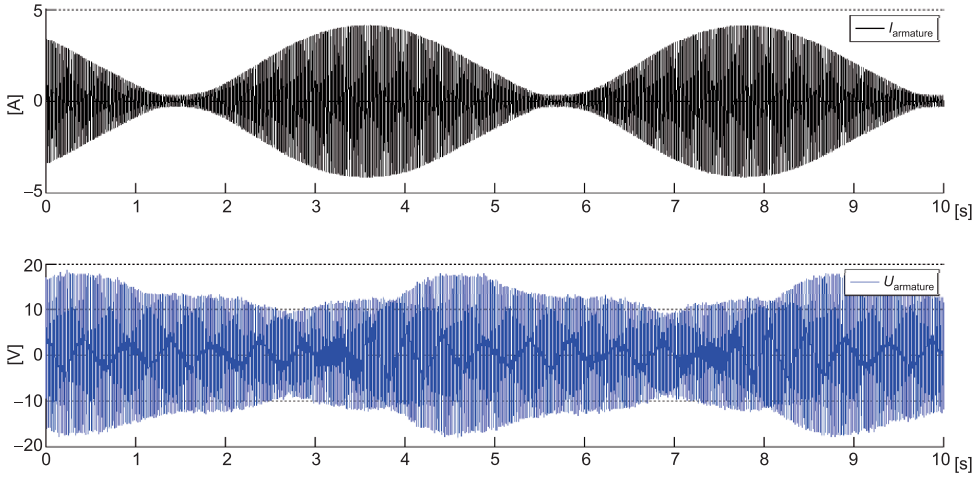

Fig. 7. Current and voltage waveforms used for limited slip method

The determinations of the generators X_d'', X_q'' parameters were done for stand still conditions. Two stator windings were supplied via a single phase autotransformer and voltmeter was connected to the field winding. The maximum inducted voltage indicates that the rotor is positioned along *d* axle and the minimum indicates *q* axle rotor position. For known *d* and *q* rotor positions, the measurement setup from Fig. 8 was used to measure input (stator) voltage and current as well as winding losses for short circuited field winding [16].

$$X_d'' = \sqrt{Z_d''^2 - R_d''^2} \tag{5}$$

$$Z_d'' = \frac{U}{2I} \tag{6}$$

$$R_d'' = \frac{P}{2I^2} \tag{7}$$

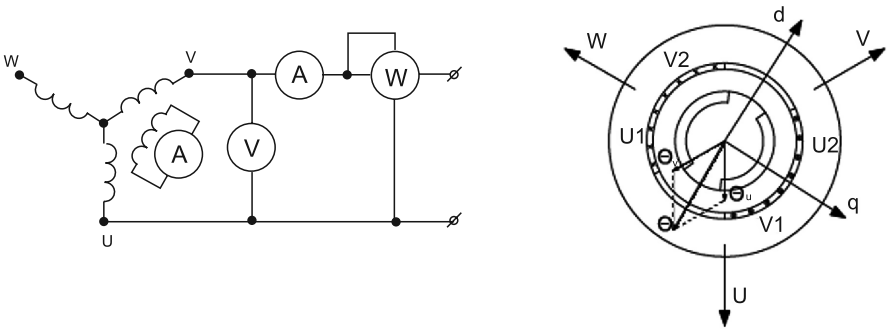

Fig. 8. Wiring diagram used to determine the X_d", X_q" reactance [16]

The measured parameters were compared to the data obtained from the manufacturers of the generators and DC machines. This comparison showed some differences.

Parameter name		Gen. 10 kVA	Gen. 20 kVA	Gen. 16.8 kVA
Nominal apparent power	Sn (VA)	**10000**	**22000**	**16000**
Nominal voltage	Vn (V)	**400**	**400**	**400**
frequency	fn (Hz)	**50**	**50**	**50**
Nominal field current	ifn (A)	**4.3**	**6.9**	**7.85**
Stator				
Stator winding resistance	Rs(ohm)	0.71 (**0.87**)	0.37(**0.36**)	0.55(**0.54**)
Field				
Field winding resistance	Rf (Ohm)	23.72 (**21.19**)	13.50 (**12.00**)	11.90(**9.79**)
Field reactance	Lf (H)	Not calculated	Not calculated	Not calculated
Cage				
Rotor cage equivalent resistance	Rkd' (Ohm)	**1.6**	**1.16**	**1.3**
Mechanical parameters				
Moment of inertia for generator only	*J* (kg.m^2)	**0.023**	**0.065**	**0.058**
Moment of inertia for whole genset setup	*J* (kg.m^2)	0.066	0.085	0.075
Inertia constant for whole genset	H	0.20	0.34	0.26
Number of pole pairs	–	1	1	1
Reactances and time constants of the generators in SI units				
Reactance	X_d	**41.6**	32.3 (**27.1**)	**38.2**
Reactance	X_d'	**2.9**	**2.1**	**2.6**
Reactance	X_d"	2.67 (**0.9**)	1.53 (**0.9**)	1.68 (**1.0**)

Reactance	X_q	**23.4**	4.6 **(11.8)**	**16.6**
Reactance	X_q"	1.33	0.8	0.86
Time constant	T_{do}' (ms)	**525**	**600**	**600**
Time constant	T_d' (ms)	**36**	**47**	**41**
Time constant	T_{do}' (ms)	**5.8**	**6**	**6**
Reactances and time constants of the generators in pu				
Reactance	X_d	**2.60**	**3.73**	**3.82**
Reactance	X_d'	**0.18**	**0.29**	**0.26**
Reactance	X_d"	**0.055**	**0.12**	**0.10**
Reactance	X_q	**1.46**	**1.62**	**1.66**
Time constant	T_{do}' (ms)	**525**	**600**	**600**
Time constant	T_{do}" (ms)	**5.8**	**6**	**6**
Time constant	T_d' (ms)	**36**	**47**	**41**

In the above table, bold values are given by the machine manufacturer and others are calculated or estimated from the measurements.

In real life models of the system, the dynamic response is not only affected by the parameters of system elements but also by the time constants of used regulators. These regulators in the system include, for example, PID regulators of the DC motor drives which are responsible for the mechanical response of the DC motor propelling generator. The regulators enable work of the DC motor (equivalent of the turbine) in two basic control modes – for constant speed and for constant torque. The first mode of work corresponds to the 'swing mode' generator, where speed is controlled and generator active power changes to match system requirements. The constant torque mode is used to control generator active power, regardless of its speed. This type of work is popular in the power system, when power station works on the active power demand given from power authorities, however, during standalone work, the generator will change its speed as the load changes [19–21]. As mentioned above, the DC motor control also has adjustable limits to the controlled quantities, but not only are the values of the controlled quantities are adjustable, but also the speed of changes of these quantities.

The field regulator for each generator was built using a programmable controller with an analog data acquisition module for generator voltage and custom design PWM power module for field winding supply. Of course, the controller uses a programmable PID procedure [7, 8].

The settings of the PID controllers have a great influence on system dynamics and stability. Experiments showed that at certain excitation and speed regulator settings, even a single generator working on resistive load can, during steady state work, fall into oscillations. This happened due to the fact that time constants of the regulators were almost equal or one was a multiple of the second. Thus, the knowledge of regulator settings is crucial for the prediction of the system dynamics.

5. The development of Matlab Simulink model of laboratory setup

The static condition of work and dynamic response of the system were investigated during real life model tests. Due to the fact that short circuits and changes of the real life system structure cause stress to model elements and the system work setup for a required steady state is long and difficult process, the Matlab Simulink model was built to emulate real life laboratory system. The structure of the digital model was built using standard Simulink blocks, such as generator, turbine, transformers, π-section line models and RL loads. The parameters obtained from the identification procedure from laboratory setup were then used in the developed digital model (Fig. 9). First, outcomes of the simulation where the values of system parameters and the settings and limits of the regulators were applied to the standard Simulink models of generators, lines, turbines (equivalent of DC motor) and transformers were not satisfactory. This means that stable work of the system couldn't be reached in a reasonable time. Thus, the excitation regulators and the regulators of the turbine were modified, but still results were not satisfactory due to the interaction of the modified regulators with additional elements of control present in used steam turbine models. Only when the steam turbine model (STG) was replaced by a hydro turbine, the simulations showed convergence to a steady state work within the expected time [6, 15].

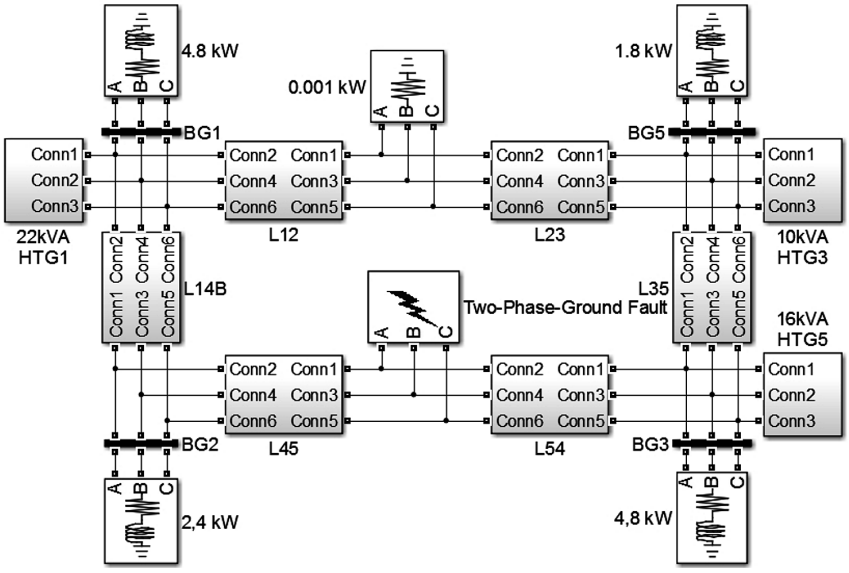

Fig. 9. The power system model created in Matlab/Simulink [15]

6. The range of tests and their results

At first, the laboratory setup was built in power lab and the properties of the model were tested. These properties include static power flow distribution as well as system response to the disturbances applied for chosen system states in several locations such as short

circuits, line disconnection, generator shut down or rapid change in generator load and/or its excitation [2, 4].

During the simulation of the Matlab model, it was noticed that the adequacy of the simulation results is strongly dependent on the parameter values and the complexity of used single element models. The values of the parameters had to be approximated from the real life lab model. Some of parameters required to perform the simulation were obtained from the manufacturers of the system elements (generators, transformers) or found using advanced parameter identification techniques. The initial assumption that the simulations of the dynamics of the multi-node system can be done using nonlinear complex models had to be verified, since the model was not stable or showed very narrow stability limits. Thus, the structure of the model was built using elements with linear characteristics. Actually, two models were finally built – one to perform the simulation for the solver operating in continuous mode to allow analysis of the system waveforms in the time domain and the second in phasor mode to allow tracking of the system state trends and shortening real times of the simulation.

6.1. The comparison of the results obtained from the real system and simulation

The results section shows the comparison of the measurements taken from the laboratory model and results obtained from the simulations for both steady state and the dynamic response of the system. Three generation nodes were used due to the failure of the coupling in one of the generator-DC motor sets.

Several simulations were performed to compare the lab setup and digital model performance at chosen steady state regimes of work. In real life and in simulation, two generators were working as PV generators, i.e. constant active power and constant voltage at the output and a third one was working as a swing bus with constant speed control [1, 2, 22].

The results of one of the comparisons are shown in the figures below:

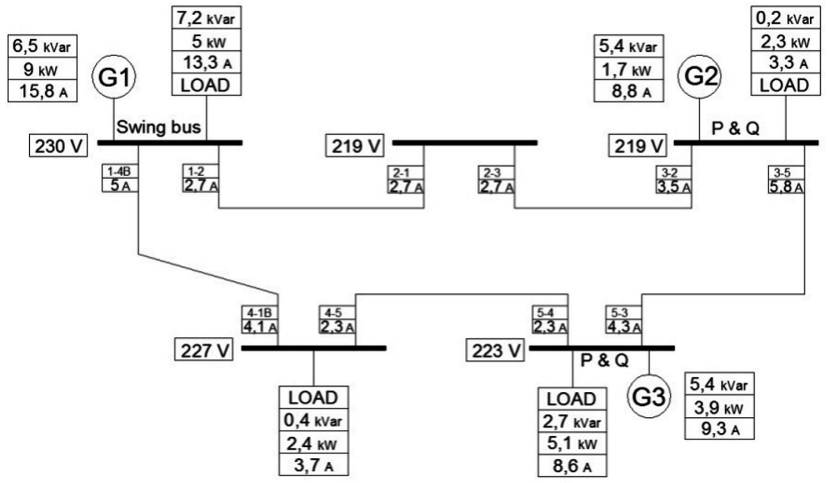

Fig. 10. Example of power flow in the laboratory model for steady state work

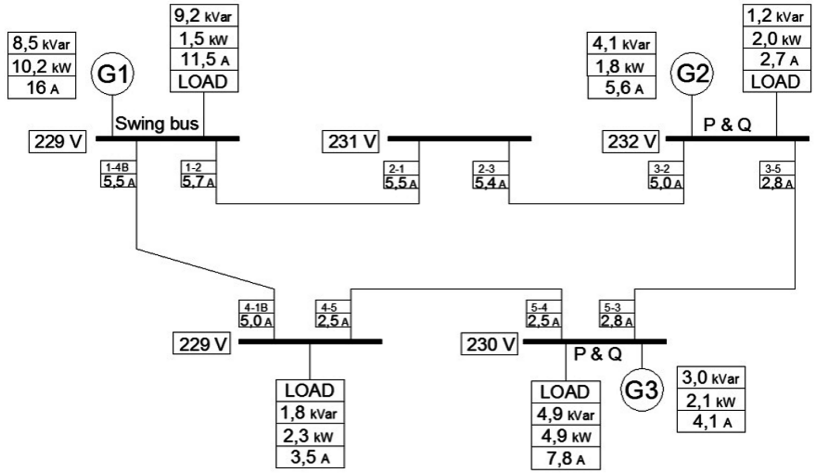

Fig. 11. Example of power flow simulation for steady state work

The research showed that it is very difficult to obtain similar conditions of work in the system and the simulation circuit even for the same loads and the same regime of work. This statement especially concerns the reactive power distribution. The system is built as an equivalent of the 400 kV version and includes relatively long lines, this introduces large capacitances, since the whole system consists of 25 π-sections of line models building

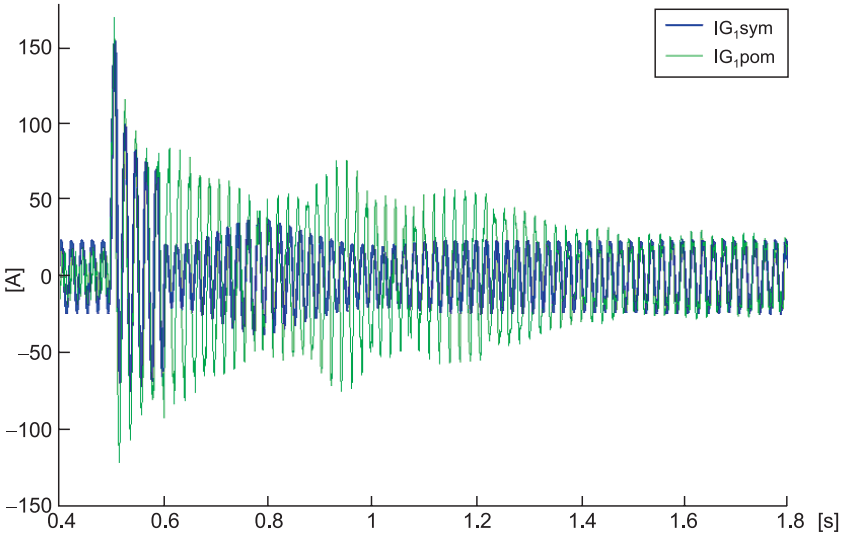

Fig. 12. The currents of generator 1 acquired from real life system ($IG1_1pom$) and obtained from the simulation ($IG1_1sym$) for 0.1 s short circuit and for shorted phase *L*2–*L*3 with ground between second and third section of line 4–5

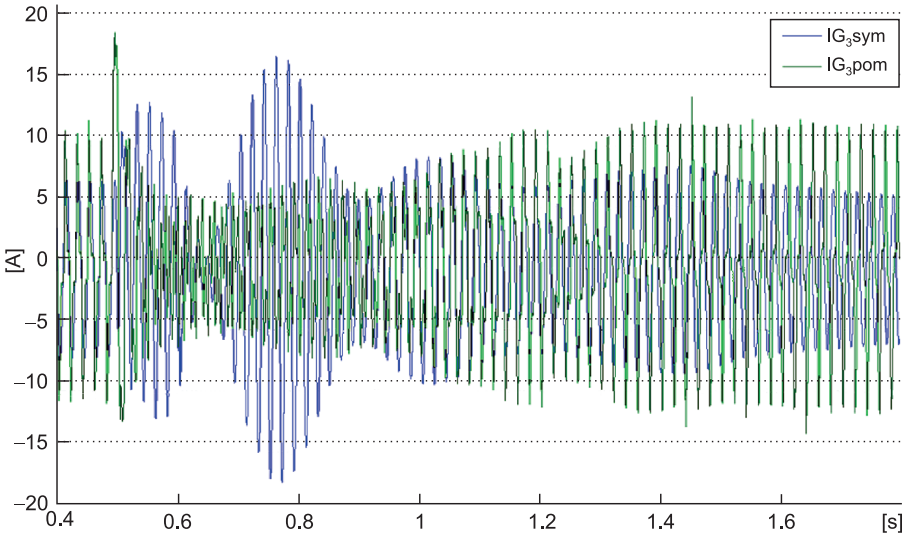

Fig. 13. The currents of generator 3 acquired from real life system ($IG3_3$pom) and obtained from the simulation ($IG3_3$sym) for 0.1 s short circuit and for 'healthy' phase (*L*1) for two phase (*L*2–*L*3) with ground shortcircuit between second and third section of line 4–5

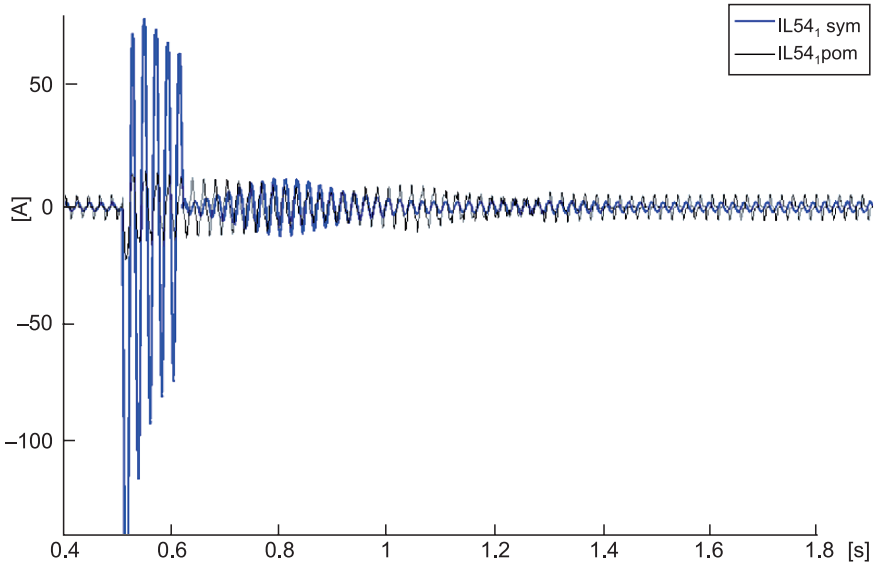

Fig. 14. The currents of line 5–4 acquired from real life system ($IL54_1$pom) and obtained from the simulation ($IL54_1$sym) for 0.1 s short circuit and for shorted phase *L*2–*L*3 with ground between second and third section of line 4–5

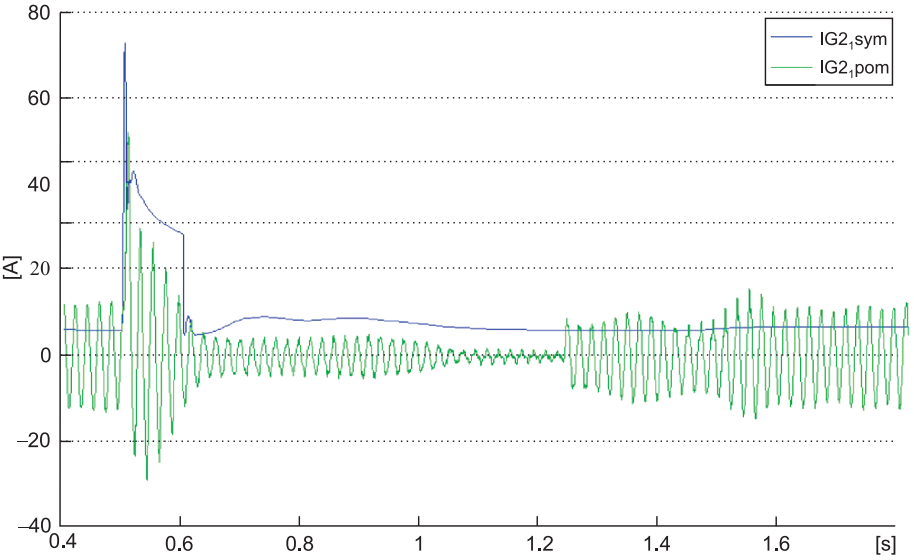

Fig. 15. The currents of generator 2 acquired from real life system ($IG2_1$pom) and obtained from the phasor simulation ($IG2_1$sym) for 0.1 s short circuit and for shorted phase *L*2–*L*3 with ground between second and third section of line 4–5

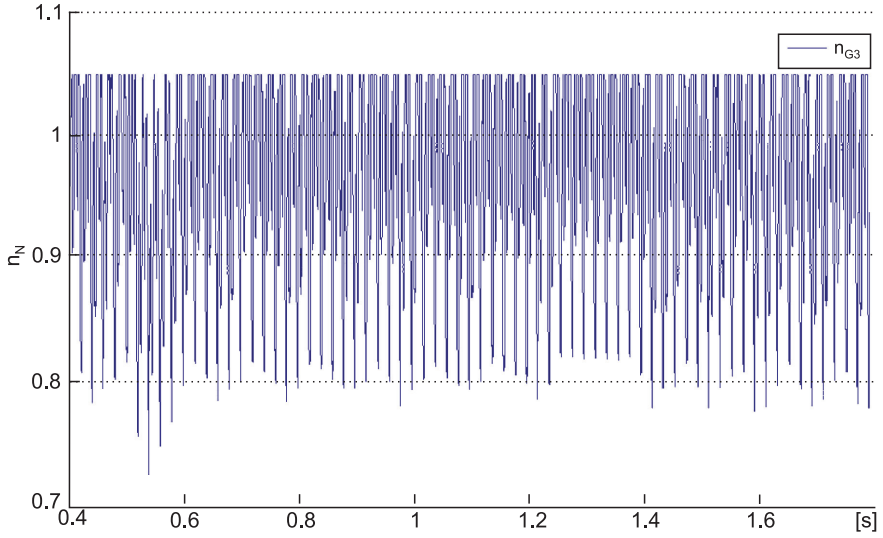

Fig. 16. The normalized speed of generator 3 acquired from real life system (n_{G3}) for 0.1 s short circuit and for shorted phase *L*2–*L*3 with ground between second and third section of line 4–5

a close loop structure and an 8 π section line at the diagonal. When the system is working using whole branches, the reactive power of line capacitors is about 7.3 kvar and for small resistive loads, it causes generator work as reactive compensators consuming reactive power.

The following figures show the currents in system elements during disturbances and dynamic response of the system and Simulink model to these disturbances. The measurement setup allows the acquisition of current waveforms from all system elements, thus, every experiment creates over 20 data sets. Usually, not all data are measured, but only the selected data – this prevents buffer overflows in data acquisition cards. The basic considered disturbance is a short circuit applied in the real system using a short circuit module [13].

The analysis of the above figure shows similar dynamic response (time of oscillation dumping) and similar amplitude during the first stage of the short circuit. This waveform was chosen since the time instant of short circuit in the real system and simulation was picked to assure the same position of disturbance with respect to the system and model voltages. This strategy assures that the value of the non periodic component for the real system and the simulation model is practically the same.

At first view, the currents in Fig. 14 are totally different, however, for the simulation the current exhibits a large non-periodic component while due to a specific position of the beginning of the disturbance, the measured current is almost free of this component. However, the oscillation dumping is almost the same, indicating similar dynamic properties of the lab setup and the Simulink model.

7. Conclusions

The described research work shows the process of the development of a five node power system model at Cracow University of Technology. The system was designed to assess the factors which have the influence on system stability, to build a base for FACTS devices application and to research system stability and controllability. The control of the electrical power system is associated with the overall activities called ‘smart grid’ which are the main activities promoted by the EU. The developed system will also be used as the base for researching the influence of renewable energy sources on the power system and for evaluation of different types of their connections to the grid.

Due to the fact that system is tested using a short circuit module, it does not include protection devices and the operation of the system requires basic knowledge about system behavior. This knowledge was gained during the experiments performed over the system during the two years of research work. The parameters of the system were obtained from the manufacturers of the system elements or were measured and calculated.

The identification of system elements was necessary not only to build the Matlab Simulink model but also to evaluate the system’s dynamics. Of course, the lab model dynamics differs from real life system dynamics since the downscaling was used only to scale electrical quantities – powers, voltages and currents, but was not applied to generators moment of inertia.

The Simulink model was built using standard blocks available in the library, thus the identification and estimation of the system parameters had to include all values necessary for

simulation. The simulation models were built for two solvers – for continuous and for phasor solver. The main problem during simulation of the complicated multi-node, multi generator close loop system includes the determination of the initial condition and establishment of the generator modes of work.

The results of the simulation showed similar dynamics of the digital model to the dynamics of the real life laboratory setup i.e. similar times of oscillation dumping, however, the values of the short circuit currents had different amplitudes.

References

[1] Potamianakis E.G., Vournas C.D., *Modeling and Simulation of Small Hybrid Power Systems*, IEEE PowerTech Conference, 2003.

[2] Andersson G., *Modelling and Analysis of Electric Power Systems*, ETH Zurich, 2009.

[3] Cokkinides G.J., Mohagheghi S., *A laboratory setup of a power system scaled model for testing and validation of EMS applications*, PowerTech, 2009 IEEE Bucharest.

[4] Gomez-Exposito A., Conejo A.J., Canizares C., *Electric Energy Systems: Analysis and Operation*, CRC Press, 2009.

[5] Handke A., Mitkowski E., Stiller J., *Sieci elektroenergetyczne*, Wydawnictwo Politechniki Poznańskiej, Poznań 1978.

[6] *Dynamic Models for Steam and Hydro Turbines in Power System Studies*, IEEE Trans. Power Appar. Syst., Nov./Dec. 1973, 1904-1915.

[7] Heffron W.G., Phillips P.A., *Effect of modern aplidyne voltage regulator on under-excited operation of large turbine generators*, Trans. Am. Inst. Electr. Eng., Part 3, 71, 1952, 692-697.

[8] Mak F.K., *Design of nonlinear generator exciters using differential geometric control theories*, Decision and Control, Proceedings of the 31st IEEE Conference, 1992.

[9] Mentor I, User guide.

[10] Miller P., Wancerz M., *Wpływ sposobu wyznaczania parametrów linii 110 kV na dokładność obliczeń sieciowych*, Przegląd Elektrotechniczny, ISSN 0033-2097, R. 90, Nr 4/2014.

[11] Kacejko P., Machowski J., *Zwarcia w systemach elektroenergetycznych*, wyd. 2, WNT, Warszawa 2009.

[12] Plamitzer A., *Maszyny elektryczne*, WNT, Warszawa 1982.

[13] Parise G., Massimiano M., Halpin, M., *Short circuit analysis on a simple power system network: the "characteristic" currents metod*, System Theory Proceedings of the Twenty-Seventh Southeastern Symposium on, ISSN 0094-2898, 1995, 30-34.

[14] Miller P., Wancerz M., *Problematyka wyznaczania i ewidencji parametrów linii WN z wykorzystaniem baz danych*, Poznan University of Technology Academic Journals, 74 (2013), ISSN 1897-0737, 2013.

[15] Matlab-Simulink, *Documentation and library*, Matlab R13a, 2013.

[16] Latek W., *Badanie maszyn elektrycznych w przemyśle*, Wydawnictwo Naukowo-Techniczne, Warszawa 1979.

[17] Norma PN-78 E-04252.

[18] Norma PN-E-06704.

[19] Szymanski Z., *Analysis of the stability an electro energetic grid with great load converter power supply system*, Compatibility in Power Electronics, CPE, 2007, 1-8.

[20] Andersson G., *Dynamics and Control of Electric Power Systems*, Lecture 227-0528-00, ITET ETH EEH – Power Systems Laboratory, ETH Zurich, February 2012.

[21] Kundur P., *Power System Stability and Control*, McGraw-Hill Inc., New York 1994.
[22] Bergen A.R., Vittal V., *Power System Analysis*, 2 ed., Prentice Hall, 2000.

TECHNICAL TRANSACTIONS | **CZASOPISMO TECHNICZNE**
ELECTRICAL ENGINEERING | ELEKTROTECHNIKA
2-E/2015

JERZY SZCZEPANIK*, TOMASZ SIEŃKO*

MICROPROCESSOR CONTROLLED MATRIX CONVERTER CONNECTOR FOR POWER SYSTEMS

STEROWANY MIKROPROCESOROWO PRZEKSZTAŁTNIK MACIERZOWY DO APLIKACJI W SYSTEMACH ELEKTROENERGETYCZNYCH

Abstract

A matrix $N\times M$ multiphase converter is a simple structure incorporating $N\times M$ bi-directional switches, connecting N input phases to M output phases and able to convert input voltages into output voltages of any shape and frequency. However, commutation problems and complicated control algorithms keep it from being utilized on a large scale. This paper gives a solution to the control system of the multiphase matrix converters for power system application. The practical application of multiphase matrix converters (MC) in power systems involves the study of application requirements, possible converter topologies and the development of new, reliable control algorithms. The MC is working as a connection device between power systems or as an interconnection device within the power system. The proposed tasks performed by the MC in the power system are power flow control and power flow oscillation dumping. The device can be viewed as new FACTS device-series power system connector, based on straightforward energy conversion.

Keywords: *Area Based Control*, *Matrix Converter Control*, *Multiphase Matrix Converter*

Streszczenie

Wielofazowy przekształtnik macierzowy $N\times M$ jest stosunkowo prostą strukturą złożoną z $N\times M$ dwubiegunowych zaworów łączących N faz wejściowych z M fazami wyjściowymi. Struktura ta teoretycznie może przekształcić dowolne napięcia wejściowe w dowolne napięcie wyjściowe (np. o innej fazie lub częstotliwości). Niestety problemy komutacyjne oraz trudne do implementacji algorytmy sterowania ograniczają możliwość stosowania tego urządzenia. Artykuł przedstawia nową metodę sterowania oraz sposób jej implementacji na mikroprocesor dla wielofazowego przekształtnika macierzowego. Metoda ta jest oparta na sterowaniu obszarowym i przeznaczona do zastosowania w systemie elektroenergetycznym. Praktyczna aplikacja przekształtnika musi w takim wypadku uwzględniać ograniczenia narzucane przez ten system, a wynikające z jego charakteru. Badania obejmują zatem stworzenie nowej procedury sterowania przekształtnika oraz analizę jego pracy w charakterze przesuwnika fazowego z uwzględnieniem narzuconych ograniczeń. Proponowane funkcje przekształtnika to kontrola rozpływu mocy czynnej w systemie oraz zastosowanie przekształtnika w urządzeniach typu FACTS.

Słowa kluczowe: *sterowanie obszarowe*, *sterowanie przekształtnikiem macierzowym*, *wielofazowy przekształtnik macierzowy*

DOI: 10.4467/2353737XCT.15.091.3923

* Ph.D. Eng. Jerzy Szczepanik, Eng. M.Sc. Tomasz Sieńko, Institute of Electromechanical Energy Conversion, Faculty of Electrical and Computer Engineering, Cracow University of Technology.

1. Introduction

FACTS technology is very promising for the power system control. In this paper, a new FACTS unit based on a matrix converter is investigated. Figure 1 shows a schematic diagram of a proposed controller, which consists of two power transformers and a matrix converter installed between them. Power transformers have 3-phase high voltage windings and *N*-phase windings connected to the *N*×*N* matrix converter (MC). Such a controller has three phase input and output, but energy transfer occurs in an *N*-phase system. The structures of the proposed devices incorporate transformers on both sides of the converter, this is determined by the necessity to decrease voltage levels to the power electronic equipment requirements and output voltage level control. The MC in this application is not used for voltage level regulation and only frequency and phase of the output is controlled. The simulations of such devices have already been done and reported in the previous authors' papers [1, 2].

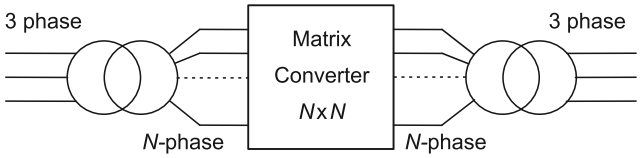

Fig. 1. A diagram of a voltage phase controller

The proposed field of application is a power system. This environment determines several requirements which have to be fulfilled in order to assure the proper operation of the MC based converter as an interconnection device. The MC converter based device has to 'produce' sinusoidal voltages as it works between two voltage sources with relatively low internal impedances (in conventional machine drive applications, sinusoidal currents are required [3–17]) and control (adapt) phases and frequencies on both sides of the apparatus. Such a device can control network power flow by shifting the phase of its output voltage, this results in changes of active power flow via network branches. Several other requirements such as continuous current flow, low contents of low order harmonics and lack of short circuits on both sides of the converter were taken into consideration during the device development. The PWM (pulse with modulation) switching strategies were not utilized in power system applications due to high power transfer, relatively large switching losses and control problems during their operation. Thus, in the proposed application, the MC works as a device that creates output voltage as a combination of the input voltages.

Multiphase (more than three phase) MC structures [18–23] were investigated as more promising for the proposed application due to the bad performance of the previously researched three phase systems. This bad performance of 3×3 structures means, in real life applications, a low and angle shift dependent voltage transfer, a high content of low order harmonics in converter voltages and currents [24–26], and the necessity to transfer entire power (at a given instant) through a maximum of only three switches (a minimum of two have to be open to assure current flow).

The main task of this research is to develop a multiphase MC based power system link characterized by a much better performance than the three phase version. The crucial part

of the project was the development of the control strategy most suitable for a proposed application and then the design of the control algorithm which can be applied in the real life digital controller. In order to produce sinusoidal voltages, the investigated strategies have to utilize all available values of input voltages, thus, they create outputs not only from fragments of the voltages lying at the envelope of the input voltages (as PWM based techniques) but they also use intermediate input voltage values.

2. The Development of The MC Control Algorithm

In the proposed field of application, the MC is a device which creates output voltage as a combination of the input voltages. Thus, for the multiphase MC structure, the first intuitive approach to the control system is to build the output voltage for a chosen output phase at a certain instant from the input phase, which voltage is at this instant closest to the desired one (the 'as close as possible' approach). The second option is to create output voltage from part of the certain input phase in the neighborhood of the point at which this input phase crosses the desired output waveform (the 'crossing point' approach). These algorithms are easy to build as an analog control system and can be easily simulated using for example, Matlab programming. The algorithm at a certain instant simply compares all input phases to the desired output waveform, chooses the input which is the closest and switches on the switch between the output and this chosen phase. Thus, in theory, the algorithm can be used to create with a certain adequacy, any shape of output from any waveforms of the input.

In this research, and for a proposed application, the shapes of waveforms are close to sinusoids, both at the input and at the output. For the 'as close as possible' algorithm, the switches are not turned 'on' for the same period of time, but the advantage of this strategy appears when the intervention of the MC is not required. Then, the desired output is equal to the input and there is no switching necessary – input phases are connected straight to the output. For switching strategy 'around crossing point' the switching periods are constant and, for example, for a 12×12 MC structure, they last for the time equivalent of 15 degrees. Thus, the switching algorithm can be simplified and the parameters of the output are constant – voltage transfer, *THD* and phase shift between the applied one and the phase of the first harmonic of the output.

The algorithms constructed in the proposed way do not guarantee to satisfy all requirements of the application, for example, short circuits are excluded. Several simulations were completed to research properties of the MC working under proposed controls. It can be noticed that the second approach can be considered as a special case of the first one for a certain phase shift between input and output waveforms. The waveforms obtained from analog simulation are shown in Figs. 2 and 3.

It is visible that the output waveform of the MC becomes closer to the desired one as the number of input phases increases (Fig. 2). The structures incorporating 6×6, 12×12 and 12×3 matrix of the switches were investigated in this research due to the fact that the six and twelve phase transformers are already on the market and they are used in power systems, for example, in DC link applications. The structure of the 12×12 MC incorporates 144 two-way switches, this was considered as a maximum due to the cost of the device.

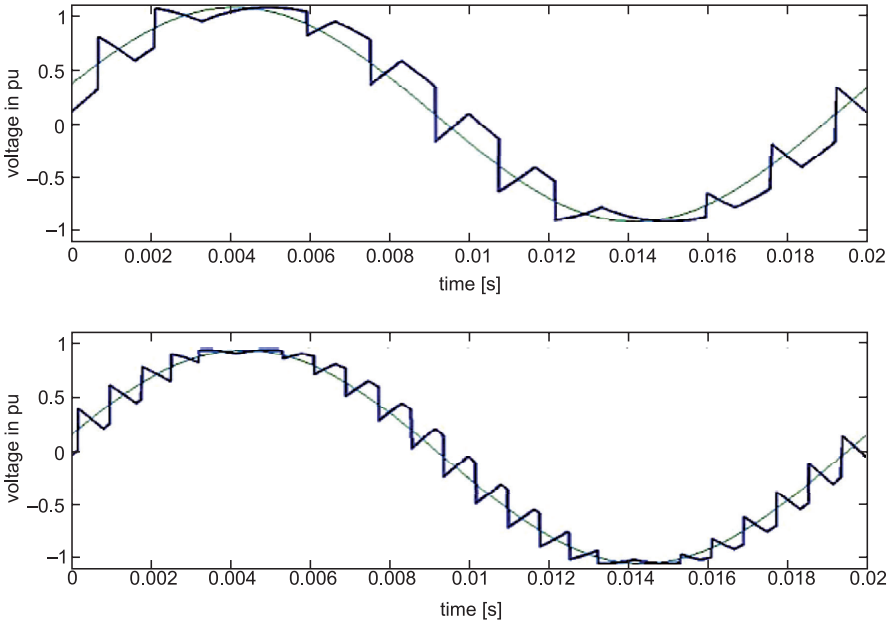

Fig. 2. Output waveform of the 6×6 (upper figure) and 12×12 MC (lower figure) under proposed 'as close as possible' control approach for 50 Hz to 50 Hz conversion and phase shift

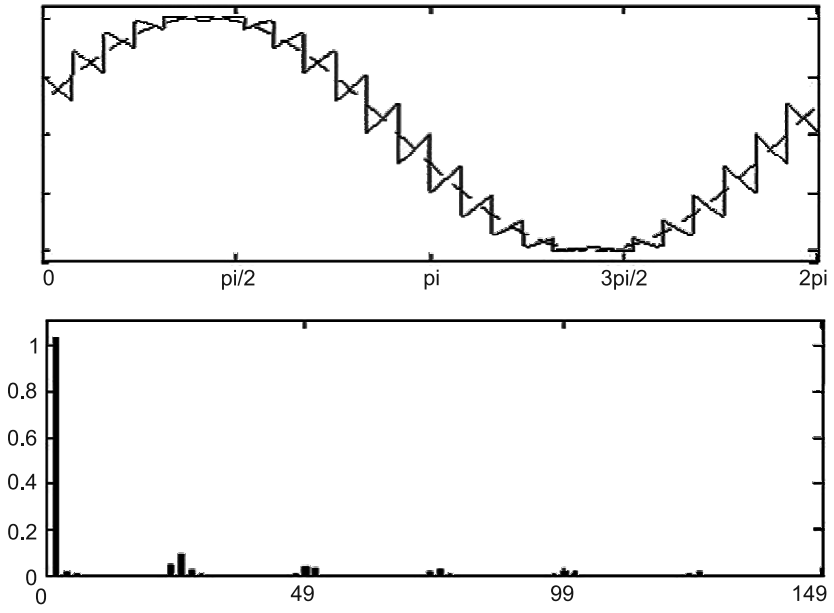

Fig. 3. Output waveform of the 12×12 MC under proposed 'crossing point' control approach versus the desired sinusoidal waveform (upper figure) and it's FFT (lower figure)

The proposed control strategies can be viewed as similar to the multilevel converter control strategies. It can be also noted that for input frequencies higher than 50 Hz, the adequacy of the desired waveform approximation by the MC converter increases. It can be simply explained by the fact that during the whole period of the 50 Hz output, there are more possibilities to find input waveforms close to the desired output waveform. This property of the MC working under the proposed control makes it suitable for the connection of the high frequency generators to the grid.

Properties of the investigated control algorithm are very promising – Fig. 3 shows the 12×12 MC output voltage waveform and its FFT for the second control approach, which is the worst distortion case for the 'as close as possible' approach. The converter currents and voltages are showing small harmonic distortions and contain only high order harmonics, which are easy to filter.

Due to the fact that in real life, it is impossible to implement the proposed control schemes using the digital controller and not all requirements are satisfied, the research led to developing a correlation of algorithms with already known ones which are easily applicable for a multiphase MC. The vector control strategy and the 'area' based control scheme was found to be the most promising in the digital controller application.

3. The 'area' Based Control Scheme For a Multiphase MC

In general, the output voltage for every output phase of the MC can be written as:

$$V_{\text{out}}(t) = G_1(t) \cdot V_1(t) + G_2(t) \cdot V_2(t) + \ldots + G_n(t) \cdot V_n(t) \tag{1}$$

where:

$G_n(t)$ – membership function for a given output phase and n-th input phase,
$V_n(t)$ – voltage for the n-th input phase.

The $G_n(t)$ membership function specifies at which time instant and for how long a certain m-th output phase voltage consists of the n-th input phase voltage. During the interval, when output voltage consists of a fragment of the n-th input voltage, the $G_n(t)$ function achieves the value '1' and in the other cases, its value equals '0' (Fig. 4).

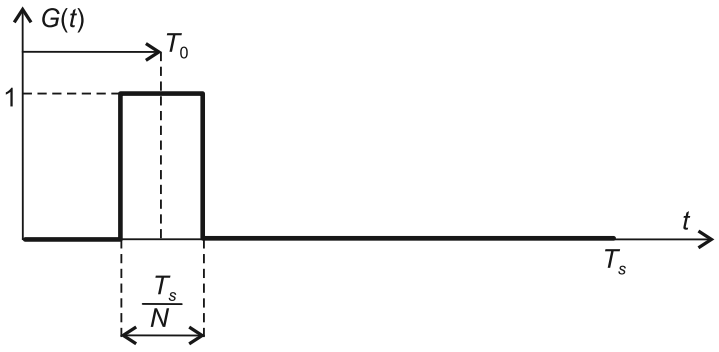

Fig. 4. An example basic membership function

In fact, the membership function specifies the MC control strategy and the shape of the output voltage waveform to be obtained. All existing control strategies can be expressed as a search for the specific membership function. Of course, if the MC creates output voltages from fragments of input ones, it also introduces ties to its input and output currents. Then the relation of all input quantities (voltages and currents) and output ones can be stated as [27, 28]:

$$\begin{bmatrix} V_N \\ I_M \end{bmatrix} = \begin{bmatrix} G & 0 \\ 0 & G^T \end{bmatrix} \begin{bmatrix} V_M \\ I_N \end{bmatrix} \tag{2}$$

where G is matrix of a membership functions.

The control algorithm used in this research adopted the so-called 'area' approach described in [29, 30]. This control strategy is based on a geometrical interpretation of functions describing actual state of the MC switches, since the shape of the membership function depends on the relative position of a certain input phase with respect to the desired output. Thus, the membership function can be viewed as a function of input and output voltage running phases where time is a parameter and all control processes can be analyzed in a two-dimensional space. For every switch (valve) in the MC structure, the state of this device can be determined at any instant on the plane where the value of the coordinate on the X axis is the value running phase of the input at this instant, and similarly, the Y axis represents the running phase at the output. Time is a parameter determining the values of the running phases, thus any time instant is represented by a unique point on the plane. If the running phases are continuous functions of time, the points determined on the plane by running phases (coordinates) are forming, as time elapses, a continuous curve. This curve is called the trajectory. When input and output frequencies are constant and running phases are linear functions of time (as in considered control scheme for sinusoidal waveforms), then the trajectory is a linear function in the considered space:

$$y = \frac{\omega_1}{\omega_2} x + \varphi \tag{3}$$

where φ is an initial angle difference between input and output.

If input and output waveforms are periodical, then the plane over which the membership function is defined can be limited to the rectangle of the size one period by one period.

When frequencies are different at the input and output, as time elapses, the running phase of higher frequency achieves the full period first then phase of lower frequency and at this point, phase of higher frequency is shifted to '0' (equivalent of repetition sequence in the second period). Thus, in such a space when any one of the input or output running phases reaches the border of this space, the trajectory is shifted to 0 (Fig. 5).

For the proposed application, the input and output waveforms of the MC are sinusoidal, thus, the proposed control space is limited to the square ($(0, 2\pi) \times (0, 2\pi)$) which corresponds to the 360 degrees by 360 degrees square. Since the state of the switch is regarded as a function of running phases, it can be observed that inside the control space, the points representing the 'on' state are forming a certain area over which the membership function obtains the value '1'. This area is called the conduction area and it is attached to a certain

single switch. If the trajectory, determining the relative position of the input and output waveforms, has common points with this area, that switch is in the ‘on’ state. Otherwise, the switch is in the ‘off’ position. Please note that due to the long time period of the research and different requirements of the simulation and controller software, running phases of the input and output waveforms are given in radians or degrees.

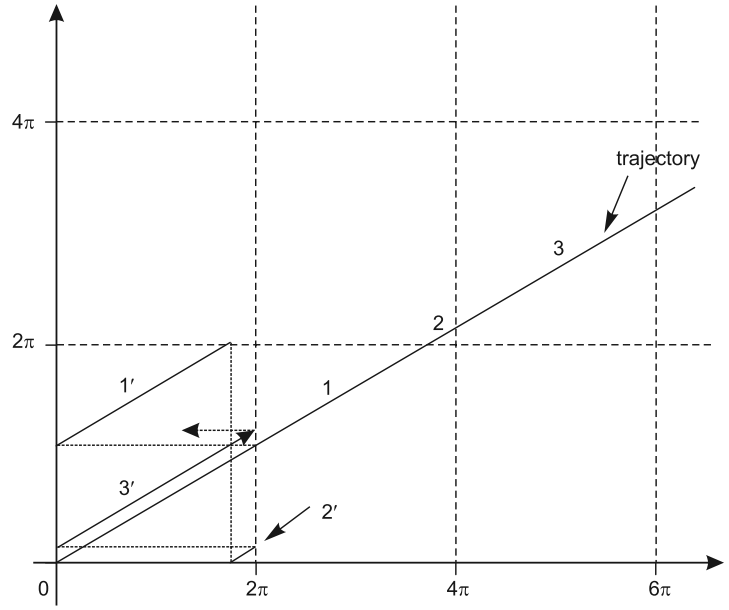

Fig. 5. Reduction of the trajectory into ((0, 2π) × (0, 2π)) subspace for periodical sinusoidal waveforms

In such an approach, the position and the shape of the area in control space determines when and how long the switch will be open, thus, it determines the switch control strategy. The advantage of the proposed approach is that the shape of the conduction area is independent of frequency and initial phase shifts of input and output waveforms. The proposed control scheme requires one and only one control space together with the conduction area for every switch, thus for $N \times M$ MC structure, the generation of $N \times M$ control spaces is required.

It can be noted that for the considered strategy of the conversion, the output waveform is created from parts of the input waveforms which are close to the waveform crossing. For two sinusoidal waveforms, the given waveform and the desired waveform, both with the same amplitude, the determination of the waveform crossing point can be done by solving a simple equation:

$$\sin \vartheta_1 = \sin \vartheta_2 \tag{4}$$

where:

ϑ_1, ϑ_2 – running phases of the input and output waveforms.

The solution is:

$$\vartheta_1 = \vartheta_2 + 2k\pi \quad \text{or} \quad \vartheta_1 = \pi - \vartheta_2 + 2k\pi \tag{5}$$

where $k \in C$.

In the proposed control space, the graphic interpretation of the above equations create the following diagram (Fig. 6).

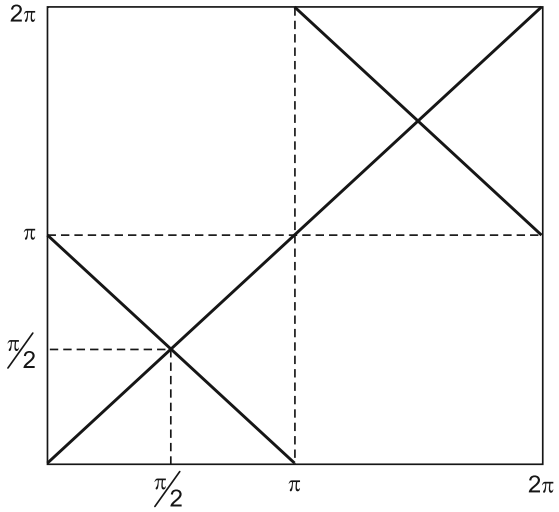

Fig. 6. Diagram corresponding to the solution of the equation (8)

These divagations can be repeated for all N input phases. What changes for the n-th input is the argument (running phase) of the first sinusoidal function in formula (4) which results in the following statement:

$$\sin(\vartheta_1 - 2\pi n / N) = \sin \vartheta_2 \tag{6}$$

Its solution is similar as in the case of the first phase and it is shifted along the X axis by $2\pi \cdot n/N$.

The conduction areas for the 'as close as possible' approach for the first switch have to lay in the vicinity of the lines from Fig. 6 since these lines represent the crossing points of the sinusoidal waveforms. The shapes of the conduction areas are, in theory, arbitrary, but if the input and output voltages assume the form of sinusoidal functions with the mean value during the period equal to zero (zero offset), the conduction areas for every switch have to be shaped according to the following rules [31]:

- They have to have the same shape for every switch which assures symmetry in every phase.
- The area corresponding to the conduction area of the first switch (G_{11}) is symmetrical in relation to the diagonals of the ((0,2π) × (0,2π)) space, this allows the creation of a symmetrical waveform (Fig. 6).

– For N input and M output phases, the following conduction areas are obtained by repeatedly shifting the base conduction area (G_{11}) by $2\pi/N$ along the X axis and by $2\pi/M$ along the Y axis ($N \times M$ switches).
– To avoid a short-circuit at the input, any cross-section of every conduction area along the X axis cannot be longer than $2\pi/N$, since if conduction areas which are used to drive switches connected to a certain output phase do not have common points, there are no short circuits caused by these switches between the input terminals. The same statement can be derived for the output terminals of the MC.
– Any cross-section of every conduction area along the Y axis cannot be longer than $2\pi/M$ to avoid a short-circuit at the output.
– Another stated condition is that $N \times M$ – this means that the number of input phases is equal to or greater than the number of output phases.
– For square structures ($N \times N$), if the sum of the conduction areas associated to one input or one output phase covers all $((0,2\pi) \times (0,2\pi))$ space, then the current of this phase is continuous which means that this phase is always connected respectively to the output or input phase.

For any MC structure, the control space should be covered by the conduction areas minimum two times at every point, which corresponds to minimum two switches turned 'on'. This condition is necessary to allow the current flow through MC when the structure without the neutral conductor is used.

The generations of the areas for the 'as close as possible' approach were conducted using an analog control algorithm by performing 360 simulations and increasing the phase shift between the input and output waveforms every one degree for every following

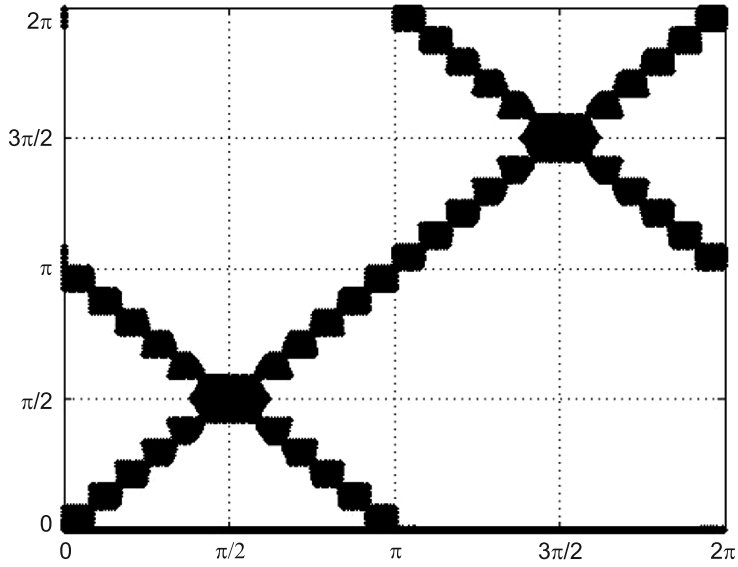

Fig. 7. Conduction areas generated from the intuitive control approach for the application in 'area' based algorithm for a switch 11 (switch between first output and first input phase)

simulation. The parts of trajectories along which the function F achieves the value '1' belong to the conductions areas. The generated conduction areas for a 12×12 structure are shown in Fig. 7. Of course, the layout of the generated areas is the same as the layout of lines representing the solution to equation (7) and it is shown in Fig. 6, since the points along these lines represent the situation when the output is equal to the input.

A similar generation procedure can be performed for the earlier described 'crossing point' approach or for the 'two closest' approach where the output sinusoidal waveform is created from two closest to it input waveforms [32].

The conduction areas similar to the one from Fig. 7 allow generating an output voltage waveform as a combination of the 'closest' parts of the input voltages sinusoids using the 'area' based approach. However, this control scheme does not satisfy all previously stated conditions required from the MC in the power system application, thus, the conduction areas had to be modified (Figs. 8–10).

The conduction areas for every switch are created from a basic structure obtained for a G_{11} switch by shifting the structure in the Y and X direction by the multiplication of the switch index and π/N.

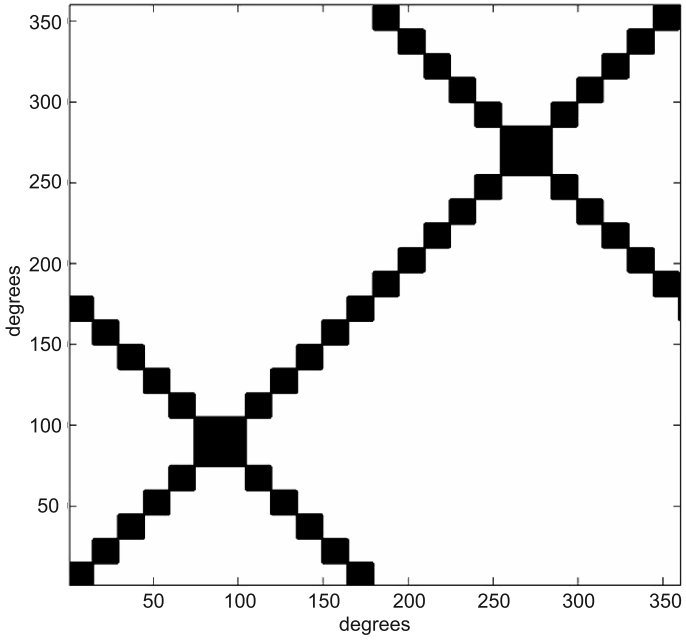

Fig. 8. G_{11} conduction area applied to the 'area' based MC control algorithm created on the basis of the areas from Fig. 4 and on the basis of the stated conditions

Figure 9 shows the shape of the conduction area for the 'crossing point' approach [33–36].

The performances of the proposed MC control schemes were investigated using Matlab Simulink software. A matrix lattice was build using a standard switch from SimPowerSystems library – source, loads and measuring blocks are standard Simulink blocks.

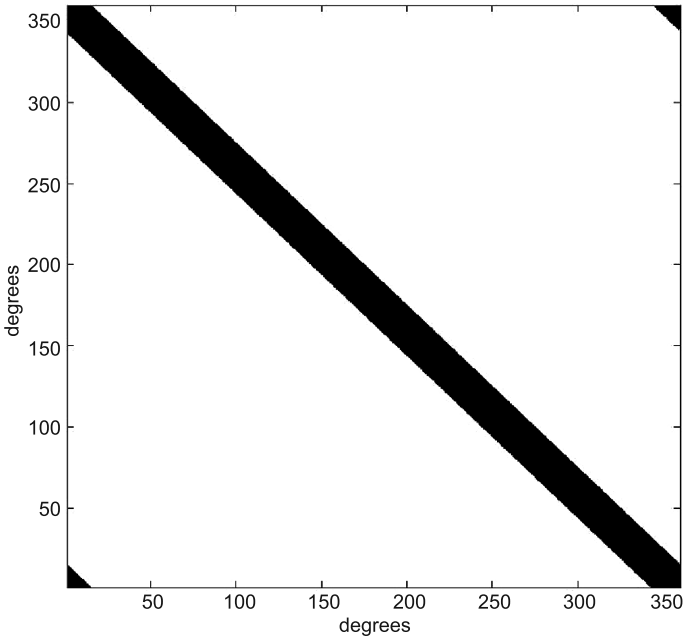

Fig. 9. Basic G_{11} conduction area for a crossing point approach

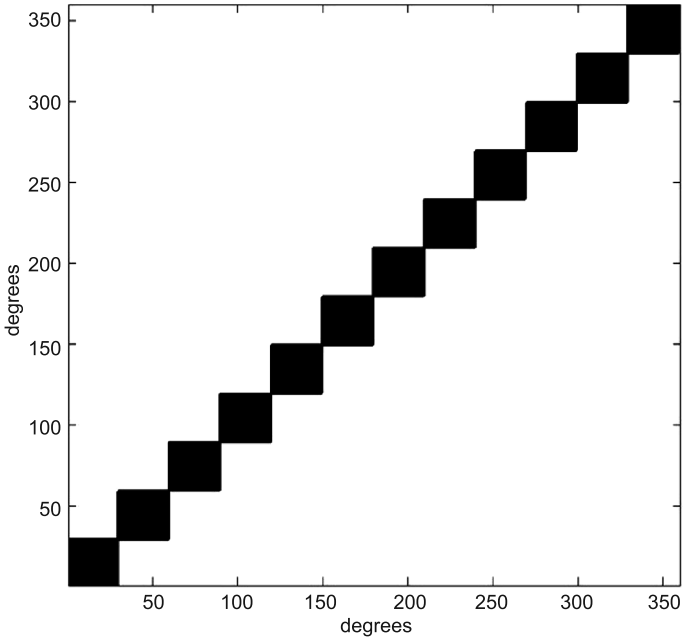

Fig. 10. Basic G_{11} conduction area for a two closest approach

The conduction areas for the proposed control scheme were generated assuming one degree resolution, using the developed software in the form of 360×360×144 matrix stored in the Matlab workspace. Each 360×360 layer of this matrix represents the conduction areas for a specific switch. The conduction areas are grouped in 12 layer structures, each representing conduction areas of row or column of MC switch lattice.

At a certain instant, the position of the point on the trajectory (its coordinates) representing phases of the input and output voltage at this instant, is compared with the layout of the conduction areas in every layer. If this point is situated inside the conduction area at a certain layer, the switch represented by this layer assumes the 'on' state.

This technique can be easy adapted for a digital control as a direct memory search technique for earlier generated conduction areas. The control algorithm for the purpose of the simulation has been written as a Matlab's *S*-function, where inputs are input and output frequencies, phase shift and simulation time. The 360×360×144 matrix of the conduction areas is implemented as a constant parameter of the *S*-function. The output of the *S*-function is a 144 column vector representing the states of all the switches – '0' is equal to the 'off' state and '1' is equal to the 'on' state of the switch.

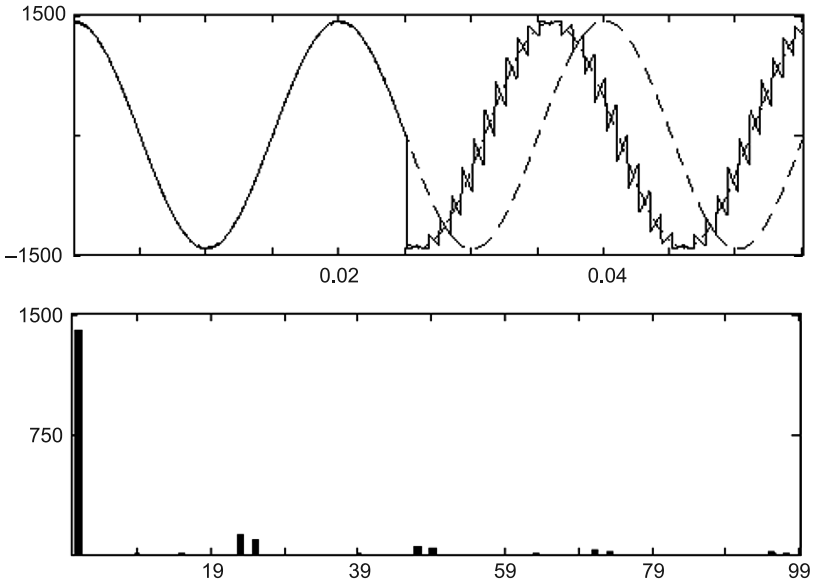

Fig. 11. The output voltage of the 12×12 MC at instant $t = 0.25$ s phase shift 75 degrees was applied and its *FFT* (dash line – waveform of first phase input, dash-dot line first harmonic output waveform)

The simulations of the proposed structure were done for the constant input voltages and constant load values. For the initial simulations, only a symmetrical supply of frequency being a multiple of output frequency and symmetrical loads were considered. This limitation was included only because in the other cases, the results are not so easy to interpret.

4. The Development of the Real Life MC Control System

The control algorithm is usually performed by the microprocessor controller. The proposed algorithm was chosen among the others due to the fact that it is easily applicable to digital control. The ((0,2π) × (0,2π)) planes with conduction areas can be easily generated for a chosen control strategy and a given number of switches in the MC lattice (one plane for one switch). Every plane can be divided into cells with a certain accuracy. For example, the accuracy of one degree can be achieved by dividing each plane to 360×360 cells. The value of membership function over each cell is '0' or '1', thus, one bit is enough to describe the membership function in each cell. Thus, the function over each plane is represented by 360×360×1 bit = 129 600 bits, which equals 16 200 bytes.

For a 12×12 MC structure, the 144 planes have to be generated, thus, the memory required to store all planes has to be greater than 2.2 MB. If the frequency at the output is close to 50 Hz, the required accuracy determines the frequency of switching. For 1º accuracy, the value of the membership function has to be updated every $\Delta t = 55 \cdot 10^{-6}$ s, which corresponds to 50×360 = 18 kHz switching frequency. The term 'switching frequency' does not determine the change of the switch state, but denotes that at every time interval Δt, the processor base controller has to find a new set of 144 values determining the states of switches and shifts them simultaneously to the output. Of course, the state of the specific switch changes, if the trajectory enters or leaves the conduction area.

Due to the special memory arrangement, the required operations performed in Δt time interval consist of memory cell address calculation from time and trajectory equation and the memory reading from the chosen cell (each cell consists of 18 bytes = 144 bits). For

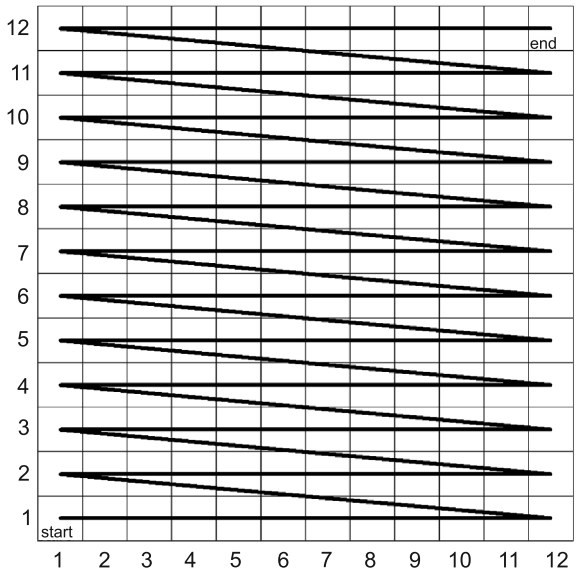

Fig. 12. The decomposition of the three dimensional (360×360×144) matrix into the two--dimensional and memory write procedure

MC lattices smaller then 12×12 – for example for 6×6 structures – only the first 36 bits form each memory cell are filled and the rest is topped by zeros to fill all 144 bits. Then, only the first 36 outputs are taken into consideration and the rest is ignored. This approach allows the development of only one memory search program for every size of the MC lattice (in the case of this research, the size is limited to 12×12 lattice). The zero crossing detectors are necessary to synchronize input and output voltages with trajectory and to determine the frequencies at both sides.

The processor used is a 128 MHz 32 bit device, so for a chosen switch update timing, it uses less than 1/4 of Δt time period to perform the memory search procedure, thus, it is possible to digitize $((0,2\pi) \times (0,2\pi))$ space two times denser in each direction to 720×720 cells. The work of the built controller is shown in Figs. 13 to 14. For the 6×6 structure, 50 Hz to 50 Hz conversion and 15 degrees of the phase shift of the output phase with respect to the input phase, the trajectory (Fig. 13) is delayed with respect to the input phase by 15 degrees. Then, the shape of the membership function of the first input phase in the first output phase is shown in Fig. 13 by a dotted line.

In the real application of the controller, the main problem is the zero sensing procedure and the delay caused by this procedure. The problem of the position of zero voltage becomes a serious problem especially for distorted input voltages (multiple zero crossing, not the same time period between following zero crossing points). The delay caused by the zero sensing procedure was investigated and was found to be the same for every measurement for the same procedure, thus, the correction is not an issue.

Laboratory model of MC was built as 6×6 structure using 36 bi-directional switches built using single IGBT and four diodes structure (Fig. 15).

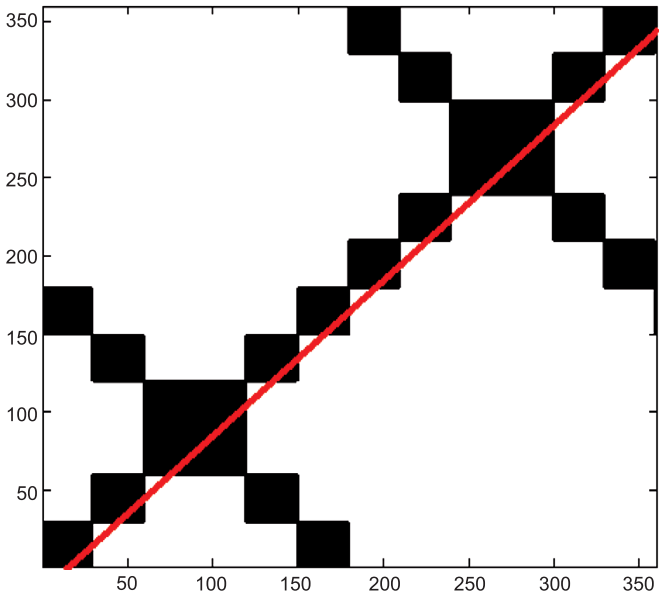

Fig. 13. Trajectory in the G_{11} control plane – the desired phase shift is 15 degrees

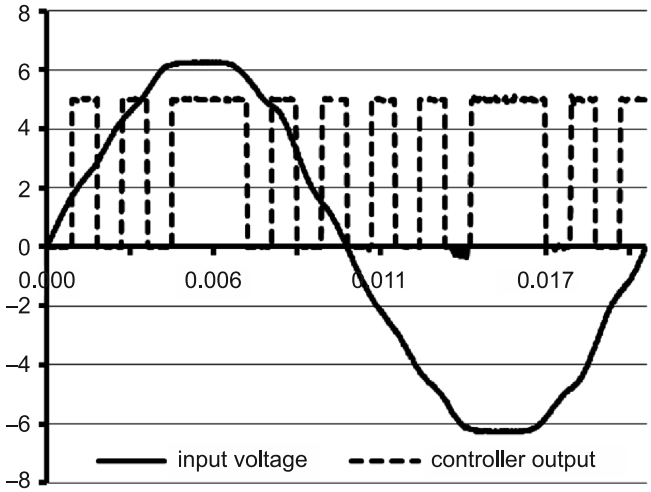

Fig. 14. The membership function for the G_{11} switch versus the voltage of the first input phase for the 15 degrees phase shift – real life measurement – *X* axle – time in [s], *Y* axle – voltage [V]

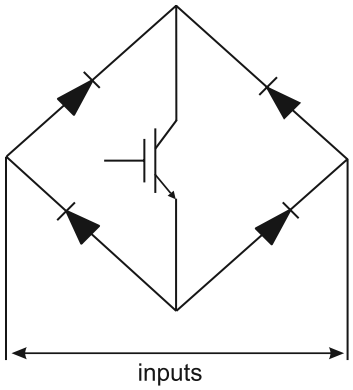

Fig. 15. Structure utilizing single IGBT transistor and four diodes

The advantage of this switch setup includes the usage of a single switching element which requires the generation of only one control signal to fully control the switch current and some properties during commutation. These properties include the possibility of selection diodes with switching times slightly longer than IGBT what reduces diodes switching losses.

The six phase transformers were built using three toroidal three winding transformers for each side of the converter. The primary windings arrangement is the Wye connection, whereas secondary windings are connected in Wye and reversed Wye creating truly six phase system (phases spaced by 60 degrees).

5. The results of the real life model tests

The model of the MC and two six to three phase transformers were tested in the laboratory under following conditions:

- Input of the MC was supplied from the grid via a 230/48 V three to six phase transformers.
- Additional capacitors connected in Wye were connected at the MC input to create truly voltage source inverter (for all six phases).
- Switches were protected by snubber circuits.
- The resistive load was applied as six phase load connected in Wye.
- The reactive load was applied as three phase load supplied via six to three phase transformer and protected using varistors.

The main investigated property includes the potential of the practical application of the proposed control schemes. The tests were lead for all proposed controls and for resistive and reactive loads. The points of interests taken into account in this research include the commutation problems, the shape of the input and output current and voltage waveforms, the order of produced harmonics, *THD* and voltage transfer.

Due to the fact that the 'as close as possible' and 'two closest' strategies operate over the envelope of the waveform of input voltages (which is not a constant line), the output voltage can be created only from the voltages available at the input at the same instant. This fact causes the output voltage transfer to become a function of the input-output phase shift. For the 'crossing point approach', where output voltage waveforms are created only from parts of input sinusoids, which are crossing the desired output sinusoids, the voltage transfer is angle shift independent and is equal to the worst case for the 'as close as possible' control. For all strategies, if the number of input phases increases, the voltage transfer increases – this is associated with the size area closed by the envelope of the waveforms of the multiphase system.

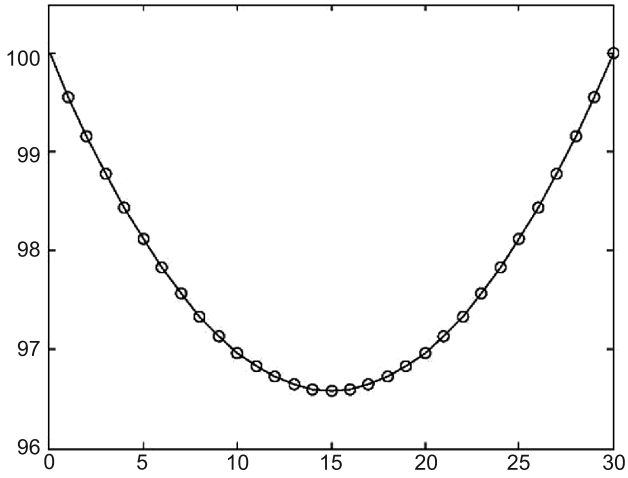

Fig. 16. Voltage transfer versus angle shift for 'two closest' control and 12×12 MC

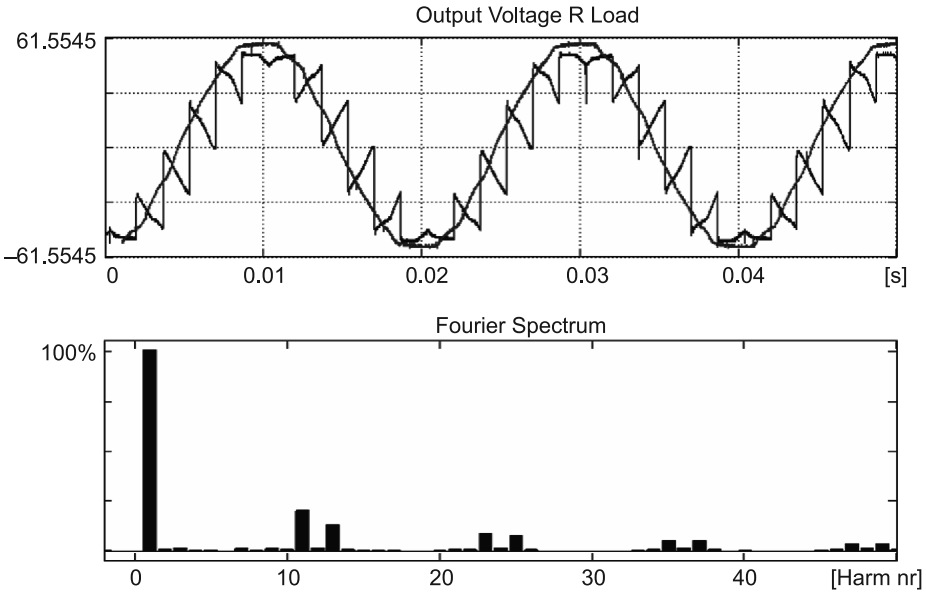

Fig. 17. Output voltage waveform versus input one and output *FFT* for the 'crossing point' approach resistive load and 10 degrees phase shift

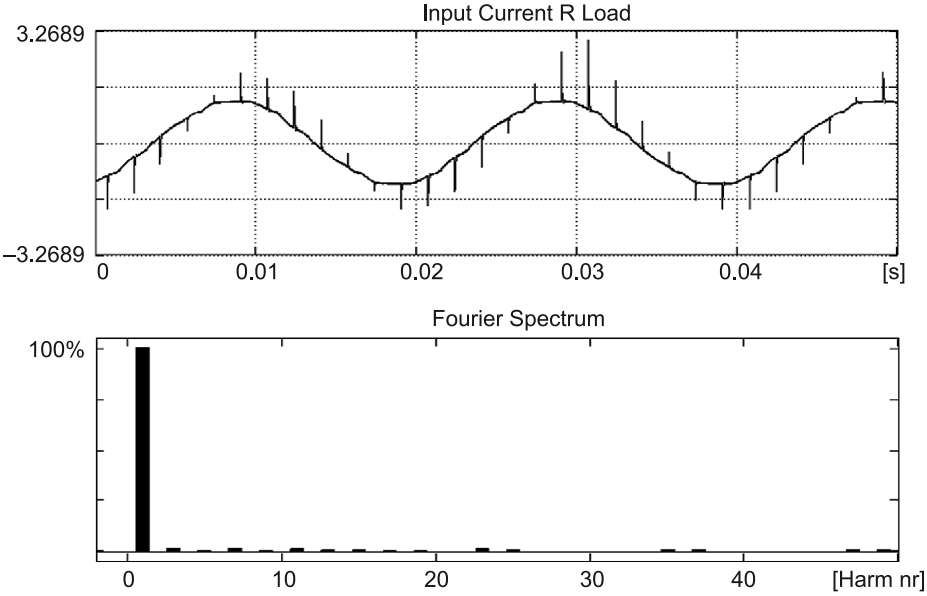

Fig. 18. Input current waveform and its *FFT* for the 'crossing point' approach resistive load and 10 degrees phase shift

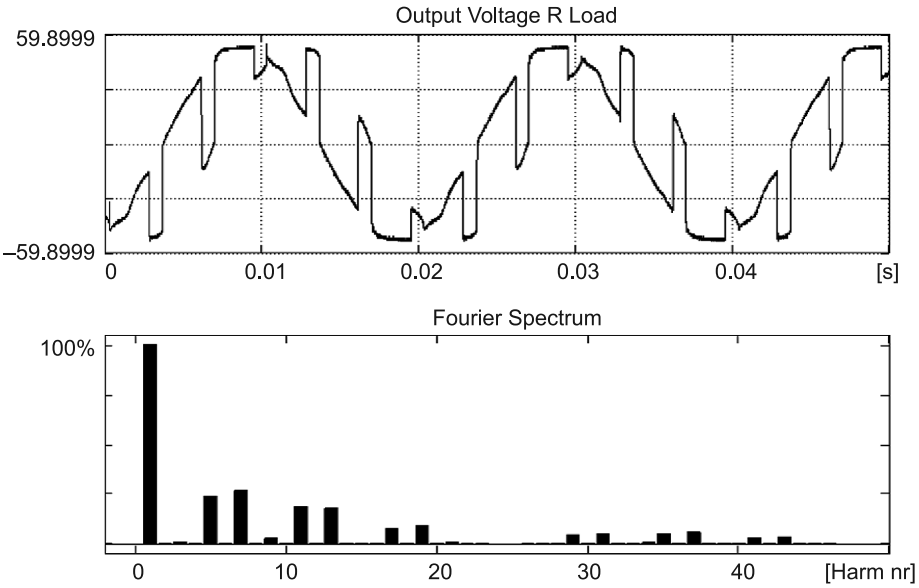

Fig. 19. Output voltage waveform and its *FFT* for the 'two closest' approach resistive load and 10 degrees phase shift

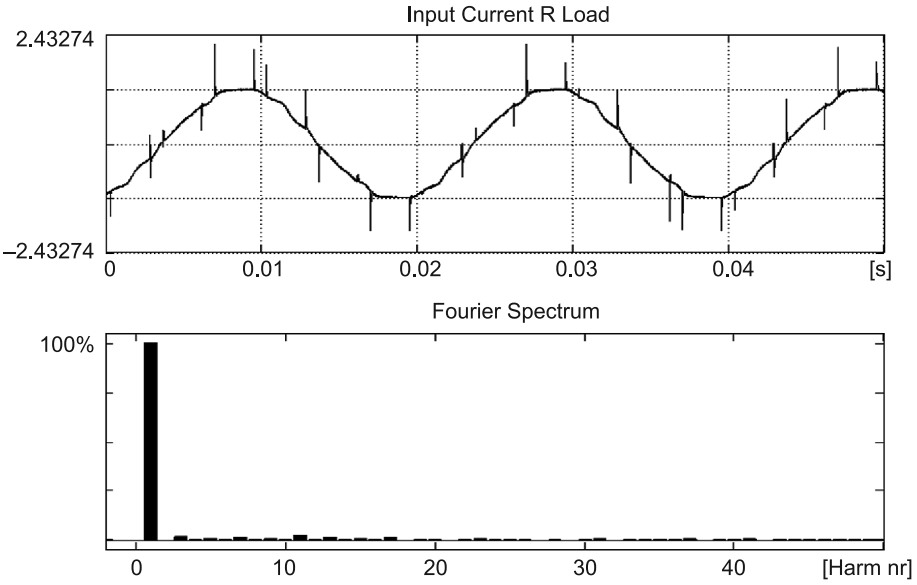

Fig. 20. Input current waveform and its *FFT* for the 'two closest' approach resistive load and 10 degrees phase shift

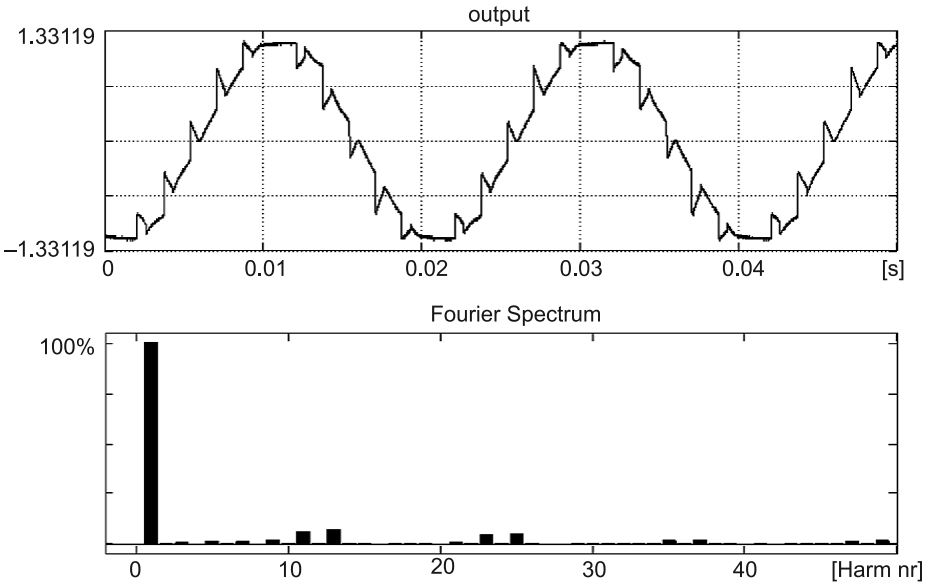

Fig. 21. Output voltage waveform and its *FFT* for the 'as close as possible' approach resistive load and 10 degrees phase shift

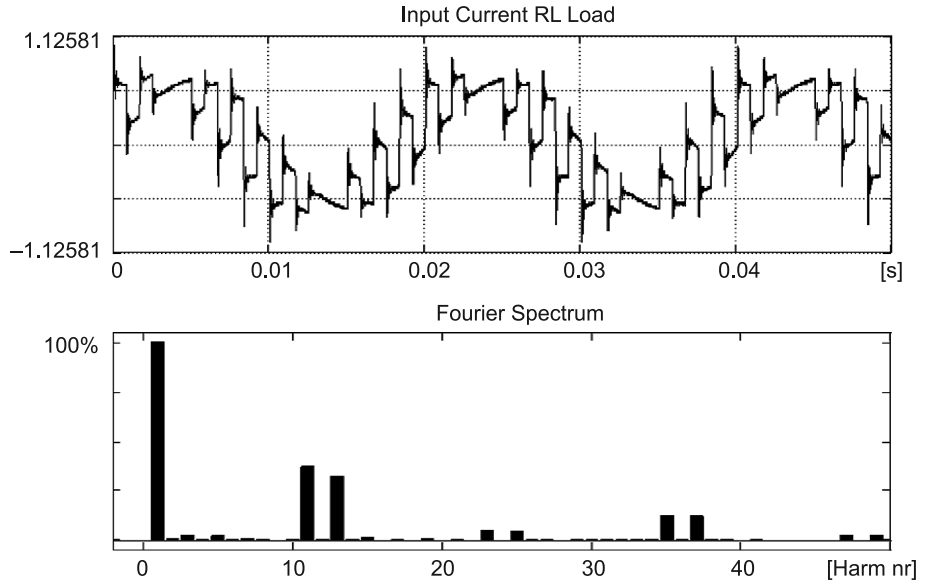

Fig. 22. Output voltage waveform and its *FFT* for the 'two closest' approach inductive load ($R = X$) and 10 degrees phase shift

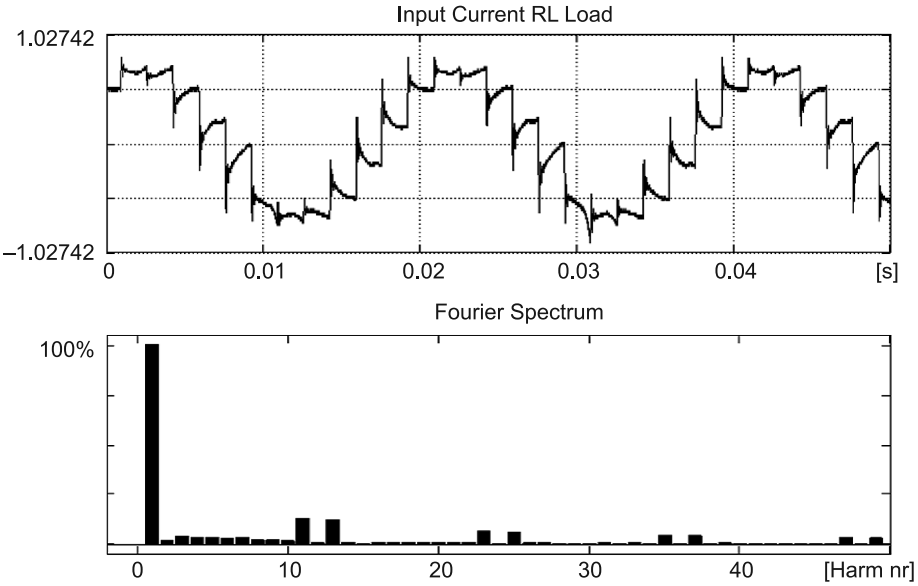

Fig. 23. Output voltage waveform and its *FFT* for the 'crossing point' approach inductive load and 10 degrees phase shift

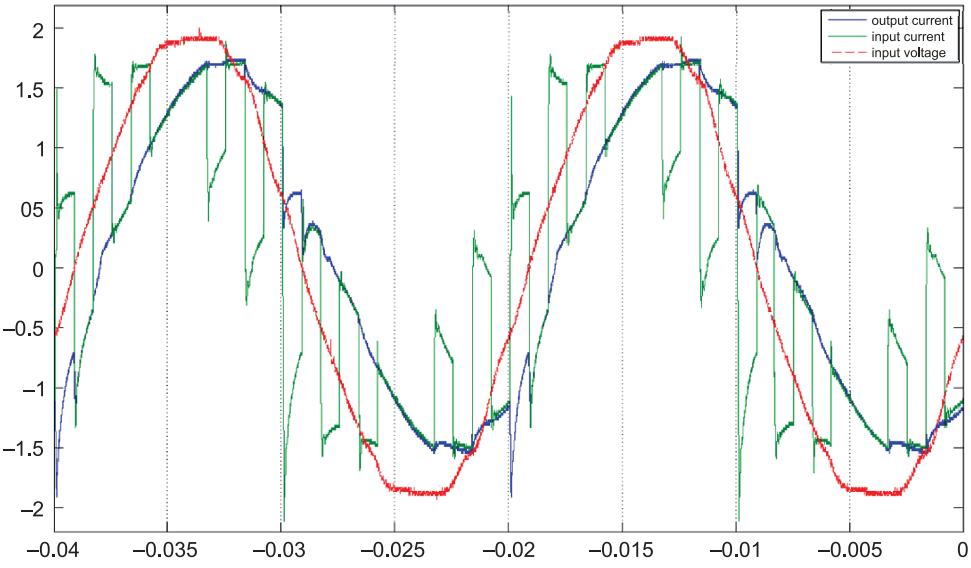

Fig. 24. Input voltage waveform (red) versus input (green) and output current (blue) for the 'as close as possible' approach inductive load and 12 degrees phase shift

The example of dependency of voltage transfer versus angle shift for 'two closest' control achieved by series of the consecutive simulations is shown in Fig. 16. The above figure shows only the 0 to 30 degrees range, since for the 12×12 MC situation repeats every 30 degrees. Similar curves can be obtained for the 'as close as possible' approach. For both control strategies, for the N phase system, minimum voltage transfer and maximum distortion occurs for $\pi/N+k\cdot 2\cdot\pi/N$ and maximum voltage transfer and minimum distortion for $k\cdot 2\cdot\pi/N$.

Figures 17 and 18 show output voltage and its *FFT* and input current and its *FFT* for resistive load for MC working under the 'crossing point' algorithm, Figs. 19 and 20 represent the same waveforms for the 'two closest' approach and Fig. 21 shows the output voltage for the 'as close as possible' approach.

Figures 22 and 23 present the output voltage of the converter for an inductive current and the 'two closest' and 'crossing point' approaches.

Figure 24 shows relative position of the input voltage and input and output currents for the 'as close as possible' approach. It is visible that as phase shift changes, the position of the first harmonic of the input current shifts with respect to the input voltage.

6. Conclusions

The tests performed in the laboratory using the real life model confirmed the results obtained during computer simulations. The proposed method of delivering the vectors of switches states, based on the developed memory search technique was found to be reliable and fast enough to use, even for a twice as dense digitalization of the conduction area (360×360 division was originally used). The matrix, built from proposed switches (28 A, 600 V rated IGBT and diodes) was found to be unexpectedly durable even in the case of overcurrents and overvoltage caused by operator errors.

The main problem noticed and investigated during laboratory research was associated with the commutation of the switches. The commutation problems were attributed to the type of the converter source and load. In the laboratory setup, the converter works from the voltage source (large capacitor bank) into the inductive load. For this setup, the considered commutation setup included the instantaneous change of the control signal for all switches, commutation delay characterized by introduction of '0' state between the changes of control signal and commutation overlap where the switches already 'on' are kept 'on' for little longer while new set of switches is already turned 'on'.

The first approach (instantaneous switching) was applied for laboratory setup and caused slight overcurrents at the input and overvoltages at the output. The second approach also applied in the lab caused overvoltages at the output and due to the speed of IGBT produced discontinuity of the currents. The commutation overlap was tested during simulation and in the lab for use when both sides of the converter had an inductive character to prevent overvoltages.

Due to a lack of funds, the MC has not yet been introduced into the power system to control the power flow, but an appropriate laboratory setup was already made.

Further research associated with the MC application in power systems will include the modification of the synchronization method, since methods based on the detection of input

voltage were found to be unreliable and the application of the output synchronization for adaptation of the MC to work between systems with two different frequencies. The research has to include the evaluation of the MC dynamic properties which requires the adaptation of the control circuitry in order to be able to introduce step change into input signals (angle and frequency change).

Other directions of research should include the adaptation of the controller to make it able to create a controlled length of overlap during commutation in circuits with inductive elements on both sides of the converter or a controlled length of '0' state during commutation with a capacitive character on one side of the converter.

References

[1] Szczepanik J., Sieńko T., *Nowoczesne urządzenia do kontroli rozpływu mocy w systemie elektroenergetycznym oparte na wielofazowym przekształtniku macierzowym*, Zeszyty Naukowe Wydziału Elektrotechniki i Automatyki Politechniki Gdańskiej Nr 32, 2013, pp. 83-86.

[2] Szczepanik J., Sieńko T., *New Multiphase Matrix Converter Based Device for Power Flow Control*, Acta Energetica, 04/17 (2013), pp. 14-21, doi: 10.12736/issn.2300-3022.2013413.

[3] Empringham L., Kolar J.W., Rodriguez J., Wheeler P.W., Clare J.C., *Technological Issues and Industrial Application of Matrix Converters: A Review*, Industrial Electronics, IEEE Transactions on, vol. 60, no. 10, Oct. 2013, pp. 4260, 4271, doi: 10.1109/TIE.2012.2216231.

[4] Rodriguez J., Rivera M., Kolar J.W., Wheeler P.W., *A Review of Control and Modulation Methods for Matrix Converters, Industrial Electronics*, IEEE Transactions on, vol. 59, no. 1, Jan. 2012, pp. 58, 70, doi: 10.1109/TIE.2011.2165310.

[5] Kolar J.W., Friedli T., Rodriguez J., Wheeler P.W., *Review of Three-Phase PWM AC–AC Converter Topologies, Industrial Electronics*, IEEE Transactions on, vol. 58, no. 11, Nov. 2011, pp. 4988, 5006, doi: 10.1109/TIE.2011.2159353.

[6] Wheeler P.W., Rodriguez J., Clare J.C., Empringham L., Weinstein A., *Matrix converters: a technology review*, Industrial Electronics, IEEE Transactions on, vol. 49, no. 2, Apr. 2002, pp. 276, 288, doi: 10.1109/41.993260.

[7] Casadei D., Serra G., Tani A., Zarri L., *A review on matrix converters*, Przegląd Elektrotechniczny, vol. 82, nr 2, 2006, pp. 15-25, ISSN 0033-2097.

[8] Friedli Th., Kolar J.W., *Milestones in Matrix Converter Research*, IEEJ Journal of Industry Applications, vol. 1, 2012, pp. 2-14.

[9] Nguyen T.D., Hong-Hee Lee, *Dual Three-Phase Indirect Matrix Converter With Carrier-Based PWM Method*, Power Electronics, IEEE Transactions on, vol. 29, no. 2, Feb. 2014, pp. 569, 581, doi: 10.1109/TPEL.2013.2255067.

[10] Sun Y., Xiong W., Su M., Li X., Dan H., Yang J., *Topology and Modulation For a New Multi--Level Diode-Clamped Matrix Converter*, Power Electronics, IEEE Transactions on, vol. PP, no. 99, 2015, p. 1, doi: 10.1109/TPEL.2014.2305711.

[11] Keping You, Dan Xiao, Rahman M.F., Uddin M.N., *Applying Reduced General Direct Space Vector Modulation Approach of AC–AC Matrix Converter Theory to Achieve Direct Power Factor Controlled Three-Phase AC–DC Matrix Rectifier*, Industry Applications, IEEE Transactions on, vol. 50, no. 3, May–June 2014, 2243, 2257, doi: 10.1109/TIA.2013.2285956.

[12] Rivera M., Rojas C., Wilson A., Rodriguez J., Espinoza J., Baier C., Muñoz J., *Review of predictive control methods to improve the input current of an indirect matrix converter*, Power Electronics, IET, vol. 7, no. 4, April 2014, pp. 886, 894, doi: 10.1049/iet-pel.2013.0327.

[13] Nguyen T.D., Hong-Hee Lee, *A New SVM Method for an Indirect Matrix Converter With Common-Mode Voltage Reduction*, Industrial Informatics, IEEE Transactions on, vol. 10, no. 1, Feb. 2014, pp. 61, 72, doi: 10.1109/TII.2013.2255032.

[14] Dasika J.D., Saeedifard M., *A post-fault modulation strategy to control the matrix converter under an open-switch failure*, Applied Power Electronics Conference and Exposition (APEC), 2014 Twenty-Ninth Annual IEEE, 16–20 March 2014, pp. 1522, 1529, doi: 10.1109/APEC.2014.6803509.

[15] Laskody T., Prazenica M., Kascak S., *Space vector PWM for two-phase four-leg matrix converter*, ELEKTRO, 19–20 May 2014, pp. 324, 327, doi: 10.1109/ELEKTRO.2014.6848911.

[16] Dabour S.M., Rashad E.M., *A new continuous PWM strategy for three-phase direct matrix converter using indirect equivalent topology*, Power Electronics, Machines and Drives (PEMD 2014), 7th IET International Conference on 8–10 April 2014, pp. 1, 6, doi: 10.1049/cp.2014.0383.

[17] Garcia C., Rivera M., Lopez M., Rodriguez J., Pena R., Wheeler P., Espinoza J., *A Simple Current Control Strategy for a Four-Leg Indirect Matrix Converter*, Power Electronics, IEEE Transactions on, 2015, vol. PP, no. 99, p. 1, doi: 10.1109/TPEL.2014.2321562.

[18] Moin Ahmed SK., Abu-Rub H., Iqbal A., *Multiphase Matrix Converter Topologies and Control*, [in:] *Power Electronics for Renewable Energy Systems, Transportation and Industrial Applications*, eds. H. Abu-Rub, M. Malinowski, K. Al-Haddad, John Wiley & Sons, Ltd, Chichester, UK 2014, doi: 10.1002/9781118755525.ch15.

[19] Levi E., Bodo N., Dordevic O., Jones M., *Recent advances in power electronic converter control for multiphase drive systems*, Electrical Machines Design Control and Diagnosis (WEMDCD), 11–12 March 2013 IEEE Workshop on, pp. 158, 167, doi: 10.1109/WEMDCD.2013.6525176.

[20] Ahmed S.K.M., Iqbal A., Abu-Rub H., *Generalized Duty-Ratio-Based Pulsewidth Modulation Technique for a Three-to-k Phase Matrix Converter*, Industrial Electronics, IEEE Transactions on, vol. 58, no. 9, Sept. 2011, pp. 3925, 3937, doi: 10.1109/TIE.2010.2098373.

[21] Rahman K., Iqbal Am., Abduallah A.A., Al-ammari R., Abu-Rub H., *Space vector pulse width modulation scheme for three to seven phase direct matrix converter*, Applied Power Electronics Conference and Exposition (APEC), 16–20 March 2014 Twenty-Ninth Annual IEEE, pp. 595, 601, doi: 10.1109/APEC.2014.6803369.

[22] Bojoi R., Neacsu M.G., Tenconi A., *Analysis and survey of multi-phase power electronic converter topologies for the more electric aircraft applications*, Power Electronics, Electrical Drives, Automation and Motion (SPEEDAM), 20–22 June 2012 International Symposium on, pp. 440, 445, doi: 10.1109/SPEEDAM.2012.6264566.

[23] Ahmed Sk Moin, Abu-Rub Haitham, Salam Zainal, Iqbal Atif, *Dual matrix converters based seven-phase open-end winding drive*, Industrial Electronics (ISIE), 1–4 June 2014 IEEE, 23rd International Symposium on, pp. 2105, 2110, doi: 10.1109/ISIE.2014.6864942.

[24] Szczepanik J., Sienko T., *A new concept of application of multiphase matrix converter in power systems*, EUROCON, 2007, The International Conference on &# 34; Computer as a Tool&# 34; 1535-1540 2007 IEEE.

[25] Szczepanik J., Sienko T., *New control strategy for multiphase matrix converter*, Systems Engineering, 2008, ICSENG, 19th International Conference IEEE.

[26] Szczepanik J., Sienko T., *The Study of Implementation of Multiphase Matrix Converter in Power Systems*, Przegląd Elektrotechniczny, nr 89, 2013.

[27] Sieńko T., *Schemat zastępczy przekształtnika macierzowego dla stanów dynamicznych przy sterowaniu jednookresowym*, Czasopismo Techniczne, z. 1- E/2012, pp. 123-134.

[28] Sieńko T., Sobczyk T.J., *Modelling concept of N×M matrix converter under periodic control for dynamic states*, Archives of Electrical Engineering, vol. 63, no. 2, 2014, pp. 305-315.

[29] Sobczyk T.J., *Control strategy of matrix converters*, Proc. of European Conf. on Power Electronics and Applications (EPE), 1993, vol. 4, pp. 93-97.
[30] Sobczyk T.J., *The matrix converter – a universal power electronic unit*, Prace Instytutu Elektrotechniki, 2002, vol. 211, pp. 6-21.
[31] Sobczyk T., Szczepanik J., Rudek P., *Application of Matrix converter as an inter-connection device in the power system*, Czasopismo Techniczne, z. 3-E/2006, pp. 23-36.
[32] Sienko T., Szczepanik J., Sobczyk T.J., *Voltage phase controller for power systems*, Electrical Power Quality and Utilisation, 2007, EPQU, 9th International Conference on 1–6 2007, IEEE.
[33] Sobczyk T.J., Sienko T., *Application of matrix converter as a voltage phase controller in power systems*, Power Electronics, Electrical Drives, Automation and Motion, 2006, SPEEDAM, International Symposium on, IEEE, pp. 1322-1325.
[34] Sobczyk T.J., Sienko T., *Matrix converters control for high speed generators*, Electric Machines and Drives, 2005, IEEE International Conference on, IEEE, pp. 1975-1980.
[35] Sobczyk T.J., Sienko T., Danilewicz J.B., *Study of asymmetrical regimes in matrix converters for multi-phase high speed generators*, Power Tech, 2005, IEEE Russia, pp. 1-6.
[36] Sienko T., Sobczyk T., *Matrix converter control for applications to multi-phase high-speed microgenerators*, Archives of Electrical Engineering, vol. 53, no. 2, 2004, pp. 217-228, Polish Scientific Publishers.

TECHNICAL TRANSACTIONS | **CZASOPISMO TECHNICZNE**
ELECTRICAL ENGINEERING | ELEKTROTECHNIKA
2-E/2015

ANDRZEJ SZROMBA*

CONDUCTANCE CONTROL OF A SHUNT ACTIVE POWER FILTER AND ACTIVE ENERGY BUFFER

ENERGOELEKTRONICZNY FILTR AKTYWNY I BUFOR ENERGII AKTYWNEJ STEROWANY KONDUKTANCYJNIE

A b s t r a c t

There are many types of control method for shunt active power filter (SAPF) investigated up until now. The authors describe complex methods of determining active filter reference currents or powers. This paper is dedicated to a simple, but universally used control algorithm based on the load equivalent conductance approach. This method allows for non-active current compensation, energy buffering, and energy redistribution among loads under compensation. It is also useful for voltage-source as current--source inverter based active filters, and for DC system as well as for AC single or three-phase filters.

Keywords: *active filter*, *active current*, *load equivalent conductance*, *indirect current control*, *energy buffering*, *harmonics and interharmonics*

S t r e s z c z e n i e

Zadaniem energoelektronicznego filtru aktywnego jest kompensacja prądu nieaktywnego w gałęzi źródła zasilania. Znanych jest wiele metod pozyskiwania informacji niezbędnych do skompensowania tego prądu. Często są to wyrafinowane metody, bardzo złożone zarówno pod względem pojęciowym, jak i obliczeniowym. W niniejszym artykule przedstawiono nieskomplikowaną, lecz wydajną i wielofunkcyjną metodę uzyskiwania wzorca składowej czynnej prądu obciążenia. Jest ona oparta na pojęciu konduktancji zastępczej obciążenia. Umożliwia nie tylko kompensację prądu nieaktywnego, ale również sterowanie przepływem energii czynnej, w tym jej rekuperację i redystrybucję do kompensowanych obciążeń. Opisana metoda może być stosowana w obwodach jedno- i wielofazowych, a także w obwodach zasilanych sygnałem stałym. Może też zostać użyta wobec filtru aktywnego opartego i na falowniku napięcia, i na falowniku prądu.

Słowa kluczowe: *energoelektroniczny filtr aktywny*, *prąd aktywny*, *konduktancja zastępcza*, *buforowanie i redystrybucja energii*, *harmoniczne*

DOI: 10.4467/2353737XCT.15.092.3924

* Ph.D. Eng. Andrzej Szromba, Faculty of Electrical and Computer Engineering, Cracow University of Technology.

1. Introduction

In general, the SAPF control techniques may be classified as based upon either undesirable or desirable components of load current (or power). When focusing on undesirable components (Fig. 1), the load current waveform is analysed to compute specific attributes of its distortion. The distortion is characterised by harmonic components (their amplitudes, frequencies and phases), more and more often also including a DC component, interharmonics and subharmonics, fluctuations of harmonics amplitudes and even noise – which may be handled separately due to differences in measurement techniques and outcomes. These components are then used as the reference for filtering the current forming. This technique is often referred to as the open-loop control method. It is supposed to be flexible by means of choosing components to be compensated. Such control strategy utilizes versatile and complex types of harmonic current extraction, using either frequency-domain or time-domain methods: various types of Fourier transform; wavelet transform; Clark/Park direct and inverse transformation; signal filtration etc. The dynamic performance of an active filter mainly depends on how exactly and how quickly the harmonic components are extracted from the load current. Scientists and engineers debate the accuracy of various methods of harmonic detection, its dynamics and stability, ease and cost of implementations, etc.

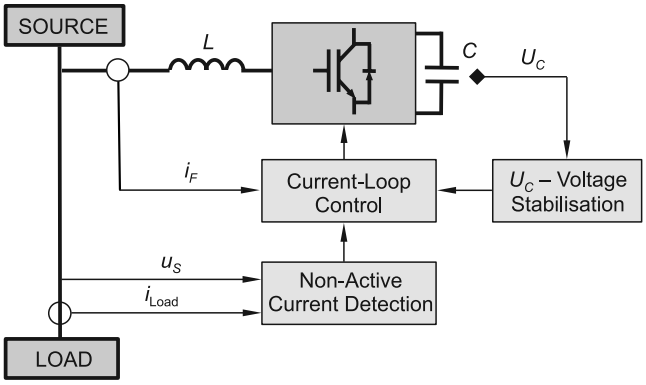

Fig. 1. Non-active current based control of SAPF

Using the principle ‘keep it as simple as possible’, the active current based control strategy may be focused on only one load current component – on its active component, Fig. 2. The active component has to be sinusoidal, in-phase with the source voltage and balanced in the case of a three-phase system. It is now clear that the only quantity to obtain is the amplitude of a sine wave signal, this is much easier than calculating the numbers of harmonic/interharmonic/subharmonic attributes. Finally, having the active component amplitude, the active filter controls the source current to be equal to the active component of the load current.

This technique is often referred to as the closed-loop control or the global compensation. Voltage and current signals are mostly used to determine the load active current [1–11], this is known as the direct current control method.

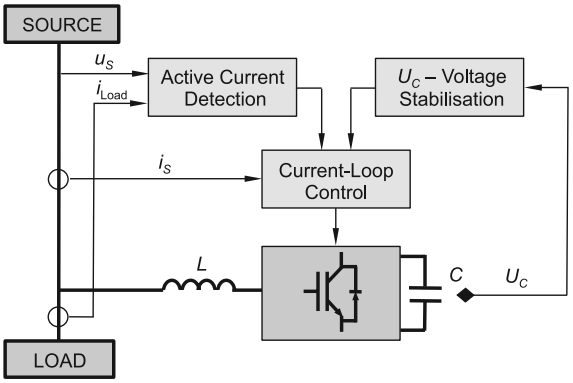

Fig. 2. Active current based control of SAPF

Alternatively, the active current based control strategy may be implemented using the indirect control method [2, 12–30]. Then, the active current is determined on the basis of energy stored in the filter's capacitor *C* and reactor *L*. Such technique are developed in this paper. The base structure of the considered active filter is shown in Fig. 3.

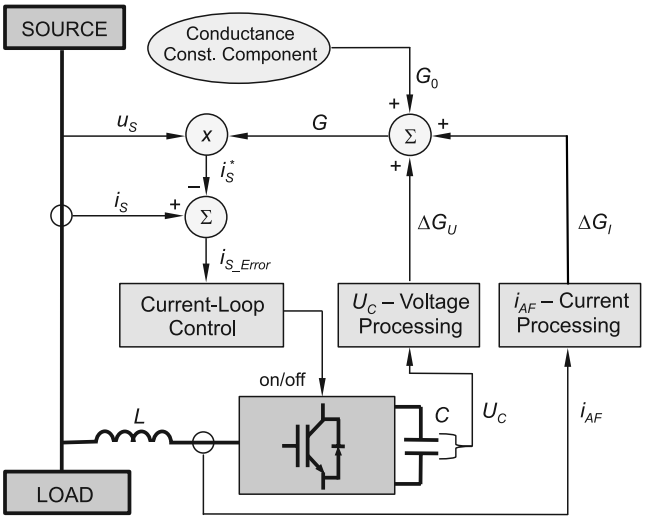

Fig. 3. The indirectly controlled SAPF considered in this paper

This paper describes a concept and then the simulation analysis of the conductance controlled SAPF with the capability of active energy flow control.

Fryze's idea of load equivalent conductance is employed in this paper. This conductance is related to the load active power. It may be positive or negative – dependent upon the direction of the active energy flow. Using this conductance, the reference signal for the source current can be determined. No harmonic extraction is needed, hence computational

effort of the filter's control module may be significantly reduced. Such a control technique allows the shaping of the source current to be strictly active and enables buffering the flow of the active energy.

2. In-circuit energy relations

For energy delivering, the active current is necessary and the non-active current is unwanted. This is in good agreement with Fryze's active current idea [31].

The active power P for the n-th period T is defined as:

$$P_{nT} = \frac{1}{T} \int_{(n-1)T}^{nT} u_S i_S dt \tag{1}$$

$n = 1, 2, 3, \ldots$; u_S, i_S are the source voltage and the current.

Power P_{nT} is the sum of the powers of all circuit components supplied by the source, including the active filter. Within each period T, the active power (1) may be considered as the sum of a constant predefined component P_0 and variable component ΔP_{nT}:

$$P_{nT} = P_0 + \Delta P_{nT} \tag{2}$$

Then, the Fryze's equivalent conductance for the n-th period T may be determined:

$$G_{nT} = \frac{P_{nT}}{U_S^2} \tag{3}$$

$$G_{nT} = \frac{P_0 + \Delta P_{nT}}{U_S^2} = G_0 + \Delta G_{nT} \tag{4}$$

where:

$$G_0 = \frac{P_0}{U_S^2} \quad \text{(see Fig. 3)} \tag{5}$$

and

$$\Delta G_{nT} = \frac{\Delta P_{nT}}{U_S^2} = \frac{P_{nT} - P_0}{U_S^2} \tag{6}$$

The conductance variable component (6) can only be known if the active power (1) is already obtained. The whole time period T is needed to calculate this power, so the information on the magnitude of the component ΔG is always delayed for one period T:

$$G_{nT} = \frac{P_0 + \Delta P_{(n-1)T}}{U_S^2} = G_0 + \Delta G_{(n-1)T} \tag{7}$$

The conductance (7) is then used to produce the source current reference signal $i_{S,nT}^*$:

$$i_{S,nT}^* = (G_0 + \Delta G_{(n-1)T})\, u_S \tag{8}$$

Due to maintaining constant magnitude of the equivalent conductance within each period T, the source current may be pure sinusoidal if the source voltage signal u_S is provided as non-distorted [9, 32].

The definition (1) requires measuring the load voltage and current. However, in this paper, the load active power is determined indirectly on the basis of energy stored in the filter's reactance elements C and L. The filter's energy change during period T_1 is:

$$\Delta W_{1T,AF} = (P_0 - P_{1T})T \tag{9}$$

where $\Delta W_{1T,AF}$ is the change of energy stored in the filter's capacitor C and inductor L.

Let the instantaneous energy stored in the capacitor be denoted as w^{DC} and the inductor's energy as w^{AC} (on the DC-side and AC-side of the filter, respectively). Initial energy is denoted as W^{DC} and W^{AC}, respectively. The after n periods T change of filter energy is:

$$\begin{aligned}
\Delta W_{AF} &= \left[(W_0^{DC} + W_0^{AC}) - (w_{1T}^{DC} + w_{1T}^{AC})\right] + \left[(w_{1T}^{DC} + w_{1T}^{AC}) - (w_{2T}^{DC} + w_{2T}^{AC})\right] + \cdots + \\
&+ \left[(w_{(n-2)T}^{DC} + w_{(n-2)T}^{AC}) - (w_{(n-1)T}^{DC} + w_{(n-1)T}^{AC})\right] + \left[(w_{(n-1)T}^{DC} + w_{(n-1)T}^{AC}) - (w_{nT}^{DC} + w_{nT}^{AC})\right] = \\
&= W_0^{DC} + W_0^{AC} - w_{1T}^{DC} - w_{1T}^{AC} + w_{1T}^{DC} + w_{1T}^{AC} - w_{2T}^{DC} - w_{2T}^{AC} + \cdots + \\
&+ w_{(n-2)T}^{DC} + w_{(n-2)T}^{AC} - w_{(n-1)T}^{DC} - w_{(n-1)T}^{AC} + w_{(n-1)T}^{DC} + w_{(n-1)T}^{AC} - w_{nT}^{DC} - w_{nT}^{AC} = \\
&= (W_0^{DC} - w_{nT}^{DC}) + (W_0^{AC} - w_{nT}^{AC})
\end{aligned} \tag{10}$$

Finally, the filter energy change ΔW_{AF} may be described as:

$$\Delta W_{AF} = \sum_{1}^{n} \Delta P_{nT} T = \frac{C(U_{C0}^2 - U_{C,nT}^2) + L(I_{AF0}^2 - I_{AF,nT}^2)}{2} \tag{11}$$

where:

- C – the capacity of the filter's capacitor,
- U_{C0} – the capacitor's initial voltage,
- $U_{C,nT}$ – the capacitor's voltage at the end of the n-th period T,
- L – the filter's inductor,
- I_{AF0} – the filter's initial current,
- $I_{AF,nT}$ – the filter's current at the end of n-th period.

3. Filter's control structure

Using (8) and (11), the reference current is:

$$i_{S,nT}^{*} = \left[G_0 + \frac{C(U_{C0}^2 - U_{C,(n-1)T}^2) + L(I_{AF0}^2 - I_{AF,(n-1)T}^2}{2TU_S^2} \right] u_s \tag{12}$$

The control structure diagram corresponding with the formula (12) is shown in Fig. 4. In the Figure 4, the one T period time delay effect (7), is executed using *sync* and *S/H* modules. The *sync* module generates synchronization pulses at the end of each period T. The *S/H* module is a sample-and-hold device.

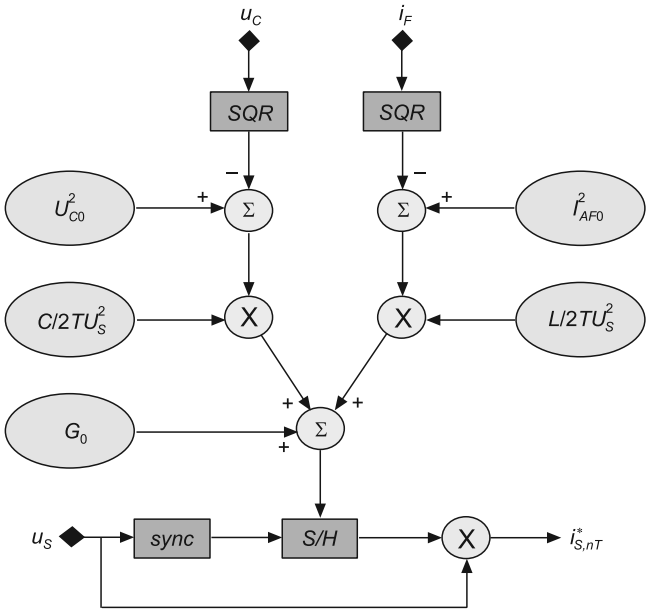

Fig. 4. Filter's control structure on the base of formula (12)

There are possibilities for reducing the complexity of the formula (13) and the control structure shown in Fig. 4:

a) by neglecting filter initial current. The filter's initial current I_{AF0} (at the instant of filter turn-on) is null, therefore the filter initial current I_{AF0}^2 in (12) may be zeroed, so:

$$i_{S,nT}^* = \left[G_0 + \frac{C(U_{C0}^2 - U_{C,(n-1)T}^2) - LI_{AF,(n-1)T}^2}{2TU_S^2} \right] u_s \tag{13}$$

b) by neglecting the filter's inductor energy. The initial magnitude of the filter's capacitor voltage U_{C0} is significantly higher then the peak $U_{S\max}$ of the supply source voltage, for example $U_{C0} \cong 1.5U_{S\max}$. Changes of the capacitor voltage may be presupposed to be about $\pm 0.1U_{C0}$. Taking the capacitor's capacity and voltage to be 4 mF and 500 V respectively, the initial capacitor's energy is 500 J and the capacitor's energy variation is 100 J. Taking the inductor's inductance to be 5 mH and presupposing the inductor's peak current 15 A, the inductor's energy variation is 0.6 J. Therefore the conductance variable component may be obtained only as a function of the filter's capacitor voltage:

$$i_{S,nT}^* = \left[G_0 + \frac{C(U_{C0}^2 - U_{C,(n-1)T}^2)}{2TU_S^2} \right] u_s \tag{14}$$

Disregarding the filter's inductor energy may cause insignificant alterations of the variable component (6).

c) by substituting U_C for U_C^2. The simplified conductance variable component ΔG_{nT} introduced in (14) is:

$$\frac{C(U_{C0}^2 - U_{C,(n-1)T}^2)}{2TU_S^2} \tag{15}$$

this may be rewritten as:

$$\alpha_{U\wedge 2}(U_{C0}^2 - U_{C,(n-1)T}^2), \quad \text{where} \quad \alpha_{U\wedge 2} = \frac{C}{2TU_S^2} \tag{16}$$

For capacitor voltages U_{C0} = 500 V, $U_{C\max}$ = 520 V and $U_{C\min}$ = 480 V, the component (16) may be replaced by:

$$\alpha_{U\wedge 1}(U_{C0} - U_{C,(n-1)T}), \quad \text{with} \quad \alpha_{U\wedge 1} = 1.95 \cdot 10^{-3} \tag{17}$$

this sufficiently linearises equation (14). Finally, the reference current is:

$$i_{S,nT}^* = \left[G_0 + \alpha_{U\wedge 1}(U_{C0} - U_{C,(n-1)T}) \right] u_s \tag{18}$$

The diagram of the filter's control structure corresponding with formula (18) is shown in Fig. 5. This structure is simpler when compared with the structure shown in Fig. 4.

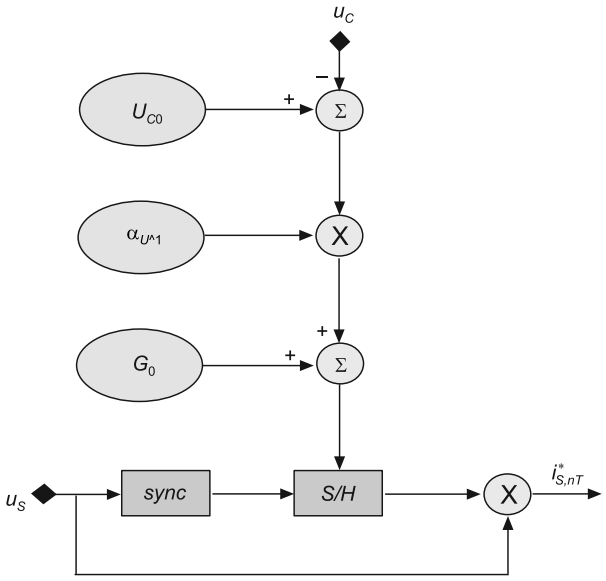

Fig. 5. Filter's control structure on the base of formula (18)

4. Simulations

Simulations shown in this section verify the main feature of the considered filter working in a single-phase circuit. All waveforms are obtained using the Intusoft ICAP software. Parameters of the simulated circuit are as follows:

- Source: $U_S = 230$ V, $R_S = 50$ mΩ, $L_S = 100$ μH.
- Load: time-dependent resistor, $R = 0$ for each 1st and 3rd quarter of each period T, and $R = 20$ Ω for each 2nd and 4th quarter of each period T.
- Conductance constant component $G_0 = 43.5$ mS.
- Filter's reactance elements $C = 4$ mF and $L = 5$ mH.

Figures 6 and 7 show essential signals in the circuit. Equation (18) and the filter structure depicted in Figs. 3 and 5 are used. The period-table detailed filter action.

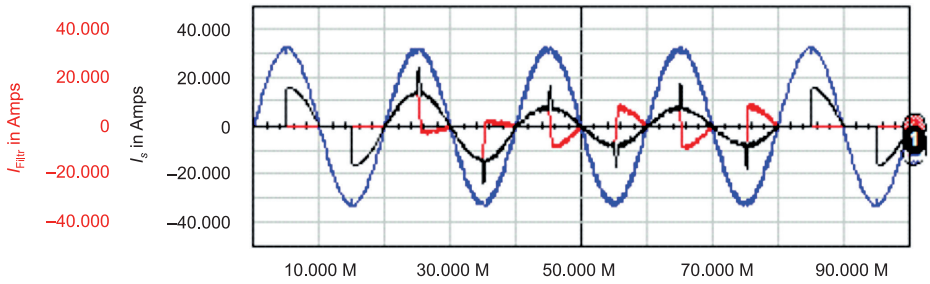

Fig. 6. Source voltage (blue), filter current (red) and source current (black)

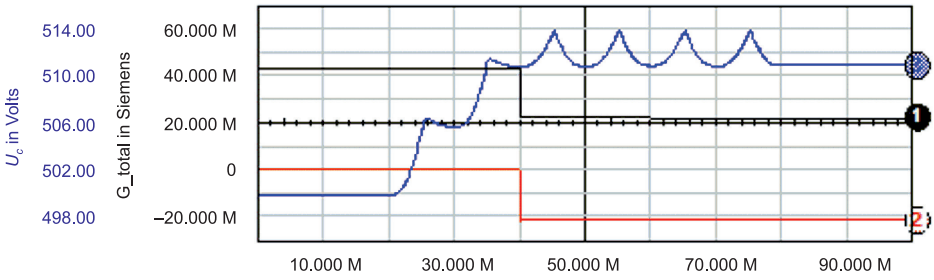

Fig. 7. Filter capacitor voltage (3, blue), and conductance signals: total G (1, black) and variable component ΔG (2, red) – shown in the same scale

Figures 6 and 7 period-table:

0–20 ms: Filter is inactive. Load/source current *RMS* is 8.2 A.

20–40 ms: Filter is active. Source current is determined by G_0 and is greater than load current: *RMS* 10.3 A and 8.2 A, respectively. Filter current *RMS* is 7.2 A. It comprises load non-active current and an excessive active component $(G_0 - G_{2T})u_S$ of source current. Because of this excessive current component, the filter's capacitor voltage rises and the conductance signal on the input terminal of the *S*/*H* element diminishes. That means that in the next period T, the source current will be lowered.

40–60 ms: Corrected magnitude of the equivalent conductance is latched by the *S/H* element at instant t = 40 ms. The variable component ΔG is negative: –20.5 mS. The total conductance and source current are lowered to the accurate magnitudes of 23 mS and *RMS* 6 A, respectively.
60–80 ms: Regular compensation of non-active current.
80–100 ms: Filter is inactive.

The second simulation experiment, Fig. 8, compares source current when using the full reference current formula (12) and then the simplified formula (18). From the figure, it results that these formulae are equivalent to each other.

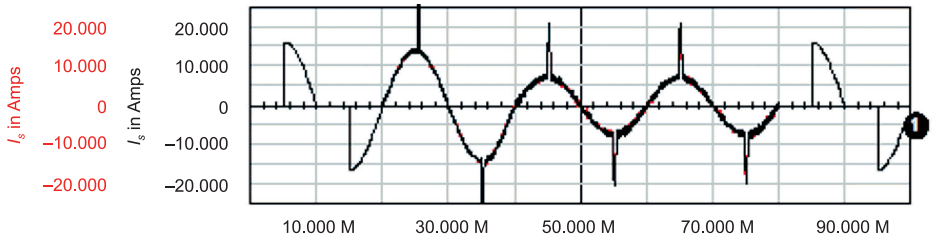

Fig. 8. Source current when full-formula (12) is used (red) and then for simplified formula (18) (black). The red waveform is covered by the black waveform

Third simulation, Figs. 9 and 10: the filter acts without an initial load active power prediction, this means with $G_0 = 0$, see (18).

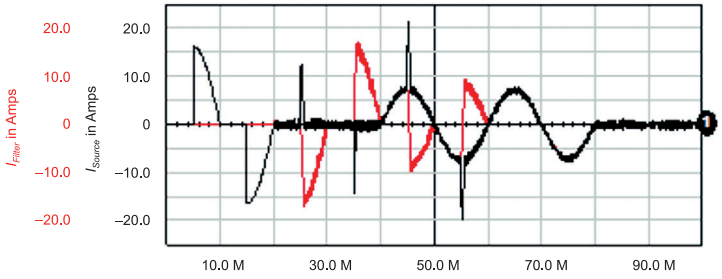

Fig. 9. Source current (black) and filter current (red)

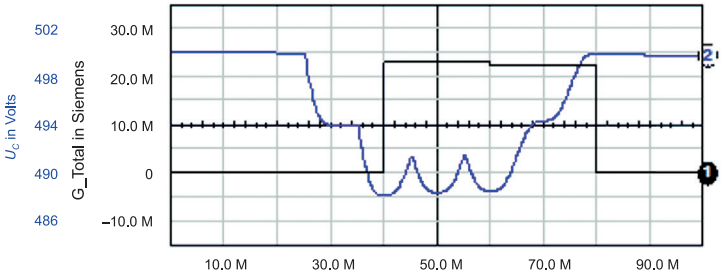

Fig. 10. Load equivalent conductance signal (1) and filter's capacitor voltage (2)

Figures 9 and 10 period-table:
0–20 ms: Filter is off. Load/source current *RMS* is 8.2 A.
20–40 ms: Filter is on. Source current is not flowing due to the conductance condition $G_0 = 0$. Filter current equals load current, i.e. it comprises load active and non-active current components. Filter's capacitor energy diminishes, thus the instantaneous equivalent conductance signal gradually increases.
40–60 ms: The instantaneous equivalent conductance signal is latched at $t = 40$ ms in the *S*/*H* element. The latched signal magnitude is positive and equals 23 mS. Source current *RMS* is 6 A. The filter performs compensation for load non-active current.
60–80 ms: The load is turned off at $t = 60$ ms. However, due to the fact that $G > 0$, the source current is still flowing and charging the filter's capacitor. The capacitor voltage gradually rises to the initial voltage U_{C0}.
80–100 ms: The equivalent conductance signal on the output of the *S*/*H* element falls to zero at the instant when $t = 80$ ms – the source current falls to zero at the same instant. The filter automatically returns to its initial state and is ready to contingent next compensation.

There are a few points which characterise filter action without prediction of initial load active power, this means with $G_0 = 0$:

- The source current is shaped to be active within (0, *T*) time delay.
- The filter's capacitor discharging is a measure of the total equivalent conductance.
- The filter's capacitor acts with lower voltage compared to action with non-zero magnitude of the predefined component G_0.
- After switching the load off, the filter returns to its initial state.

Both modes of filter operation, with or without prediction of initial load active power P_0, are functional and may be used alternatively, dependent upon user requirements.

5. Three-phase filter

Formula (12) may be modified in order to obtain the per-phase active current signal $i^*_{S(k),nT}$ in a three-phase system:

$$i^*_{S(k),nT} = \frac{G_{(n-1)T}}{3} u_{S(k)} \tag{19}$$

$$i^*_{S(k),nT} = \left[\frac{G_0}{3} + \frac{C(U^2_{C0} - U^2_{C,(n-1)T}) + L(I^2_{AF0(k)} - I^2_{AF(k),(n-1)T})}{6TU^2_S} \right] u_{S(k)} \tag{20}$$

where:
$L = L_{FA} = L_{FB} = L_{FC}$
$k = A, B, C.$

After several simplifications, which were described in section 3, equation (20) may be written as:

$$i^*_{S(k),nT} = \left[\frac{G_0}{3} + \alpha_{U\wedge 1}(U_{C0} - U_{C,(n-1)T}) \right] u_{S(k)} \tag{21}$$

Now, the per-phase control structure diagram corresponding with formula (21) may be arranged as is shown in Fig. 11. Voltage signals $u_{S(k)}$ should be provided as positive-sequence fundamental components of respective source phase voltages. A phase-locked-loop system may be used for extracting these components.

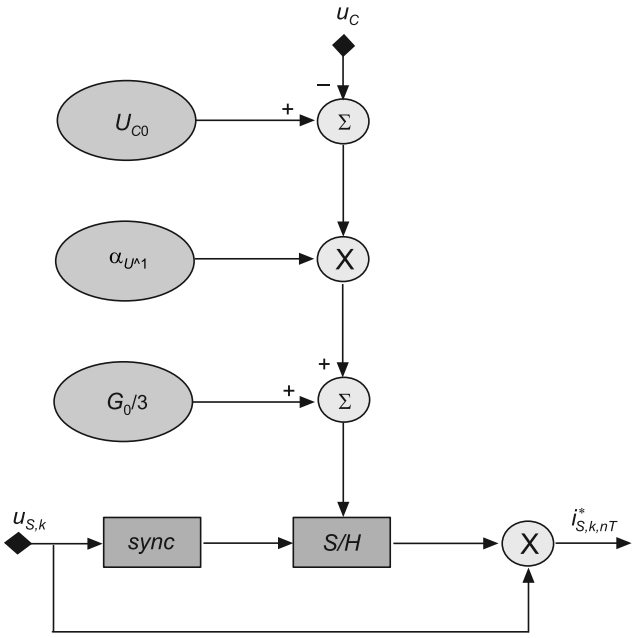

Fig. 11. Per-phase control structure of three-phase active filter

The filter's control circuit shown in Fig. 11 was verified using simulations. Load phase currents were designed to be full of non-active components, especially interharmonics. Such currents are rather impossible in case of a real load, but they are chosen intentionally to show the capability of the active current focused active filter for compensation of complex currents.

Load currents are modelled using three current sources and a time-dependent resistance. Current sources operate in Δ-configuration and generate interharmonics 20 A/60 Hz, 20 A/70 Hz and 25 A/90 Hz in phase *A*, *B*, and *C*, respectively. The time-dependent resistance is connected in parallel with the current source 20 A/60 Hz and changes periodically from zero to 20 Ω with the period 23 ms and duty cycle 11/23. Figure 12 presents load phase currents with source phase voltages. Such a constructed load works asymmetrically. During time period 0–200 ms, source apparent powers are 2350 VA in phase *A*, 2100 VA in phase *B* and 2270 VA in phase *C*. Mean phase powers are 394 W in phase *A*, 403 W in phase *B* and 27 W in phase *C*.

Detection of *DC* components, harmonics, interharmonics and unbalance of such complex signals may be difficult and ambiguous. Note that for the presented control technique, which is focused on active current component only, such load current complexity is not a problem.

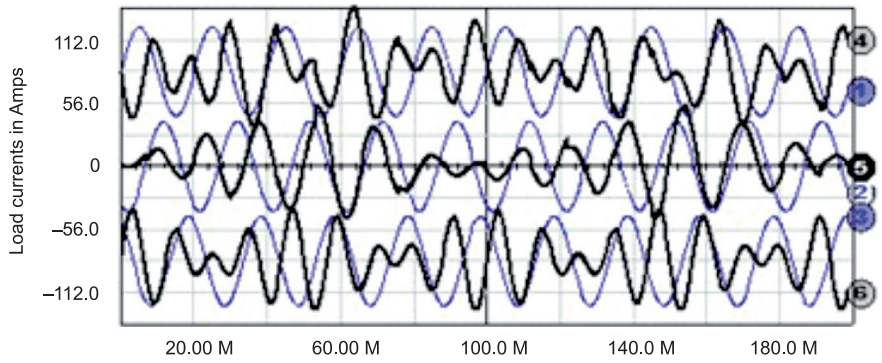

Fig. 12. Load phase currents with source phase voltages

There are two basic methods of bringing successively computed equivalent conductance magnitudes G_{nT} (19) into use:

a) at the same instance for phases A, B, C – for example synchronically with phase voltage of phase A, as shown in Fig. 13,
b) successively for phases A, B, C – synchronically with source phase voltages A, B, C, as shown in Fig. 14.

Dependent upon the method used, source currents may be different, but they are sinusoidal within each cycle T separately considered, what is shown in Figs. 13–15.

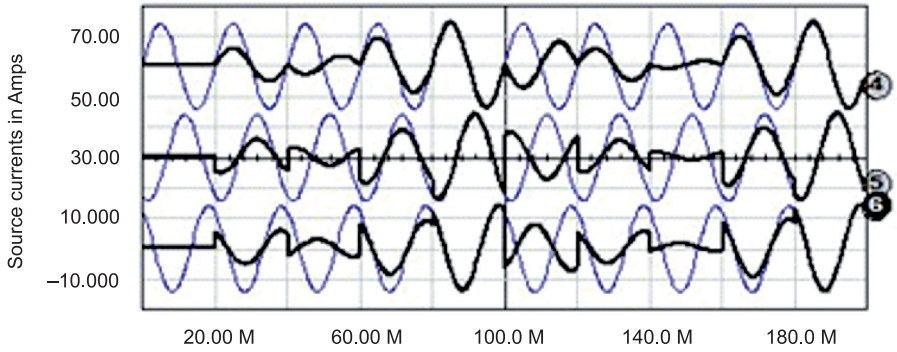

Fig. 13. Source reference currents. Phase currents are synchronised using voltage signal of phase A

Dependent upon the method used, source 'power tracks' may also be different due to differences in power buffering: it starts instantly for all phases in method a), or successively in method b). Figure 15 illustrates such an effect showing the filter's capacitor voltage and the equivalent conductance signal G_T for both synchronisation methods. Mean values and standard deviation of the conductance signal are 32 mS and 18 mS for method a); and 23 mS and 53 mS for method b), respectively.

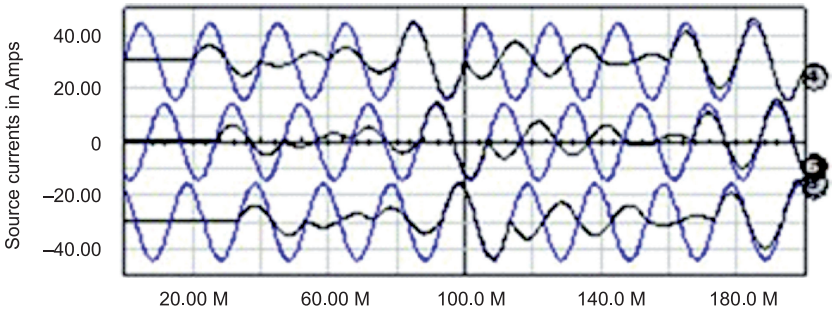

Fig. 14. Source reference currents. Phase currents are synchronised separately, in accordance with corresponding source phase voltage signals

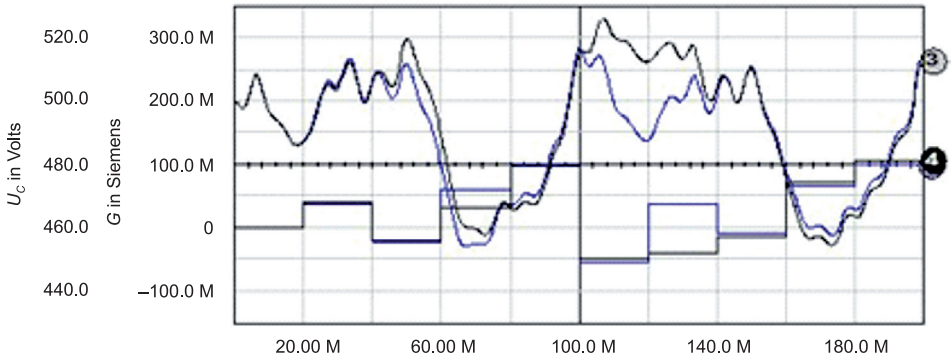

Fig. 15. Comparison of the filter's capacitor voltage and equivalent conductance signal. Synchronisation method a) blue waveforms, method b) black waveforms

For load and source currents shown in Figs. 12–14, *DC* components and amplitudes of current harmonics were obtained by simulation. They were performed separately for some successive *T* periods using the fundamental frequency corresponding to the source voltage cycle. Then, the other set of harmonics was extracted using base frequency of 10 Hz, which is equal to the greatest common divisor of frequencies of the three current sources (60 Hz, 70 Hz and 90 Hz) used to model the load. Fundamental observations can then be highlighted:

1. Source currents *RMS* are significantly reduced. For the time period 0–180 ms, the *RMS* for load phase *A*, *B* and *C* are 23.1 A, 21.0 A and 22.7 A, respectively. For the corresponding time period 20–200 ms, they are 6.2 A for each phase for both synchronisation methods.
2. Source phase currents are in-phase or are in-counter-phase with corresponding phase voltages.
3. Source phase currents are balanced, but *DC* components and current sudden changes may appear in phase *B* and *C* if the load active power changes and if synchronisation method a) is chosen.

4. There are no higher harmonics and *DC* components in source phase currents, but source currents may become unbalanced if the load active power changes and synchronisation method b) is selected.
5. There are significant changes to source current amplitude from one period *T* to another if there are big changes in load active power.

Effects reported in 3–5 above may be reduced if implement controlling of active energy flow. This possibility is considered in section 7.

6. *DC*-system active filter

The active current component is useful by means of carrying the active power. The non--active current component may not only appear in *AC* systems but also in a *DC*-supplied circuit and may be regarded as energetically useless. Hence, compensation may also be advantageous in *DC*-systems. In addition, some new benefits may appear if an energy flow control function implemented in the filter action, see section 7. For example, the life-time of a *DC*-battery depends on the characteristics of the battery's current [33]. If using a properly controlled filter, the battery may work more efficiently and the lifetime of the battery may be increased.

Let us consider an elementary electric circuit consisting of a *DC* voltage source and a varying load. A constant time period *T* may be designated for the circuit. For any *n*-th period *T*, the active power P_{nT} is:

$$P_{nT} = \frac{1}{T}\int_{(n-1)T}^{nT} U_S i_S dt = U_S \frac{1}{T}\int_{(n-1)T}^{nT} i_S dt = U_S I_{Sav,nT} \tag{22}$$

where:

$n = 1, 2, 3, \ldots$; U_S and i_S are source voltage and current,

$I_{Sav,nT}$ – average current in period T_n.

The in-period source current i_{nT} may be split into an active component $i_{p,nT}$ and a non--active component $i_{q,nT}$:

$$i_{nT} = i_{p,nT} + i_{q,nT} \tag{23}$$

The active current is equal to the current average:

$$i_{p,nT} = \frac{P_{nT}}{U_S^2} U_S = \frac{U_S I_{Sav,nT}}{U_S^2} U_S = I_{Sav,nT} \tag{24}$$

This current may be used as the reference for the source current. Using (2)–(13):

$$I^*_{S,nT} = \left[G_0 + \frac{C(U_{C0}^2 - U_{C,(n-1)T}^2) - LI_{AF,(n-1)T}^2}{2TU_S^2} \right] U_S \tag{25}$$

After simplifications (see section 3) equation (25) may be written in the final form:

$$I^*_{S,nT} = \left[G_0 + \alpha_{U\wedge 1}(U_{C0} - U_{C,(n-1)T}) \right] U_S \tag{26}$$

The corresponding structure of the filter control circuit is shown in Fig. 16.

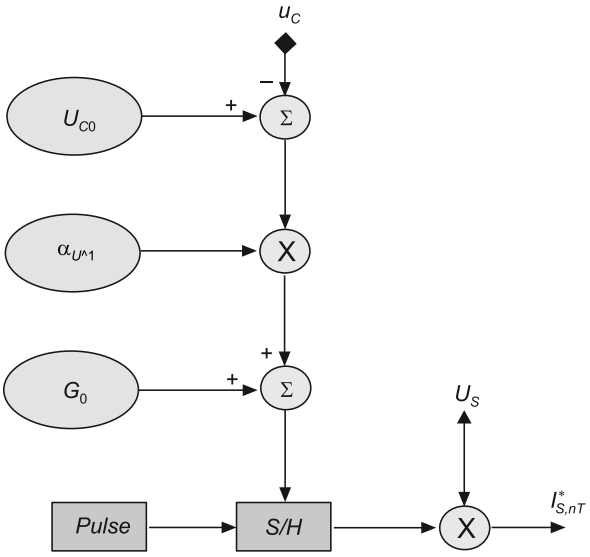

Fig. 16. *DC*-filter control circuit corresponding with (26)

Simulation verification of the considered control method in the *DC*-system was performed. The full-formula (25) and then the simplified formula (26) were examined. The constant component G_0 was set to 80 mS, which is about the mean in the time period 0–100 ms. Figure 17 presents the load current (1, black), the source current (2, green) and the filter current (3, red).

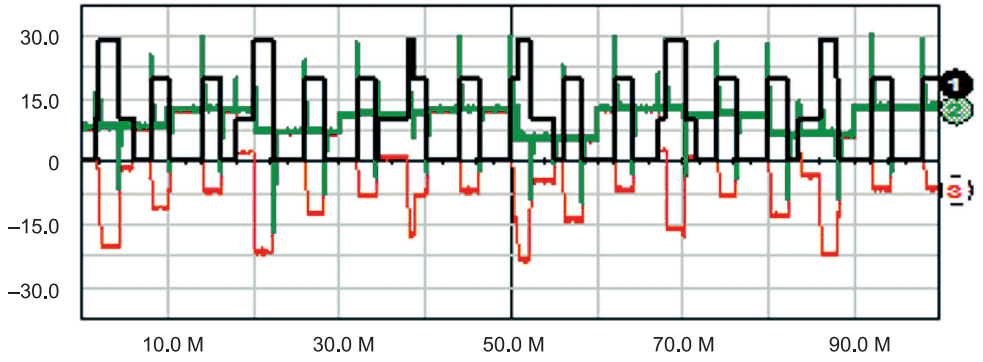

Fig. 17. Load current (1, black), source current (2, green) and filter current (3, red)

The source current *RMS* is significantly reduced. The multi-period load current *RMS* for the time period 0–100 ms is 14.3 A, but the source current within the same time period is diminished to 10.6 A. For the same time, the filter current is 10.8 A.

7. Simultaneous compensation and active energy flow control

As was shown in section 2, the filter acts in a two-step regime. During the first step, the load equivalent conductance is computed and latched, and during the second step, this already time--invariant conductance is used to shape the source current (note, these two steps are performed simultaneously for each cycle of supply voltage). Changes of load active power impacts energy stored in filter's reactance elements. From this perspective, the active filter already buffers some amount of active energy. Such natural mechanism of energy buffering can be developed to build new properties of the active filter. In this paper, two forms of active energy flow regulation are discussed:

a) the *averaging-mode,* which is based on a kind of 'cycle-by-cycle' inertia. In this mode, the filter averages changes of source currents. It virtually converts the actual variable load to be seen as more time-invariant-like,
b) the *storing-mode*. In this mode, the filter can store some amount of energy in its capacitor for future use.

The three-phase circuit with synchronisation by phase *A* is chosen to show features of the filter acting using averaging or storing mode. The load contains the same three current sources operating in the same configuration as described in section 5.

Other filter systems described in the paper were systematically simulated to confirm the usefulness of these two modes of filter operation. The observed filter features were very similar, so there is no need to show these results here.

In order to implement the averaging-mode, the parameter $\alpha_{U^{\wedge}1}$ (21) is reduced to 25% of its nominal magnitude. As a result, *RMS* of source phase reference currents, measured for the time period 20–200 ms, is diminished from 6.2 A to 1.1 A. The filter buffers changes of load active power, hence the source can work more smoothly. Standard deviation of conductance signal G_{nT}, which may be used as a measure of changeability of source active power, is reduced from 48.8 mS to 10.2 mS. Natural versus averaging-mode of filter operation is shown in Fig. 18.

In order to emphasise that the storing-mode is related to energy flow control, the source instantaneous powers are chosen to illustrate features of this mode.

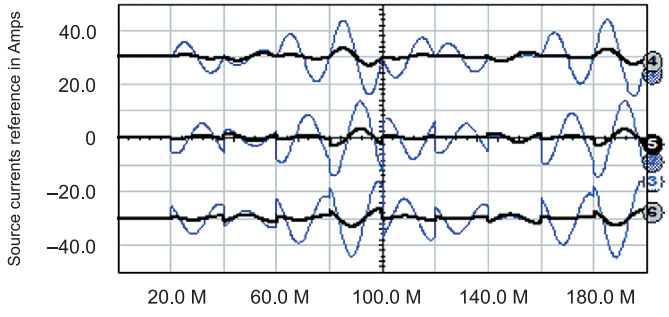

Fig. 18. Phase source currents for the natural and then for the averaging-mode. Synchronization method a) is applied. Phase currents *RMS* are reduced from 6.2 A (blue waveforms) to 1.1 A (black waveforms)

Before switching the active filter on the source phase, instantaneous powers are non--sinusoidal and non-periodical. Additionally, during the load work there are T periods when the load consumes energy, and there are other periods when the load generates energy. As a result, the total instantaneous source power is also highly irregular, Fig. 19.

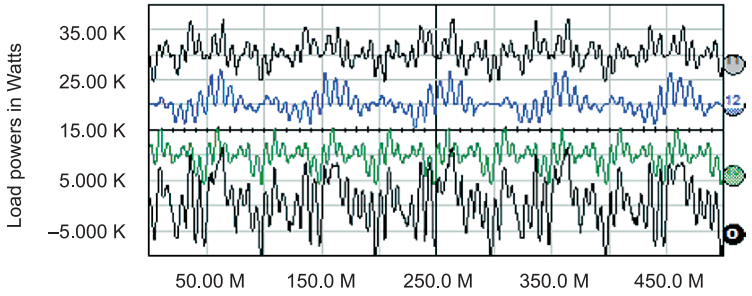

Fig. 19. Source instantaneous powers in phase A, B, C and total power as the sum of phase powers. There is no active filter action yet

After the active filter is switched on, source phase currents become sinusoidal and balanced, so phase instantaneous powers become sinusoidal and balanced and the source total instantaneous power becomes constant within each voltage cycle, Fig. 20.

In the example, there are time periods when the load generates energy. Note, generated powers are different for each load phase, Fig. 19. If implementing the storing-mode, this energy can be stored in the filter's capacitor for future use without sending it to the source. In the storing-mode, the active filter persistently compensates for the non-active phase current components and acts simultaneously as a local energy accumulator. In order to store the 'from-load' energy in the filter, negative magnitudes of the conductance signal G_{nT} are blocked. As a result, all source instantaneous powers have only positive magnitudes, Fig. 20.

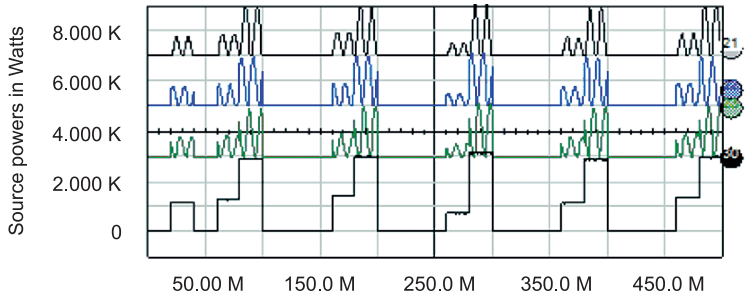

Fig. 20. Source instantaneous powers in phase A, B, C and source total power. Storing-mode is used

Unfortunately, the source works in a pulsing-like way. Standard deviation of the equivalent conductance signal may be a measure of such a disadvantageous pulsation. In the example, the standard deviation and the mean of the conductance are 38.9 mS and

29.4 mS, respectively. This pulsation may be alleviated if combining the storing-mode with the averaging-mode. In order to add the averaging-mode to the filter action, the parameter $\alpha_{U\wedge 1}$ (21) was reduced to 25% of its nominal magnitude. As a result, the standard deviation and the mean of the conductance are reduced to 12.6 mS and 23.4 mS, respectively. Source powers are shown in Fig. 21.

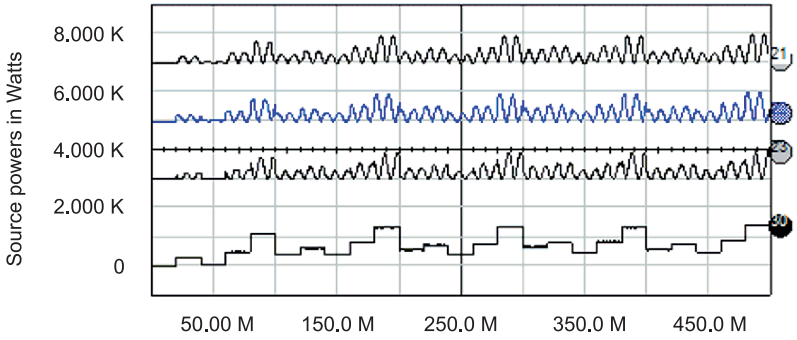

Fig. 21. Source instantaneous powers in phase *A*, *B*, *C* and total power. Storing-mode and averaging-mode are applied concurrently

8. Universality of filter's control method

The considered filter is as universal in its control algorithm as in its hardware structure. The same filter arrangement may be used in *DC*, single-phase and three-phase system for the following reasons:

a) the load equivalent conductance is always determined using energy stored in the filter's capacitor. Hence the same form of function of the filter's capacitor voltage may be utilized to obtain the reference current,
b) the common hardware structure utilises the three-leg inverter. If using the filter in single-phase or in *DC*-system, the filter can act as a two-leg subsystem of the whole device, see Fig. 22.

In addition, if utilising the Current Source Inverter based active filter, equation (10) is still valid. Equations similar to (18), (21) and (26) may be written, respectively, as:

$$i^*_{S,nT} = \left[G_0 + \alpha_{I\wedge 1}(\mathrm{I}_{L0} - I_{L,(n-1)T}) \right] u_S \tag{27}$$

or

$$i^*_{S(k),nT} = \left[\frac{G_0}{3} + \alpha_{I\wedge 1}(I_{L0} - I_{L,(n-1)T}) \right] u_{S(k)} \tag{28}$$

or

$$i^*_{S,nT} = \left[G_0 + \alpha_{I\wedge 1}(\mathrm{I}_{L0} - I_{L,(n-1)T}) \right] U_S \tag{29}$$

Structures shown in Figs. 5, 11 and 16 are also valid if replacing the initial capacitor voltage U_{C0} for the initial filter's *DC*-side inductor current constant I_{L0}.

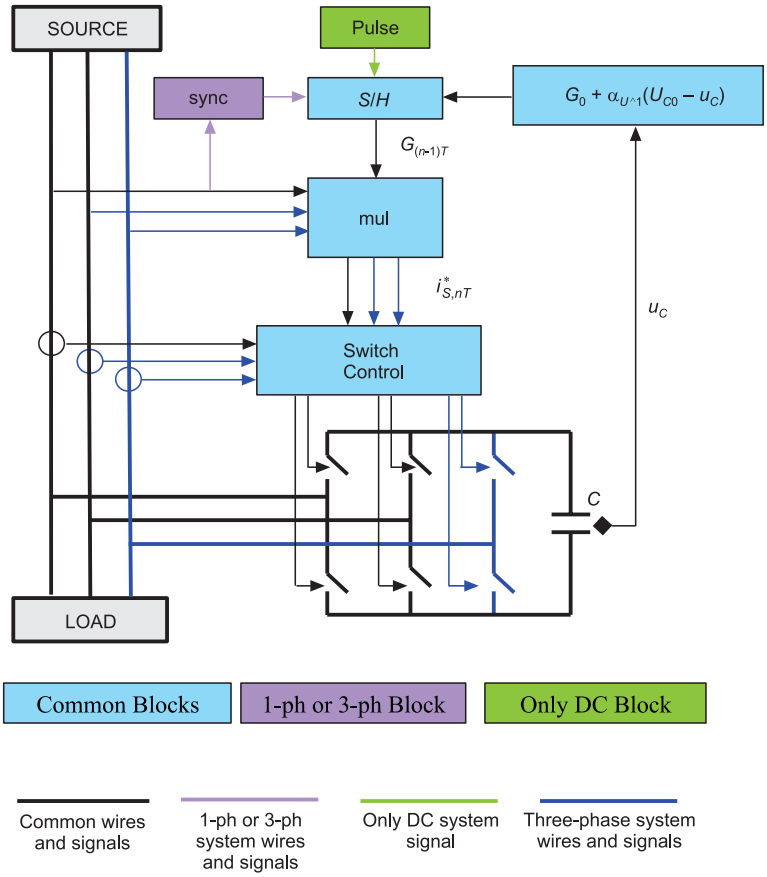

Fig. 22. Universal filter structure

9. Conclusion

Certain changes of energy stored in the active filter's reactance elements may be utilised as the source of information concerning the load active current component. This component can then be used as the reference signal for compensation. After analysis, it turned out that this energy-based control method may be substituted with the simplified strategy, which is based on measuring and simple processing of the filter's capacitor *DC*-side voltage or the filter's inductor *DC*-side current. The described control method allows using the filter not only to compensate the non-active current but, additionally, to buffer the bi-directional flow of active energy between the source and compensated loads. In such a case, the filter acts simultaneously as a local energy accumulator. The control algorithm is universal and may be employed in *DC*, single-phase and three-phase active filters.

References

[1] Asiminoaei L., Blaabjerg F., Hansen S., *Detection is key. Harmonic detection methods for active power filter applications*, IEEE Ind. Appl. Mag., 2007, Vol. 13(4), 22-33.

[2] Miret J., Castilla M., Mattas J., Guerrero J.M., Vasquez J.C., *Selective harmonic-compensation control for single-phase active power filter with high harmonic rejection*, IEEE Trans. on Ind. Electr., 2009, Vol. 56(8), 3117-3127.

[3] Mariethoz S., Rufer A.C., *Open loop and closed loop spectral frequency active filtering*, IEEE Trans on Pow. Electr., 2002, Vol. 17(4), 564-573.

[4] Rahmani S., Al-Haddad K., Fnaiech Y., *Comparison of two PWM techniques for a single-phase shunt active power filter applying indirect current control*, IEEE Int. Conf. on Ind. Techn., 2004, 639-644.

[5] Farrokhi M., Jamali S., Mousavi S.A., *Fuzzy logic based indirect current control of the shunt active power filter*, IEEE Univ. Pow. Eng. Conf., 2004, 489-493.

[6] Singh B.N., Singh B., Chandra A., Rastgoufard P., Al-Haddad K., *An improved control algorithm for active filter*, IEEE Trans. on Power Delivery, 2007, Vol. 22(2), 1009-1020.

[7] Nedeljković D., Nemec M., Drobnić K., Ambrožić V., *Direct current control of active power filter without filter current measurement*, Int. Symp. on Pow. Electron., Electr. Drives, Aut. and Mot., 2008, 72-76.

[8] Khadkikar V., Chandra A., Singh B.N., *Generalised single-phase p-q theory for active power filtering: simulation and DSP-based experimental investigation*, IET Pow. Electron., 2009, Vol. 2(1), 67-78.

[9] Orts-Grau S., Gimeno-Sales F.J., Segui-Chilet S., Abellen-Garcia A., Alcaniz-Fillol M., Masot--Peris R., *Selective compensation in four-wire electric systems based on a new equivalent conductance approach*, IEEE Trans. on Ind. Electr., 2009, Vol. 56(8), 2862-2874.

[10] Vardar K., Akpinar E., *Comparing ADALINE and IRPT methods based on shunt active power filter*, Euro. Trans. Electr. Power, 2011, Vol. 21, 924-936.

[11] Wu J.-C., Jou H.-L., *Simplified control method for the single-phase active power filter*, IEE Proc.--Electr. Power Appl., 1996, Vol. 143(3), 219-224.

[12] Tang Y., Loh P.C., Wang P., Choo F.H., Gao F., Blaabjerg F., *Generalized Design of High Performance Shunt Active Power Filter With Output LCL Filter*, IEEE Trans. on Ind. Electr., 2012, Vol. 59(3), 1443-1452.

[13] Piróg S., *PWM rectifier and active filter with sliding-mode control*, EPE Trondheim, 1997.

[14] Singh B.N., Chandra A., Al-Haddad K., *Performance comparison of two control techniques applied to an active filter*, Int. Conf. on Harm. and Qual. of Power, 1, 1998, 133-138.

[15] Huang S.-J., Wu J.-C., *A control algorithm for three-phase three-wired active power filters under nonideal mains voltages*, IEEE Trans. on Power Electr., 1999, Vol. 14(4), 753-760.

[16] Chandra A., Singh B., Singh B.N., Al-Haddad K., *An improved control algorithm of shunt active filter for voltage regulation, harmonic elimination, power-factor correction, and balancing of nonlinear loads*, IEEE Trans. on Ind. Electr., 2000, Vol. 15(3), 495-507.

[17] Azevedo H.J., Ferreira J.M., Martins A.P., Carvalho A.S., *Direct current control of an active power filter for harmonic elimination, power factor correction and load unbalancing compensation*, EPE, Toulouse 2003.

[18] Nunez-Zuniga T.E., Pomilio J.A., *Shunt active power filter synthesizing resistive loads*, IEEE Trans. on Ind. Electr., 2002, Vol. 17(2), 273-278.

[19] Hamadi A., Al-Haddad K., Lagace P.J., Chandra A., *Indirect current control techniques of three-phase APF using fuzzy logic and proportional integral controller: Comparative analysis*, Int. Conf. on Harm. and Qual. of Power, 2004, 362-367.

[20] Singh B.N., *Sliding mode control technique for indirect current controlled active filter*, IEEE Annual Reg. 5 Conf., 2003, 51-58.
[21] Strzelecki R., Benysek G., Jarnut M., *Power quality conditioners with minimum number of current sensor requirement*, Int. School on Nonsin. Currents and Compensation, 2008, 1-4.
[22] Watson R.V., *Sampled energy control of a single-phase shunt active power filter synthesizing a resistive load*, EPE 2009.
[23] Chen Z., Luo Y., Chen M., Shi L., Li J., *Design and implementation of a high performance aeronautical active power filter*, IEEE Ann. Conf. IECON, 2010, 2032-2037.
[24] Fei J., Li T., Zhang S., *Indirect current control of active filter using novel sliding mode controller*, Workshop on Control and Modeling for Power Electronics, 2012, 1-6.
[25] Szromba A., *A shunt active power filter: development of properties*, COMPEL, 2004, Vol. 23(2), 735-46.
[26] Szromba A., *Energy controlled shunt active power filters*, COMPEL, 2007, Vol. 26(4), 1142--1160.
[27] Szromba A., *Sampled Method of Active Power Filter Control (Part I)*, Electric. Pow. Quality and Utilisation J., 2005, Vol. 11(2), 91-98.
[28] Szromba A., *Sampled Method of Active Power Filter Control (Part II)*, Electric. Pow. Quality and Utilisation J., 2006, Vol. 12(1), 16-25.
[29] Bhattacharya A., Chakraborty C., *A Shunt Active Power Filter With Enhanced Performance Using ANN-Based Predictive and Adaptive Controllers*, IEEE Trans. on Ind. Electr., 2011, Vol. 58(2), 421-428.
[30] Hwang J.-G., Park Y.-J., Choi G.-H., *Indirect current control of active filter for harmonic elimination with novel observer-based noise reduction scheme*, Electric. Engineering, 2005, Vol. 87, 261-266.
[31] Fryze S., *Wirk-, Blind-, und Scheinleistung in Elektrischen Stromkreisen mit nichtsinusformigem Verlauf von Strom und Spannung.*, ETZ 53, 1932, 596-599, 625-627, 700-702.
[32] Moreno V., Pigazo A., *Modified FBD method in active power filters to minimize the line current harmonics*, IEEE Trans. on Pow. Deliv., 2007, Vol. 22(1), 735-746.
[33] Savoye F., Venet P., Millet M., Groot J., *Impact of periodic current pulse on Li-Ion battery performance*, IEEE Trans. on Ind. Electr., 2012, Vol. 59(9), 3481-3488.

TECHNICAL TRANSACTIONS | **CZASOPISMO TECHNICZNE**
ELECTRICAL ENGINEERING | ELEKTROTECHNIKA
2-E/2015

ZBIGNIEW SZULAR*

THREE-PHASE SQUIRREL-CAGE INDUCTION GENERATOR EXCITED BY CAPACITOR BATTERY

TRÓJFAZOWY GENERATOR INDUKCYJNY KLATKOWY WZBUDZANY BATERIĄ KONDENSATORÓW

Abstract

The generation of electrical energy in small power plants which use renewable energy sources is often implemented with the use of induction generators. This paper presents a proposal of an energy generation system which is constructed with the use of a three-phase self-excited squirrel-cage induction generator. The idea of this proposal consists of a control method of the generator rotor magnetic flux linkage via fully controlled power electronic switches. The energy produced by the induction generator is transferred to a DC link via an uncontrolled rectifier and a DC-DC chopper. The proposed solution allows us to generate energy with the use of a relatively simple and reliable electrical machine. Additional important advantages of this concept are a small number of controlled elements, and an easy control method.

Keywords: *self-excited cage induction generator*, *bi-directional switch*, *capacitor battery*

Streszczenie

Wytwarzanie energii w małych elektrowniach wykorzystujących odnawialne źródła energii jest często realizowane w oparciu o generatory indukcyjne. W artykule przedstawiono propozycję układu sterowania wzbudzeniem generatora indukcyjnego klatkowego. Idea rozwiązania polega na sterowaniu sprzężonego strumienia magnetycznego wirnika generatora dzięki baterii kondensatorów dołączonych do obwodu stojana za pośrednictwem łączników energoelektronicznych. Energia wytwarzana w generatorze jest przekształcana za pośrednictwem prostownika niesterowanego oraz przerywacza i dostarczana do obwodu DC. Rozwiązanie to pozwala wytwarzać energię za pomocą maszyny o względnie prostej i niezawodnej, a tym samym taniej konstrukcji uzupełnionej o dodatkowe układy energoelektroniczne. Zalety tej koncepcji to mała liczba elementów sterowanych i łatwe sterowanie.

Słowa kluczowe: *samowzbudny generator indukcyjny klatkowy*, *łącznik dwukierunkowy*, *bateria kondensatorów*

DOI: 10.4467/2353737XCT.15.093.3925

* Ph.D. Eng. Zbigniew Szular, Institute of Electromechanical Energy Conversion, Faculty of Electrical and Computer Engineering, Cracow University of Technology.

1. Introduction

Cage induction generators are usually driven by wind, water or gas turbines which provide mechanical energy to the generator. In the simplest solution, the generator is directly connected to the power grid which, in turn, has to provide the reactive power which is necessary to excite the magnetic flux in the induction generator. The advantage of such a solution is simplicity and the ability to transfer from the generator mode to the motor mode and vice versa. Unfortunately, the main disadvantage is the restriction to only work in a very narrow range of angular speed changes. The second method of power generation, with the use of a squirrel cage induction generator, is an application of the PWM rectifier [1] or AC-AC dual active bridge converter [2–6], especially with a two or multilevel structure [7]. The fundamental advantage of these systems is the direct possibility of cooperation with an autonomous power grid in a wide range of rotational speed changes. On the other hand, an application of the AC-AC dual active bridge converter causes the complexity of the processing power both in terms of the topology and the control system. The induction generator can also be excited by the capacitor battery connected to the stator winding terminals [8]. In order to ensure a stable operation, the capacity of the battery should be continuously adjustable – the fulfillment of this condition is technically complicated. However, continuous adjustment of the battery capacity can be carried out by a series connection of capacitors and insulated gate bipolar transistors (IGBT) and their appropriate switching [9].

2. Topology of the energy generation system

The energy generation system with the self-excited cage induction generator and capacitor battery is shown in Fig. 1. The star-connected capacitors C_A, C_B, C_C of the excitation circuit are connected to the stator terminals A, B, C. Two capacitors are connected in series with two-direction fully controlled switches S_A and S_B. A three-phase diode rectifier

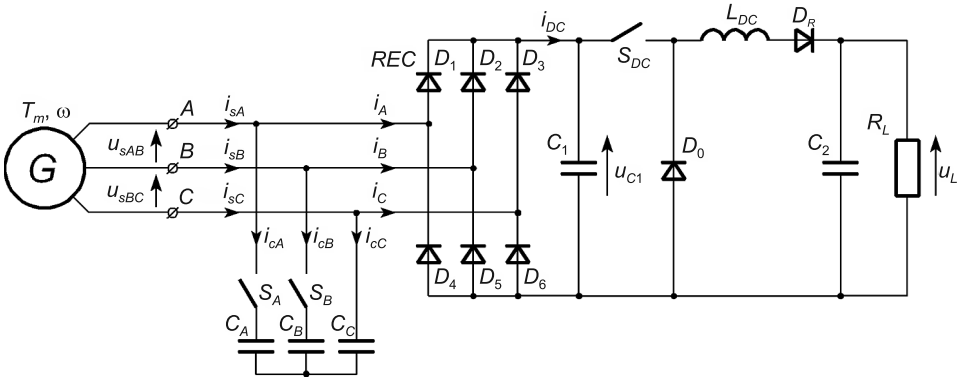

Fig. 1. System of energy generation with the self-excited cage induction generator and capacitor battery

REC with a capacitor C_1 on the output is also connected to the stator terminals. In addition, this circuit contains the fully controlled switch S_{DC}, the inductive choke L_D, the diode D_R, the reverse diode D_0 and the capacitor C_2 on the output of the system. The capacitor C_2 can form an integral part of the voltage source inverter that converts DC voltage to AC voltage. The resistor R_L represents the external load. It should be added that the items L_{DC}, D_R, D_0 and C_2 are not necessary if the load does not have a capacitive character. Bi-directional switches S_A and S_B can be constructed with the use of the IGBTs in one of two ways, as shown in Fig. 2.

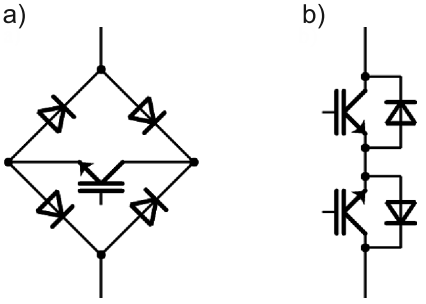

Fig. 2. The schemes of the bi-directional fully controlled switches: a) with a single transistor and a diode bridge; b) with two transistors connected in series in common emitter configuration

3. Description of the generator operation

The generator starts at a predetermined angular speed by the initial charge in the excitation circuit capacitors, or it can use the residual magnetism of the machine. In the second case, it is possible to consider additional shunting of the semiconductor excitation circuit switches at the initial stage of generator excitation. At the beginning, all switches are turned on. The required value of the capacity of the battery capacitors first of all depends on the generator's nominal parameters and on the generator's angular speed [8]. The lower the angular speed is, the higher the required battery capacity should be. Thus, the battery capacity is determined by the minimum angular speed of the induction generator. An increase in the angular speed causes an increase in the stator voltage. This condition occurs as long as the switches remain turned on. When the generator output voltage reaches the assumed value, the capacitor battery is disconnected. In the absence of passive power, both the magnetic flux of the generator and the magnitude induced voltage decrease. When the magnitude of the stator voltage drops to the specified value, the capacitor battery is turned on again, and in consequence, the magnitude of the stator voltage increases again. In practice, the frequency of such periodic switching of the transistors is in the range from several hundred hertz to a few-dozen kilohertz. The basis of correct operation is to ensure higher voltage of the capacitor C_1 with respect to the voltage of the capacitor battery. Otherwise, the two--direction switches would be damaged by the pulse current flow. The capacitor C_1 and one of the battery capacitors should be pre-charged in order to initialize the generator

operation. During correct operation of the energy generation system, the voltage of the capacitor C_1 is always higher than the highest voltage of the battery capacitors. As long as the switches are turned on, the voltage of the capacitor C_1 is always equal to the maximum voltage of the capacitor battery. When the IGBTs are turned off, the voltages of the battery capacitors have a constant value. In turn, due to the inductive character the stator current, they cannot change their value abruptly. Hence, the currents i_A, i_B, i_C flowing to the rectifier *REC* remain different from zero. In view of the fact that the sum of the battery currents is always equal to zero, the current flowing to the capacitor C_1 does not change its value during the switching process. This capacitor is still charged, so its voltage increases and is higher than the maximum voltage of the capacitor battery. It is worth underlining that the capacitor can be discharging by the external load. To avoid this risk, the external load has to be periodically disconnected from the generation system. This process proceeds synchronously with respect to the switching of the capacitor battery with the use of the additional switch S_{DC} in the DC circuit. It is worth underlining that all IGBTs are turned on and turned off by means of a common signal.

4. Parameter adjustment of energy generation system

The battery capacity depends on the parameters of the induction generator and operating conditions [8, 10]. This capacity can be determined with the use of the relationship:

$$C_A, C_B, C_C \geq \frac{1}{\omega_{\min}^2 L_m} \tag{1}$$

where:

$\omega_{\min} = 2\pi f_{\min}$; for the analysis, it has been assumed that the capacity is equal to 100 μF,
L_m – magnetizing inductance.

The capacitor C_1 of the DC circuit should be selected due to the amount of energy which is stored in this capacitor when the battery of the capacitors C_A, C_B, and C_C is disconnected from the energy generation system. The worst case occurs when the voltage of capacitor C_1 has its maximum admissible value and the stator currents are equal to the nominal value, whereas the DC output circuit is not loaded. Then, the total energy occurring in the magnetic circuit of the induction generator is transferred to capacitor C_1 causing an increase in its voltage. On this basis, capacity C_1 can be determined as follows:

$$C_1 \geq \frac{\frac{3}{2} L_s \cdot I_{s\max}^2}{u_{\max}^2 - u_{CN}^2} \tag{2}$$

where:

$u_{CN}^2, u_{\max}^2$ – the nominal and the maximum voltage of the capacitor C_1, respectively,
$I_{s\max}$ – amplitude of the stator current,
L_s – inductance of the stator phase.

To ensure a smooth waveform of the output voltage, the system is equipped with an output filter composed of the induction choke L_{DC} and the capacitor C_2. Parameters of the

filter can be selected with a simplified method. The minimum value of the induction is determined by the admissible current of the S_{DC} switch at discharged capacitor C_2 (short circuit output) during one period of the switching in the worst case. This induction can be determined with the use of the relationship:

$$L_{DC} \geq \frac{U_{C1}}{f_{i\min} I_0 \delta I} \tag{3}$$

where:

U_{C1} – voltage of the capacitor C_1 at the time of turning on the switches,
$f_{i\min}$ – the minimum frequency of the switching,
δI – current growth of the induction choke L_{DC},
I_0 – initial current of the choke L_{DC} at the time of turning on the switches.

In a similar manner, the capacitance C_2 can be selected. The minimum value of the capacity is determined by admissible voltages of the capacitor whereas the DC output circuit is not loaded at the maximum possible current of the S_{DC} switch during one period of the switching in the worst case. On this basis, capacity C_2 can be determined as follows:

$$C_2 \geq \frac{L_{DC} I_{LDC\max}^2}{U_{C2\max}^2 - U_{C20}^2} \tag{4}$$

where:

$I_{LDC\max}$ – the maximum current of the choke L_{DC} at the time of turning off the switches,
$U_{C2\max}$ – admissible voltage of the capacitor C_2,
U_{C20} – the initial voltage of the capacitor C_2.

Numerical calculations were carried out for a typical induction generator with nominal parameters: P_N = 3 kW; U_{sN} = 220/380 V; I_{sN} = 11.6/6.7 A; f_{sN} = 50 Hz; $\cos\varphi_N$ = 0.835; n_N = 1430 r/min.; p = 2. Parameters of the equivalent circuit of the induction generator have the following values: R_s = 2 Ω; $R_r^{/}$ = 1.42 Ω; $L_{\sigma s}$ = 12.2 mH; $L_{\sigma r}^{/}$ = 12.2 mH; L_m = 202 mH.

5. Numerical analysis of the system

A monoharmonic model in phase coordinates of the cage induction generator has been applied in numerical analysis [11]. This model takes into account only the basic harmonic of the magnetic field assuming linearity of the magnetic circuit. The matrix form of the equations which describe the model of the induction generator in phase coordinates has the following form:

$$\mathbf{U} = \mathbf{R} \cdot \mathbf{I} + \mathbf{L}_1 \frac{d}{dt}\mathbf{I} + p \cdot \omega \cdot \mathbf{L}_2 \cdot \mathbf{I} \tag{5}$$

where:

$$\mathbf{U} = \begin{bmatrix} u_a \\ u_b \\ 0 \\ 0 \end{bmatrix}, \qquad \mathbf{I} = \begin{bmatrix} i_a \\ i_b \\ i_c \\ i_d \end{bmatrix}, \qquad \mathbf{R} = \begin{bmatrix} 2R_s & -R_s & 0 & 0 \\ -Rs & 2R_s & 0 & 0 \\ 0 & 0 & 2R_r^{/} & -2R_r^{/} \\ 0 & 0 & -2R_r^{/} & 2R_r^{/} \end{bmatrix}$$

$$\mathbf{L_1} = \begin{bmatrix} 2L_s & -L_s & 2L_m & -L_m \\ -L_s & 2L_s & -L_m & 2L_m \\ 2L_m & -L_m & 2L_r & -L_r \\ -L_m & 2L_m & -L_r & 2L_r \end{bmatrix}, \qquad \mathbf{L_2} = \begin{bmatrix} 0 & 0 & 0 & 0 \\ 0 & 0 & 0 & 0 \\ 0 & \sqrt{3}L_m & 0 & \sqrt{3}L_r \\ -\sqrt{3}L_m & 0 & -\sqrt{3}L_r & 0 \end{bmatrix}$$

The equation of the electromagnetic torque is given by:

$$T_e = \sqrt{3}pL_m(i_U i_M - i_W i_K) \tag{6}$$

where:

i_U, i_V, i_W – the stator phase currents,
i_K, i_L, i_M – the rotor phase currents.

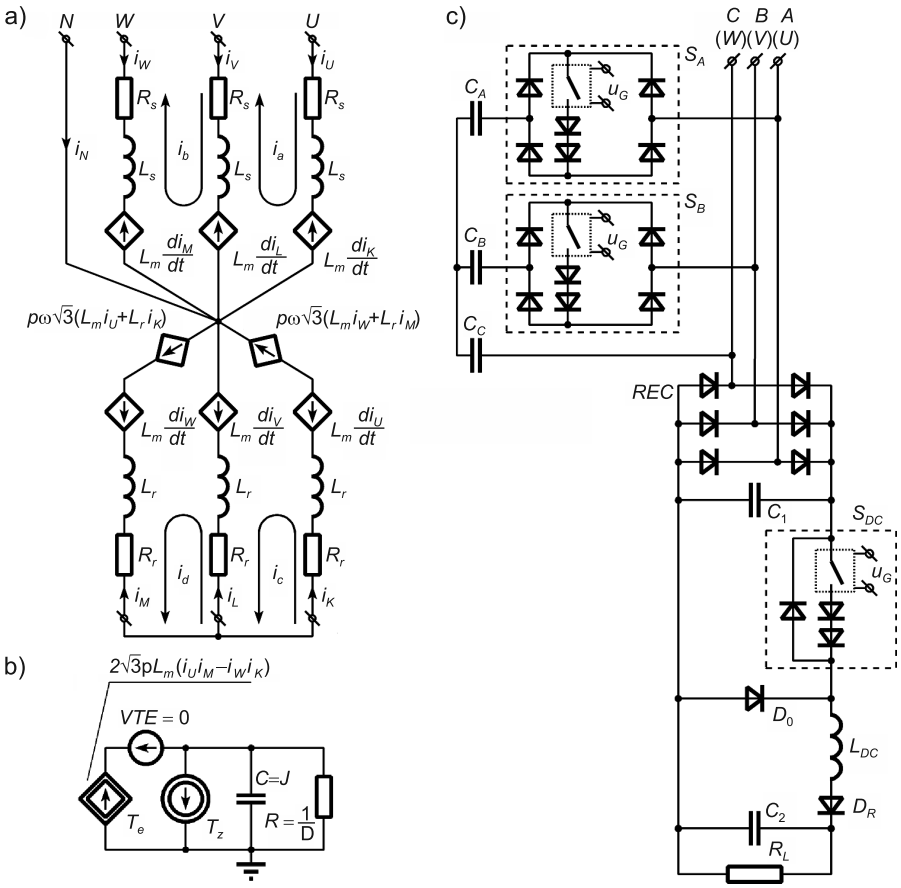

Fig. 3. Numerical model of the three-phase squirrel-cage induction generator: a) the equivalent circuit of the voltage equations; b) a replacement scheme of the motion rotary equation; c) the equivalent circuit of the external system connected to the induction machine

On the basis of equations (5) and (6), an electric equivalent circuit (Fig. 3) was built and this circuit was implemented in the IsSPICE simulation program. Transistors: S_A, S_B, S_{DC} were modeled on the basis of the model of the voltage-controlled switch. All switches are controlled by means of a common signal u_G. This model takes into account the basic parameters such as the static resistance of the transistor at blocking-bias and the resistance forward-bias. The optional neutral wire N is not used in this case.

The stable operation of the proposed energy generation system requires the use of an adjustment control unit which takes into account the following parameters: u_{sAB}, i_{sA}, ω, f_s, u_{DC} (Fig. 4). Initial validation of the correctness of the energy generation system has been performed for the scalar control with an assumed rotor magnetic flux linkage Ψ_r^r. The output signal m_a from the controller is proportional to the relative conduction time of the switches, and this signal is used for the switching of the IGBTs.

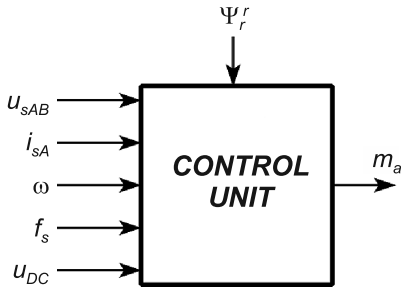

Fig. 4. The control unit of the squirrel-cage induction generator

Numerical calculations were carried out for the assumed angular speed which was equal to 157 rad/s. The switching frequency of IGBTs was fixed at 1 kHz. The other operating parameters did not exceed the nominal values. The generation system was controlled due to the relative magnetic flux linkage Ψ_r^r. This flux changes its value from zero to the maximum relative value which is equal to 0.8 at about 1.2 sec., and next, the magnetic flux has a constant average value until 3 sec. when the load resistance rises three times. The main task is maintaining the load voltage on the constant value equal to 675 V. As a result, the magnetic flux decreased. At 5 sec. the load resistance returned to the previous value. Figure 5a shows some chosen waveforms of the energy generation system from the start point to the steady state and operating of the proposed system after disturbance. In turn, Figure 5b presents analogous waveforms during the stable operation.

Figure 6 presents three chosen static characteristics of the squirrel-cage induction generator system as a function of the load power at the assumed angular speed equal to 157 rad/s, while the load voltage was equal to 250 V.

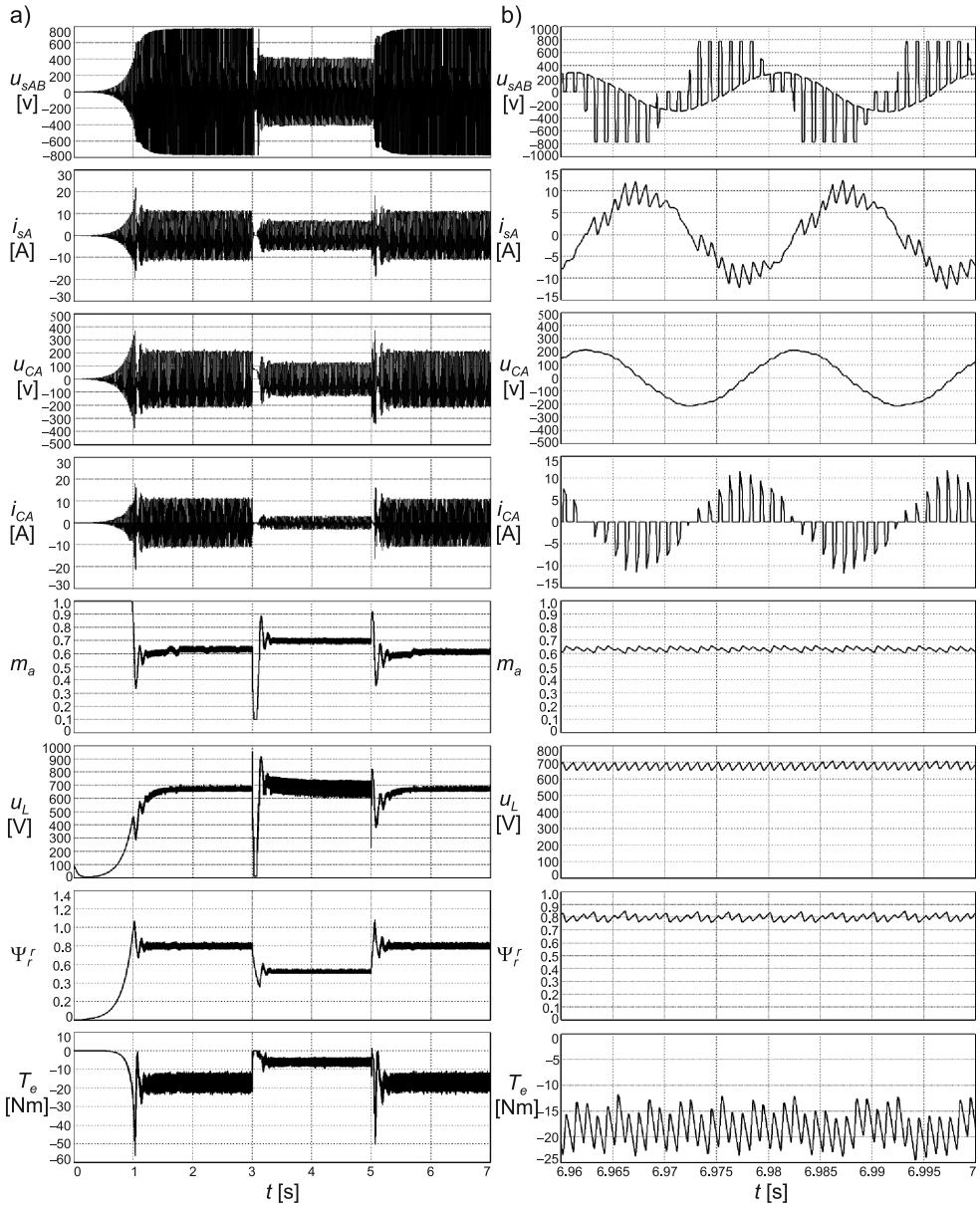

Fig. 5. Waveforms of chosen variables of the system of energy generation for: a) start-up of the generator and its transient states; b) zoomed in of a stable operating area

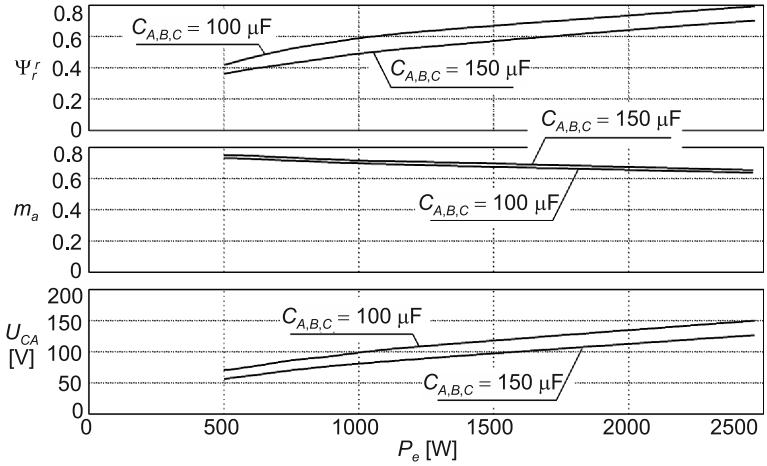

Fig. 6. Characteristics of the rotor magnetic flux linkage Ψ_r^r, the deep modulation coefficient m_a, and the rms voltage U_{CA} of the capacitor C_A for the assumed operating parameters

6. Conclusions

Analysis of numerical calculation results allows us to state the correctness of the proposed energy generation system. This system has several advantages in comparison with existing solutions; the most important feature to the application of the cheapest and reliable squirrel-cage induction machine. The proposed system has only three IGBTs in its simplified version. It is necessary to stress that the DC output voltage can be boosted up, and all IGBTs are switched with the use of only one control signal. The proposed energy generation system can operate in a wide range of angular speed; this is very important in cases of using renewable energy sources. Additionally, unlike the PM generators, the magnetic flux of the induction generator can be decreased safely when the angular speed is too high. It is understood that validation of the correctness of the proposed energy generation system requires comprehensive research with the use of the laboratory stand.

References

[1] Jakubowski B., Pieńkowski K., *Sterowanie autonomicznym generatorem indukcyjnym ze wzbudzeniem przekształtnikowym*, Zeszyty Problemowe – Maszyny Elektryczne, Nr 88/2010, 123-128.

[2] Borkowski D., Węgiel T., *Optymalizacja przetwarzania energii dla małych elektrowni wodnych z generatorami pracującymi ze zmienną prędkością obrotową*, Zeszyty Problemowe – Maszyny Elektryczne, Nr 92/2011, 121-126.

[3] Sobczyk T., Mazgaj W., Węgiel T., Szular Z., *Power electronic unit for small water plants with variable speed PM generator*, XXI Symp. Electromagnetic Phenomena in Nonlinear Circuits EPNC 2010, Dortmund–Essen 2010, 41-42.

[4] Sobczyk T., Mazgaj W., Węgiel T., Szular Z., *Energy conversion in small water plants with variable speed PM generator*, Archives of Electrical Engineering (część B, poz. 183), 2011, Vol. 60, No. 2, 159-168.
[5] Mazgaj W., Szular Z., Węgiel T., Sobczyk T., *Small Hydropower Plant with variable speed PM generator*, Przegląd Elektrotechniczny (część B, poz. 1160), 2011, Vol. 60, No. 2, 159-168.
[6] Mazgaj W., Szular Z., Węgiel T., *Control methods for PWM rectifier cooperating with variable speed PM generator*, Archives of Control Sciences, Vol. 23(LIX), No. 4, 2013, 495-504.
[7] Bueno E.J., Cóbreces S., Rodríguez F.J., Hernández Á., Espinosa F., *Design of a Back-to-Back NPC Converter Interface for Wind Turbines With Squirrel-Cage Induction Generator*, IEEE Transactions on Energy Conversion, Vol. 23, No. 3, September 2008, 932-945.
[8] Miksiewicz R., *Modelowanie samowzbudnych prądnic indukcyjnych,* Zeszyty Problemowe – Maszyny Elektryczne Nr 1/2013, pp. 121-127.
[9] Szular Z., *Trójfazowy samowzbudny generator indukcyjny*, Zeszyty Problemowe – Maszyny Elektryczne, Nr 104/4/2014, KOMEL, Katowice, 201-206, ISSN 0239-3646.
[10] Orlewski W., *Badanie pracy generatorowej maszyny asynchronicznej wzbudzanej kondensatorami*, Zeszyty Problemowe – Maszyny Elektryczne, Nr 84/2009, 113-116.
[11] Drozdowski P., Szular Z., *Energooszczędny dwuetapowy rozruch silników indukcyjnych klatkowych*, Napędy i Sterowanie, Nr 10/2006, 44-48, ISNN 1507-7764.

TECHNICAL TRANSACTIONS | **CZASOPISMO TECHNICZNE**
ELECTRICAL ENGINEERING | ELEKTROTECHNIKA
2-E/2015

JAROSŁAW TULICKI*, MACIEJ SUŁOWICZ*

NON-INVASIVE DIAGNOSTICS OF THE ROTOR THE ASYNCHRONOUS MOTOR WITH USING START UP STATOR CURRENT

NIEINWAZYJNA DIAGNOSTYKA WIRNIKA SILNIKA ASYNCHRONICZNEGO Z WYKORZYSTANIEM PRĄDU ROZRUCHOWEGO STOJANA

Abstract

This article presents the idea of asynchronous motor's non-stationary stator starting current, filtration methods, in the non-invasive diagnosis of the rotor cage. The mathematical description of the selected analysis forms is omitted in favor of an indication of the practical aspects of the method application and the obtaining of sample analysis results. The object of the study was the single cage induction motor with exchangeable rotors for different faults, machine's load was a generator with field current control system, which was used to control the load torque.

Keywords: *cage damage*, *time-frequency analysis*, *start-up current*

Streszczenie

W artykule przedstawiono ideę metod filtracji niestacjonarnego sygnału prądu rozruchowego stojana zwartego silnika asynchronicznego w bezinwazyjnej diagnostyce klatki wirnika. Pominięto opis matematyczny wybranych form analiz na rzecz wskazania praktycznych aspektów zastosowania danej metody oraz uzyskanych przykładowych wyników analiz. Obiektem badań był silnik jednoklatkowy z wymiennymi wirnikami, o różnym stopniu uszkodzenia klatki wirnika, obciążony prądnicą obcowzbudną, gdzie poprzez zmianę prądu wzbudzenia regulowano moment mechaniczny.

Słowa kluczowe: *uszkodzenie klatki*, *analiza czasowo-częstotliwościowa*, *prąd rozruchowy*

DOI: 10.4467/2353737XCT.15.094.3926

* M.Sc. Eng. Jarosław Tulicki, Ph.D. Eng. Maciej Sułowicz, Department of Electrical and Computer Engineering, Institute of Electromechanical Conversion, Cracow University of Technology.

1. Introduction

The primary diagnostic signal in the assessment of the cage rotor windings of the asynchronous motor, based on the current waveform of the stator, is the so-called first slip component [1, 3, 6], which was established as a result of damage to the rotor cage, which is described by the following relationship:

$$f_0 = f(1-2s) \tag{1}$$

where:

f_0 – frequency of the slip component,
f – frequency of the fundamental component,
s – slip.

In the steady-state, the basic requirement for effective evaluation of the rotor cage is to operate the motor at the rated torque, this condition it is not always possible to meet. Not what otherwise looks like the possibility of diagnosis cage rotor windings based on the signal of start-up current, where the only requirement is to have only minimal motor moment of inertia. Differentiator diagnostic component is its distinctive shape during start--up, which takes the form of an inverted 'V'. At the time of the connection of the machine to the network, the slip component has a frequency equal to that of the network with the approach of the rotor speed to half speed synchronous, diagnostic signal frequency tends to zero, to again after half the frequency of the synchronous speed achieved depends on the value of slip at steady state. This means that at a certain frequency range, the diagnostic signal reaches the same frequency twice. As an indicator of the state of the rotor cage in a steady state, utilizes the difference of network component with a sliding component in decibel scale [11, 12, 14]. Exceeding value 42–45dB, means damage to the rotor windings.

The same relationship can be used to develop the diagnostic indicator in starting the asynchronous motor based on the following equation:

$$K = 20\left(\log_{10}\frac{A_0}{A} - \log_{10}\frac{A}{A}\right) = \log_{10}\left(\frac{A_0}{A}\right)^{20}$$

$$\frac{A_0}{A} = 10^{-\frac{K}{20}} \cdot 100\% \tag{2}$$

where:

A_0 – amplitude of the slip component,
A – amplitude of the fundamental component.

From the above equation, it follows that the ratio of diagnostic signal amplitude to the amplitude of the network component at the same time boot, does not exceed 0.5–0.8%.

Therefore, in the latter section of this article, an ordinate scale was adopted, as the ratio of the maximum diagnostic signal of the input signal after filtration to the network component attributable to a moment of impulse component of a slip. It should also be noted that the number of broken cage bars was not linearly dependent on the assumed rate of damage.

2. Measuring system

The object of measurement tests was the Sg-112M asynchronous motor, loaded by a DC generator. By changing the field current of the DC generator with an auto-transformer and uncontrolled rectifier, the load torque was regulated. In the laboratory, rotors with varying degrees of asymmetry were available – symmetrical and with one, two and three broken cage bars respectively. The motor was supplied with a voltage of reduced amplitude, this was in order to simulate heavy starting conditions.

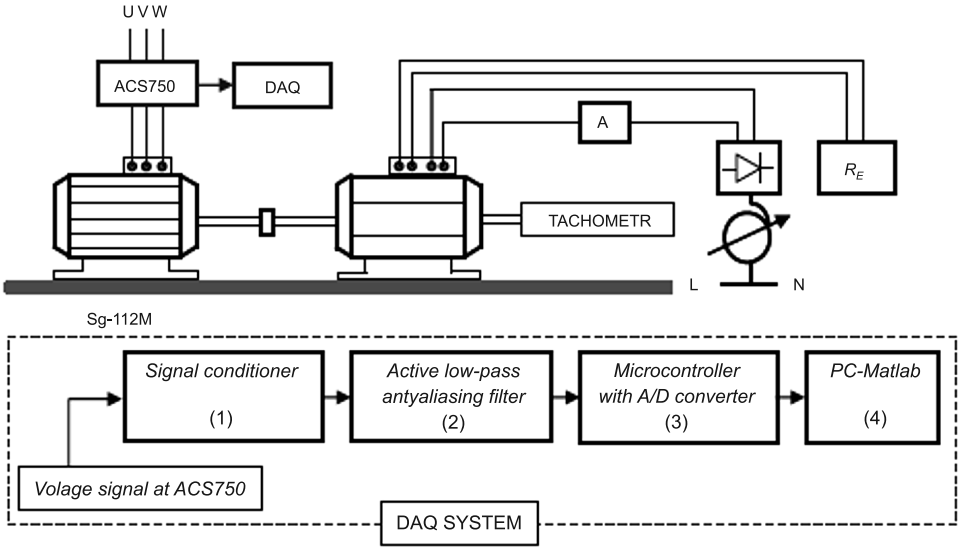

Fig. 1. Diagram of the measurement system

As a data acquisition system, a prototype measuring device was used, consisted of a pre-amplifier, operating as a voltage signal conditioner with current sensors ACS750. Next, with a third-order active filters, of Bessel characteristics, and 2 kHz cut-off frequency and border frequency 19.5 kHz, at sampling level 40 kS/s. As part of the analog-digital processing, a microcontroller with a transmitter A/D with about a 12 bit resolution connected to a PC with Matlab software via the USB port, was used.

3. Methods for diagnosing of the cage rotor damage

3.1. Low-pass filtering

The direct method of low-pass filtering [1, 7, 10, 11] is one of the primary methods of diagnosis of a rotor cage based on the signal of the stator current in transition. In engineering practice, there is a tendency to use the above-mentioned form of digital filtering of the analyzed signal. A digital low-pass filter is required to characterize with mainly small distortion in the passband and a narrow-band transition. These terms and conditions,

as a compromise meet the Chebyshev algorithm, high order and distortion in the passband at level –1dB. It is customary to use filters with a cut-off frequency in the range of 10–25 Hz, the reason for this is that the presence of interference of electrodynamic components with frequencies greater than 25 Hz, which lead to the erroneous reading of the diagnostic signal amplitude. Also within this range frequency, it can be seen that the slip component with respect to a network component, maintains a relatively constant value during start-up. Frequencies below 10 Hz read from the slip component cannot be reliable, this is due to the significant increase in the speed of the rotor with the approach of the mid-synchronous speed, thus, capturing two diagnostic pulses may not be possible.

In the following figures, example calculation results using a low-pass filter with a limiting frequency of 15 Hz are presented, and the y-axis is scaled in accordance with the reference information from point 1. In order to compare the results of analyzes for the various methods of the time-frequency filter, in the rest of the work, all waveforms are referenced to the above-mentioned frequencies. It is also worth mentioning that the described electrodynamic phenomena, accompanying diagnostic signal extraction, subject to the same change in time, regardless of the type of filter used and will not be cited in the rest of the article.

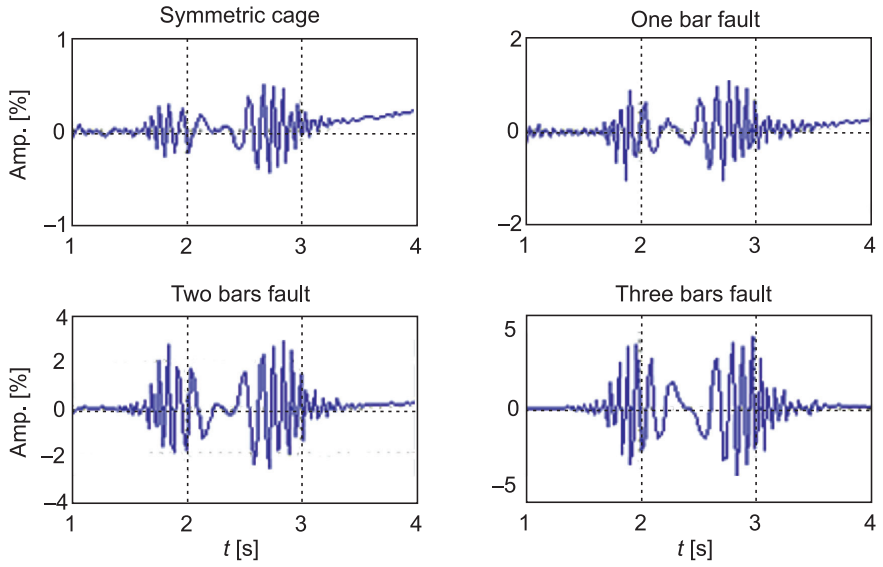

Fig. 2. Low Pass filtering effect

3.2. Short term Fourier transform

Short-Time Fourier Transform [5, 7, 13, 16] is the simplest method of non-stationary signal analysis and is based on dividing the analyzed signal at equal intervals, then in each of the separated portion of the waveform, Fourier transform is carried out. The ultimate result of the STFT is the sum of the modules of the results obtained in each of the compartments. The essential negative effect, on the above-described transformation, is the phenomenon

of time-frequency uncertainty, i.e. using short intervals, increase the resolution in the frequency domain is obtained, for long time periods, the results have good resolution in the timeline. In practice, it is preferred to use described transformation with i.e. 'overlapping time windows', where part of the signal is analyzed in the actual window originated from the compartments immediately preceding and following. The method of overlapping windows consequently allows reducing the negative effects of STFT consisting of covering the harmonics with similar frequencies.

Customarily, the result of the application of time-frequency analysis presented in the hardly readable multispectrum form. Therefore, in the results of signal filtering below, the multispectrum is divided into a 2D map of energy in time and frequency domain. In a decibel scale in relation to the network component and the course of the amplitude of the observed frequency in the time domain. The axis ordinate is scaled as the ratio of the observed frequency to the mains frequency, in a time window, in which the maximum diagnostic signal occurred. Examples of the results of calculations, for all transforms, damage was limited to two bars of the rotor cage.

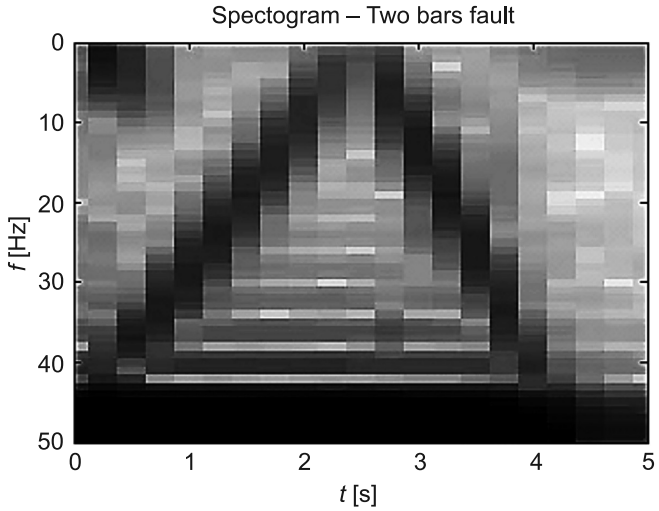

Fig. 3. Spectrogram – Two bars fault

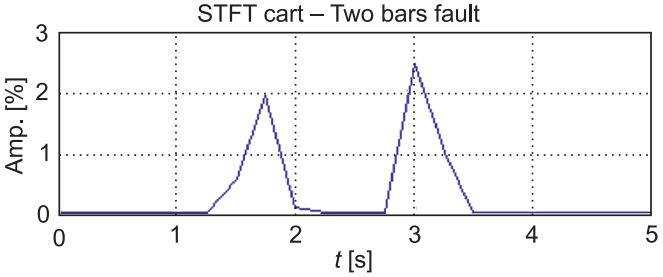

Fig. 4. STFT chart – Two bars fault

3.3. Gabor transform

Gabor transform [7, 13, 16] is a special type of short-time Fourier transform, as STFT is based on the division of analyzed signal, on local compartments by a time window. The difference between the STFT and the classical Gabor transformation, consists of as the time window, Gaussian weighting function. Characteristic feature Gauss function is similarity to the overall function of wavelet, except that the scale factor has a constant value throughout the analysis. In addition, the uncertainty principle, at any desired time interval, always reaches a local minimum, and as a consequence, makes the maximum concentration of energy in the time and frequency domain. The axis ordinate, chart the Gabor transform for the observed frequency, is scaled in the same way as in the case of the transform STFT.

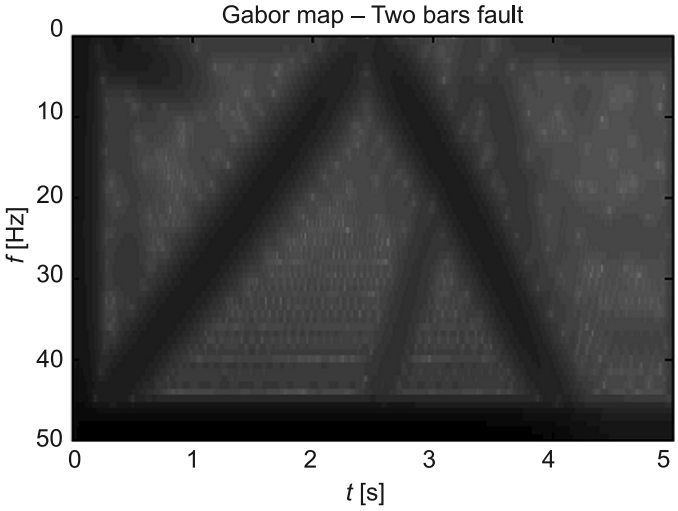

Fig. 5. Gabor map – Two bars fault

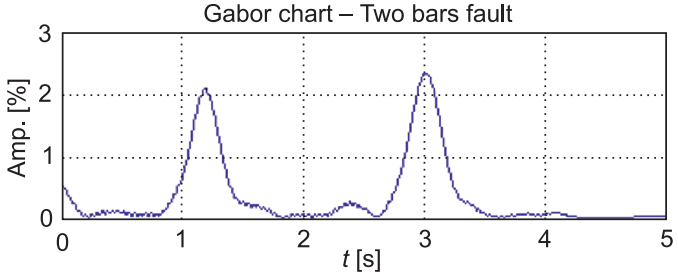

Fig. 6. Gabor chart – Two bars fault

3.4. Wavelet transform

Wavelet Transform [1, 5–7, 10, 13, 16] is a kind of time-frequency transformation of non-stationary signals, involving the matching (comparison) of the selected wavelet function

with a specific carrier frequency signal waveform at a given level of decomposition. In the technical diagnostics squirrel-cage induction machines, uses two types of described transformations, respectively as a continuous form (CWT) and discrete form (DWT). The distinguishing feature of CWT is the so-called scale parameter that determines the quality of the results of calculations in the time and frequency, i.e. with increasing the value of the coefficient scale, a better fit of wavelets in the frequency domain is obtained, in the opposite case, in the time domain. Scalogram is a two-dimensional map of highlighted signal energy values for the coordinate system scale-time, wherein, in the event of a perfect fit wavelet to signal, the scale is exactly the inverse of the frequency. In the case of quantized signals, the scale factor can be a description of the following formula:

$$a = \frac{f_s \cdot f_w}{f_0} \tag{3}$$

where:

a – scale factor,
f_s – sampling frequency,
f_w – wavelet frequency,
f_o – observed frequency.

Formula (3) shows that the sampling frequency 40 kS/s, the network frequency corresponds to the value of scale equal to $a = 800$, the frequency of 15 Hz corresponds to the scale of the values of $a = 2800$. This fact is used to scale the y-axis (Fig. 6), dividing the observed frequency scale corresponding to the scale of the network frequency. The main disadvantage of CWT is the phenomenon of redundancy arising from the need to adopt a multivalent series of scale factor to best fit the wavelet function to the processed signal. Eliminating the phenomenon of redundancy, is obtained by applying a discrete form WT, thus dispensed with trying to get the exact result of the calculation. Some substitute the scale factor in discrete transform WT, is finite decomposition of the analyzed signal, consisting in dividing the research signal in the frequency domain, the number of compartments is defined as the level of decomposition, according to the formula:

$$n = \log_2 \frac{f_s}{f_o} - 1 \tag{4}$$

where:

n – level of decomposition.

In each of the compartments, a low pass filter and a high pass filter should be performed, called respectively detail and approximation. Formula (4) shows that the sampling frequency 40 kS/s, observed frequency corresponds to a value of the decomposition level $n = 10$. In the case of using CWT, Morlet wavelet was used as a function of analyzing, and for the application of a DWT, DB45 wavelet was used as a function of analyzing.

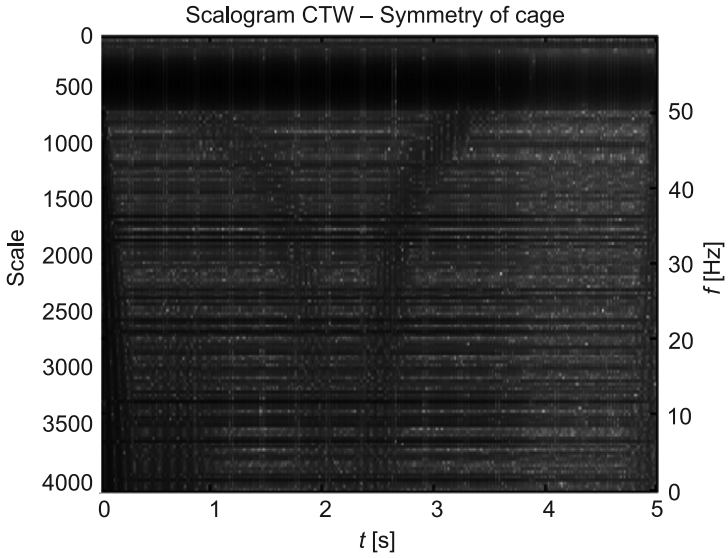

Fig. 7. Scalogram CWT – symmetry of cage

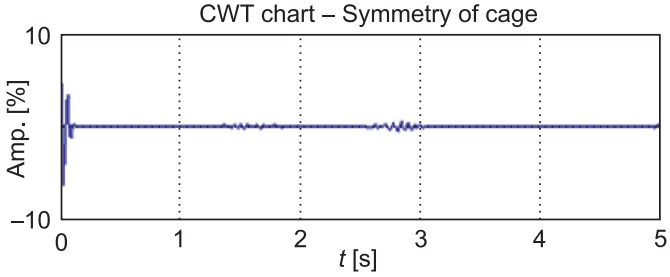

Fig. 8. CWT chart – symmetry of cage

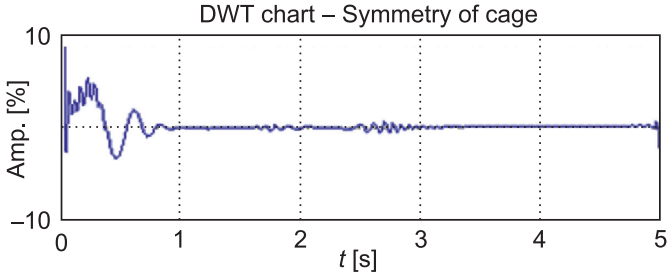

Fig. 9. DWT chart – symmetry of cage

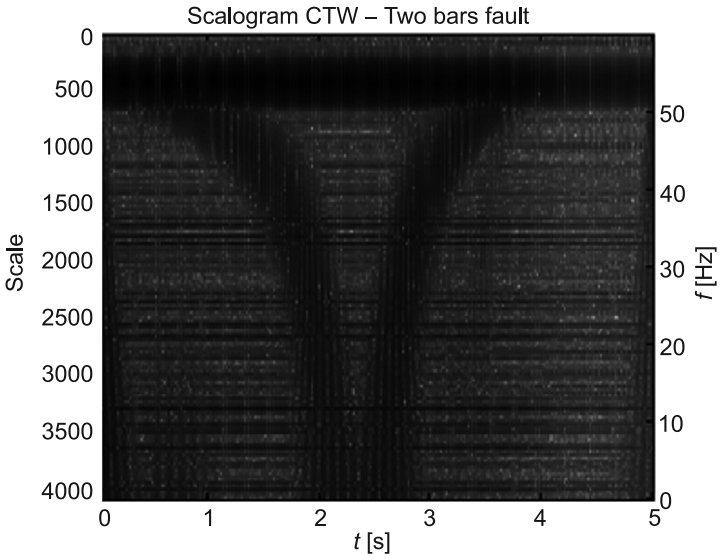

Fig. 10. Scalogram CWT – Two bars fault

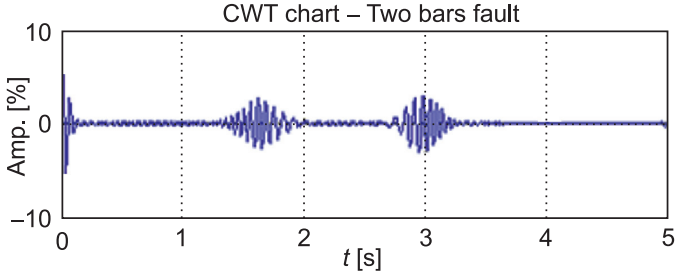

Fig. 11. CWT chart – Two bars fault

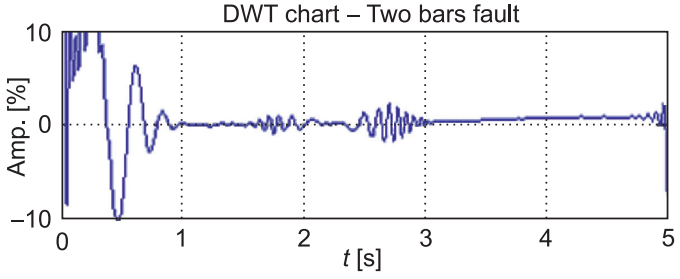

Fig. 12. DWT chart – Two bars fault

3.5. Wigner–Ville transform

The Wigner–Ville transform [15, 16], is characterized by best total resolution in the time and frequency of the above mentioned transformations. The uniqueness of the described transform, involves the use of the analyzed signal, as a function of the time window. It follows that any other time-frequency conversion can be obtained by averaging the transform WV. Although transform described in an ideal way, ideally maps the modulated signals linearly, in the case of nonlinear modulation, the result of the calculation is the sum of the squares of the components of the test signal and an additional factor, complementary solution of the parabolic equation. Commonly an additional member of the aforementioned equation, called parasitic interference, influencing the readability of the instantaneous spectrum.

In order to reduce interference, in practice, so-called pseudo transformation WV is used, which is a compromise between high resolution and decrease the effect of frequency signals generated by the transform itself. As the pseudo transform WV, effectively performed out using FFT, the axis ordinate, is scaled in the same way as in the case of STFT and Gabor transform.

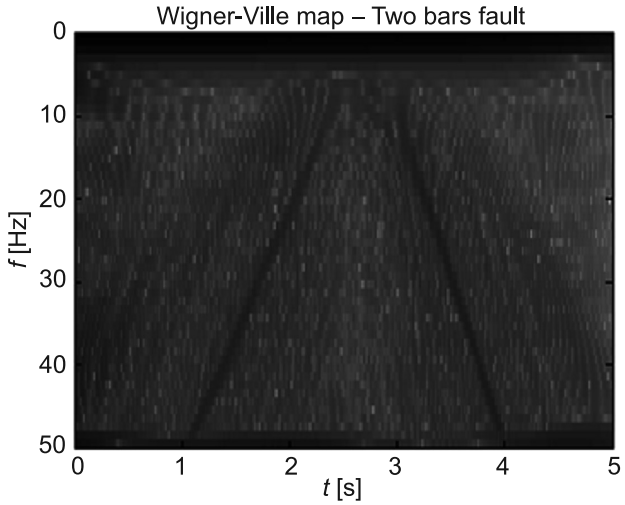

Fig. 13. Wigner–Ville map – Two bars fault

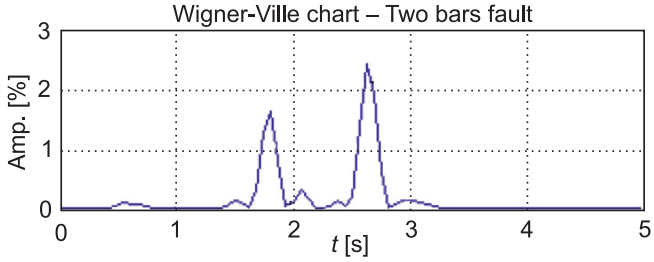

Fig. 14. Wigner–Ville chart – Two bars fault

4. Conclusions

In the presented results, over estimate of condition asynchronous motor winding, on the basis of the stator current waveform in transition, it should be noted that the presented diagnostic signal extraction method, have the advantages of registering only the starting current of one phase of the stator and do not require the measurement of speed. The measurement of speed, for the start of the ongoing over 1.5 s, should be considered as optimal, because of the distinctive mark of the slip component in the band 0–50 Hz. Although the object of the research was an asynchronous motor, it should be noted that the presented methods of analysis can be successfully used to diagnose the winding synchronous motor starter, due to the convergence of electrical phenomena resulting from damage to the rotor. Additionally, irrespective of the form of time-frequency analysis, damage indicator values obtained, did not show significant differences for the same type of defect of the rotor, which directly binds to form the diagnostic signal frequency changes over time, which can be considered as a modulated linearly. Significant differences in quality are noticeable only in the energy distribution of the time-frequency map, readability of which increases with the advancement numerical transform used.

In conclusion, analysis of non-stationary pattern of start-up current, allows for some assessment of the state of the rotor cage without any knowledge of the history of the motor's operation and its design parameters. A serious disadvantage is the limited ability to conduct this type of diagnosis at the start of short duration, where the separation of the time interval in which it can be assumed as a constant rotational speed, is considered to be problematic. The way out of this situation can be used as a pre-filter processing of the measurement signal, adaptive algorithm – this is the subject of ongoing work by the authors of this article.

References

[1] Antonino-Daviu J.A., Rusek J., Riera-Guasp M., Roger-Folch J., *Traditional Versus Wavelets Low-Pass Filtering in Diagnosing of Cage Asymmetries in Induction Machines*, Elektrotechnika i Elektronika, 2006, t. 25, z. 2, 119-123.

[2] Dybowski P., Rams W., Rusek J., *Problemy praktycznej diagnostyki maszyn indukcyjnych w przemyśle*, Zeszyty Problemowe – Maszyny Elektryczne, 2007, nr 76, BOBRME Komel, 109-113.

[3] Dziechciarz A., Sułowicz M., *Zastosowanie analizy falkowej do diagnozowania uszkodzeń w silniku indukcyjnym podczas pracy przy zmiennym obciążeniu*, Czasopismo Techniczne, Seria Elektrotechnika, 1-E/2012, 49-64.

[4] Innes A.G., *The Detection of Broken Rotor Bars in Variable Speed Induction Motor Drives*, Dissertation, University of Tasmania, 1999.

[5] Kowalski C.T., Kanior W., *Ocena skuteczności analiz FFT, STFT i falkowej w wykrywaniu uszkodzeń wirnika silnika indukcyjnego*, Prace Naukowe Instytutu Maszyn, Napędów i Pomiarów Elektrycznych Politechniki Wrocławskiej, nr 27, 2007.

[6] Pons-Llinares J., Climente-Alarcón V., Puche-Panadero R., Antonino-Daviu J.A., *Bar breakage detection on Squirrel Cage Induction Motors via Transient Motor Current Signal Analysis based on the Wavelet Transform. A Review*, Departamento de Ingeniería Eléctrica Universidad Politécnica de Valencia.

[7] Rad M., *Diagnostyka wirnika maszyn indukcyjnych z wykorzystaniem analizy falkowej i układów uczących się*, rozprawa doktorska, Akademia Górniczo-Hutnicza im. Stanisława Staszica w Krakowie, Kraków 2009.
[8] Skwarczyński J., Tertil Z., *Maszyny elektryczne*, Wydawnictwo Akademii Górniczo-Hutniczej im. Stanisława Staszica w Krakowie, Kraków 1989.
[9] Sobolewski A., *Zastosowanie klasyfikatorów neuronowych w diagnostyce uszkodzeń wirnika silnika indukcyjnego*, autoreferat rozprawy doktorskiej, Białystok 2008.
[10] Sułowicz M., Petryna J., Weinreb K., Guziec K., *Porównawcze pomiary defektów klatek rozruchowych silników indukcyjnych pod kątem wykorzystania w diagnostyce*, Zeszyty Problemowe – Maszyny Elektryczne, nr 99, 2013, BOBRME Komel, 77-83.
[11] Swędrowski L., *Pomiary w diagnostyce silników indukcyjnych klatkowych*, Wydawnictwo Politechniki Gdańskiej, Gdańsk 2013.
[12] Szymaniec S., *Pomiary i analiza sygnałów dla potrzeb diagnostyki*, Zeszyty Problemowe – Maszyny Elektryczne, nr 94, 2012, BOBRME Komel, 93-98.
[13] Tumański S., *Technika Pomiarowa*, Wydawnictwa Naukowo-Techniczne, Warszawa 2007.
[14] Yasser G., *Diagnosis and Fault Detection in Electrical Machines and Drives Based on Advance Signal Processing*, Dissertation, Department of Electrical, Electronic, and Information Engineering "Guglielmo Marconi", 2014.
[15] Zając M., *Monitorowanie układu elektromechanicznego metodą analizy czasowo-częstotliwościowej*, Czasopismo Techniczne, Seria Automatyka, 1-AC/2012, 157-169.
[16] Zieliński T.J., *Cyfrowe przetwarzanie sygnałów. Od teorii do zastosowań*, Wydawnictwa Komunikacji i Łączności, Warszawa 2007.

TECHNICAL TRANSACTIONS | **CZASOPISMO TECHNICZNE**
ELECTRICAL ENGINEERING | ELEKTROTECHNIKA
2-E/2015

WOJCIECH WROŃSKI*, MACIEJ SUŁOWICZ*, ARKADIUSZ DZIECHCIARZ**

DYNAMIC AND STATIC ECCENTRICITY DETECTION IN INDUCTION MOTORS IN TRANSIENT STATES

DIAGNOSTYKA EKSCENTRYCZNOŚCI DYNAMICZNEJ I STATYCZNEJ W SILNIKU INDUKCYJNYM W PRZEJŚCIOWYM STANIE PRACY

Abstract

The following paper presents possibilities for the application of selected time-frequency analysis methods in the fault detection of cage induction machines in transient states. The starting phase current of the machine was chosen as a diagnostic signal. Selected faults were eccentricities – static and dynamic. In order to increase the selectivity of the obtained signal transformations, a notch filter was used to remove the base harmonic of the phase current. Two approaches of fault detection were compared. In the first approach, the characteristic feature of fault was extracted using DWT analysis. Next, TMCSA methodology was applied in which characteristic harmonics related to faults were shown on a time-frequency plane. In this case, applied methods were a Gabor transformation, STFT, CWT and Wigner–Ville's transformation. In the analysis, a phase current signal approximated by DWT was used. DWT approximation was applied to filter higher harmonics which improves the resolution of the obtained transformations.

Keywords: *cage induction motor fault detection*, *TMCSA*, *time-frequency methods*, *Notch filter*, *transient phase current*, *dynamic and static eccentricity*, *voltage asymmetry*

Streszczenie

W artykule przedstawiono możliwości zastosowania wybranych metod analizy czasowo-częstotliwościowej do diagnostyki uszkodzeń silników indukcyjnych klatkowych w przejściowych stanach pracy. Jako sygnał diagnostyczny wybrano prąd fazowy silnika podczas rozruchu. Wybranymi przypadkami uszkodzeń silnika są ekscentryczność statyczna i dynamiczna. W celu poprawienia selektywności otrzymanych transformat wykorzystano filtr Notcha do usunięcia harmonicznej podstawowej prądu. Porównano dwa podejścia diagnostyczne wykrywania uszkodzeń. Pierwsze za pomocą analiz wielorozdzielczych z użyciem DWT, polegające na wyróżnieniu charakterystycznego wzorca związanego z uszkodzeniem. Drugie podejście polegało na zastosowaniu metodologii TMCSA, czyli ekstrakcji charakterystycznych harmonicznych związanych z uszkodzeniami zależnych od poślizgu na płaszczyznach TF. W tym wypadku rozważanymi metodami analizy były transformacje Gabora, STFT, Wignera–Ville'a oraz CWT. Do tych analiz został wykorzystany sygnał prądu aproksymowany z użyciem DWT, w celu odfiltrowania widma czasowo-częstotliwościowego o wyższych częstotliwościach, aby poprawić rozdzielczość otrzymywanych transformat.

Słowa kluczowe: *silnik indukcyjny klatkowy*, *diagnostyka uszkodzeń*, *TMCSA*, *metody czasowo-częstotliwościowe*, *filtr notch*, *prąd fazowy w stanie przejściowym*, *ekscentryczność statyczna i dynamiczna*, *niesymetria napięć*

DOI: 10.4467/2353737XCT.15.095.3927

* M.Sc. Eng. Wojciech Wroński, Ph.D. Eng. Maciej Sułowicz, Department of Electrical and Computer Engineering, Institute of Electromechanical Conversion, Cracow University of Technology.

** M.Sc. Eng. Arkadiusz Dziechciarz, Technical University of Cluj-Napoca, Faculty of Electrical Engineering.

1. Introduction

This paper presents possibilities for the application of selected time-frequency methods of signal analysis in fault detection of cage induction machines in transient states. Fault diagnosis of induction motors using Fourier transformation or FFT algorithms, can be used only in steady states because it is a frequency analysis method of signals. Because of that, this method is insufficient in the case of transient states when diagnostic signals related to faults vary in time. Applying time-frequency methods of signal analysis allows for analyzing time changing diagnostic signals related to faults of induction motors in transient states.

In this paper, methodology of static and dynamic eccentricity detection in transient states and with supply voltage asymmetry will be presented. Supply voltage asymmetry will be considered as distortion in eccentricity detection which has not yet been presented in literature. Two approaches of fault detection will be compared – using multi-resolution analysis with DWT and analysis on TF planes using Gabor transform, STFT, CWT and Wigner–Ville's transform which use TMCSA (transient motor current signature analysis) methodology that is the extraction of characteristic slip dependent harmonics related to faults. The selected diagnostic signal is a stator phase start-up current. In order to improve selectivity of the obtained transforms, a notch filter was used to remove the base harmonic of the current of frequency equal to that of the supply voltage.

2. Measurement system and data capturing

For cage induction machine diagnosis using selected methodology, it is necessary to collect diagnostic signals of phase current and rotational speed. A waveform of rotational speed will be used to find the actual harmonics related to faults in the case of analysis on a TF plane – this makes it easier to localize these harmonics. The examined cage induction motor Sg112-M4 was supplied directly from the network and is connected with a DC generator. The schematics of the system for fault detection is shown in Fig. 1.

Parameters of examined motor are: $P_N = 4$ kW; $U_N = 380$ V; $I_N = 2.867$ A; $\cos\varphi_N = 0.84$; $n_N = 1445$ rpm; Number of rotor bars – $N_r = 28$.

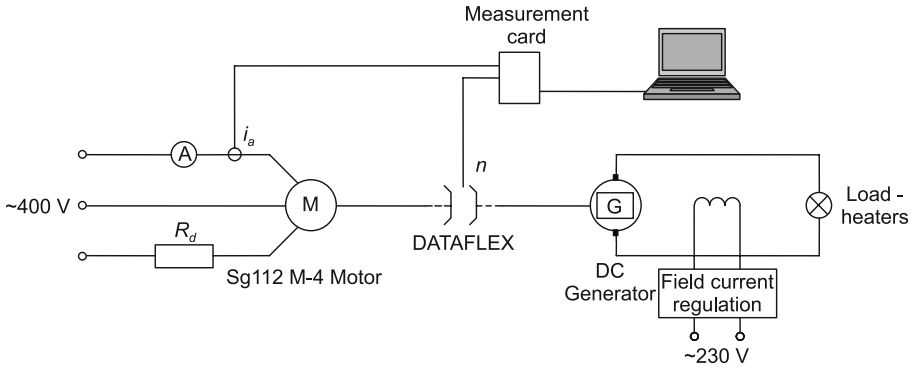

Fig. 1. System of cage induction motor fault detection

The dynamic eccentricity of the motor is realized by using a special replaceable rotor with steel sheets non-centrically placed on the shaft. Static eccentricity is realized by specially prepared bearing shields with a shifted center of symmetry axis.

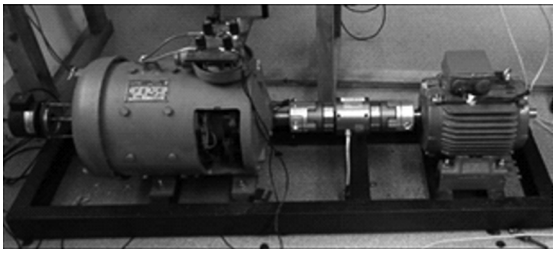

Fig. 2. Laboratory test bench

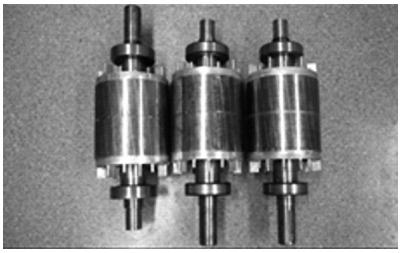

Fig. 3. Set of exchangeable rotos

Voltage asymmetry was realized by the connecting of additional resistor R_d to one phase of the stator. For the collecting of the current signal, current transducer LEM HY 15 was used, and for rotational speed signal collecting, DATAFLEX® 22/5 transducer was used.

The following diagnostic data were collected for nominal load ($I \cong 3$ A) of the machine:

- healthy motor (i_sym),
- dynamic eccentricity (i_de),
- static eccentricity (i_se),
- static eccentricity and supply voltage asymmetry (i_senn).

3. Selected methods of signal analysis

In the case of non-stationary signals, their characteristic features vary in time. In this case, Fourier transform proves to be insufficient because the spectra of those signals vary in time and the Fourier analysis gives averaged results (in the analysis window). The solution for this inconvenience was proposed by Gabor as a short time Fourier transform STFT and next introduction and development of wavelet transform methods [4].

Frequency analysis of non-stationary signals should be performed using a base of decomposition contained of selective functions in time and frequency domain. The signal's decomposition is made by shifting the analyzing function in the time domain and modulation in the frequency domain. Impulse waveforms are used for this because in the time domain, it decides the time range of the analysis and in the frequency domain, its spectrum decides the frequency range of the analysis [2].

Because each of the impulse waveforms covers a specified time and frequency range, some amount of signal for a certain time-frequency cell is selected. Areas of those cells should not intersect with each other, and when summed up, should be equal to the time-frequency plane area. Two basic strategies for time-frequency plane division and corresponding chessboards are presented in Figure 4 [1].

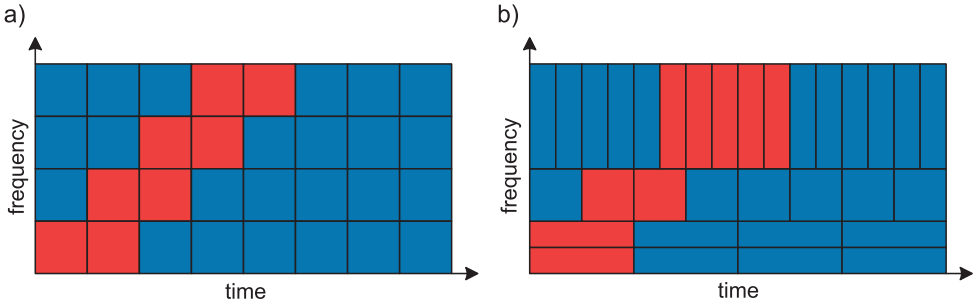

Fig. 4. Base chessboards of time-frequency decomposition of signals: Gabor's transform–Short Time Fourier Transform (a);wavelet transform (b). Red shows non-zero coefficients of the example time-frequency decomposition of the signal with the frequency changing linearly [1]

3.1. Gabor's transform

According to [1], in the time-frequency Gabor transform, the analyzed signal is introduced as a sum of the base functions which are derived from the prototype function i.e. the Gaussian window, by shifting it in the time and frequency domain. The TF atom of the prototype function is localized in the time-frequency space around point ($t = 0, f = 0$) and is of a random shape. As a result of the prototype function shifting, we obtain the TF decomposition structure analogous to that presented in Fig. 4a). In Gabor's decomposition, the area and orientation of the TF atoms are constant.

The time-frequency Gabor decomposition of the continuous signalis defined as [1]:

$$x(t) = \sum_{m,n=-\infty}^{+\infty} c_{m,n} g_{m,n}(t) \tag{1}$$

where $g_{m,n}(t)$ means time shifted by $m \cdot \Delta t$ and frequency shifted by $n \cdot \Delta f$ any base function (prototype) $g(t)$ of energy equal to one (Δt, Δf – specified translation in time and frequency domain) [1]:

$$g_{m,n}(t) = g(t - m \cdot \Delta t) e^{j2\pi(n \cdot \Delta f)t}, \quad \Delta t \cdot \Delta f \leq 1 \tag{2}$$

and $c_{m,n}$ are decomposition coefficients, calculated from equation [1]:

$$c_{m,n} = \int_{-\infty}^{+\infty} x(t) \gamma^*_{m,n}(t)\, dt, \; \gamma_{m,n}(t) = \gamma(t - m \cdot \Delta t) e^{j2\pi(n \cdot \Delta f)t} \tag{3}$$

In equation (3), $\gamma(t)$ is a prototype function (window) of analysis which has to be biorthogonal to the synthesis prototype function (window g(t) (2). Because the base function $g(t)$ should have a large energy concentration both in the time and frequency domain, the most commonly used function is a Gaussian window. Equation (3) is an analysis equation (signal $x(t) \rightarrow$ decomposition coefficients $c_{m,n}$), and (1) − synthesis equation (decomposition coefficient $_{cm,n} \rightarrow$ signal $x(t)$). Because we use the same window g(t) area and shape of the TF atom related to functions $g_{m,n}(t)$ are constant. As a result of the window translation in the time and frequency domain, we obtain the chessboard of decomposition presented in Fig. 4a) [1].

The time-frequency Gabor's representation of continuous signal $x(t)$ is defined as [1]:

$$S_x(mT, nF) = \left| c_{m,n} \right|^2 \tag{4}$$

3.2. STFT transform

In [13], the application of STFT(short time Fourier transformation) was described as a solution to the problem of localization of the feature occurring in the diagnostic signal in time. This transform, apart from frequency analysis, allows localizing the characteristic frequency components occurring in time, using time windows.

According to [1],the continuous, short time Fourier transform STFT can be considered as non-discretized in time and frequency domain Gabor transform. High redundancy is typical for this transform. During analysis and synthesis, the same window is used.

The definition of this transform in time and frequency domain [1]:

$$\mathrm{STFT}_x^T(t, f) = \int_{-\infty}^{+\infty} x(\tau)\gamma^*(\tau - t)\, e^{-j2\pi f\tau} d\tau \tag{5}$$

The spectrogram related to the STFT is defined as[1]:

$$S_x^{\mathrm{SPEC}}(t, f) = \left| \mathrm{STFT}_x(t, f) \right|^2 \tag{6}$$

In [2] it is given, that the spectrogram is usually obtained using one of the basic windows: rectangular; Hamming; Hanning; and others.

In the STFT wide window, $\gamma(t)$ increases the resolution in the frequency domain and decreases the resolution in the time domain. The narrow window does exactly the opposite. It is impossible to obtain a high resolution in both domains simultaneously [1].

3.3. Wigner–Ville's transform

In the transforms of Gabor and STFT presented so far, the problem of a proper size window selection forced to compromise between the precision of the analysis and the analysis of the entire spectrum of components contained in the signal. This problem is a basic drawback of time-frequency analysis until the window of a varying length was used. An attempt of adapting the selection of the window size for the local features of the signals, is made in Wigner–Ville's transform. In this transform, the signal also plays the role of the window [2].

The time-frequency transform of the Wigner–Ville (WV) perfectly shows the linear change of frequency in the TF space. The transform of the Wigner–Ville is defined as [1]:

$$\mathrm{WV}_x(t, f) = \int_{-\infty}^{+\infty} x\left(t + \frac{\tau}{2}\right) x^*\left(t - \frac{\tau}{2}\right) e^{-j2\pi f\tau} d\tau \tag{7}$$

where $x(t)$ is a real signal (Wigner's definition) or analytical (Ville's definition). The analytical signal (8), related to the real signal $x(t)$, is a complex signal whose real part is signal $x(t)$ and the imaginary part is a result of the Hilbert transform of $x(t)$ of [1, 5]:

$$z(t) = x(t) + jH[x(t)] \tag{8}$$

The transform of Wigner–Ville solves the problem of the window size selection for analysis. All components contained in the signal are analyzed, each of them is localized with optimal time precision as precisely as is possible due to Heisenberg's uncertainty theorem [2]. In [4] it is proved that the resolution of the WV transform is twice as large as that of the STFT.

The basic drawback of the WV transform is the interference in the obtained time--frequency spectral matrices.

3.4. Wavelet transform

The wavelet transform is one of the most popular and most dynamically developed methods of time-frequency analysis of non-stationary signals and is a method with constant percentage bandwidth $\Delta f/f_0 = \text{const}$ [1].

The development of this transform is a result of the increased demand for time-frequency analysis of variable window size which could provide high frequency resolution for low-frequency components and accurate time localization for high-frequency components of transient signals [4].

3.4.1. Continuous wavelet transform CWT

Continuous wavelet transform of signal $x(t)$ is defined in the time and frequency domain in the following way [1]:

$$\mathrm{CWT}_x^T(t,a) = \frac{1}{\sqrt{|a|}} \int_{-\infty}^{+\infty} x(\tau)\gamma^*\left(\frac{\tau - t}{a}\right) d\tau \tag{9}$$

The division by $|a|$ keeps the wavelets' energy constant after rescaling. The function $\gamma(t)$ is an analyzing function [1].

Scalogram, related to the wavelet transform is defined in the following way [1]:

$$S_x^{\mathrm{SCAL}}(t,a) = \left|\mathrm{CWT}_x(t,a)\right|^2 \tag{10}$$

In [3], the problem of interpretation scale-frequency relation, concerning the sampling frequency, was introduced. The dependence describing the central frequency of the base wavelet $\gamma(t)$ is of the following form [3]:

$$\omega_0 = \frac{1}{2\pi} \int_0^{\infty} \omega \left|\Phi(\omega)\right|^2 d\omega \tag{11}$$

where:

$\Phi(\omega)$ – Fourier transform of $\varphi(t)$.

Furthermore, the bandwidth of the base wavelet, which can be related to the Heisenberg cube in the direction of frequency axis, is of the form [3]:

$$B_0 = \omega_{\max} - \omega_{\min} \tag{12}$$

For small scale coefficients, the wavelet transform extracts the high frequency components of the analyzed signal and for larger scale coefficients, the effect is exactly the opposite. While the scale coefficient increases, the frequency bandwidth decreases, this

means that the resolution in the frequency domain is greater. The central frequency ω_0 and bandwidth B_0 depend on the chosen analyzing wavelet [3].

3.4.2. Discrete wavelet transform DWT

The continuous wavelet transform gives a lot of redundant information. This is why its parameters such as time t and scale coefficient a are sampled obtaining the coefficient of the wavelet series analogically to the Fourier series [2, 4].The DWT has a constant TF atom and realizes the time-frequency signal decomposition scheme presented in Fig. 4b) [2].

The discrete wavelet transform is strictly related to the multi-resolution signal analysis [2]. Example of three level discrete wavelet analysis with wavelet filters is presented in Fig. 5,where h_d is a low-pass filter, corresponding to scaling function, h_g is a high-pass filter corresponding to the wavelet function [4]. Since the calculation of wavelet coefficients $c_{m,n}$ and $d_{m,n}$ from their definition is very difficult, in practice, we use filters related to the wavelet and scaling functions [2, 4].

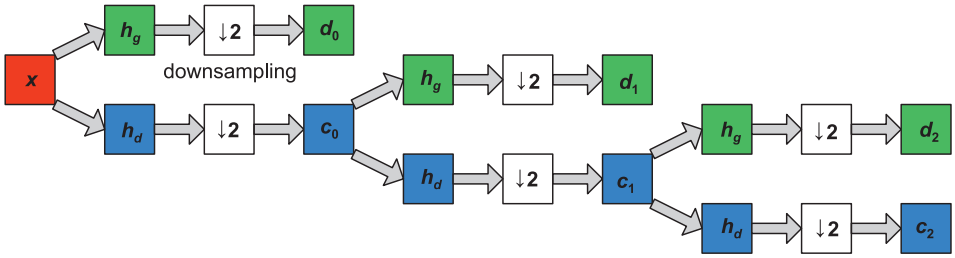

Fig. 5. Three level discrete wavelet analysis using wavelet filters [4]

DWT allows writing signal $x(t)$ as a sum of approximation a_n and details d_j [10]:

$$x(t) = a_n + d_n + \cdots + d_1 \tag{13}$$

where [10]:

- n – level of decomposition,
- a_n – approximation of signal on level n,
- d_j – detail of signal on level j.

Equation(13) realizes Mallat's algorithm which shows that each wavelet signal is related to a specified frequency bandwidth. If F_s (in samples per second) is sampling the frequency of the analyzed signal $x(t)$, then the detail of signal d_j contains information concerning the signal's components of frequencies from interval [8, 10]:

$$f(d_j) \in [2^{-(j+1)} F_s,\ 2^{-j} F_s]\ \text{Hz} \tag{14a}$$

approximation a_n contains low frequency components that belong to interval [8, 10]:

$$f(a_n) \in [0,\ 2^{-(n+1)} F_s]\ \text{Hz} \tag{14b}$$

The DWT performs filtration process shown in Fig. 6.

Filtration is not ideal, which causes the adjacent bandwidths to interfere. This may become an issue since some frequency components (base harmonic) might be partially

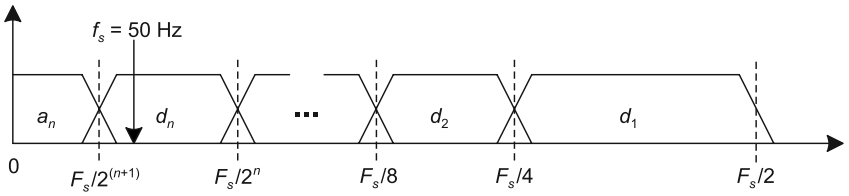

Fig. 6. Filtration process performed by DWT [8, 10]

filtered in an adjacent bandwidth covering other frequency components in this bandwidth [10].

4. Methodology of induction machines' diagnosis using time-frequency analysis methods

4.1. Application of induction motors' diagnosis methods in transient state based on TMCSA

The presented methodology of induction motors fault detection is based on the TMCSA method.

In recent years, methods of electrical machine diagnostics in transient states became of more interest. A variety of methods based on transient stator current analysis were proposed. Those methods are known as TMCSA (transient motor current signature analysis), and can be described as a generalization of traditional MCSA methods applied for diagnostics in steady states. The well-known MCSA methods are based on stator current's Fourier spectrum analysis in steady states. Theoretical experiments prove that different types of faults in electrical machines generate or amplify some frequency components in stator currents related to particular faults of the machine [7].

TMCSA uses methods of non-stationary signals analysis. Signal forming can be performed with wavelet analysis or through using filters. Spectral analysis is performed on the time-frequency plane using linear transforms like STFT and wavelet transform or square transform such as Wigner–Ville's transform [11].

In concluding, TMCSA is a technology which allows diagnosing the motor by analyzing the current during rotational speed change. Diagnostics with TMCSA are, in general, based upon the extraction of typical components on the TF plane related to particular types of faults. These methods replace traditional methods based of the Fourier transform which are not dedicated for the analysis of signals in transient states [6].

The presented method of diagnosis was based on performing the following analyses:

– First, the diagnostic signal of stator phase currentwas processed by notch filtering order to filter the base harmonic of the frequency equal to that of supply voltage.

Next, for such a prepared signal, two approaches of fault detection were compared:

– Multi-resolution signal analysis was performed with DWT in order to extract typical components related to faults.

– Time-frequency analyses on the TF plane was performed using various transforms – Gabor's, STFT, Wigner–Ville' sand CWT, in order to extract characteristic harmonics related to faults. Approximation signal obtained from DWT will be used for analysis.

4.2. Application of notch filter

In the presented approach, a notch filter was used for the initial filtration of the measured current signal, to increase the selectivity of the transforms and better distinguishing of harmonics related to faults, by removing the base harmonic of the frequency equal to that of supply voltage.

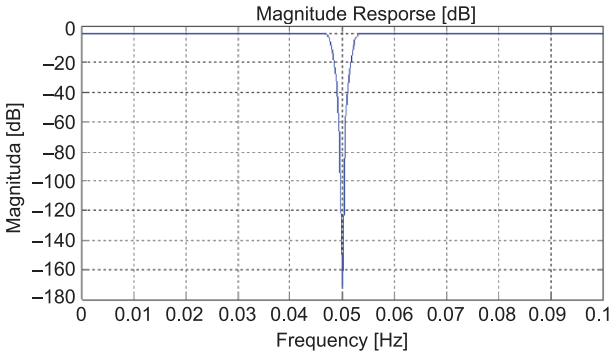

Fig. 7. Frequency characteristic of designed Notch filter

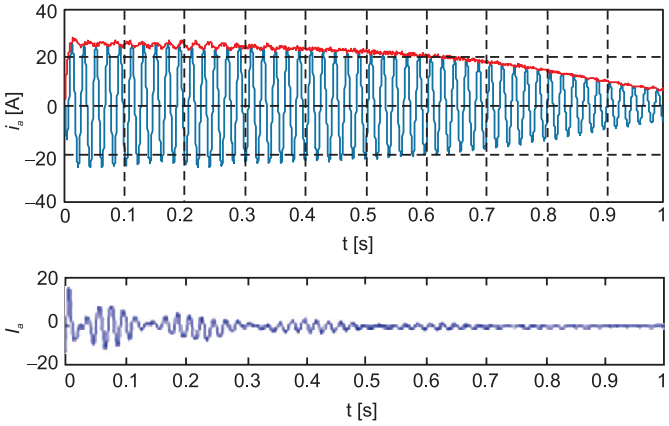

Fig. 8. Current waveform i_sym (top) and after filtration with the notch filter (bottom)

The notch filter, which is of IIR type, designed for certain frequency, removes that harmonic of signal. Input parameters of this filter are cut-off frequency$F0$, and frequency bandwidth 3-dB BW or quality factor Q. For these specifications, by increasing filter order N, one can obtain a filter closer to the ideal [14].

For the applied notch filter, in order to remove the base harmonic, the following parameters were chosen:

– $N = 10$ – filter order.
– $F0 = 50$ Hz – cutoff frequency,
– $BW = 5$ Hz – bandwidth 3-dB,
– $Q = F0/BW$ – obtained quality factor.

In the picture below, there is presented frequency characteristic of the designed notch filter. Obtained attenuation of base harmonic reaches 170 dB.

In the picture below, there is presented an example waveform of the motor's current for healthy motor, and with filtered base harmonic using the designed notch filter. It is not an ideal filtration and base harmonic is partially present in analyzed signal.

4.3. DWT based diagnostic approach

A diagnostic approach based on the DWT will be used in the case of a multi-resolution analysis perform. In [8] a general scheme of a DWT based method for eccentricity detection based on transient current analysis was presented. It allows for extraction in the transient state characteristic harmonics that are related to fault occurrence. These typical harmonics are reliable for fault detection because it is very less likely that a specific waveform of a particular harmonic in transient state was caused by a different phenomenon unrelated to the fault. Moreover, those harmonics allow distinguishing particular faults based on waveforms contained in wavelet signals.

In this paper, this approach is used to detect previously mentioned faults. In Figure 9, a scheme of DWT based methodology for fault detection in the induction machine is presented [8].

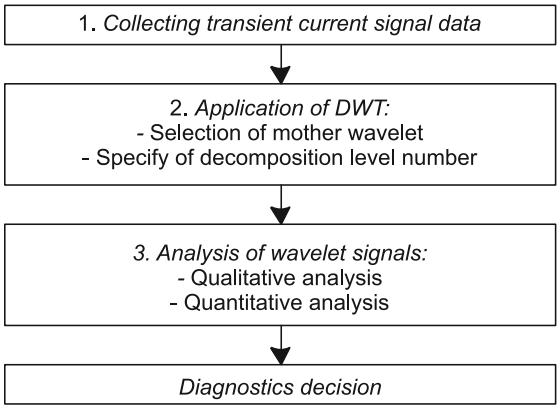

Fig. 9. Methodology scheme of DWT based diagnostic [8]

1. Collecting current signal's samples in transient state

Collected current signal in transient state is a basic signal for diagnosis. The standard sampling frequency of data acquisition device equal to 2 or 5 kS/s ensures a good

resolution according to equations (14a and b), introducing different sets of frequency bandwidths [8].

In the performed analyses, the sampling frequency was equal to F_s = 5 kS/s.

2. Application of DWT

Before using DWT, mother wavelet and the number of decomposition levels must be specified [8].

1) Choice of mother wavelet

Daubechies wavelet of 45order ('db45') was chosen for the analysis. According to [8], this kind of wavelet of an order higher than 20 gives satisfying results.

2) Specifying number of decomposition levels

The number of decomposition levels depends on the desired low frequency components. Waveforms of these components are represented by DWT signals of high level [8].

In the case of examined faults, low frequency components are not taken into account.

In order to find number of decomposition levels n_f equation, that describes approximation a_{nf} level below supply frequency [8, 9]:

$$n_f = \text{integer}\left[\frac{\log(F_s / f_s)}{\log(2)}\right] \tag{15}$$

For F_s = 5000 samples per second and f_s = 50 Hz, we obtain a level of decomposition equal to n_f = 6. Using equations (14a and b) bandwidths for specified sampling frequency for each DWT signal are presented in Table 1. [8].

Table 1

Frequency bandwidths of DWT signals for F_s = 5000 S/s [8]

Level	Bandwidth [Hz]
d1	1250–2500
d2	625–1250
d3	312.5–625
d4	156.25–312.5
d5	78.12–156.25
d6	39.06–78.12
a6	0–39.06

Using this distribution of wavelet signals allows following changes related to different faults.

3. Analysis of wavelet signals

The next step is to perform qualitative and quantitative analysis in order to evaluate the obtained DWT decomposition signals [8].

1) Qualitative analysis

The purpose of qualitative analysis is to detect the presence of characteristic components caused by slip dependent fault harmonics. It is obtained by analyzing oscillations that occur in wavelet signals [8].

2) Quantitative analysis

When the machine's condition is initially diagnosed, using qualitative identification of characteristic components, it is possible calculate quantitative parameters of particular faults in order to evaluate the degree of damage to the machine [8].

For the performed analyses, the following quantitative factors were assumed:

– In the case of the multi-resolution DWT analysis, the percentage energy E of wavelet signals and percentage energy differences [13]:

$$W = \left| \frac{E_z - E_u}{E_z} 100\% \right| \tag{16}$$

where:

E_z, E_u – energy of signal with and without fault.

In this case, detail d6 containing base harmonic is omitted.

– For time-frequency analyses – energy of the harmonic related to the fault obtained from transform E [dB] and absolute energy difference:

$$\Delta E = \left| E_z - E_u \right| \text{ [dB]} \tag{17}$$

4. Diagnostic decision

When qualitative patterns related to faults are defined and the quantitative degree of damage is specified, it is possible to make a diagnostic decision [8].

4.4. Detection of dynamic and static eccentricity

The problem of dynamic and static eccentricity detection using TMSCA method has not yet been fully examined. This paper presents attempts for the detection of these faults in transient states of the machine during start-up.

In [12], for monitoring of the stator winding condition and also the supply voltage asymmetry considered as distortion in static eccentricity detection, amplitude of frequency component was presented.

$$f_{nn} = 3 f_s \tag{18}$$

Also, harmonics that prove the presence of dynamic and static eccentricity, respectively in low and medium frequency bandwidths were presented [12]:

$$f_{ednn}(s) = f_s \left(k \frac{1-s}{p} \pm m \right) \tag{19}$$

$$f_{esnn}(s) = f_s \left(k N_r \frac{1-s}{p} \pm m \right) \tag{20}$$

where:

$k = 1, 2, 3, \ldots,$

$m = 1, 3, 5, \ldots,$

In Figure 10, spectrum of stator current in phase A, for nominal load ($I \cong 3$ A) supplied form voltage of frequency $f_s = 50$ Hz, in steady state – MCSA method, for healthy motor Fig. 10a, dynamic eccentricity occurrence Fig. 10b, static eccentricity occurrence Fig. 10c and static eccentricity occurrence with voltage asymmetry Fig. 10d. Once can observe the increase of odd multiples of network frequency and increase of harmonics described by (19) for $k = 1$ and $m = 3$ and by (20) for $k = 1$ and $m = 1$[12].

These harmonics that are typical for eccentricity occurrence are also present in a healthy motor and are equal to frequency components caused by load variations. For that reason, eccentricity detection is more difficult [12].

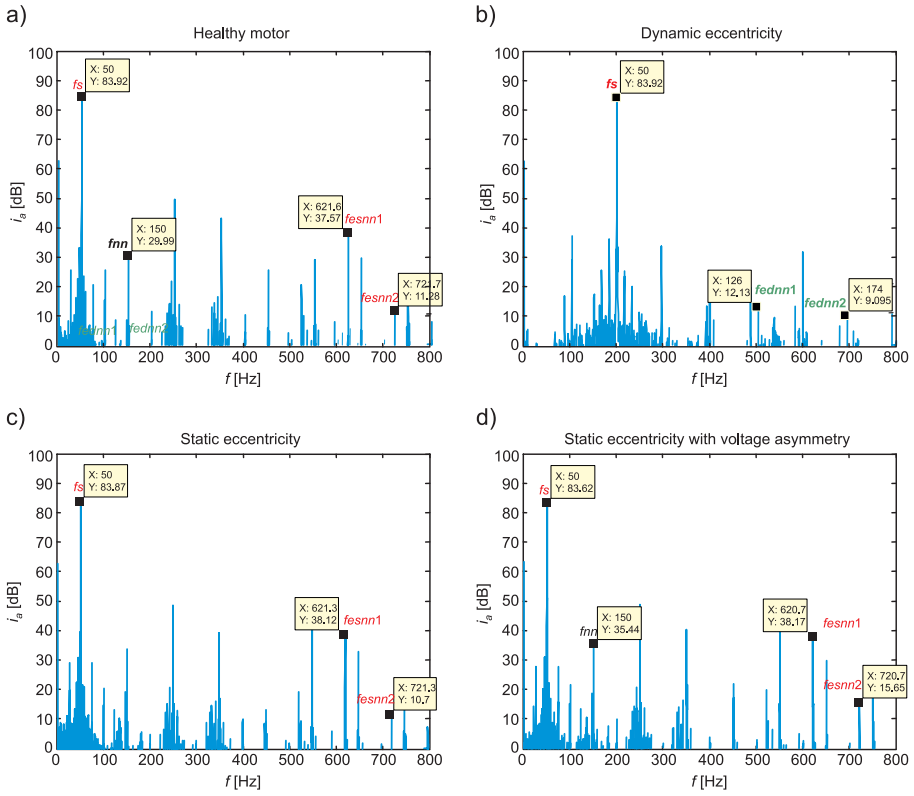

Fig. 10. Stator current spectrum of loaded machine (nominal load) with $Fs = 50$ Hz and a) no fault, b) dynamic eccentricity, c) static eccentricity, d) static eccentricity with voltage asymmetry [12]

The attempt of eccentricity detection is made using the TMCSA method, using the following harmonics (indexes mean different variants of the equation: 1 for „–”, 2 for „+”):

– dynamic eccentricity: (19) for $k = 1$ and $m = 3$: $f_{ednn1,2}$,
– static eccentricity: (20) for $k = 1$ and $m = 1$: $f_{esnn1,2}$,
– supply voltage asymmetry: (18) f_{nn}; (19) for $k = 1$ and $m = 3$: $f_{ednn1,2}$; (20) for $k = 1$ and $m = 1$: $f_{esnn1,2}$.

Characteristic patterns of harmonics are shown in the picture below on the slip--frequency plane (where the slip is replaced by a rotational speed for a motor with four poles $p = 2$):

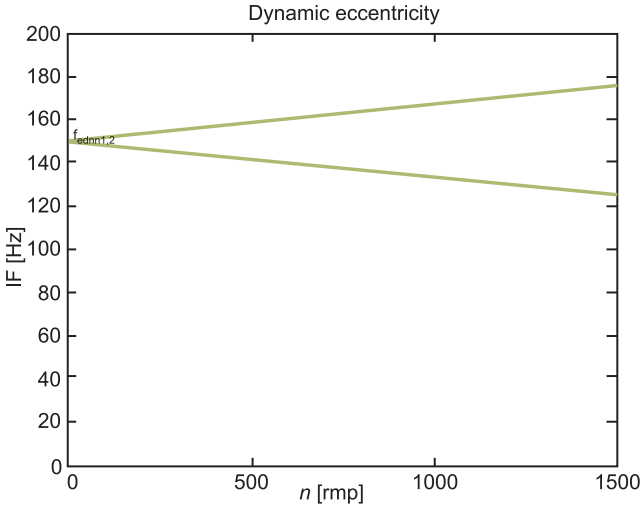

Fig. 11. Characteristic harmonics for dynamic eccentricity on slip-frequency plane

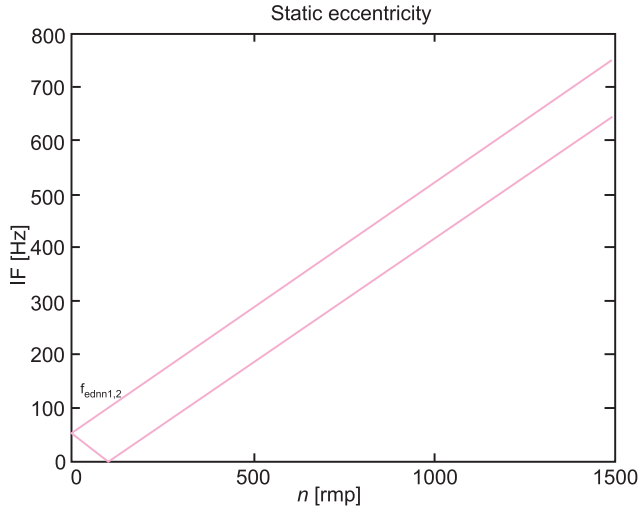

Fig. 12. Characteristic harmonics for static eccentricity on slip-frequency plane

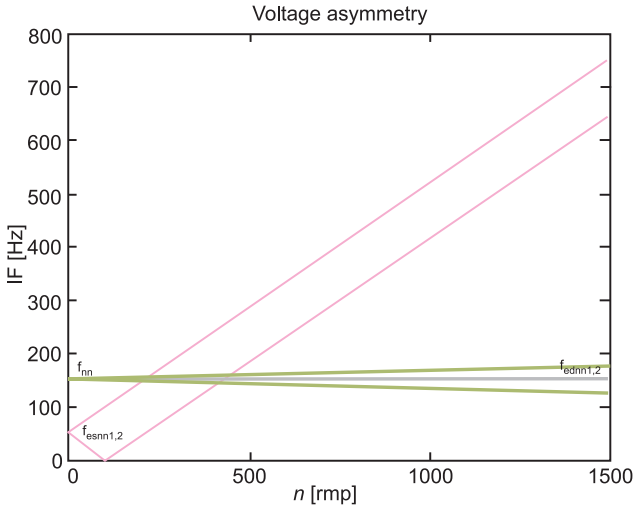

Fig. 13. Characteristic harmonics for voltage asymmetry on slip-frequency plane

In the case of using DWT for multi-resolution analysis, for sampling frequency set to F_s = 5000 samples per second and decomposition level of the current signal equal to n_f = 6, according to equation (15) in obtained frequency bandwidths of DWT wavelet signals, presented in Table 1, characteristic components related to fault occurrence will be sought. Bandwidths of DWT with contained harmonics are presented in Table 2.

Table 2

Frequency bandwidths of DWT signals for F_s = 5000 S/s for diagnosis of dynamic eccentricity (ED), static eccentricity (ES) and voltage asymmetry (NN)

Level	Bandwidth [Hz]	Characteristic harmonics		
		ED	ES	NN
d1	1250–2500			
d2 (a1)	625–1250		$f_{esnn1,2}$	$f_{esnn1,2}$
d3 (a2)	312.5–625		$f_{esnn1,2}$	$f_{esnn1,2}$
d4 (a3)	156.25–312.5	f_{ednn2}	$f_{esnn1,2}$	$f_{ednn2}, f_{esnn1,2}$
d5 (a4)	78.12–156.25	$f_{ednn1,2}$	$f_{esnn1,2}$	$f_{nn}, f_{ednn1,2}, f_{esnn1,2}$
d6 (a5)	39.06–78.12		$f_{esnn1,2}$	$f_{esnn1,2}$
a6	0–39.06		f_{esnn1}	f_{esnn1}

* approximations relating to upper frequency limits of particular details are given in parenthesis

One can notice that bandwidth containing harmonics related to faults in the case of dynamic eccentricity includes DWT signals d4 and d5, and for static eccentricity with voltage asymmetry, from d2 to a6. Analysis of detail d6 is omitted since it contains base harmonic.

For particular fault cases, DWT approximations of the current signal for the analyses on the TF planes, are obtained from the following signals of wavelet transform performed using Daubechies wavelet of 45th order ('db45'):

- dynamic eccentricity: a3,
- Static eccentricity: a1,
- Voltage asymmetry: a1.

5. Results of analyses of particular fault cases

The following analyses were performed:

- *Multi-resolution analysis with DWT*
  - Dynamic eccentricity detection (ED): analysis of wavelet signals d4 and d5 (for wavelet filter: 'db45').
  - Static eccentricity detection (ES) and voltage asymmetry (NN): analysis of wavelet signals d2 – a6 (for wavelet filter: 'db45').
- *Time frequency analyses on TF planes*

  Energy of characteristic fault related harmonics:
  - $f_{ednn1,2}$ – for dynamic eccentricity,
  - $f_{esnn1,2}$ – for static eccentricity,
  - $f_{nn}, f_{ednn1,2}, f_{esnn1,2}$ – for voltage asymmetry.

  For time period: $t = 0.9$ s
  - Signal of DWT approximation: a3 – for dynamic eccentricity (for wavelet filter: 'db45').
  - Signal of DWT approximation: a1 – for static eccentricity and voltage asymmetry (for wavelet filter: 'db45').

  The following parameters of the time-frequency analysis were set:

  A. Gabor's transform

  Base function $g(t)$: Blackman's window.

  Parameters: $\Delta M = 4$ – time step; $\Delta N = 4$ – frequency step.

  B. STFT transform

  Analysis time window function $\gamma(t)$: Hanning's window.

  Window length M : $M = 512$ samples $\Rightarrow M \cong 0.1$ s, with $F_s = 5000$ samples per second

  C. Wigner–Ville transform

  Window length M : $M = 512$ samples $\Rightarrow M \cong 0.1$ s, with $F_s = 5000$ samples per second

  D. Continuous wavelet transform (CWT)

  Morlet's wavelet was selected.

In the case of time-frequency analyses performed with continuous wavelet transform (CWT) scale related to instantaneous frequency of characteristic fault harmonics for time t, obtained from the graph in Fig. 14.

For time-frequency analyses performed with CWT, a scale range from 1 to 64 with 0.125 step was set.

This scale range allows obtaining a better resolution of CWT transform for the middle frequencies range containing the examined harmonics as shown in figure below.

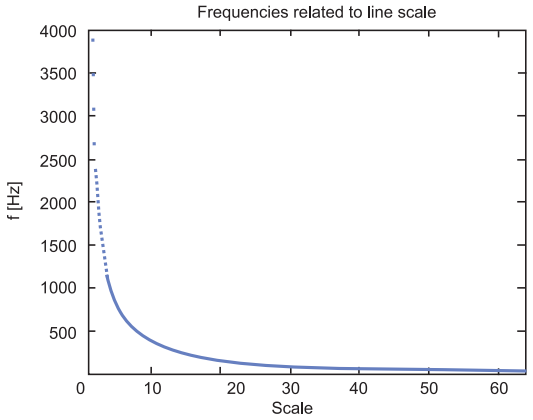

Fig. 14. Frequency vs. Scale curve for Morlet wavelet for S = 1:0,125:64

Programs for performing Gabor's, STFT and Wigner–Ville's transforms were based on algorithms given in [1]. For performing DWT and CWT and transforms and designing the notch filter, library functions of MATLAB were used.

– *Multi-resolution analysis with DWT*

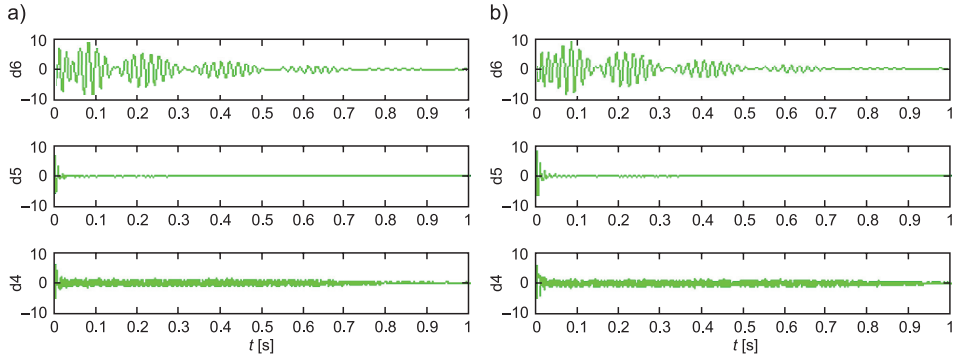

Fig. 15. Dynamic eccentricity detection: analysis of d4 and d5: a) i_sym, b) i_de

Table 3

Quantitative factors for ED detection: analysis of d4 and d5

Case	E (db45)	
	Decomposition signal	
	d5	d4
i_sym	5.4724	0.3529
i_de	7.1124	0.3639

Case	W [%] (db45)	
	Decomposition signal	
	d5	d4
i_de	29.97	3.12

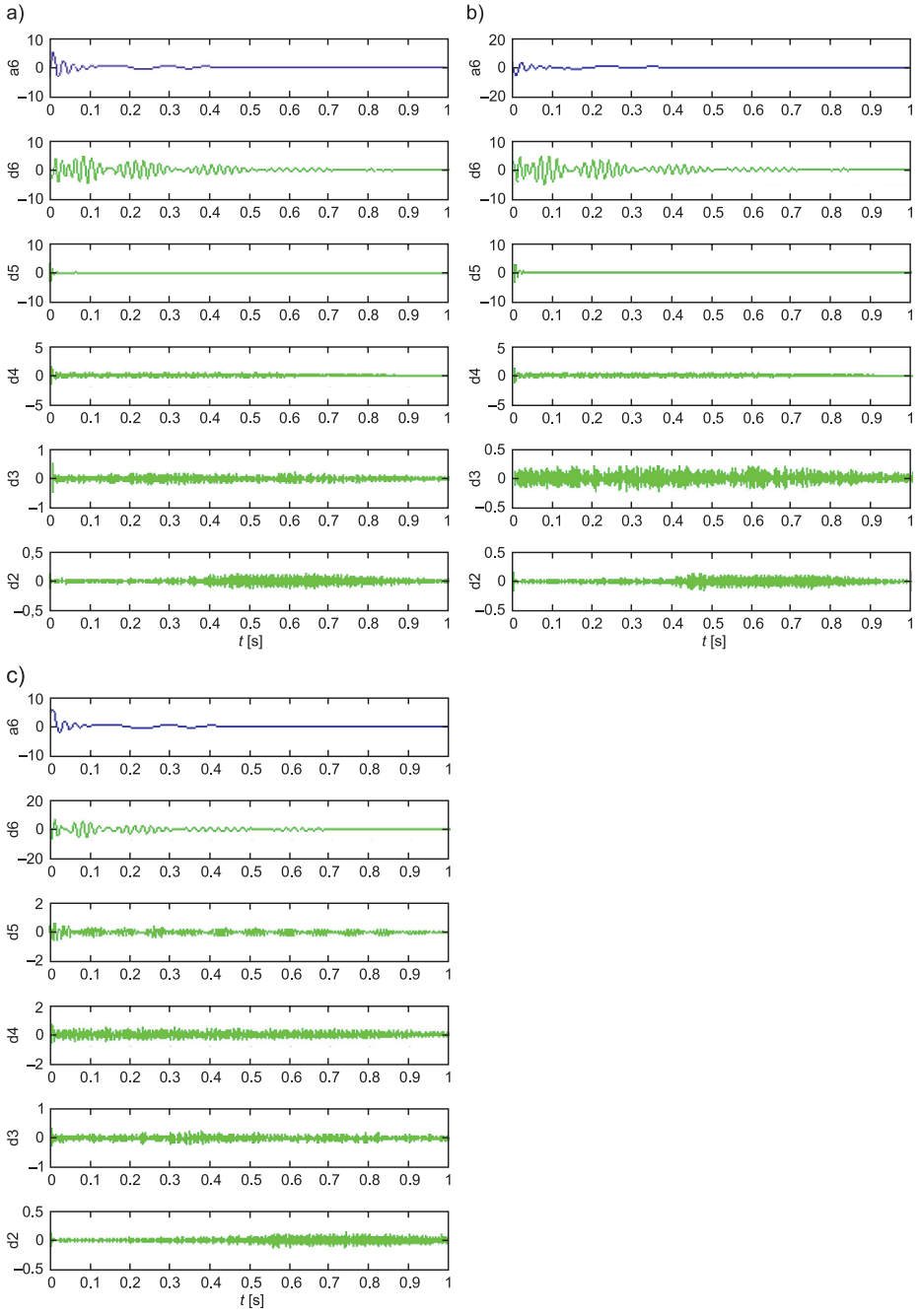

Fig. 16. Detection of static eccentricity and voltage asymmetry: analysis d2 – a6: a) i_sym, b) i_se, c) i_senn

Table 4

Quantitative factors for ES and NN detection: analysis d2 – a6

Case	*E* (db45)				
	Decomposition signal				
	a6	d5	d4	d3	d2
i_sym	83.8955	5.4724	0.3529	0.019	0.004
i_se	85.2914	5.118	0.2886	0.015	0.0037
i_senn	70.1393	0.2611	0.1306	0.0127	0.0029

Case	*W* [%] (db45)				
	Decomposition signal				
	a6	d5	d4	d3	d2
i_se	1.66	6.48	18.22	21.05	7.50
i_senn	16.40	95.23	62.99	33.16	27.50

– *Time-frequency analysis on TF planes*

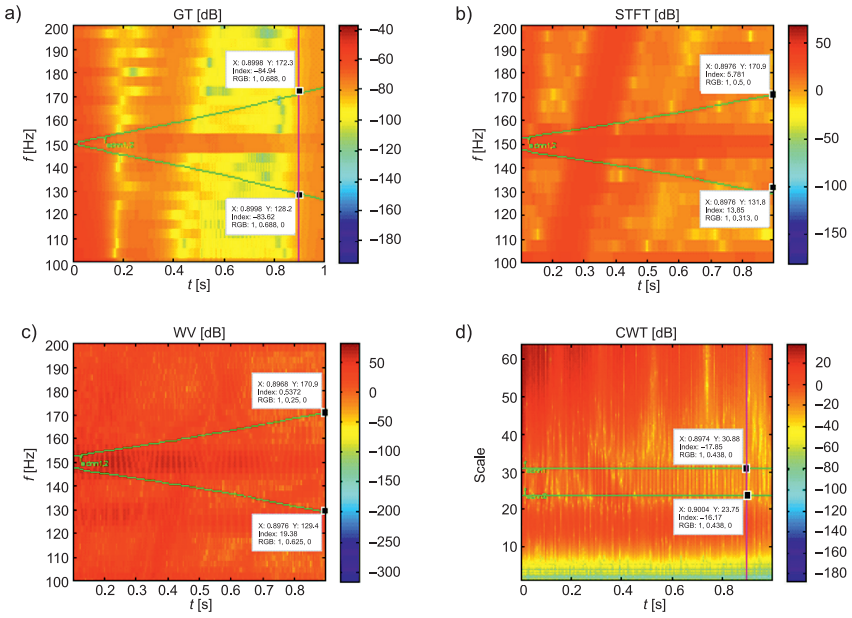

Fig. 17. Signal of DWT approximation: a3 – for ED: i_de:
a) GT; b) STFT; c) WV; d) CWT

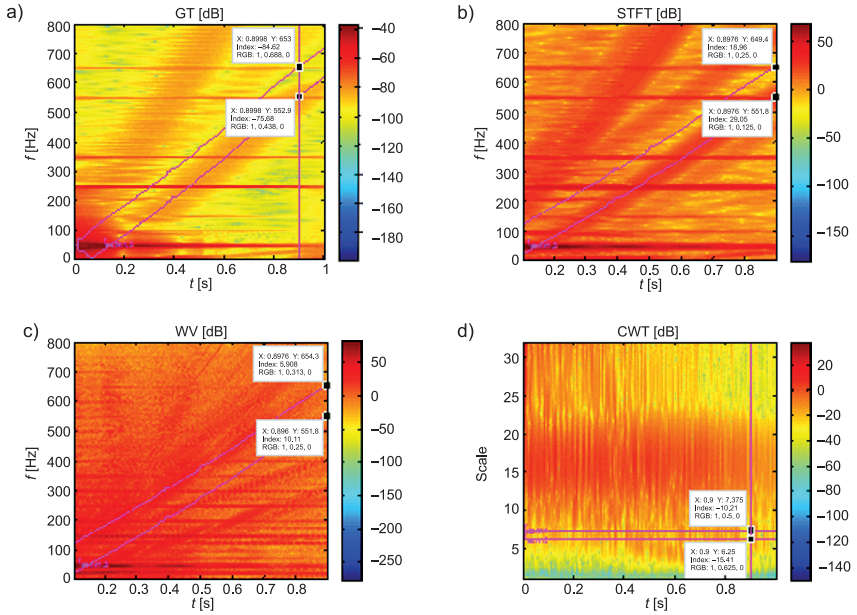

Fig. 18. Signal of DWT approximation: a1 – for ES: i_se:
a) GT; b) STFT; c) WV; d) CWT

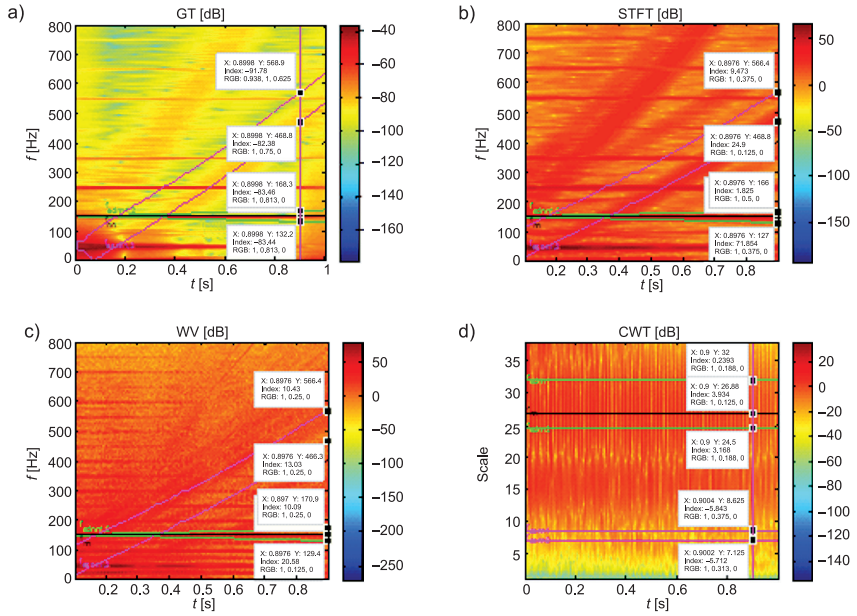

Fig. 19. Signal of DWT approximation: a1 – for ES and NN: i_senn:
a) GT; b) STFT; c) WV; d) CWT

Table 5

Quantitative factors for particular signals of DWT approximations for dynamic eccentricity occurrence case

Case	*GT* (a3: db45): *E* [dB]	
	Harmonic	
	fednn1	fednn2
i_sym	–92.1	–97.21
i_de	–83.62	–84.94
	STFT (a3: db45): *E* [dB]	
i_sym	–2.531	–14.95
i_de	13.85	5.781
	WV (a3: db45): *E* [dB]	
i_sym	8.798	–26.61
i_de	19.38	0.5372
	CWT (a3: db45): *E* [dB]	
i_sym	–19.91	–21.28
i_de	–17.85	–16.17

Case	*GT* (a3: db45): Δ*E* [dB]	
	Harmonic	
	fednn1	fednn2
i_de	8.48	12.27
	STFT (a3: db45): Δ*E* [dB]	
i_de	16.381	20.731
	WV (a3: db45): Δ*E* [dB]	
i_de	10.582	27.1472
	CWT (a3: db45): Δ*E* [dB]	
i_de	2.06	5.11

Table 6

Quantitative factors for particular signals of DWT approximations for static eccentricity and voltage asymmetry considered as distortion occurrence case

Case	*GT* (a1: db45): *E* [dB]				
	Harmonic				
	fednn1	fednn2	fesnn1	fesnn2	fnn
i_sym	–92.67	–98.37	–87.53	–103.8	–85.06
i_se			–75.68	–84.62	
i_senn	–83.44	–83.46	–82.38	–91.78	–61.8
	STFT (a1: db45): *E* [dB]				
i_sym	–2.532	–14.97	21.62	–5.074	19.58
i_se			29.05	18.96	
i_senn	7.854	1.825	24.9	9.473	41.37
	WV (a1: db45): *E* [dB]				
i_sym	8.809	-8.79	–5.753	–5.628	13.83
i_se			10.11	5.908	
i_senn	20.58	10.09	13.03	10.43	35.27

	CWT (a1: db45): *E* [dB]				
i_sym	–19.58	–21.73	–19.36	–24.57	–17.58
i_se			–10.21	–15.41	
i_senn	0.2393	3.168	–5.843	–5.712	3.934

Case	***GT* (a1: db45): Δ*E* [dB]**				
	Harmonic				
	fednn1	fednn2	fesnn1	fesnn2	fnn
i_se			11.85	19.18	
i_senn	9.23	14.91	5.15	12.02	23.26
	STFT (a1: db45): Δ*E* [dB]				
i_se			7.43	24.034	
i_senn	10.386	16.795	3.28	14.547	21.79
	WV (a1: db45): Δ*E* [dB]				
i_se			15.863	11.536	
i_senn	11.771	18.88	18.783	16.058	21.44
	CWT (a1: db45): Δ*E* [dB]				
i_se			9.15	9.16	
i_senn	19.8193	24.898	13.517	18.858	21.514

6. Conclusion

The aim of performed analyses was the efficiency evaluation of the presented methodology of detecting dynamic and static eccentricity. Supply voltage asymmetry was considered as distortion of harmonics based method of static eccentricity detection. The obtained results of the performed analyses are as follows:

– Multi-resolution analysis with DWT:

  In the obtained DWT decompositions, one can notice changes showing the occurrence of particular faults. For slip dependent harmonics, these changes are details covering the highest ranges at the end of start-up– d4 for dynamic eccentricity, d2 and d3 for static eccentricity and d2-d5 for static eccentricity with voltage asymmetry.

  In the case of percentage energy of DWT signals, dynamic eccentricity occurrence causes the rise of the percentage energy of signals d4 and d5, however, when static eccentricity occurs, the percentage energy of details d2-d5 decreases. In the case of the simultaneous occurrence of static eccentricity and voltage asymmetry, the decrease of the percentage energy of details d2-d5 becomes significant.

In the case of TF analyses, when analyzing energies of the examined harmonics one can notice their increase when a fault occurs. It happens for all transforms both for a3 approximation for dynamic eccentricity and for a1 approximation for static eccentricity with voltage asymmetry.

In the obtained transforms, harmonics $f_{ednn1,2}$ are not clearly visible. The waveform of $f_{esnn1,2}$ harmonic is visible in all TF transforms except that in Wigner–Ville's transform, one can distinguish waveforms of two harmonics. Harmonic f_{nn} waveform is also clearly visible.

It can be concluded that the proposed methodology is effective in the detection of the examined faults both for multi-resolution analysis with DWT and time-frequency analyses on the TF plane.

General observations and conclusions can be formed:

- With TF analyses using Gabor transform, Wigner–Ville's transform, STFT and CWT, all examined machine faults were successfully diagnosed, thanks to the localization of typical slip dependent harmonics, which is a TMCSA method. In the current signal's decompositions obtained by DWT multi-resolution analysis, it is more difficult to observe characteristic features of faults. Also, analysis of wavelet signals percentage energy values, one cannot find any particular dependencies related to fault occurrence.
- Using the notch filter in order to remove the base harmonic of current signal of frequency equal to that of supply voltage, made it easier to distinguish characteristic fault harmonics in the time-frequency transforms. Although using the notch filter allowed the removal of a significant part of the base harmonic, the filtration is not ideal and a part of the base harmonic remained. This combined with the Gibbs effect, which is connected with filtration and signal processing, still causes the deterioration of the obtained transforms and decompositions' quality.
- In conclusion, one can say that using the presented methodology of time-frequency analysis application in fault detection of cage induction machines and simple data acquisition system for collecting phase current and rotational speed signal, it was possible to detect the examined machine's faults. Also, using a rotational speed signal allowed obtaining the actual harmonics' waveforms and localize them of TF plane in specified moment, especially in cases where those harmonics were hard to observe which happened for dynamic eccentricity.

References

[1] Zieliński T.P., *Cyfrowe przetwarzanie sygnałów. Od teorii do zastosowań*, WKŁ, Warszawa 2005.

[2] Augustyniak P., *Transformacje falkowe w zastosowaniach elektrodiagnostycznych*, Wydawnictwo AGH, Kraków 2003.

[3] Białasiewicz J.T., *Falki i aproksymacje*, WNT, Warszawa 2000.

[4] Zygarlicka M., *Wybrane metody przetwarzania obrazów w analizach czasowo-częstotliwościowych na przykładzie zakłóceń w sieciach elektroenergetycznych*, rozprawa doktorska, Politechnika Opolska, Opole 2011.

[5] Szabatin J., *Podstawy teorii sygnałów*, WKŁ, Wydawnictwo V, Warszawa 2007.
[6] Riera-Guasp M., Pineda-Sánchez M., Perez-Cruz J., Puche-Panadero R., Roger-Folch J., Antonino-Daviu J., *Diagnosis of Induction Motor Faults via Gabor Analysis of the Current in Transient Regime*, IEEE Transactions on Instrumentation and Measurement, Dec. 2012, Vol. 61, No. 6, 1583-1596.
[7] Pineda-Sánchez M., Riera-Guasp M., Pons-Llinares J., Climente-Alarcón V., Perez-Cruz J., *Diagnosis of Induction Machines under Transient Conditions through the Instantaneous Frequency of the Fault Components*, XIX International Conference on Electrical Machines – ICEM, Rome 2010.
[8] Riera-Guasp M., Antonino-Daviu J.A., Pineda-Sanchez M., Puche-Panadero R., Perez-Cruz J., *A General Approach for the Transient Detection of Slip-Dependent Fault Components Based on the Discrete Wavelet Transform*, IEEE Transactions on Industrial Electronics, Dec. 2008, Vol. 55, No. 12, 4167-4180.
[9] Riera-Guasp M., Antonino-Daviu J.A., Roger-Folch J., Pilar Molina Palomares M., *The Use of the Wavelet Approximation Signal as a Tool for the Diagnosis of Rotor Bar Failures*, IEEE Transactions on Industry Applications, May/June 2008, Vol. 44, No. 3, 716-726.
[10] Antonino-Daviu J.A., Riera-Guasp M., Pineda-Sanchez M., Pérez R. B., *A Critical Comparison Between DWT and Hilbert–HuangBased Methods for the Diagnosis of Rotor Bar Failures in Induction Machines*, IEEE Transactions on Industry Applications, Sep./Oct. 2009, Vol. 45, No. 5, 1794-1803.
[11] Pineda-Sanchez M., Riera-Guasp M., Antonino-Daviu J.A., Roger-Folch J., Perez-Cruz J., Puche-Panadero R., *Diagnosis of Induction Motor Faults in the Fractional Fourier Domain*, IEEE Transactions on Instrumentation and Measurement, Aug. 2010, Vol. 59, No. 8, 2065-2075.
[12] Wolkiewicz M., Kowalski Cz.T., *Nieinwazyjne metody wczesnego wykrywania zwarć zwojowych w silniku indukcyjnym zasilanym z przemiennika częstotliwości, cz. I*, BOBRME Komel, Zeszyty Problemowe – Maszyny Elektryczne, 2010, nr 87, 145-150.
[13] Kowalski Cz.T., Kanior W., *Ocena skuteczności analiz FFT, STFT i falkowej w wykrywaniu uszkodzeń wirnika silnika indukcyjnego*, Prace Naukowe Instytutu Maszyn, Napędów i Pomiarów Elektrycznych Politechniki Wrocławskiej Nr 60, Studia i Materiały Nr 27, 2007.
[14] Help programu MATLAB R2011b.

AUTOMATIC CONTROL

AUTOMATYKA

TECHNICAL TRANSACTIONS | **CZASOPISMO TECHNICZNE**
ELECTRICAL ENGINEERING | ELEKTROTECHNIKA
2-E/2015

VOLODYMYR FEDAK, ADRIAN NAKONECHNY*

ADAPTIVE WAVELET THRESHOLDING FOR IMAGE DENOISING USING SURE MINIMIZATION AND CLUSTERING OF WAVELET COEFFICIENTS

ZASTOSOWANIE ADAPTACYJNYCH PROGÓW DO REDUKCJI SZUMÓW OBRAZÓW ZA POMOCĄ MINIMIZACJI SURE I KLASTEROWANIA WSPÓŁCZYNNIKÓW FALKOWYCH

Abstract

Images and video are often coded using block-based discrete cosine transform (DCT) or discrete wavelet transform (DWT) which cause a great deal of visual distortions. In this paper, an extension of the intra-scale dependencies of wavelet coefficients is proposed to improve denoising performance. This method incorporates information on neighbouring wavelet coefficients that are inside of manually created clusters. Extensive experimental results are given to demonstrate the strength of the proposed method.

Keywords: *artifacts*, *denoising*, *wavelet transformation*

Streszczenie

Obrazy i nagrania wideo są często kodowane z użyciem blokowej dyskretnej transformacji kosinusowej (DCT) lub dyskretnej transformacji falkowej (DWT), które powodują znaczne zakłócenia wizualne. W niniejszej pracy proponuje się rozszerzenie zależności między współczynnikami falkowymi dotyczącymi skali w celu zmniejszenia zaszumienia sygnału zakodowanego. Zaproponowana metoda zakłada wykorzystanie informacji o sąsiadujących współczynnikach falkowych, które znajdują się wewnątrz manualnie utworzonego klastra. W artykule zaprezentowano obszerne wyniki doświadczalne w celu wykazania jakości proponowanej metody.

Słowa kluczowe: *artefakty*, *odszumianie*, *transformacja falkowa*

DOI: 10.4467/2353737XCT.15.096.3928

* Ph.D. student Volodymyr Fedak, Prof. Adrian Y. Nakonechny, Computer System And Automatics, Lviv Polytechnic National University.

1. Artifacts in images

All the time, we need to obtain, process, and deliver information. This information is not just limited to text files or simple messages; nevertheless, various visual pieces of information can be transmitted including image and video files. However, transmission channels have limited bandwidth and storage devices hold limited capacity. Digital video is broadcasted and stored in an encoded form; therefore, it requires less information (bits) than the original. At low bit-rates, the coarse quantization exploited during compression results in visually annoying coding artifacts [1].

Compression artifacts are a particular class of data errors that are usually the consequence of quantization in loss-prone data compression. These distortions can be classified into the following types:

Blocking artifacts. This type of image distortion is the most visible degradation of all artifacts. This effect is caused by all block-based coding techniques. It is a well-known fact that all compression techniques divide the image into small blocks and then compress them separately. Due to the coarse quantization, the correlation among blocks is lost, and horizontal and vertical borders appear.

Ringing artifacts. The ringing effect is caused by the quantization or truncation of high frequency coefficients and can also come from improper image restoration operations. Ringing artifacts are visible for all compression techniques especially when the image is transformed into the frequency domain. Moreover, it appears as distortion along sharp edges in the image. This artifact occurs very often when the DWT encoder is used. Furthermore, it may be observed after the image has been de-coded using a frequency coder.

Blur effect. Blurring is another artifact resulting from the absence of high frequencies in low bit rate video. It appears around sharp edges, and all image details become blurred. This effect is very similar to the ringing artifact, and sometimes it is hard to distinguish between them.

Different techniques may be used to reduce the most annoying artifacts and all of these techniques can be divided by filtering domain (spatial, frequency). Different authors provide versatile methods of image quality improvements and sometimes, the most challenging task is to choose the necessary technique. Spatial algorithms modify image pixel values. These approaches are usually used together with edge detection algorithms to prevent the blurring effect, many classical image denoising methods are based on a local average. The restored value at a pixel is obtained as an average of its neighboring pixels. The most classical algorithm is Gaussian filtering. In this case, the restored value is obtained as a weighted average where the weight of each pixel depends on the distance to a restored one – this low pass filter tends to blur the image. The neighborhood filters avoid the blurring effect by restricting the average to pixels having a similar grey level value. The idea is that grey level values inside a homogeneous region slightly fluctuate while pixels belonging to different regions have a larger grey level difference. The neighborhood filter takes an average of the values of pixels which are simultaneously close in their grey level values and spatial distance. The most encouraging results can be obtained using the NLM approach [2]. Efficiency of this algorithm is proven in many different areas and this algorithm tries to take advantage of the redundancy and self-similarity of the image. The NLM algorithm estimates

the value of x as an average of the values of all the pixels. The probability that one pixel is similar to the other is determined by looking at the difference in the luminance value and the difference in position between two pixels in the neighbourhood filters.

Another direction of image restoration is using wavelet based techniques.

The multi-resolution analysis performed by the WT has been shown to be a powerful tool in order to achieve good denoising. In the wavelet domain, the noise is uniformly spread throughout the coefficients, while most of the image information is concentrated in the few largest coefficients (sparsity of the wavelet representation).

The most straightforward way of distinguishing information from noise in the wavelet domain consists of thresholding the wavelet coefficients [3–5]. Using a soft-thresholding filter is the most popular strategy and has been theoretically justified by Donoho and Johnstone [6]. They propose a three steps denoising algorithm:

1) the computation of the forward WT,
2) the filtering of the wavelet coefficients,
3) the computation of the IWT of the result obtained.

They use the discrete wavelet transform (DWT) and the soft-thresholding filter. Because it is not made any explicit hypothesis on the noise-free image, it results in a non-parametric method.

In this article, an efficient algorithm based on adaptive thresholding and wavelet coefficients dependencies for image denoising is presented. The proposed algorithm can effectively reduce noise in static images. The experimental results show that the proposed approach significantly outperforms the BiShrink, Neigh Shrink and Block Shrink approaches. Evaluations have been performed on different images and with different noise levels.

2. Existing approaches for image denoising

In modern digital systems and video broadcast chains, image compression is applied to reduce bandwidth or storage size. Post-processing of the decoded image sequence is an acceptable technique to achieve a better perceived picture quality [10]. Furthermore, modern consumer vision products like televisions and PCs use image enhancement and restoration techniques to improve the objective and subjective picture quality. All postprocessing algorithms and methods can be divided into the following types [1]:

- spatial filtering,
- filtering in the frequency/wavelet domain,
- temporal filtering,
- hybrid algorithms (mainly combines spatial and frequency filtering).

Many approaches have been proposed in the literature aiming at the alleviation of artifacts in the images. As a great number of algorithms have been developed in recent times, it would be rational to overview these approaches which threshold the wavelet detail coefficients for two-dimensional (2-D) signals. An overview of spatial techniques has been conducted in our previous work [7].

Frequency algorithms transform images to frequency domains and modify DCT (discrete cosine transform) or DWT (discrete wavelet transform) coefficients.

The effect of averaging the spatially closest pixels can also be achieved in the Fourier or wavelet domain. The average of the spatially closest pixels is then equivalent to the cancellation of the high frequencies. As the analogous spatial filter, this cancellation leads to the blurring of the image and a Gibbs effect. The optimal filter in the Fourier domain is the Wiener filter – this does not cancel the high frequencies but attenuates all of them.

In the wavelet domain, the noise is uniformly spread throughout the coefficients, while most of the image information is concentrated in the few largest coefficients (sparsity of the wavelet representation).

Consequently, regarding the three steps denoising algorithm, there are two tools to be chosen: the WT (wavelet transform) and the filter. In [8] the UDWT (undecimated discrete wavelet transform) is used, in [9] the DTCWT (dual tree complex wavelet transforms), and in [10] the DWT.

From the first category, we can mention: the hard-thresholding filter that minimizes the min-max estimation error and the efficient SURE-based inter-scales point-wise thresholding filter [10], which minimizes the mean square error (MSE). To the second category belong filters obtained by minimizing a Bayesian risk under a cost function, typically a delta cost function (MAP estimation [11]) or the minimum mean squared error [8]. The denoising algorithms proposed in [10] exploit the inter-scale dependence of wavelet coefficients. The method proposed in [8] also takes into account the intra-scale dependence of wavelet coefficients. The statistical distribution of the wavelet coefficients changes from scale to scale. The coefficients of the WT have a heavy tailed distribution.

2.1. Image filtering using wavelet thresholding

The wavelet denoising methods filter each coefficient from the detail sub-bands with a threshold function to obtain modified coefficients. The denoised estimated by inverse wavelet transform of the modified coefficients. Here, the threshold plays an important role in the denoising process. There are two thresholding functions frequently used. The soft--threshold function (also called the shrinkage function):

$$soft(d, \lambda) = sign(d) * [| d | - \lambda]_+ \tag{1}$$

takes the argument and shrinks it towards zero by the threshold T. The other alternative is the hard-thresholding function:

$$hard(d, \lambda) = \begin{cases} d, \text{if } | d \geq \lambda | \\ 0, \text{if } | d < \lambda | \end{cases} \tag{2}$$

which keeps the input if this input is larger than the threshold; otherwise, it is set to zero. The wavelet thresholding procedure removes noise by only thresholding the wavelet coefficients of the detail sub-bands, while keeping the low resolution coefficients unaltered.

Hard thresholding keeps existing coefficients whereas soft thresholding shrinks the coefficients above the threshold in absolute value.

More frequently, it's started to use adaptive threshold. Our proposed denoising method also uses such a type of thresholding (Fig. 2).

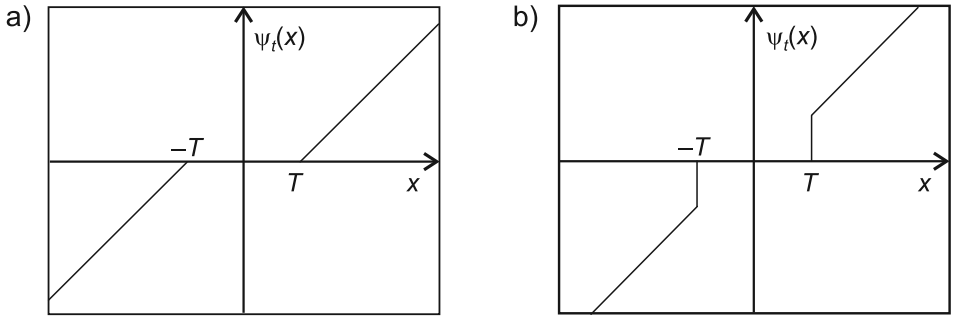

Fig. 1. Thresholding functions: a) soft threshold, b) hard threshold

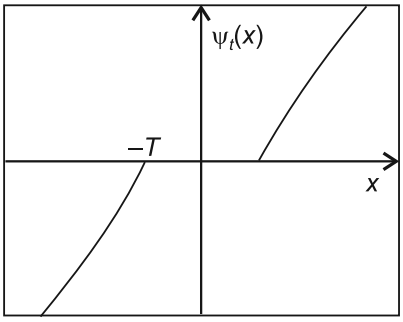

Fig. 2. Adaptive thresholding function

The adaptive thresholding doesn't modify wavelet coefficients that have high magnitudes (this is a drawback of soft thresholding) and doesn't have disruptions of wavelet coefficients close to T (this is a drawback of hard thresholding).

2.2. Wavelet dependencies and shrinkages types

In general, four types of wavelet coefficient dependencies can be considered. This is illustrated in Fig. 3:

c) Intra-scale and intra-band dependencies,
d) Inter-scale and inter-band dependencies,
e) Inter-band and intra-scale dependencies,
f) Inter-scale and intra-band dependencies.

The most frequently used de-nosing methods use only two types of dependencies: intra-scale and intra-band, and inter-scale and intra-band dependencies. The wavelet coefficients that represent the image also have large magnitudes at these scales, locations and orientations (d). However, the signs and relative magnitudes of these coefficients will depend on the exact shape, location and orientation of the structure they represent. The inter--scale dependencies indicate that if a parent coefficient is large, then its child coefficient is also large. However, currently there are no strict correlations between parent/child

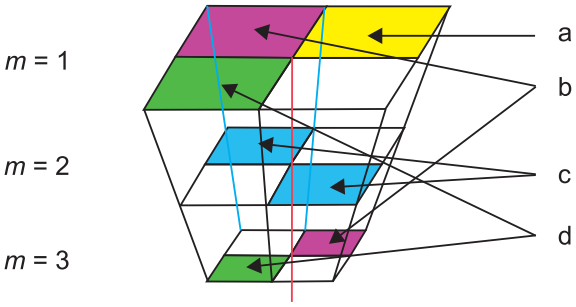

Fig. 3. Wavelet coefficient's dependencies

wavelet coefficients [11]. It's possible to indicate such a type of dependencies but only between two consecutive scales.

The method that uses inter-scale dependencies is called bivariate shrinkage [11]. The bivariate shrinkage function can be interpreted as follows:

$$w_1 = \frac{\left(\sqrt{y_1^2 + y_2^2} - \frac{\sqrt{3\sigma_n^2}}{\sigma}\right)}{\sqrt{y_1^2 + y_2^2}} y_1 \tag{3}$$

where y_1, y_2 – noisy coefficients in the scale 1 and 2. σ is defined as marginal variance. This estimator requires prior knowledge of the noise variance σ_n. In order to estimate noise variance, a robust median estimator is used from the finest scale wavelet coefficients [12].

$$\sigma_n = \frac{median\left(|w_s|\right)}{0.6745} \tag{4}$$

And marginal variance is defined as:

$$\sigma = \sqrt{(\sigma_y^2 - \sigma_n^2} \tag{5}$$

where σ_y is defined as:

$$\sigma_y^2 = \frac{1}{M} \sqrt{\sum_{y_i \in N(k)} y_i^2} \tag{6}$$

Another method that uses intra-scale dependencies is called Neigh Shrink [13]. The shrunken wavelet coefficient according to the neigh shrink is given by this formula:

$$\bar{w}_{i,j} = w_{i,j} \beta_{i,j} \tag{7}$$

where $w_{i,j}$ – noisy wavelet coefficient; $\bar{w}_{i,j}$ – denoised wavelet coefficient; the shrinkage factor $\beta_{i,j}$ can be defined as:

$$\beta_{i,j} = (1 - T_{UNI}^2 / S_{i,j}^2)_+ \tag{8}$$

There, the + sign at the end of the formula means to keep the positive value while set it to zero when it is negative and T_{UNI} is the universal threshold, which is defined as:

$$T = \sqrt{2\sigma \ln(N)} \tag{9}$$

And $S_{i,j}^2$ is a summation of the wavelet coefficients in the neighbouring window centered at the wavelet coefficient to be shrunk (Fig. 4):

$$S_{i,j} = \sum_{\in B_{i,j}} w_{k,l}^2 \tag{10}$$

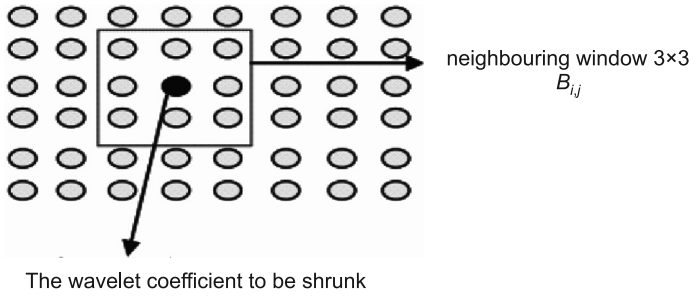

Fig. 4. Wavelet coefficients of neighbouring window

Another method that uses the SURE optimization technique (that minimizes the mean square error) is a block shrink. Suppose $w = \{w_i,\ i = 1, 2, \ldots, d\}$ and $S_B^2 = \sum_{\in B_{i,j}} w_{k,l}^2$. If S_B^2 is less than or equal to the threshold λ, then within the b block, the wavelet coefficient w_i is set to zero. Otherwise, wavelet coefficient is shrunk according to (7). The optimal threshold λ and block size L are derived by minimizing Stein's unbiased risk estimate (SURE) [14]:

$$(\lambda^s, L^s) = \arg_{\lambda,L} SURE(w, \lambda, L) \tag{11}$$

where:

$$SURE(w, \lambda, L) = \sum_{b}^{m} SURE(w_b, \lambda, L) \tag{12}$$

and

$$\begin{cases} SURE(w_b, \lambda, L) = L + \dfrac{\lambda^2 - 2\lambda(L-2)}{S_b^2} & \text{if} \quad (S_b^2 > \lambda) \\ S_b^2 - 2L \quad \text{if} \quad (S_b^2 > \lambda) \end{cases} \tag{13}$$

$m = d/L$ is the number of blocks.

3. Image denoising using SURE minimization and clustering of wavelet coefficients

The proposed method of wavelet shrinkage uses adaptive wavelet thresholding. In order to find a better threshold, the proposed approach uses SURE minimization and intra-scale and intra-band dependencies of wavelet coefficients. The general flow chart of the proposed wavelet shrinkage algorithm for noise reduction is depicted in Fig. 5. The main idea is that the signal is transformed using DWT to the wavelet domain and thereafter LH, HL, and HH sub bands are processed. The wavelet coefficients processing consists of the following steps:

- clustering; clusters are created from wavelet coefficients (all details are described in section 3.1),
- determining the threshold parameter for each cluster type (details are in section 3.2),
- thresholding (details in section 3.3).

After this processing, wavelet coefficients are again transformed to the original format.

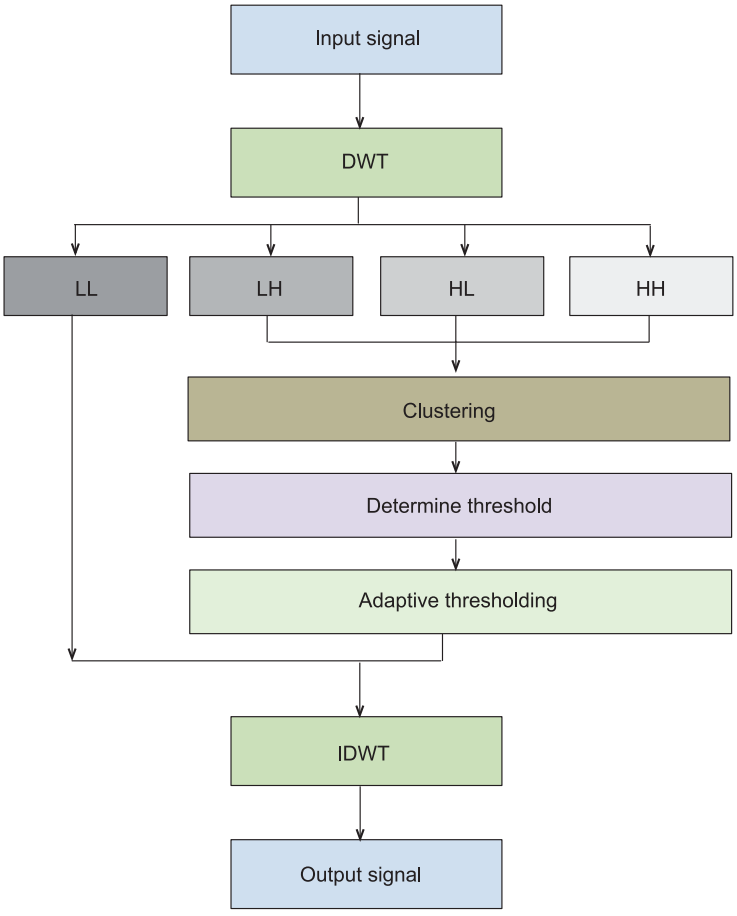

Fig. 5. Flow chart of the proposed wavelet shrinkage algorithm for noise reduction

3.1. Wavelet coefficients clustering

It has been determined that better results of image denoising can be obtained after clustering of the wavelet coefficients (coefficients need to be clustered in the LH, HL, HH). Better results can be received when cluster satisfies the following requirements:

- the absolute average value of wavelet coefficients shouldn't be much greater than the wavelet coefficient to be shrunk,
- denoising provides better results when a cluster contains more than 6–12 wavelet coefficients,
- if wavelet coefficients in the cluster have a greater value, the obtained results should be better.

Thus, the proposed method uses the following clusters (Fig. 6).

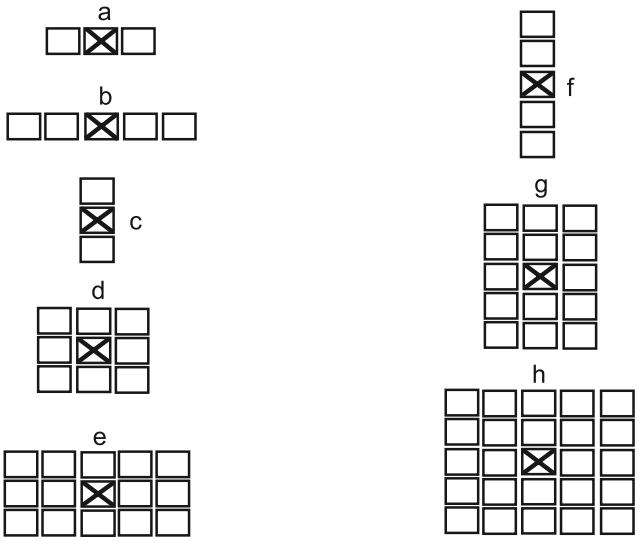

Fig. 6. Wavelet clusters that are formed from 5×5 blocks

Practically greater blocks are used: 6x6 and 7×7 blocks; therefore, the amount of different cluster types are greater than is displayed on Fig. 6.

Let w_o be the estimator of the unknown nosiness coefficient. Each cluster is created for the purpose of thresholding each noisy coefficient $w_{i,j}$:

$$A_{x,y} = \arg\max_{B_{i,j}} \left(\frac{1}{i \cdot j} \sum_{A_{x,y}} w_{i,j}^2 \right) \tag{14}$$

where $A_{x,y}$ cluster that is found from wavelet coefficients that have maximum value in the block $B_{i,j}$, $w_{i,j}$ – wavelet coefficients that belong to block $B_{i,j}$.

Additional weights are added to the clusters that have more than 4 × 3 = 12 wavelet coefficients:

$$Acl = 1.3 \cdot \frac{1}{i \cdot j} \sum_{A_{x,y}} w_{i,j}^2 \quad (\text{if} \quad x \cdot y > 12) \tag{15}$$

where:

Acl – a square average of wavelet coefficient inside cluster $A_{x,y}$,
1.3 – determined experimentally (using a database with images).

As is mentioned, additional weight is added to the cluster that contains wavelet coefficients with a similar value to the shrunken wavelet coefficient:

$$Acl = 15 \cdot \frac{1}{i \cdot j} \sum_{A_{x,y}} w_{i,j}^2 \quad (\text{if} \quad abs(w_o^2 - w_{i,j}^2) < 1.4 w_o^2) \tag{16}$$

3.2. Determine the better threshold parameter

The next step is to choose an appropriate threshold value. Different wavelet coefficients are shrunken differently with different threshold values that are found for different cluster types. The optimal λ and L of every sub band should be data-driven and minimize the mean squared error (MSE) or Steins risk of the corresponding sub band and for specified cluster type (Stein proved that MSE can be found unbiasedly for a given noise level. For these purposes, a robust median estimator can be used).

In the proposed algorithm, the optimal threshold λ for each cluster type are derived by minimizing Stein's unbiased risk estimate:

$$SURE(w_o, \lambda, L) = N_s + \sum_n \left\| g_n(w_n) \right\|_2^2 + 2 \sum_2 \frac{\delta g_n}{w_n} \tag{17}$$

where:

L – cluster type (Fig. 6),
λ – threshold,
N_s – a noisy coefficient.

$$\left\| g_n(w_n) \right\|_2^2 = \begin{cases} \dfrac{\lambda^4}{S_n^4} w_n^2 & (\lambda < S_n) \\ w_n^2 & (otherwise) \end{cases} \tag{18}$$

where S_n is the summation of wavelet coefficients in the cluster L; and $\dfrac{\delta g_n}{w_n}$

$$\frac{\delta g_n}{w_n} = \begin{cases} -\lambda^2 \dfrac{S_n^2 - 2w_n^2}{S_n^4} & (\lambda < S_n) \\ -1 & (otherwise) \end{cases} \tag{19}$$

3.3. Thresholding

Thresholding is conducted in a similar manner as to how it's performed in the Neigh shrink method [13]. The wavelet coefficients are shrunken according to the Neigh shrink using this formula:

$$\bar{w}_{i,j} = w_{i,j}\beta_{i,j} \tag{20}$$

where:

$w_{i,j}$ – noisy wavelet coefficient,

$\bar{w}_{i,j}$ – denoised wavelet coefficient,

the shrinkage factor $\beta_{i,j}$ for specified cluster types is defined as:

$$\beta_{i,j} = (1 - T_{UNI}^2 / S_{i,j}^2)_+ \tag{21}$$

and $S_{i,j}^2$ is a summation of the wavelet coefficients in the cluster centered at the wavelet coefficient to be shrunk:

$$S_{i,j} = \sum_{\in B_{i,j}} w_{k,l}^2 \tag{22}$$

4. Results

In this section, an objective analysis of the proposed wavelet shrinkage algorithm with an adaptive thresholding is evaluated. We have experimented with various noisy images and report the results for the three 512×512 standard test images: Lena, Barbara and Mandrill (Fig. 6). The DWT is used with a symlet wavelet with eight vanishing moments with four scales. They are contaminated with Gaussian random noise with standard deviations of 10, 20, 30, 40, 50, 60, 70, 80, 90 and 100. In practice, the noise standard deviation is unknown and during experiments, it's initially estimated using (4). Our results are measured by the PSNR in decibels (dB) and MSE.

Our method was compared with BiShrink that uses inter-scale intra-band and intra-scale intra-band wavelet coefficients dependencies. In addition, we compared our method

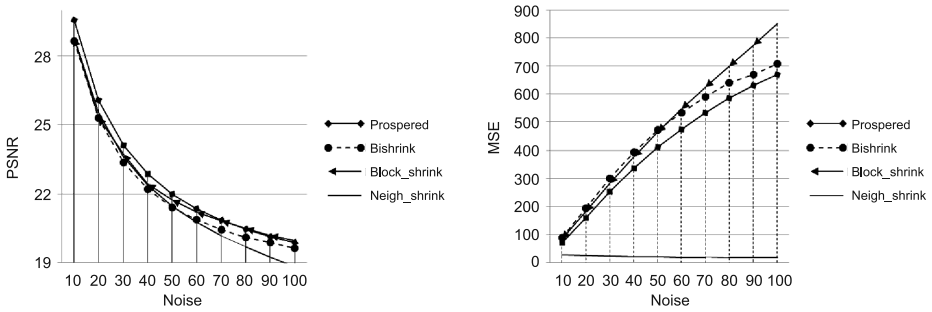

Fig. 7. Comparison of the PSNR and MSE for the Barbara image on different noise levels

with the Neigh shrink, according to paper [15], this method produces the most promising results. In comparison to other methods, the Block shrink (only this method is based on SURE) also produced quite good results. The comparison charts for the Mandrill image is depicted on Fig. 7.

Extensive results are described in the Table 1 ('*' indicates the best result among all four denoising methods).

Table 1

Comparison of PSNR and MSE for different wavelet methods

Image	Sigma	Proposed		BiShrink		Block_shrink		Neigh_shrink	
		PSNR	MSE	PSNR	MSE	PSNR	MSE	PSNR	MSE
Mandrill	10	**32.842***	**33.796***	32.140	39.729	31.594	45.048	32.714	34.809
	20	**29.000***	**81.847***	28.253	97.222	27.695	110.556	28.758	86.555
	30	**26.903***	**132.657***	26.159	157.455	25.919	166.399	26.498	145.648
	40	**25.519***	**182.483***	24.786	215.991	24.798	215.399	24.933	208.827
	50	**24.514***	**229.980***	23.828	269.321	23.995	259.183	23.759	273.622
	60	**23.740***	**274.808***	23.179	312.725	23.392	297.763	22.830	338.938
	70	**23.119***	**317.085***	22.691	349.942	22.914	332.384	22.062	404.434
	80	**22.633***	**354.600***	22.296	383.272	22.517	364.228	21.396	471.456
	90	**22.174***	**394.161***	21.942	415.816	22.166	394.884	20.802	540.652
	100	21.813	428.316	21.629	446.896	**21.828***	**426.83***	20.261	612.364
Barbara	10	**32.842***	**33.796***	32.140	39.729	31.594	45.047	32.713	34.809
	20	**29.001***	**81.847***	28.253	97.222	27.695	110.556	28.757	86.555
	30	**26.904***	**132.657***	26.159	157.455	25.919	166.399	26.497	145.647
	40	**25.519***	**182.483***	24.786	215.991	24.798	215.398	24.932	208.827
	50	**24.514***	**229.980***	23.828	269.320	23.994	259.182	23.759	273.621
	60	**23.741***	**274.808***	23.179	312.724	23.392	297.762	22.829	338.937
	70	**23.12***	**317.085***	22.691	349.942	22.914	332.383	22.062	404.434
	80	**22.633***	**354.600***	22.296	383.271	22.517	364.228	21.396	471.455
	90	**22.174***	**394.161***	21.942	415.816	22.166	394.884	20.801	540.651
	100	21.813	428.316	21.628	446.896	**21.828***	**426.83***	20.260	612.363

Lena	10	**34.610***	**22.493***	34.322	24.033	33.821	26.97	34.533	22.894
	20	**31.380***	**47.328***	31.126	50.171	30.720	55.085	31.083	50.666
	30	**29.524***	**72.559***	29.370	75.171	29.152	79.046	28.895	83.849
	40	**28.219***	**97.984***	28.106	100.562	28.042	102.050	27.274	121.783
	50	**27.231***	**123.025***	27.141	125.597	27.166	124.851	25.989	163.714
	60	**26.46*0**	**146.908***	26.407	148.704	26.431	147.883	24.924	209.258
	70	**25.807***	**170.764***	25.779	171.840	25.802	170.922	24.004	258.622
	80	25.238	194.666	25.114	200.276	**25.255***	**193.902***	23.171	313.249
	90	24.733	218.680	24.730	218.809	**24.777***	**216.442***	22.430	371.585
	100	24.29	242.313	24.235	245.215	**24.346***	**239.009***	21.750	434.541

As described in Table 1, the proposed method provides better results from among all mentioned denoising methods. Results are especially better for images with high texture details. In comparison to Neigh Shrink, the difference is more than 3 db when the amount of noise is high. However, for images with fewer textures block shrink also provides quite good results and when the amount of noise is high, these results are even slightly better than in the proposed method.

5. Conclusions

The presented method demonstrated that the adaptive wavelet thresholding method for image denoising using SURE minimization and clustering of wavelets provides significant improvement in comparison to the existing image denoising methods. In order to show the effectiveness of the new algorithm, several examples are presented and compared with effective techniques in the literature. The objective analysis demonstrated that the proposed method significantly outperforms the BiShrink, Neigh shrink and block shrink approaches. Evaluations have been performed on different images and with different noise levels. Results are especially better for images with high texture details. However, for images with fewer textures, block shrink also provides quite good results and when the amount of noise is high, these results are even slightly better than in the proposed method.

This article demonstrated that the clustering of the wavelet coefficient might be beneficial and also provides a new direction for future research. This technique can especially be used altogether with other techniques which explore inter-scale dependencies or can even be combined with other image denoising methods.

References

[1] Fedak V.I., Nakonechny A.Y., *Artifacts suppression in images and video. Non-Local Means as algorithm for reducing image and video distortions*, Hluboka nad Vltavou, Czech Republic 2009.

[2] Buades A., *Image and film denoising bynon-local means*, Ph.D. Thesis in Journal of Visual Commincation and Image Representation, March 2004, Vol. 1, No. 1, pp. 2–4, Article No. VC970378.

[3] Luisier F., Blu T., Unser M., *A New SURE Approach to Image Denoising: Inter-Scale Orthonormal Wavelet Thresholding*, IEEE Transactions on Image Processing, 2007, Vol. 16, No. 3, pp. 593–606.

[4] Zhou Z.-F., Shui P.-L., *Contourlet-based image denoising algorithm using directional windows*, Electronic Letters, 2007, Vol. 43, No. 2, pp. 92–93.

[5] Olhede S.C., *Hyperanalytic denoising*, IEEE Transactions on Image Processing, 2007, Vol. 16, No. 6, pp. 1522–1537.

[6] Donoho D.L., Johnstone I.M., *Ideal spatial adaptation by wavelet shrinkage*, Biometrika, 1994, Vol. 81, No. 3, pp. 425–455.

[7] Fedak V., Nakonechny A., *Spatio-temporal algorithm for coding artifacts reduction in highly compressed video*, Technical Transactions Automatic Control, 2013.

[8] Pizurica A., Philips W., *Estimating the probability of the presence of a signal of interest in multiresolution single and multiband image denoising*, IEEE Transactions on Image Processing, 2006, Vol. 15, No. 3, pp. 654–665.

[9] Shui P.-L., *Image Denoising Algorithm via Doubly Local Wiener Filtering With Directional Windows in Wavelet Domain*, IEEE Signal Processing Letters, 2005, Vol. 12, No. 6, pp. 681–684.

[10] Luisier F., Blu T., Unser M., *A New SURE Approach to Image Denoising: Inter Scale Orthonormal Wavelet Thresholding*, IEEE Transactions on Image Processing, 2007, Vol. 16, No. 3, pp. 593––606.

[11] Achim A., Kuruoglu E.E., *Image Denoising Using Bivariate -Stable Distributions in the Complex Wavelet Domain*, IEEE Signal Processing Letters, 2005, Vol. 12, No. 1, pp. 17–20.

[12] Donoho D.L., Johnstone I.M., *Ideal spatial adaptation by wavelet shrinkage*, Biometrika, 1994, Vol. 81, No. 3, pp. 425–455.

[13] Chen G.Y., Bui T.D., *Multi-wavelet Denoising using Neighboring Coefficients*, IEEE Signal Processing Letters, 2003, Vol. 10, No. 7, pp. 211–214.

[14] Stein C., *Estimation of the mean of a multivariate normal distribution*, Ann. Statist., 1981, Vol. 9, pp. 1135–1151.

[15] Rohit Sihag, Rakesh Sharma, Varun Setia Wavelet, *Thresholding for Image Denoising*, International Conference on VLSI, Communication & Instrumentation (ICVCI), 2011.

TECHNICAL TRANSACTIONS | **CZASOPISMO TECHNICZNE**
ELECTRICAL ENGINEERING | ELEKTROTECHNIKA
2-E/2015

VOLODYMYR SAMOTYY*, ULYANA DZELENDZYAK**

OPTIMIZATION OF SYSTEM PARAMETERS CONTROLLING ELECTRIC FURNACE TEMPERATURE USING GENETIC ALGORITHMS

OPTYMALIZACJA PARAMETRÓW UKŁADU STEROWANIA TEMPERATURĄ PIECA ELEKTRYCZNEGO Z WYKORZYSTANIEM ALGORYTMU GENETYCZNEGO

Abstract

The optimization of the parameters of the electric furnace temperature control was considered. The optimization was executed using genetic algorithms. The model takes into account nonlinearity, which is connected with the penetration of heat. Also, it is connected with losses of heat due to convection and radiation. The genetic algorithm determines the selection of parameters of the mathematical model in which the system accurately reproduces the input action.

Keywords: *genetic algorithm*, *individual*, *population*, *mutation*, *target function*, *electric furnace*

Streszczenie

W artykule przedstawiono optymalizację parametrów układu sterowania temperaturą pieca elektrycznego. Optymalizacja odbywa się za pomocą algorytmu genetycznego. Model pieca uwzględnia nieliniowości związane z przenikaniem ciepła oraz stratami ciepła przez konwekcję i promieniowanie. Algorytm genetyczny określa parametry modelu matematycznego, dla których system maksymalnie dokładnie odtwarza sygnał wejściowy.

Słowa kluczowe: *algorytm genetyczny*, *osobnik*, *populacja*, *mutacja*, *funkcja celu*, *piec elektryczny*

DOI: 10.4467/2353737XCT.15.097.3929

* Prof. Ph.D. D.Sc. Eng. Volodymyr Samotyy, Department of Automatic Control and Information Technology, Faculty of Electrical and Computer Engineering, Cracow University of Technology.

** Ass. Prof. Ph.D. Eng. Ulyana Dzelendzyak, Department of Computerized Automatic Systems, Lviv Polytechnic National University.

1. Introduction

The electric furnace is a very common object in various technical and household systems; therefore, the control of its temperature is of great practical importance. The pent temperature control system was created for electric furnaces – this raises questions regarding the estimation of its dynamic properties, in particular, its inertia. The first step which is necessary to reach this point is to create a mathematical model of furnaces' temperature control systems which has the ability to perform the physical process in the most adequately way. Certainly, such a system will be nonlinear and inertial because the mathematical model will be reduced to the system of nonlinear differential equations. To adequately perform the physical processes in the furnace, it is recommended to write the differential equations in partial derivatives. This is due to the spread of temperature in time and space. The independent variables of this model are spatial coordinates and time. In this article, the spatial variables are not considered it is limited by the time. This makes it possible to record a mathematical model of the furnace using the usual derivatives. Such a simplification distorts the true picture of the physical process. However, it is possible to carry out a quantitative assessment of the dynamic work of the system using such a model. Finally, the control system is described by a system of nonlinear differential equations. The reason for the nonlinearity of these equations is the dependence of the parameters of the current furnace temperature and the heater. In particular, the electrical resistance of the heater is also nonlinearly dependent on temperature. As the temperature increases, electrical resistance also increases. However, if the temperature varies slightly, it could be considered as a constant.

Electric furnaces are objects with many parameters, these are time constants, structural factors and parameters furnace heater. It is characterized by a significant number of variables, as a result, it creates a large space of search. Therefore, there is no way to enumerate all solutions in a reasonable time. This leads to the application of a genetic algorithm in solving optimization problems. For efficient operation of the temperature control of an electric furnace, it is necessary to optimize its parameters. In genetic algorithms, during the modelling of parametric optimization target function is used. In this case, such a function is representative of the difference between the desired results and those that are available. If we are interested in the output signal of the system, it should be a difference between the desired output signal and the available output signal. In an electric furnace, the output of the system changes its temperature over time.

We are dealing with two independent mathematical models. The first independent mathematical model reflects the change in time of the state variables of the system. It is based on the nonlinear dynamic equation in ordinary derivatives and on being solved by numerical methods. The second independent mathematical model using evolutionary methods selects the parameters of the system, so the dynamic characteristics of the system should be close to the desired. For each new set of numerical values of parameters we have an absolutely independent task, which is related to the other set. Therefore, this algorithm is easy to parallelise, which enables improving its performance.

2. Analysis of publications

To determine the optimal parameters of control systems a variety of approaches are used. The most widely used two directions. In the first direction neural Networks are used. The second direction is based on genetic algorithms and the other. The cause of using depends on the particular problem and its adaptation to a specific method. The minimax methods are known, but they are cumbersome and often determine only a local optimum.

In [1] the problem of modelling nonlinear control systems is considered. The structured nonlinear parameter optimization method (SNPOM is a structured nonlinear parameter optimization method), which is adapted to the radial basis function (RBF is a radial basis function) of network is proposed. This is non-linear model of parameters' optimization depending partly on Levenberg–Marquardt method for nonlinear optimization of parameters. Compared with some other algorithms, SNPOM accelerates the computing convergence of searching process of parameters' optimization models RBF type. In [2] the procedure for implementing the Taguchi's method for electromagnetic optimization problems is shown. Optimization procedure is used for the development of antenna arrays. Compared with traditional methods of optimization, Taguchi's method is easy to implement and it quickly reaches the optimal solutions. In [3], the numerical optimization combined with finite element (FE – finite element), which plays an important role in the development of electromagnetic devices is performed. The parametric description of the investigated objects executed and the optimization problem is formed. Special attention is paid to the symbolic description of the model to minimize computation time and process of definition the optimization task. In [4] the new optimization algorithms for the optimal configuration of controllers PI, belonging to a class of second-order processes with integral component and variable parameters are proposed. Sensitivity analysis relatively to the parameters' changing of controlled process leads to increased sensitivity of the model. The increase in output sensitivity function through the integral criterion of absolute error in determining the objective functions and related optimization problems are solved by the systems Particle Swarm Optimization (PSO) and Gravitational Search Algorithms (GSA).

In [5] a concept for the optimization of nonlinear functions using the methodology of cluster particles represented. The evolution of multiple paradigms is shown but attention is focuses on the implementation of one of them. The measurement of productivity paradigm, including nonlinear function of optimization is described the process of neural network training is suggest. The relationship between the particle and cluster optimization using genetic algorithms is described. In [6] an optimization task that contains gaps, nonlinearity or high dimension is performed. It is difficult to solve it using conventional numerical methods because it requires high time costs. The tool that solves this problem using optimization particle Games Gaming Particle Swarm Optimization (GPSO) is suggested. This algorithm is implemented on the hardware using the graphics processor (GPU). The paper used this utility to optimize the allocation of radio resource. This study is a powerful tool that can be used to solve various disciplinary optimization tasks such as training of artificial neural networks, function maximization/minimization for universal plug and play mobile communication systems, and planning. A nonlinear mathematical model of electric furnace which will be explored is given in [7].

3. The mathematical model of control system

To adjust the temperature in the furnace, a conventional analogue closed linear stabilising system with automatic control (Fig. 1) and with full original information can be used. This system works in such a way: action u, which was setting, comes to the difference scheme, where it is deducted from the voltage u_{MT} output proportional to the temperature of the furnace. The resulting difference is amplified by an electronic amplifier (EA) and fed to the motor (M) shaft through a reduction gear (RG) which is connected to a potentiometer (PT). The potentiometer is a part of the scope of the heating furnace element (OE) and a change in its resistance leads to a change of temperature in the furnace t_{EO}. The temperature using the measuring transducer MT is converted into a voltage that is fed to the difference scheme. Time will be denoted as τ. To simplify the model, it is necessary to suggest the assumption that the measuring transducer has a linear characteristic. Its parameters are chosen to achieve the desired temperature and its output voltage must be equal to setting action. In such a case, the amplifier input voltage will be at zero and the motor will not rotate. The system will go into equilibrium.

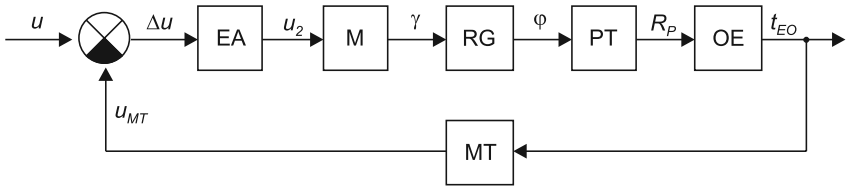

Fig. 1. The functional scheme of the automatic temperature control in an electric furnace

The mathematical model of the system's elements is considered. Linear and nonlinear elements are presented.

Electronic amplifier. This element in comparison with motor, furnace can be considered as having no lag. Therefore, it is described by the algebraic equations:

$$u_2 = \begin{cases} 0, & \text{if} \quad |\Delta u| < u_{\min} \\ K_E \Delta u + u_0, & \text{if} \quad u_{\min} < |\Delta u| < u_{\max} \\ u_{2\max}, & \text{if} \quad |\Delta u| > u_{\max} \end{cases} \quad u_0 = -K_E u_{\min}, \quad \Delta u = u - u_{MT} \tag{1}$$

DC motor. This refers to electromechanical devices and it is described by differential equations of the fourth order:

$$\frac{di_a}{d\tau} = S_a u_a - T_a u_f + E_a, \quad \frac{di_f}{d\tau} = -T_f u_a + S_f u_f - E_f, \quad \frac{d\omega}{d\tau} = (c\Phi i_a - M_R)/J, \quad \frac{d\gamma}{d\tau} = \omega \tag{2}$$

where:

$$S_a = 1/(L_a + L_{af} L_{fa}/L_f), \; T_a = S_a L_{af}/L_f, \; E_a = S_a (L_{af} r_f i_f / L_f - c\omega\Phi - \Delta u - r_a i_a),$$
$$T_f = S_a L_{fa}/L_f, \; S_f = (1 - L_{fa} T_a)/L_f, \; E_f = (L_{fa} E_a + r_f i_f)/L_f.$$

L_a – the total inductance of the consecutive circuit's armature,
L_f – the inductance of exciting winding,
L_{af}, L_{fa} – mutual inductances of the circuit's armature and the circuit of excitation,
r_a, r_f – active resistances of the circuit's armature and the circuit of excitation,
ω – the angular velocity of motor armature,
γ – the angle of rotation,
Φ – the magnetic flux of motor,
c – the constitutive constant of motor armature,
Δu – the voltage drop in the brush contact,
J – the moment of inertia of the rotor motor,
M_R – the moment of resistance.

In consideration of saturation compensated motors of electromagnetic conductor it is possible to approximate the curve of magnetization. In the unsaturated motor it is:

$$\Phi = L_f i_f / w_f \tag{3}$$

To receive the equations of DC motor with series excitation, equation (2) must be supplement by conditions:

$$i_a = i_f = i_M, \quad u_C = u_a + u_f \tag{4}$$

Solving (2) and (4) together, the equation of DC motor with series excitation will be obtained:

$$\frac{di_M}{d\tau} = S_a u_a - T_a u_f + E_a, \quad u_f = \frac{(T_f - S_a)u_C + E_f - E_a}{T_a - S_a + T_f - S_f}, \quad u_a = u_C - u_f. \tag{5}$$

Reducer. The reducer's equation is described by the linear dependence:

$$\varphi = \gamma / i \tag{6}$$

where i is a coefficient of reduction.

Potentiometer. This element is also a linear element without lag that converts the rotation angle φ in the resistance of the resistor regulator:

$$R_P = k_P \varphi \tag{7}$$

where R_P, k_P are the resistance and coefficient of conversion resistor's regulator.

An electric heating element. In Figure 2, a scheme of an electric heating element with a resistance R_P is shown. This is powered by voltage U through resistor regulator R_P.

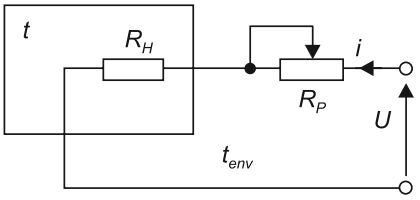

Fig. 2. A scheme of electric heating element

The temperature t is a managed quantity of the furnace. In this scheme, the control value is the resistance R_P. The values, which are disturbing are voltage U, an environment temperature t_{env} and a resistance heater R_H. According to the law of energy conservation, such an equation can be formed [7]:

$$A_E = \grave{A}_H + \grave{A}_{\text{env}} \tag{8}$$

where:

A_E – the elevated heat,
$\grave{A}_H$ – the energy, which is expended to replace the thermal state of the heater,
$\grave{A}_{\text{env}}$ – the energy, which is removed from the control object into the environment.

Considering that for an infinitely small time interval, $d\tau$ voltage of net U, resistance of heater R_H and resistor of control R_P remain the same, it is possible to determine the elevated energy using this time:

$$A_E = i^2 R_H d\tau = \frac{U^2 R_H}{(R_H + R_P)^2} d\tau \tag{9}$$

where i is the current flowing through the heater. In turn:

$$A_H = c_t m dt \tag{10}$$

where:

c_t – the specific heat of the material object,
m – the mass of the object,
dt – the change in temperature.

The energy, which is removed from the facility into the environment, is determined by the cost of the heat transfer, convection and heat's radiation and dissipation:

$$A_{\text{env}} = \lambda_H S_H (t - t_{\text{env}})\, d\tau + \kappa_r S_r (t^4 - t_{\text{env}}^4)\, d\tau \tag{11}$$

where:

λ_H – a coefficient of heat,
S_H – an equivalent heat's transfer surface,
κ_r – a coefficient of radiation,
S_r – an equivalent surface of radiation:

$$S_H = \frac{\lambda_S S_S (t_S - t_{\text{env}})}{\lambda_H (t - t_{\text{env}})}, \quad S_r = \frac{\kappa_S S_S (t_S^4 - t_{\text{env}}^4)}{\kappa_r (t^4 - t_{\text{env}}^4)} \tag{12}$$

where:

S_S – the actual surface of the object,
t_S – the temperature on the surface of this object,
λ_S, κ_S – the heat transfer coefficient and the radiation furnace surface.

By substituting (9)–(12) (8) and dividing this result by $\lambda_H S_H d\tau$ dynamic equations, an electric heating element is obtained:

$$\frac{c_t m}{\lambda_H S_H}\frac{dt}{d\tau} + t = \frac{U^2 R_H}{\lambda_H S_H (R_H + R_P)^2} + t_{\text{env}} - \frac{\kappa_r S_r}{\lambda_H S_H}(t^4 - t_{\text{env}}^4) \tag{13}$$

Time constant is $T_1 = c_t m / (\lambda_H S_H)$. The final form of the equation, which will be integrated by the Runge–Kutta's method in modelling process:

$$\frac{dt}{d\tau} = T_1^{-1}\left(\frac{U^2 R_H}{\lambda_H S_H (R_H + R_P)^2} + t_{\text{env}} - \frac{\kappa_r S_r}{\lambda_H S_H}(t^4 - t_{\text{env}}^4) - t\right). \tag{14}$$

Measuring converter. A thermocouple is used to measure the temperature, which in the first approximation can be considered as a linear element without lag:

$$u_{MT} = k_{MT} t \tag{15}$$

where k_{MT} is a coefficient of measuring transducer.

4. The implementation of the genetic algorithm

The mathematical model of the explored control system is nonlinear, it is therefore impossible to use analytical methods of parametric optimization. The appropriate modification of the genetic algorithm, which takes into account all the features of the model was performed. In order to evaluate the results of optimization which were obtained, the following fitness function was used: $F_{\text{fitn}} = \sum_i \left| t_i - t_0 \right|$, where t_0 is the given temperature, t_i is the temperature of the heating element.

For the fitness function, a sum of absolute means of differences between input and output values in the range of output value outside the statistical error of the control system is taken. For simplicity, it is considered that the transition process was completed when the resulting value is included in the limit of static error system. Be considered more adaptable individual with a lower value of the fitness function. This objective function does not account for the duration of the transition process; therefore, the result cannot be the best of the possible solutions in the terms of speed heating of furnace.

Genetic methods, which according to their nature are stochastic methods, are based on the analogy with the natural evolutionary process. Genetic methods do not impose additional requirements to the expression of the fitness function – at each iteration, it works with multiple solutions. This provides an opportunity to circumstance the whole research space in comparison to making it possible in most cases a more detailed comparison with gradient methods of multidimensional nonlinear unconstrained optimization. Genetic method predicates a ways out of local extremes.

The fitness function is one of the most influential factors on the effectiveness of the genetic algorithm because it determines the aim of algorithm. In the case of an incorrect algorithm's default it will get to a local extremum. It appears as effective data or it can be taken as a result of work because sometimes a local extremum can be better than primary data. Additionally, the genetic algorithm can reach the extremum at the circumference

of the point. The aim of the genetic algorithm is to search the following values of the model's parameters under which the fitness function value is equal to zero or it is close to zero. System's parameters which will be changed by the genetic algorithm are: $k_{\tilde{A}\tilde{I}}$ which is the amplification factor of electronic amplifier; k_{OF} is the displacement of strengthening of output quantity for input signals, its amount exceeds the threshold value; $u_{\min}$ is the threshold of sensibility if it will be exceeded the input signal becomes strengthening.

For the implementation of the optimization model, the algorithm of classic GA is simplified. Such simplifications are permissible due to the small number of chromosomes (system parameters, which are selected by the algorithm) and because of ease of the control system's mathematical model. In the simplified algorithm, the crossover's operator mutation of parental individuals is absent. The parameters of the new individual will be accidentally generated based on the parents' parameters, which are monogamous.

This simplified modification of the algorithm consists of the following stages:

1) The creation of initial population.
2) The calculation of adaptability for each species.
3) The selection of individuals according to adaptability. Some amount is selected, which is set by GA working.
4) The condition algorithm's work completion is checking.
5) If condition 4 is not satisfied, the generation of a new population based on the best selected is executed using mutation operation and it returns to condition 2.
6) If condition 4 was executed, the best individuals from the generated population would be selected. It would be the result of the algorithm's work.

Graphical interpretation of modification of the algorithm is shown in Fig. 3.

Before the program starts, it is necessary to establish the following parameters:

– the mathematical model of the control system (amplifier, engine, gearbox, heating element),
– genetic algorithm (number of generations and populations, the percentage of people who will be selected by a better indicator of adaptation),
– limits of changes in these parameters.

After the process of necessary constant reading program will calculate some service information, which is necessary for it proper work. It includes the primary parameters of the algorithm and a set of launching at the environment of execution. Only after this procedure can the important stage of work of the genetic algorithm will begin. It is a process of creation of primary population individuals. At this stage, all individuals of the first generation are successively created. During the population's individual creation, an accidental choice of the meanings of changeable parameters is occurred at the limits of the whole range of changes, which includes the changing from minimal meaning of the parameter to maximum with some stage. The meanings for whole parameters, which are selected by the algorithm are chosen in a such way that it is not depending from one another. to run the process in runtime. Only then begins an important stage of the genetic algorithm – creating initial population of individuals. At this stage, all individuals of the first generation are consecutively created. When creating an individuals of population, the selection of values of variable parameters within the entire range of variation from minimum to maximum

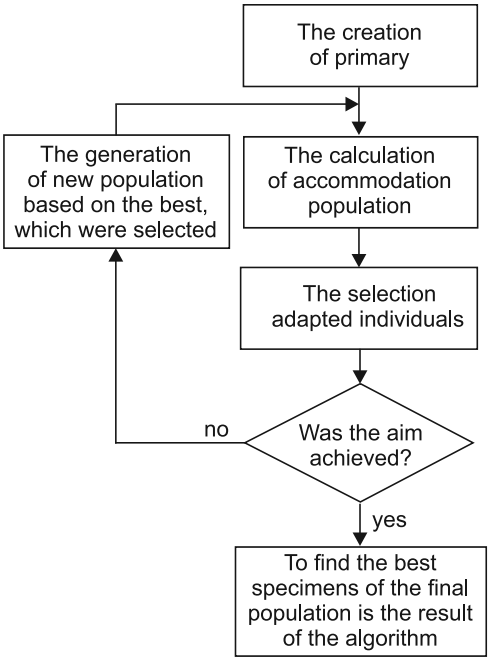

Fig. 3. The scheme of genetic algorithm's modification

setting, with a certain step is happened. Chosen values for all parameters are selected by algorithm, regardless of each other.

After creating the population for each individual held the launch of a mathematical model with a set of input parameters is occurred. In the process of modelling in iterative form fitness function for the individual is calculated. If the method for pre-set parameters was divergent, fitness function would take the maximum value for a variable of double type of C++.

After the process of fitness function meaning calculation for all individuals of generation individuals are sorted according to this value in ascending order. This means that the most adapted individuals will be at the beginning. Since the beginning of the sorted list sorted according to the prescribed percentages correlation some amount of the best individuals is chosen. Based on this, these new individuals will be generated. One of the best individuals passes in to the next generation. The rest places in generation are stuffed by new individuals, which creation is based on the best selected individuals.

When creating some new species, the mutation operator is used. For example, we have only 30 individuals out of 100; therefore, they become the basis for a new population which in turn will also have 100 individuals. 30 individuals using mutation will form 70 its descendants. The principle 'the best can get better' is established. So, the best individual will have the largest amount of descendants. The rest will have an equal amount of descendants but its division will begin from the best. This means that the worst of the 30 individuals will be able to get the child in the least. The creation of descendants occurs

sequentially, skirt all the population. If we had an equal number of new and old persons, each old individual would have the descendants. If the percentage value of new individuals was less than 50, an opportunity to get descendants would have only the best individuals. The worst individuals will not get such an opportunity at all. The principle of mutation work is described in detail.

Firstly, the possible range of variation for each of the parental settings is calculated. It is a constant percentage of the whole spectrum, for example it is 10%. This means if k_{Ai} has a general spectrum of changing from 1 to 10, the parent individual will receive the meaning of parameter, which is equal to 5.7. For the descendants, the variation of this value is within the limits from 5.2 to 6.2. The values of descendant's parameters will be changed randomly according to the possible limits of change. The important point of mutation is to reduce the possible range of descendant's parameters from 5–30% in the transition to the next generation. Thus, in each subsequent generation, descendant's mutation decreases, this gives an opportunity to receive the optimal meaning of the parameters and to reach the global minimum of fitness-function. Therefore, detached after mutation we will get a new generation of primary amount. A block diagram of a simplified implementation of the algorithm is shown in Fig. 4.

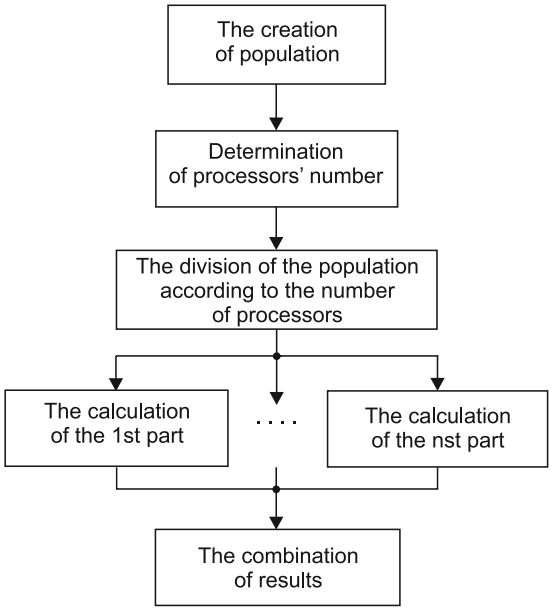

Fig. 4. The scheme of parallel computation of genetic algorithm

As a result of the program, we will get an individual with optimal parameters and a fitness function. Through substituting the values of optimal parameters in the mathematical model, it is possible to reproduce the work of the control system and estimate its results. As a significant amount of the genetic algorithm occurs randomly, multiple runs of a program will give different, but similar results.

The calculation for each individual of generation is not dependent from the others. It can be separated as detached flows, which will occur on the separate nucleus or flows of the processor's nuclear. The increase of productivity from the parallel computation is directly proportional to the number of logical processors (in the case of OS family of Windows NT).

5. Analysis of the genetic algorithm results

In computer simulations modes of the control system the following values of parameters are used:

$h = 0.04$c, $\tau_m = 3000$c, $t_0 = 150°C$, $P_{Pm} = 75\ \Omega$, $i = 1500$, $k_E = 5$, $k_{E\min} = 1$, $k_{E\max} = 10$, $u_0 = 1$ V, $u_{0\min} = 0$, $u_{0\max} = 4$ V, $u_f = 15$ V, $r_a = 0.025\ \Omega$, $r_f = 200\ \Omega$, $L_a = 0.00467$ H, $L_f = 110.8$ H, $L_{fa} = L_{af} = 10^{-5}$ H, $N_f = 2470$, $c = 70.8$ N·m/(Wb·A), $M_R = 0.2$ N·m, $J = 0.2$ N·m·s^2/rad, $c_t = 20$ N·m/(Wb·A), $\lambda_H = 1$ Wt/(m^2·K), $S_H = 1$ m^2, $m = 10$ kg, $U = 220$ V, $R_H = 40\ \Omega$, $t_{\text{env}} = 20°C$, $k_r = 10^{-6}$ Wt/(m^2·K^4), $S_r = 10^{-5}$ m^2.

During the application of the genetic algorithm, it was observed that for some number of species, it was impossible to calculate the function performance goals due to the error of calculation's implementation of output parameters of the mathematical model. A large number of errors occurred in calculations on the first generation and significantly decreased in the following calculations. This gives the opportunity to implement the conclusion that calculation errors arise in some sets of input parameters – this causes divergence of the mathematical model. There are two sorts of errors:

1) The transition process is too long. The output value during the time of integration was not included in the limits of static error of the system.
2) The divergence of integration of differential equations by the Runge–Kutta's method is a periodic character of the output value or its value can be too large.

The first type of error indicates instability or unsatisfactory work of the control system with pre-set parameters. The duration of the entrance action is too long, this is unacceptable. Using standard parameters, such action occurs within the limits of the chosen integration time. To detect this type of error, it is enough to look at the meaning of the output value or to receive an appropriate flag of position of output value in the limits of the static system's errors. This flag is reset at the beginning of the simulation and at each curve's intersection of the output value of the lower or upper limit of static error on the output of this limit, and it is set when the output curve of value crosses the upper or lower limit one more time in the limits of the system.

The second type of errors led to differences in the method of Runge–Kutta. The meanings of value, which were given by the method of Runge–Kutta, were too large. These meanings are featured in differential equation. To exclude such errors, the meanings of values are checked at every step. If at least one of them is too big (limit is set with regard to system settings 10^{-5}), the simulation was stopped.

Thus, in the first generation the exclusion of most false sets was occurred because of the large variation of parameters and diverse species composition. In the next generation, a suitable individuals were modified, so the possibility of a false set with each generation was decreased.

By trial of the genetic algorithm's run, the most successful spread range of input parameters was chosen. It was occurred setting on a large range of change of a large number of individuals of the first population and a small number of generations.

The research of the genetic algorithm occurred using such schemes:

1) The percentage change of new persons using a constant amount and population amount.
2) The change in population size using constant number of generations and the percentage of selection.
3) The change of generations using constant number and percentage of selection.

The work of GA was explored using the first scheme. The amount of generations is 4. The quantity is 10 individuals. The results of algorithm work using different percentage of selection are shown beneath.

Table 1

The results of GA's research according to the first scheme

The percentage of selection	τ_{TP} [s]	t_{OC} [°C]	F_{fitn}
0.4	941	70	416 137
0.5	917	66	377 676
0.6	977	74	447 802
0.7	903	63	362 498
0.8	955	68	482 823

Using the results of testing for the specified amount of population and the quantity of generation, there are two of the most optimal percentage of selection 0.5 and 0.7. Using this meaning of percentage, the results of optimization will be the best.

The GA's work was explored according to the second scheme. The amount of the generation is 5, the percentage of selection is 0.6.

Table 2

The results of GA's research according to the second scheme

The quantity	τ_{TP} [s]	t_{OC} [°C]	F_{fitn}
10	932	74	444 343
20	928	66	389 021
30	902	63	362 069
40	907	64	367 882

Using the results of testing for the specified amount of population and the quantity of generation, there is one the most optimal percentage of selection is 30. Using this meaning of percentage, the results of optimization will be the best.

The GA's work was explored according to the third scheme.

The amount of population is 30, the percentage of selection is 0.6.

Using the 4 population: the duration of transient process is t_{TP} = 959 s; the process of over control is t_{OC} = 70°C; the process of adaptability is 417 060. Using 6 generations: the duration of the transition process is t_{TP} = 913 s; the duration of over control process is t_{OC} = 64°C; the process of adaptability is 373 231. Using 7 generations: the duration of the transition process is t_{TP} = 912 s; over control is t_{OC} = 64°C, the process of adaptability is 373 258. The results of using 8 and more generation are repeated. Therefore, there is no sense to increase the quantity of generations. In pre-set conditions, GA gives the best result using 6 generation.

After investigating the modes of the GA's work, it is possible to choose the best. It will have these parameters the population size is 50 individuals, the number of generations is 6, the percent selection is 0.7.

The calculated curves of the transitional process of furnace's temperature are shown in Fig. 5. Curve 1 corresponds to the regime of parametric optimization, curve 2 corresponds

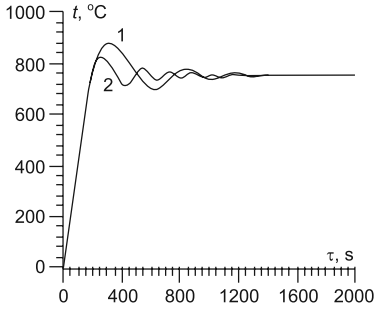

Fig. 5. The transitional process' curves of furnace temperature before optimization (curve 1) and after optimization (curve 2)

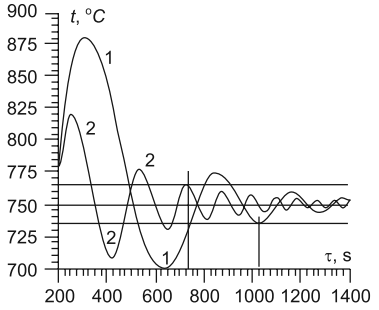

Fig. 6. The fragment of Fig. 5 in scaled-up

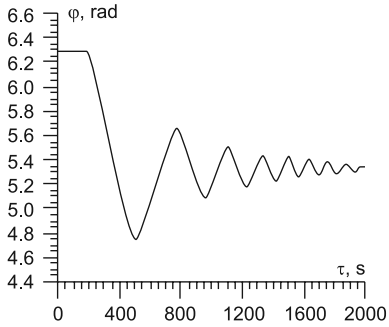

Fig. 7. The transitional process' curve of angle rotation of the potentiometer before parametric optimization

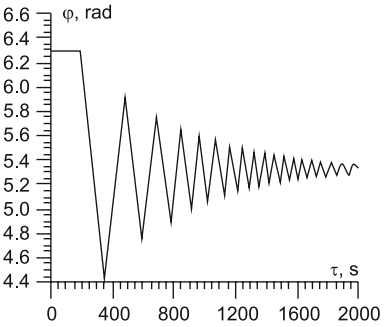

Fig. 8. The transitional process' curve of angle rotation of the potentiometer after parametric optimization

to the regime which exists after parametric optimization of genetic algorithm. To see the essence of the process in Fig. 6, better a fragment in Fig. 5 is shown on a larger scale. The established error is 2%. It is 15°C from the nominal temperature, which is 750°C. The area of this error, which was shown in Fig. 6, are performed by two horizontal lines. As we can see, curve 1 is the zone of error at time 1025 s before parametric optimization. Instead of it, curve 2 comes into this zone more quickly, in particular at time of 730 s after parametric optimization. In conclusion, it is possible to confirm that after parametric optimization, the time of transitional process decreases to 295 s. The overshoot is also decreased from 130°C to 70°C, it is almost doubled. However, the frequency of fluctuations in furnace's temperature doubly increase around factory defaults, which is 750°C.

In Figure 7 the calculated curve of transitional process of angle rotation of the potentiometer is shown before parametric optimization. In Figure 8, the curve is shown after parametric optimization. The fluctuation of the rotation angle of potentiometer occurs around factory default, which is 5.33 rad.

6. Conclusions

A mathematical model of electric furnace of temperature control which takes into account the nonlinear characteristics of the object is proposed. The energy losses from the furnace because of direct heat transfer and radiation are taken into account. Using a genetic algorithm, it is shown that it is possible to determine the optimum parameters of the electronic amplifier. This provides the ability to reduce the transition process to 295°C and to reduce overshoot at 60°C. Thus, the mathematical model of the system modes is determined as universal and ease of algorithms.

References

[1] Hui P., Ozaki T., Haggan-Ozaki V., Toyoda Y., *A Parameter Optimization Method for Radial Basis Function Type Models*, IEEE Transactions on Neural Networks, 2003, Vol. 14, No. 2, pp. 432–438.

[2] Weng W.-C., Yang F., Elsherbeni A., *Linear Antenna Array Synthesis Using Taguchi's Method: A Novel Optimization Technique in Electromagnetics*, IEEE Transactions on Antennas and Propagation, 2007, Vol. 55, No. 3, pp. 723–730.

[3] Pahner U., Mertens R., De Gersem H., Belmans R., Hameyer K., *A parametric finite element environment tuned for numerical optimization*, IEEE Transactions on Magnetics, 1998, Vol. 34, No. 5, pp. 2936–2939.

[4] Precup R., David R., Preitl S., Petriu E., Tar J., *Design aspects of optimal PI controllers with reduced sensitivity for a class of servo systems using PSO algorithms*, Facta Universitatis Series: Automatic Control and Robotics, 2009, Vol. 6, pp. 1–12.

[5] Kennedy J., Eberhart R., *Particle Swarm Optimization*, IEEE International Conference on Neural Networks (ICNN '95), Perth, Australia 1995, pp. 1942–1948.

[6] Rabinovich M., Kainga P., Johnson D., Shafer B., *Particle Swarm Optimization on a GPU*, IEEE International Conference on Electro/Information Technology (EIT), Indianapolis 2012, pp. 1–6.

[7] Garanyuk I., Samotyy V., Strepko I., *Dynamics equation of control system's elements*, Publishing Ukrainian Academy of Printing, Lviv 2006, p. 72.

TECHNICAL TRANSACTIONS | **CZASOPISMO TECHNICZNE**
ELECTRICAL ENGINEERING | ELEKTROTECHNIKA
2-E/2015

KRZYSZTOF SCHIFF*

AN IMPROVEMENT OF THE ANT ALGORITHM FOR THE MAXIMUM CLIQUE PROBLEM

UDOSKONALENIE ALGORYTMU MRÓWKOWEGO DO WYZNACZANIA KLIKI MAKSYMALNEJ

Abstract

The maximum clique problem is a very well-known NP-complete problem and for such a problem, meta-heuristic algorithms have been developed which ant algorithms belongs to. There are many algorithms including ant algorithms that have been elaborated for this problem. In this paper, a new dynamic function of selecting with a new improvement procedure in order to get a larger size of clique for the ant algorithm is presented and this search for the maximum clique in graph is compared to the best ant algorithms that are already known.

Keywords: *maximum clique*, *ant algorithm*, *desirability function*

Streszczenie

Problem kliki maksymalnej przynależy do klasy problemów NP-zupełnych i dla takich problemów opracowuje się obecnie algorytmy metaheurystyczne, do których zaliczają się algorytmy mrówkowe. W niniejszym artykule prezentowany jest algorytm mrówkowy z dynamiczną funkcją wyboru wierzchołków włączanych do tworzonej kliki przez każdą mrówkę wraz z procedurą poprawy wymiaru otrzymanej kliki poprzez wymianę wierzchołków, a otrzymany algorytm został porównany z innymi już dotychczas opublikowanymi.

Słowa kluczowe: *klika maksymalna*, *algorytmy mrówkowe*, *funkcja pożądania*

DOI: 10.4467/2353737XCT.15.098.3930

* Ph.D. Eng. Krzysztof Schiff, Department of Automatic Control and Information Technology, Faculty of Electrical and Computer Engineering, Cracow University of Technology.

1. Introduction

The maximum clique problem has been proven to be a NP-complete problem, this is why there are many meta-heuristic algorithms for this problem to which ant algorithms belong. Ant algorithms are very well suited to solving combinatorial optimization problems [1]. Ant algorithms have already been used to find a maximum clique in graphs [1–6]. The first ant algorithm for the maximum clique problem was presented in [3], which was later improved and discussed in [4]. A distributed version of an ant algorithm was formulated in [2]. This paper presents a new ant algorithm in which there is a new dynamic heuristic and a new procedure for getting a better solution by each ant – this means obtaining a larger maximal clique size.

2. The maximum clique problem

Let $G = (V, E)$ be a graph with a set of vertices V and a set of edges E. A clique C is a subset of set V in which each two vertices (v_i, v_j) are linked together by an edge e_{ij}. A maximal clique is a clique which is not included in another clique. The size of clique C is equal to a number of vertices in the subset C. A maximum clique is the maximal clique with the greatest number of vertices. The vertex degree d_i is the number of edges adjacent to this vertex i. A graph with an almost equal degree of all vertices is a graph in which almost all vertices have the equal vertex degree $d_{v1} \cong d_{vi} \cong \ldots \cong d_{vn}$, $v_i \in V$, such a graph is shown in Fig. 1.

The maximum clique problem is a NP-complete problem – this is why there are many elaborated meta-algorithms for this problem. A vertex degree is the main information which is used by all meta-heuristic algorithms for the maximum clique problem. During the creation of a maximum clique, a vertex is selected depending upon all vertex degrees. The way in which these selected vertices are included into the maximum clique C is a very important factor on which the size of maximal clique depends. When there are many vertices with the equal or almost equal vertex degree, there is no useful information for vertex selection and the way in which vertices are included into the maximum clique is not right. The selection

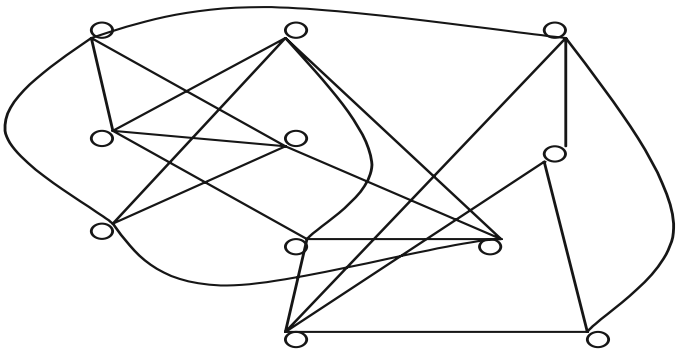

Fig. 1. A graph with almost equal degrees of all vertices

probability formula in ant algorithms includes a vertex degree as useful information, but it is very difficult for ants to make a selection in a correct manner and this is why ants have some difficulty in finding the maximum clique in a graph with almost the same vertex degree of all vertices. Since ants make their vertex selection depending upon the probability formula, they cannot ensure that this is the right way to obtain the maximum clique. If this probability formula allows an improved selection of vertices, then an obtained maximal clique would be closer to the maximum clique. It is therefore very important that the probability formula allows better distinguishing between vertices and better selection of one vertex from others – this is most appropriate in order to ensure an appropriate selection method for the creation of the maximum clique. The probability formula allows ants to better distinguish vertices when the information included in this formula is more precise; therefore, it is very important to formulate such a pattern. In this paper, apart from the more precise information included in a selection formula, an improvement procedure which has been elaborated in order to get a bigger size of received clique is included in the ant algorithm.

3. The improvement of the clique size

When a clique of some size has been found, it is unclear whether this clique is the maximal clique of the graph. In such a situation, we can try to enlarge the size of this clique by using a simple procedure, the pseudo code of which is shown as algorithm 1. We include a vertex in a clique which is not included in this clique and remove from the clique those vertices which are not connected to this new vertex by an edge; afterwards, into this clique additional vertices can be included which can create a new clique of a larger size. As an example: there is a clique of size 6 which consist of vertices 1, 2, 3, 4, 5, 6 in Fig. 2. When we include into this clique vertex 7, we can remove vertices 5 and 6, and afterwards, we can include vertices 8 and 9 – in this way, we can receive a clique with a size of 7 since the clique consist of vertices 1, 2, 3, 4, 7, 8, 9 and this size is larger than the size of the precedent clique, which has a size equal to 6. This improvement procedure is shown as algorithm 1.

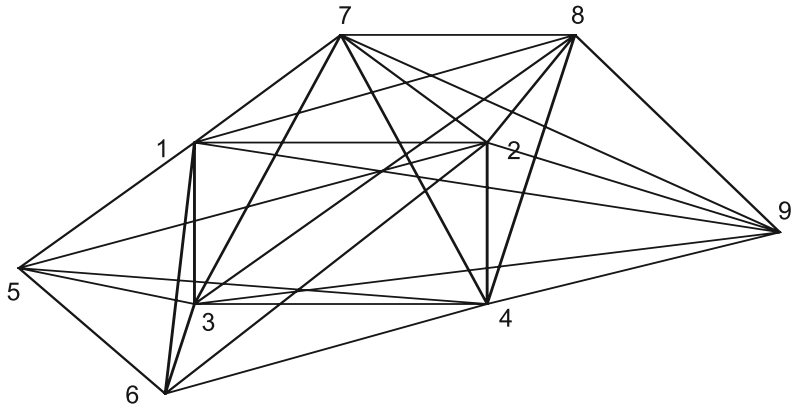

Fig. 2. Example showing how the size of a clique can be enlarged

Algorithm 1

The simple procedure for improvement of clique size

```
While (if a size of clique has been enlarged
    Begin
        For all vertices which are not included into the clique C
            Include a vertex v into the clique S
            Remove from the set S those vertices which are not adjacent to vertex v
            Check if the size of clique S is bigger than the size of the precedent clique C
            If not, return to the precedent clique C
            If yes, repeat a loop while
            If all vertices have been checked and a larger size of clique has been not found
                finish a while loop
End.
```

4. The ant method

Ants search for the best solution to encountered problems. In order to find a such solution, ants communicate with each other by means of a pheromone t. At the beginning of the general ant algorithm, which is presented as algorithm 2, on all elements $i \in M$ a [???], the maximal quantity of pheromone is deposited $t(i) = t_{max}$. The set M is the set of elements i, which can constitute a solution S to certain optimization problem. In the case of the maximum clique problem, the set M is the set of all vertices which are not included into the solution set S and which are connected by edges with all vertices which are already included into the solution set S. The general ant algorithm consists of two main loops: the first loop is connected with the number of cycles and the second loop is connected with the number of ants. With each repetition of the first loop, all repetitions of the second loop have to be performed. The best solution S_b, which was found by all ants in one cycle, is compared to the best solution S_{best}, which was found by ants in a previous cycle. In each cycle, an evaporation mechanism is also used: some of the pheromone is evaporated with the rate r from all elements $i \in M$. In each cycle, an additional quantity of pheromone is also deposited dt on these elements i which constitute a solution S_b. When all loops have been performed, the best solution is returned. At the beginning of each inner loop, a start point is prepared for each ant. From such a start point, each ant begins to create a solution to the optimization problem and then in the *while* loop, each ant selects a next element j with the probability $p(j)$ and puts it to the solution set S. The probability $p(j)$ can be expressed by the formula:

$$p(j) = \frac{t_j n_j}{\Sigma_j (t_j n_j)} \tag{1}$$

where:

- t_j – a quantity of pheromone deposited on element j, $(1 \le j \le \max)$,
- max – the maximum number of available elements from which the selection can be made,
- n_j – a heuristic, this is the desirability of including an element j into the solution set S.

Algorithm 2

The general ant algorithm

for all $i \in M$: $t(i) = t_{max}$
for all cycles
  for all ants
    make a start point
    while (a solution S is not completed) **do**
      check which elements are available to be selected, put them into the set A
      select a next element from the set A with probability $p(j)$
      add a selected element to the S
    save in the S_b a best solution, which has been found by all ants in a cycle
  if S_b is better than S_{best} then save the S_b as the S_{best} : $S_{best} = S_b$
  for all i: $t(i) = t(i) + r^* t$
  $dt = f(S_b)$
  if $i \in S_b$ then $t[i] = t(i) + dt$
return S_{best}

Such a selection as mentioned above can be made only from set A, so from these elements i which are available and which can constitute at this moment of algorithm action a solution to the optimization problem. When any element is added to the solution set S, not all elements from the set A still satisfy constraints and from the previous set A, the new set A is created by only including those elements from the previous set A which satisfy constraints into this set A. In the case of the maximal clique problem, when a vertex i is included into the set S, because this vertex i is not connected together with some vertices from set A, set A should be updated in a such way that all vertices which are not connected together with a vertex i should be removed from set A. Only these vertices which can in future be included into the solution set S should be inside set A and only these vertices are available for the selection.

5. The improvement procedure in the ant algorithm

The structure of the proposed algorithm is the same as the structure of the ant algorithm which was discussed in [3], but there is a little difference between these two algorithms since in the ant algorithm which is proposed in this paper, there is an improvement procedure, which was described in section 2 and a desirability function n – both of these are new elements to the ant algorithm which do not occur in [3, 4, 6]. The procedure of improvement is used after a clique has been constructed by each ant and a new formula for the selection probability used by each ant during clique construction is expressed as follow:

$$p(v_i) = \frac{[t_{v_i} n_{v_i}]^{\alpha}}{\Sigma_{v_i \varepsilon \text{Candidates}} [t_{v_i} n_{v_i}]^{\alpha}} \tag{2}$$

where:

$n(v_i)$ – a heuristic information, desirability of vertex v_i,

$$n(v_i) = \frac{D_{v_i}}{m}, \tag{3}$$

m – the number of vertices,
D_{vi} – the vertex degree in Candidates,

Candidates – the set A of available vertices or it could be a graph structure which is built of vertices from set A and from edges which connect together vertices from the set A, degree D_{vi} is computed in accordance with formula:

$$D_{v_i} = \Sigma_{k \varepsilon \text{Candidates}} d_{ik} \tag{4}$$

$d_{ij} = 1$ when $e_{ij} \in E$ else $d_{ij} = 0$, D_{vi} is not constant and is varying during algorithm action in accordance with contents of the set A.

6. Experiments

The first conducted experiment concerns average maximum cliques sizes obtained using the algorithm presented in [4] and the algorithm in which only a new selection formula with desirability function n is used, as was presented in section 4. The first algorithm is called the ACO algorithm, the second algorithm is called the ACOwith$n$ algorithm. Both algorithms were tested for different values of graph density q\{0.97, 0.974, 0.978, 0.982, 0.986, 0.99, 0.994, 0.998\}.Tests were conducted for graphs with a number of vertices equal to $n = 200$, a number of cycles equal to $lc = 200$, a number of ants equal to $lm = 30$ and an evaporation rate equal to 0.997. An average maximum clique size from 100 measurements and differences in these sizes received for both algorithms have been shown in Table 1 and in Fig. 3. As can be seen, a new selection formula with desirability function n allows receiving a larger clique size in comparison to the case when this desirability function n is not used in a selection formula.

The second conducted experiment concerns average maximum cliques sizes obtained using the first algorithm in which only a new selection formula with desirability function n is used as is presented in section 4 and the second algorithm, in which apart from a new selection formula with a desirability function n also an improvement procedure, which is described in section 2, is used. The first algorithm is called the ACOwith$n$ algorithm, the second is called the IACOwith$n$ algorithm. Both algorithms were tested for different values of graph density q\{0.97, 0.974, 0.978, 0.982, 0.986, 0.99, 0.994, 0.998\}. Tests were conducted for graphs with a number of vertices equal to $n = 200$, a number of cycles equal to $lc = 200$, a number of ants equal to $lm = 30$ and an evaporation rate equal to 0.997. An average maximum clique size from 100 measurements and differences in these sizes received for both algorithms have been shown in Table 2 and in Fig. 4. As can be seen, a new selection formula with desirability function n and improvement procedure allows receiving a larger clique size in comparison to the case when only a new selection formula with desirability function n without the improvement procedure is used.

Table 1

Average size, difference in size for different *q* and 200 vertices

Q	0.998	0.994	0.99	0.986	0.982	0.978	0.974	0.97
ACO	171.81	139.79	121.2	106.12	95.85	87.65	80.24	74.96
ACOwith*n*	172.20	140.33	121.8	107.00	96.60	88.43	81.87	75.63
ACOwith*n*-ACO	0.39	0.54	0.6	0.88	0.75	0.78	1.63	0.67

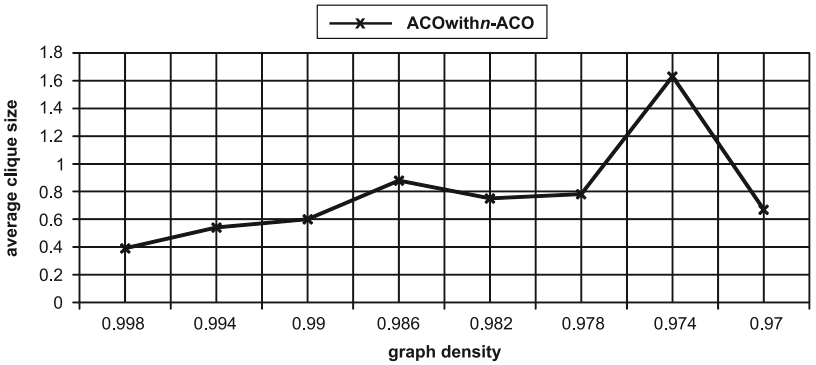

Fig. 3. Difference in average size for different *q* and 200 vertices

Table 2

Average size, difference in size for different *q* and 200 vertices

Q	0.998	0.994	0.99	0.986	0.982	0.978	0.974	0.97
ACOwith*n*	172.20	140.33	121.80	107.00	96.60	88.43	81.87	75.63
IACOwith*n*	172.29	140.94	123.41	109.98	100.23	92.58	86.12	80.91
IACOwith*n*-ACOwith*n*	0.29	0.61	1.61	2.98	3.63	4.15	4.25	5.28

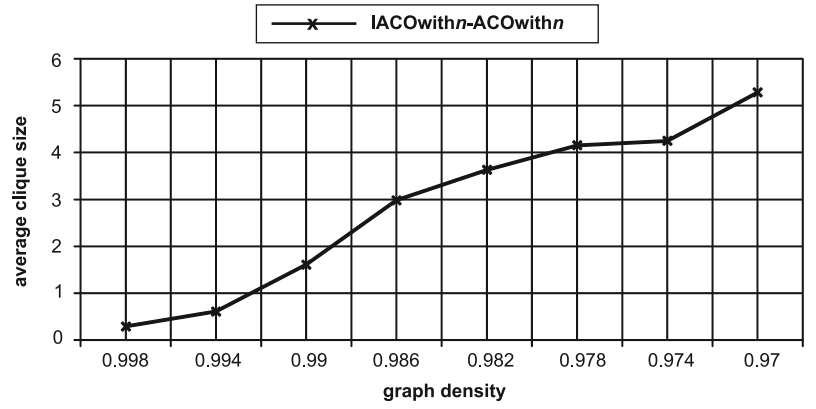

Fig. 4. Difference in average size for different *q* and 200 vertices

The last experiment concerns average maximum cliques sizes obtained using the first algorithm, which is described in [6]. This uses an improvement procedure, which is described in section 2, and the second algorithm in which a new selection formula with a desirability function *n*, which is presented in section 4, and also an improvement procedure, which is described in section 2, are used. The first algorithm is called the NACO algorithm, the second is called the IACOwith*n* algorithm. Both algorithms were tested for different values of graph density *q* {0.97, 0.974, 0.978, 0.982, 0.986, 0.99, 0.994, 0.998}. Tests were conducted for graphs with a number of vertices equal to $n = 200$, a number of cycles equal to $lc = 200$, a number of ants equal to $lm = 30$ and an evaporation rate equal to 0.997. An average maximum clique size for different graph density from 100 measurements and differences in these average maximum cliques size for both of these algorithms have been shown in Table 3 and in Fig. 5. As can be seen, a new selection formula with desirability function *n*, which has been described in section 4 and with an improvement procedure, which was described in section 2, allows receiving a bigger clique size in comparison to the case when an ant algorithm with desirability function described in [6] and with an improvement procedure is used.

This section presents only the main result of scientific investigation since the other investigation results also show that a new selection formula with desirability function *n*, which was described in section 4 and with an improvement procedure, which was described in section 2, improve the size of received clique. All used ant algorithm parameters were set experimentally.

Table 3

Average size, difference in size for different *q* and 200 vertices

Q	0.998	0.994	0.99	0.986	0.982	0.978	0.974	0.97
NACO	171.81	140.61	122.90	109.36	99.36	91.65	85.17	79.80
IACOwith*n*	172.29	140.94	123.41	109.98	100.23	92.58	86.12	80.91
IACOwith*n*-NACO	0.48	0.33	0.51	0.62	0.87	0.93	0.95	1.11

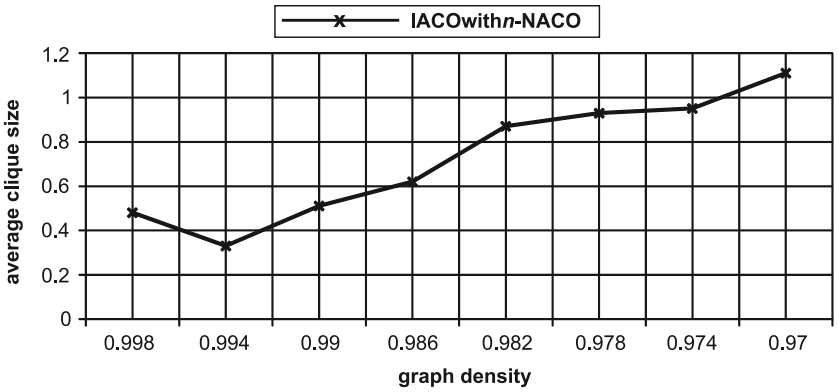

Fig. 5. Difference in average size for different *q* and 200 vertices

7. Conclusion

Experiments have shown that a selection formula with a desirability function n and an improvement procedure make an ant algorithm more powerful than over ant algorithms for the maximum clique problem when we take into consideration the size of the received clique. An improvement procedure allows getting larger cliques in comparison to the situation when this procedure is not used. Additionally, a new desirability function n is more helpful for ants to make a better selection of vertices in order to construct a maximum clique than other selection probability patterns, which have thus far been presented in scientific papers.

References

[1] Dorigo M., *Ant Algorithms for Discrete Optimization*, Artificial Life, 1999, Vol. 5, No. 2, pp. 137–172.
[2] Tang N., *Finding Maximum Cliques with Distributed Ants*, GECCO 2004, LNCS 3102, pp. 24–35.
[3] Fenet S., Solnon C., *Searching for Maximum Cliques with Ant Colony Optimization*, EvoWorkshops 2003, LNCS 2611, pp. 236–245.
[4] Xu X., Ma J., Lee J., *An Improved Ant Colony Optimization for the Maximum Clique Problem*, IEEE Third International Conference on Natural Computation, 2007.
[5] Rizzo J., *An Ant System Algorithm for Maximum Clique*, Master Thesis, The Pennsylvania State University, 2003.
[6] Schiff K., *Ant colony optimization algorithms for clustering problems*, Technical Transaction – Automatic Control, 2013, Y-110, 4-AC, pp. 77–87.

TECHNICAL TRANSACTIONS | **CZASOPISMO TECHNICZNE**
ELECTRICAL ENGINEERING | ELEKTROTECHNIKA
2-E/2015

KRZYSZTOF TOMCZYK, MAREK SIEJA*

PARAMETRIC IDENTIFICATION OF SYSTEM MODEL FOR THE CHARGE OUTPUT ACCELEROMETER

IDENTYFIKACJA PARAMETRYCZNA MODELU SYSTEMU DLA AKCELEROMETRU Z WYJŚCIEM ŁADUNKOWYM

A b s t r a c t

The paper discusses the parametric identification of a system model for the charge output accelerometer based on the simultaneous approximation of amplitude and phase characteristics. The mathematical relationships refer to three models: the mechanical, electrical and complete models, are discussed in detail.

The numerical calculations include the parametric identification of the system model for the PCB357B73 accelerometer and determination of the uncertainties associated with the parameters of this model.

Keywords: *charge output accelerometer*, *parametric identification*

S t r e s z c z e n i e

Artykuł przedstawia parametryczną identyfikację modelu systemu dla akcelerometru z wyjściem ładunkowym opartą na równoczesnej aproksymacji charakterystyk amplitudowej i fazowej. Szczegółowo omówiono w nim matematyczne relacje dotyczące trzech modeli: mechanicznego, elektrycznego i sumarycznego.

Obliczenia numeryczne obejmują parametryczną identyfikację modelu systemu akcelerometru PCB357B73 oraz wyznaczenie niepewności związanych z parametrami tego modelu.

Słowa kluczowe: *akcelerometr z wyjściem ładunkowym*, *identyfikacja parametryczna*

DOI: 10.4467/2353737XCT.15.099.3931

* Ph.D. Eng. Krzysztof Tomczyk, M.Sc. Eng. Marek Sieja, Department of Automatic Control and Information Technology, Faculty of Electrical and Computer Engineering, Cracow University of Technology.

1. Introduction

The identification of the wide range of accelerometers is generally carried out in frequency domain on the basis of the weighted linear least squares method, which allows the easy estimation of the parameters of the mathematical model for the accelerometers in an analytical manner [1, 2]. This mathematical model is, in most cases, presented as the typical system model for the seismic mass accelerometer. The numerator and the denominator of the transfer function of such accelerometers are specified by the constant value and the second degree polynomial respectively. Only if the transfer function contains the constant value in the numerator it is possible to conduct the re-parameterisation procedure of the corresponding complex frequency response – this is performed by dividing the denominator by the numerator of this response and then through the extraction of the two three--component vectors. One of these vectors contains combined parameters, while the second vector consists of the constant values or complex frequency multiplied by the constant values [2–4].

However, in the case of the complete system model for the charge output accelerometer, it is impossible to perform the re-parameterisation procedure because the polynomial occurs in the numerator of the corresponding transfer function. This makes it impossible to apply the analytical weighted least squares method for the parametric identification of this system model. Moreover, it is not possible to determine the resonant frequency and the damping ratio in the same way as for the seismic mass accelerometer, i.e. by means of the first frequency-derivative of the relation referring to the amplitude characteristic.

Both the Monte Carlo (MC) method [5, 6] and the Levenberg–Marquardt (L-M) algorithm [7] are proposed as the identification procedure of the system model for the charge output accelerometer as a response to above mentioned difficulties.

The MC method is used for minimizing the assumed cost function, represented by χ^2 test of matching the complex frequency response of the system model for the charge output accelerometer to the complex frequency response determined on the basis of the measurement data of both frequency characteristics [8–15]. The parameter values of the system model are drawn within the ranges specified by the error margins from the values determined by the L-M algorithm. This algorithm minimizes the objective function, which represents the sum of squared errors between the function describing the amplitude characteristic and the measurement data corresponding to this characteristic.

2. System model for the charge output accelerometer

The complete system model for the charge output accelerometer combines the mechanical and electric models. The system model for the charge output accelerometer can be easily obtained based on the differential equation of the seismic mass accelerometer

$$m\ddot{y}(t) + c\dot{v}(t) + kv(t) = 0 \tag{1}$$

corresponding to the mechanical construction shown in Fig. 1.

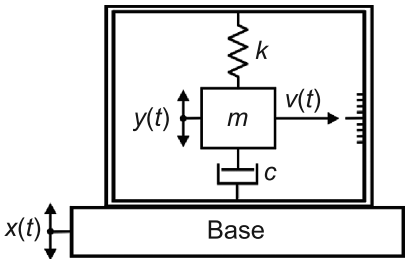

Fig. 1. Mechanical construction of the seismic mass accelerometer

In Figure 1, the following notations are assumed: $v(t)$ – the relative mass displacement (relative output); $y(t)$ – the absolute mass displacement (absolute output); $x(t)$ – the vibration (excitation); m [kg] – the seismic mass; c [kg/s] – the dumping coefficient; k [N/m] – the spring constant; $m\ddot{y}(t)$ – the moment of inertia; $c\dot{v}(t)$ – the moment of dumping; $kv(t)$ – the moment of elasticity.

For the seismic mass accelerometer, the following relation is met:

$$y(t) = v(t) + x(t) \tag{2}$$

and after substitution eq. (2) into eq. (1), we obtain the following differential equation:

$$m\ddot{v}(t) + c\dot{v}(t) + k\dot{v}(t) = -m\ddot{x}(t) \tag{3}$$

which represents the mathematical model of this accelerometer [6, 16].

2.1. Mechanical model for the charge output accelerometer

The response of the charge output accelerometer to the forcing represents the absolute mass displacement $y(t)$. Unlike to the seismic mass accelerometer, it implies the following substitution in eq. (1):

$$v(t) = y(t) - x(t) \tag{4}$$

which gives:

$$m\ddot{y}(t) + c\dot{y}(t) + ky(t) = c\dot{x}(t) + k\,x(t) \tag{5}$$

Transforming eq. (5) to the s – domain, we have:

$$\frac{m}{k}s^2Y(s) + \frac{c}{k}sY(s) + Y(s) = \frac{c}{k}sX(s) + X(s) \tag{6}$$

and

$$\frac{1}{\omega_0^2}s^2Y(s) + \frac{2\beta}{\omega_0}sY(s) + Y(s) = X(s)\left(\frac{2\beta}{\omega_0}s + 1\right) \tag{7}$$

where

$$\omega_0 = \sqrt{\frac{k}{m}}, \quad \beta = \frac{r}{2\sqrt{km}} \tag{8}$$

The quartz crystal deformation by the compression or tension force $F(t)$ generates the electric charge $Q(t)$ on the surfaces of the electrodes connected to the sides of this crystal:

$$Q(t) = k_p F(t) \tag{9}$$

where $k_p = 22 \cdot 10^{-12}$ [C/N] is the piezoelectric constant.

Figure 2 shows the mechanical construction of the charge output accelerometer.

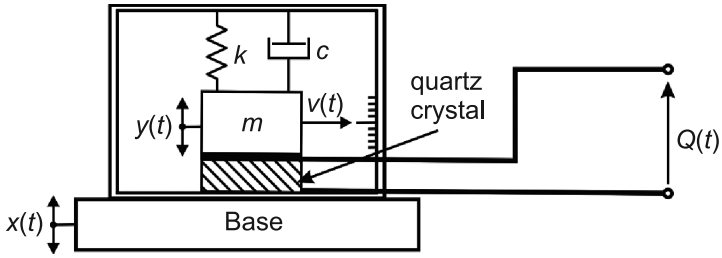

Fig. 2. Construction of the charge output accelerometer

The force that the mass m acts on the crystal is proportional to the absolute acceleration:

$$F(t) = m\ddot{y}(t) \tag{10}$$

Based on eqs. (9) and (10) and after the transformation to the s – domain, we have:

$$Y(s) = \frac{Q(s)}{s^2 m k_p} \tag{11}$$

Substitution eq. (11) into eq. (7) finally yields the mathematical model of the charge output accelerometer:

$$K(s) = \frac{Q(s)}{s^2 X(s)} = S_q \frac{2\beta\omega_0 s + \omega_0^2}{s^2 + 2\beta\omega_0 s + \omega_0^2} \tag{12}$$

where $S_q = k_p S_m$ [C/ms^2] is the charge sensitivity of the accelerometer, while $S_m = m$ [kg] is the mechanical sensitivity of the accelerometer.

2.2. Electrical model for the charge output accelerometer

The conversion of the electric charge $Q(t)$ to the voltage V is carried out by connecting the output of the accelerometer with the voltage amplifier using the low noise coaxial cable. Figure 3 shows the equivalent circuit model for the charge output accelerometer [17].

In Figure 3, the following notations are assumed: Q – the electric charge; R_a, C_a – the internal resistance and capacitance of the accelerometer; R_c – the resistance between cable screen and centre conductor, C_c – the capacitance of the cable, R_i, C_i – the inputs resistance and capacitance of the voltage amplifier.

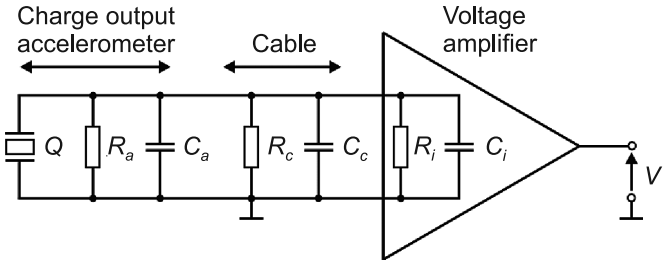

Fig. 3. Equivalent circuit model for the charge output accelerometer

Figure 4 shows the simplified circuit model of the charge output accelerometer, where:

$$R_t = R_a \,//\, R_c \,//\, R_i \tag{13}$$

$$C_t = C_a + C_c + C_i \tag{14}$$

are the total resistance and capacitance.

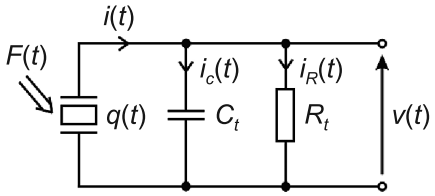

Fig. 4. Simplified circuit model for the charge output accelerometer

Analyzing the circuit shown in Fig. 4, it is easy to get:

$$\frac{V(s)}{Q(s)} = \frac{sR_t}{sR_tC_t + 1} \tag{15}$$

2.3. Complete system model of the charge output accelerometer

Substitution eq. (15) into eq. (12), gives:

$$K(s) = \frac{V(s)}{s^2X(s)} = S_v \frac{s\tau}{s\tau + 1} \frac{2\beta\omega_0 s + \omega_0^2}{s^2 + 2\beta\omega_0 s + \omega_0^2} \tag{16}$$

where $\tau = R_tC_t$ [s] and $S_v = S_eS_m$ [V/ms^2] are respectively the time constant and voltage sensitivity of the complete system model for the charge output accelerometer, and

$$S_e = k_p / C_t \ \text{[V/N]} \tag{17}$$

is the electrical sensitivity.

The frequency characteristics resulting from eq.(16) are as follows:

$$A(\omega) = \\ = S_v\,\tau\,\omega_0\,\omega\sqrt{\frac{\{\omega[\tau\omega_0\omega^2(4\beta^2-1)+\tau\omega_0^3+2\beta\omega^2]\}^2+\{\omega_0\omega^2(2\beta^2-1)+\omega_0^3-2\beta\tau\omega^4\}^2}{[(\omega_0^2-\omega^2-2\beta\tau\omega_0\omega^2)^2++(\tau\omega_0^2\omega-\tau\omega^3+2\beta\omega_0\omega)^2]^2}} \tag{18}$$

and

$$\varphi(\omega) = -\tan^{-1}\frac{\omega_0\omega^2(2\beta^2-1)+\omega_0^3-2\beta\tau\omega^4}{\omega[\tau\omega_0\omega^2(4\beta^2-1)+\tau\omega_0^3+2\beta\omega^2]} \tag{19}$$

3. Identification procedure

Let us present the system model for the charge output accelerometer in the form of the corresponding complex frequency response:

$$K(\omega,\boldsymbol{\theta}) = A(\omega,\boldsymbol{\theta})\exp[j\boldsymbol{\Phi}(\omega,\boldsymbol{\theta})] = S_v\frac{\dfrac{2\beta\omega^2\tau}{\omega_0}-j\omega\tau}{\dfrac{2\beta\omega^2\tau}{\omega_0}+\left(\dfrac{\omega}{\omega_0}\right)^2-1-j\omega\tau\left[1-\left(\dfrac{\omega}{\omega_0}\right)^2+\dfrac{2\beta}{\omega_0\,\tau}\right]} \tag{20}$$

where:

$$\boldsymbol{\theta} = [S_v,\ \omega_{0,},\ \beta,\ \tau] \tag{21}$$

is the vector of the parameters of the complete system model.

It is also assumed that the complex frequency response for the measurement data of amplitude **A** and phase **Φ** is determined as

$$\mathbf{K}(\omega_n) = \mathbf{A}(\omega_n)\exp[j\boldsymbol{\Phi}(\omega_n)], \quad n = 1, 2, \ldots, N \tag{22}$$

The identification procedure is based on eqs. (20)–(22) and includes seven main stages.

In the first stage, on the basis of the vector **A** and by the application of the L-M algorithm, the initial values $\tilde{\boldsymbol{\theta}}_i$ of the vector $\boldsymbol{\theta}$ are determined:

$$\boldsymbol{\theta}_{k+1} = \boldsymbol{\theta}_k^T - [\mathbf{J}^T(\omega,\boldsymbol{\theta}_k)\mathbf{J}(\omega,\boldsymbol{\theta}_k)+\mu_k\mathbf{I}]^{-1}\mathbf{J}^T(\omega,\boldsymbol{\theta}_k)A(\omega,\boldsymbol{\theta}_k), \quad k = 0, 1, \ldots \tag{23}$$

where:

$$\mathbf{J}(\omega,\boldsymbol{\theta}_k) = \begin{bmatrix} \dfrac{\partial A(\omega_0,\boldsymbol{\theta}_k)}{\partial\theta_0} & \dfrac{\partial A(\omega_0,\boldsymbol{\theta}_k)}{\partial\theta_1} & \dfrac{\partial A(\omega_0,\boldsymbol{\theta}_k)}{\partial\theta_2} & \dfrac{\partial A(\omega_0,\boldsymbol{\theta}_k)}{\partial\theta_3} \\ \dfrac{\partial A(\omega_1,\boldsymbol{\theta}_k)}{\partial\theta_0} & \dfrac{\partial A(\omega_1,\boldsymbol{\theta}_k)}{\partial\theta_1} & \dfrac{\partial A(\omega_1,\boldsymbol{\theta}_k)}{\partial\theta_2} & \dfrac{\partial A(\omega_1,\boldsymbol{\theta}_k)}{\partial\theta_3} \\ \vdots & \vdots & \vdots & \vdots \\ \dfrac{\partial A(\omega_{N-1},\boldsymbol{\theta}_k)}{\partial\theta_0} & \dfrac{\partial A(\omega_{N-1},\boldsymbol{\theta}_k)}{\partial\theta_1} & \dfrac{\partial A(\omega_{N-1},\boldsymbol{\theta}_k)}{\partial\theta_2} & \dfrac{\partial A(\omega_{N-1},\boldsymbol{\theta}_k)}{\partial\theta_3} \end{bmatrix} \tag{24}$$

is the Jacobian matrix with $(N-1) \times 4$ dimension and k represents the successive iteration step [6, 7]. In equation (23) $\mathbf{I}$ and μ_k are the 4×4 dimension unit matrix and the variable which changes during each iteration, respectively. The L-M algorithm determines the initial values of the vector parameters for the MC method minimizing the criterion:

$$\tilde{\boldsymbol{\theta}}_i = \min_{\theta} \sum_{n=0}^{N-1} [\mathbf{A}(\omega_n) - A(\omega_n, \boldsymbol{\theta}_k)]^2 \tag{25}$$

In the second stage, the error margins of the vector $\tilde{\boldsymbol{\theta}}_i$ are collated as:

$$\tilde{\boldsymbol{\theta}}_\delta = [\delta_0, \delta_1, \delta_2, \delta_3] \tag{26}$$

In the third stage, the type of the random number generator is selected and the number M of MC trials is assumed.

In the fourth stage, the matrices:

$$\tilde{\mathbf{A}}(\omega, \boldsymbol{\theta}) = \begin{bmatrix} \tilde{A}(\omega_0, \tilde{\boldsymbol{\theta}}_0) & \tilde{A}(\omega_0, \tilde{\boldsymbol{\theta}}_1) & \cdots & \tilde{A}(\omega_0, \tilde{\boldsymbol{\theta}}_m) & \cdots & \tilde{A}(\omega_0, \tilde{\boldsymbol{\theta}}_M) \\ \tilde{A}(\omega_1, \tilde{\boldsymbol{\theta}}_0) & \tilde{A}(\omega_1, \tilde{\boldsymbol{\theta}}_1) & \cdots & \tilde{A}(\omega_1, \tilde{\boldsymbol{\theta}}_m) & \cdots & \tilde{A}(\omega_1, \tilde{\boldsymbol{\theta}}_M) \\ \vdots & \vdots & \ddots & \vdots & \cdots & \vdots \\ \tilde{A}(\omega_n, \tilde{\boldsymbol{\theta}}_0) & \tilde{A}(\omega_n, \tilde{\boldsymbol{\theta}}_1) & \cdots & \tilde{A}(\omega_n, \tilde{\boldsymbol{\theta}}_m) & \cdots & \tilde{A}(\omega_n, \tilde{\boldsymbol{\theta}}_M) \\ \vdots & \vdots & \ddots & \vdots & \cdots & \vdots \\ \tilde{A}(\omega_{N-1}, \tilde{\boldsymbol{\theta}}_0) & \tilde{A}(\omega_{N-1}, \tilde{\boldsymbol{\theta}}_1) & \cdots & \tilde{A}(\omega_{N-1}, \tilde{\boldsymbol{\theta}}_m) & \cdots & \tilde{A}(\omega_{N-1}, \tilde{\boldsymbol{\theta}}_M) \end{bmatrix} \tag{27}$$

and

$$\tilde{\boldsymbol{\Phi}}(\omega, \boldsymbol{\theta}) = \begin{bmatrix} \tilde{\Phi}(\omega_0, \tilde{\boldsymbol{\theta}}_0) & \tilde{\Phi}(\omega_0, \tilde{\boldsymbol{\theta}}_1) & \cdots & \tilde{\Phi}(\omega_0, \tilde{\boldsymbol{\theta}}_m) & \cdots & \tilde{\Phi}(\omega_0, \tilde{\boldsymbol{\theta}}_M) \\ \tilde{\Phi}(\omega_1, \tilde{\boldsymbol{\theta}}_0) & \tilde{\Phi}(\omega_1, \tilde{\boldsymbol{\theta}}_1) & \cdots & \tilde{\Phi}(\omega_1, \tilde{\boldsymbol{\theta}}_m) & \cdots & \tilde{\Phi}(\omega_1, \tilde{\boldsymbol{\theta}}_M) \\ \vdots & \vdots & \ddots & \vdots & \cdots & \vdots \\ \tilde{\Phi}(\omega_n, \tilde{\boldsymbol{\theta}}_0) & \tilde{\Phi}(\omega_n, \tilde{\boldsymbol{\theta}}_1) & \cdots & \tilde{\Phi}(\omega_n, \tilde{\boldsymbol{\theta}}_m) & \cdots & \tilde{\Phi}(\omega_n, \tilde{\boldsymbol{\theta}}_M) \\ \vdots & \vdots & \ddots & \vdots & \cdots & \vdots \\ \tilde{\Phi}(\omega_{N-1}, \tilde{\boldsymbol{\theta}}_0) & \tilde{\Phi}(\omega_{N-1}, \tilde{\boldsymbol{\theta}}_1) & \cdots & \tilde{\Phi}(\omega_{N-1}, \tilde{\boldsymbol{\theta}}_m) & \cdots & \tilde{\Phi}(\omega_{N-1}, \tilde{\boldsymbol{\theta}}_M) \end{bmatrix} \tag{28}$$

are calculated on the basis of the parameters drawn from the ranges

$$\tilde{\boldsymbol{\theta}}_m = [\tilde{S}_{vm} \pm \delta_0, \tilde{\omega}_{0m} \pm \delta_1, \tilde{\beta}_m \pm \delta_2, \tilde{\tau}_m \pm \delta_3] \tag{29}$$

in accordance with the uniform distribution [5, 6].

In the fifth stage, the cost function:

$$\chi^2_m = \sum_{n=0}^{N-1} \frac{\left| \mathbf{K}(\omega_n) - \tilde{K}(\omega, \tilde{\boldsymbol{\theta}}_m) \right|^2}{\sigma^2_{\mathbf{K}(\omega_n)}} \tag{30}$$

for the successive MC trials is calculated, where $\sigma^2_{\mathbf{K}(\omega_n)}$ is the variance of the complex frequency response – eq. (22) [8].

In the sixth stage, both the minimum value of the vector – eq. (30) and corresponding number m_c of MC trials are determined. Resulting from this number, the vector $\tilde{\boldsymbol{\theta}}_c$ is taken as an optimal estimate of the system model for the charge output accelerometer.

In the last stage, the uncertainties associated with the vector $\tilde{\boldsymbol{\theta}}_c$ are determined as the standard deviation of the mean [18]:

$$\hat{\theta}_c^{<r>} = \sqrt{\frac{\sum_{m=0}^{M-1} (\tilde{\theta}_m^{<r>} - \bar{\tilde{\theta}}^{<r>})^2}{M(M-1)}}, \quad r = 0, 1, \ldots, 3 \tag{31}$$

where:

$$\bar{\tilde{\theta}}^{<r>} = \frac{\sum_{m=0}^{M-1} \tilde{\theta}_m^{<r>}}{M} \tag{32}$$

and

$$\tilde{\theta}_m^{<0>} = \tilde{S}_{vm}, \quad \tilde{\theta}_m^{<1>} = \tilde{\omega}_{0m}, \quad \tilde{\theta}_m^{<2>} = \tilde{\beta}_m, \quad \tilde{\theta}_m^{<3>} = \tilde{\tau}_m \tag{33}$$

In order to check the consistency of the measurement data with the system model for the charge output accelerometer corresponding to the vector $\tilde{\boldsymbol{\theta}}_C$, it is proposed to check the criterion:

$$\chi^2_{v,\alpha} \le \sum_{n=0}^{N-1} \frac{\left| \mathbf{K}(\omega_n) - \tilde{K}(\omega, \tilde{\boldsymbol{\theta}}_c) \right|^2}{\sigma^2_{\mathbf{K}(\omega_n)}} \le \chi^2_{v,1-\alpha} \tag{34}$$

where $\chi^2_{v,\alpha}$ is the α – th quantile of the χ^2 distribution of $2N - 4$ degrees of freedom and $\alpha = 0.05$ [2].

4. Results of parametric identification

The procedure discussed in section 3 was applied to the identification of the system model for the PCB357B73 accelerometer with the parameters declared by the manufacturer, i.e. sensitivity S_q = 10.2 pC/ms^2 (±5%), frequency range f_{cut} = 2 kHz (±5%), resonant frequency $f_r \ge 8$ kHz, capacitance C_a = 1500 pF and resistance $R_a = 10^8$ Ω. The PCB cable of the length equals 1 m and the capacitance C_c = 190 pF was used. The measured vectors **A** and **Φ** were determined by the application of the 'back to back' identification procedure [19] supported by LabVIEW software [16], while mathematical calculations were carried out using MathCad14 software [20].

For the L-M algorithm, the input values: $\mu_k = 0.1$ and $\tilde{\boldsymbol{\theta}}_{k=0} = [5.96,\ 57.8 \cdot 10^3,\ 0.1,\ 1.49]$ were assumed. The value of $\tilde{S}_{vk=0}$ was calculated as S_q divided by C_t for C_i = 20 pF, while the value of $\tilde{\tau}_{k=0}$ was determined for R_a = 1 GΩ, R_c = 20 GΩ and R_i = 10 GΩ. The $\tilde{\omega}_{0k=0}$ and $\tilde{\beta}_{k=0}$ were assumed in advance as equal to $57.8 \cdot 10^3$ [rad/s] and 0.1, respectively.

When the objective function for the $k + 1$ iteration step had a value greater than for the step k, the coefficient μ_k was multiplied by the constant value η. The initial value of η was assumed to be equal to 10. In the case of a decrease in the value of the objective function in $k + 1$ iteration step, the coefficient μ_k was divided by η.

For the MC method, two assumptions were made. Firstly, the total number of MC trials were equal to 10^5. Secondly, the percentage deviation of the error margins from the values of the vector $\tilde{\boldsymbol{\theta}}_i$ obtained by means of the L-M algorithm were equal to 5% for each parameter. The determined values of the vector $\tilde{\boldsymbol{\theta}}_i$ were equal to $[5.97, 55.90 \cdot 10^3, 0.21, 1.48]$.

The frequency, amplitude and phase measurement data for the system model are tabulated in Table 1, where $N = 34$.

Table 1

Frequency, amplitude and phase measurement data

F [kHz]	Amplitude **A** [mV/ms^2]	Phase **Φ** [deg.]	**F** [kHz]	Amplitude **A** [mV/ms^2]	Phase **Φ** [deg.]
0.04	6.1	–0.8	2.0	5.9	–0.2
0.05	6.2	–0.1	2.5	7.0	–0.8
0.06	5.7	–0.1	3.0	6.0	–1.6
0.07	6.0	–0.7	3.5	6.9	–1.2
0.08	6.2	–0.6	4.0	7.6	–2.5
0.09	6.3	–0.4	4.5	8.2	–3.3
0.1	5.7	–0.5	5.0	8.8	–6.1
0.2	5.8	–1.3	5.5	8.8	–9.3
0.3	5.7	–0.2	6.0	10.1	–7.3
0.4	6.1	–0.4	6.5	10.2	–10.2
0.5	5.8	–0.1	7.0	11.2	–19.8
0.6	6.2	–0.1	7.5	13.4	–35.6
0.7	5.7	0	8.0	14.2	–25.9
0.8	6.2	0	8.5	16.5	–37.6
0.9	5.7	–0.6	9.0	14.3	–74.4
1.0	5.9	–0.2	9.5	15.5	–95.6
1.5	6.3	0	10.0	13.8	–97.0

Tables 2 contains the identification results of the system model (second column) with associated uncertainties (fourth column), obtained for $m_c = 86\,540$.

Table 2

Parameters of the vectors $\tilde{\theta}_c$ and $\hat{\theta}_c$

$\tilde{S}_{vc}$ [mV/ms^2]	5.78	$\hat{S}_{vc}$ [mV/ms^2]	$5.46 \cdot 10^{-4}$
$\tilde{\omega}_{0c}$ [rad/s]	$57.37 \cdot 10^3$	$\hat{\omega}_{0c}$ [rad/s]	5.34
$\tilde{\beta}_c$	0.205	$\hat{\beta}_c$	$1.92 \cdot 10^{-5}$
$\tilde{\tau}_c$ [s]	1.56	$\hat{\tau}_c$ [s]	$1.37 \cdot 10^{-4}$

Figure 5 shows the fitting error of system model for the charge output accelerometer.

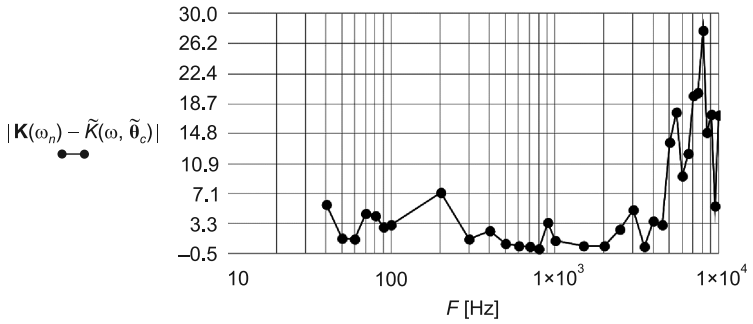

Fig. 5. Fitting error of system model for the charge output accelerometer

Based on Fig. 5, it is easy to notice that the greatest value of fitting error was obtained for the frequency equal to 8 kHz.

For both the measured data and the results of the identification, the criterion – eq. (34) was met, because the value of χ^2 =47.2 was in the range between $\chi^2_{64,0.05} = 46.6$ and $\chi^2_{64,0.95} = 83.7$.

5. Conclusions

The application of both the L-M algorithm only in the first step of the identification procedure, as well as the MC method in the following steps, results most of all from the need to determine the sensitivity from the range of 5% error specified by the manufacturer. The MC method produces the identification results within the ranges providing the practical implementation of the system model. Additionally, the MC method is the procedure recommended by the dedicated standards for determining the uncertainties associated with the parameters of such a system. The L-M algorithm as a gradient procedure works well in the case of the initial calculation of model parameters, which are a basis to the execution

of the MC method. Using only this algorithm for the identification of the system model can lead to results being outside of the non-real ranges for these systems.

Based on the obtained parameters of the system model for the charge output accelerometer, it can be easily noticed that the $\tilde{S}_{vc}$ and $\tilde{\beta}_c$ values are lower while $\tilde{\omega}_{0c}$ and $\tilde{\tau}_c$ values are higher than those obtained by the application of the L-M algorithm. Additionally, the value $\tilde{\beta}_c$ is more than two times higher than that assumed as the input parameter for the L-M algorithm. This means that as an outcome of the MC method execution, the correction of the results obtained based on the L-M algorithm was made by checking the fitting error of the phase characteristic.

References

[1] ISO/IEC Guide 98-3, *Uncertainty of measurement – Part 3: Guide to the expression of uncertainty in measurement*, 2008.

[2] Link A., Täbner A., Wabinski W., Bruns T., Elster C., *Modelling accelerometers for transient signals using calibration measurement upon sinusoidal excitation*, Measurement, 2007, Vol. 40, pp. 928–935.

[3] Tomczyk K., *Modelling of linear analogue transducers in frequency domain*, Przegląd Elektrotechniczny, 2014, No. 6, pp. 202–206.

[4] Tomczyk K., Layer E., *Accelerometer errors in measurements of dynamic signals*, Measurement, 2015, Vol. 60, pp. 292–298.

[5] Kubisa S., *Intuicja i symulacja Monte Carlo podstawą analizy niedokładności pomiarów*, PAK, 2007, No. 9, pp. 3–8.

[6] Layer E., Tomczyk K., *Measurements, modelling and simulation of dynamic systems*, Springer-Verlag, Berlin–Heidelberg–New York 2010.

[7] Tomczyk K., *Levenberg–Marquardt algorithm for optimization of mathematical models according to minimax objective function of measurement systems*, Metrology and Measurement Systems, 2009, Vol. XVI, No. 4, pp. 599–606.

[8] Isermann R., Münchhof M., *Identification of dynamic systems*, Springer-Verlag, Berlin–Heidelberg–Dordrecht–London–New York 2010.

[9] Kollar I., *On frequency-domain identification of linear systems*, IEEE Transactions on Instrumentation and Measurement, 1993, Vol. 42, Issue 1, pp. 2–6.

[10] Pintelon R., Schoukens J., *System identification: A frequency domain approach*, IEEE Press, Piscataway–New York 2001.

[11] Zhao S., Wang F., Xu H., Zhu J., *Multi-frequency identification method in signal processing*, Digital Signal Processing, 2009, Vol. 19, pp. 555–566.

[12] Guillaume P., *Frequency response measurements of multivariable systems using nonlinear averaging techniques*, IEEE Transactions on Instrumentation and Measurement, 1998, Vol. 47, Issue 3, pp. 796–800.

[13] Ljung L., *Some results on identifying linear systems using frequency domain data*, Proc. 32nd IEEE Conf. Decis. Control, San Antonio 1993, pp. 3534–3538.

[14] Sharapov V., *Piezoceramic sensors*, Springer-Verlag, Heidelberg–Dordrecht–London–New York 2011.

[15] Juang J.N., *Applied system identification*, Prentice Hall, Englewood Cliffs 1994.

[16] Tomczyk K., Sieja M., *Acceleration transducers calibration based on maximum dynamic error*, Czasopismo Techniczne, Politechnika Krakowska, No. 3-E/2006, pp. 37–49.

[17] Yu J.Ch., Lan Ch.B., *System modeling and robust design of microaccelerometer using piezoelectric thin film*, Proceedings of the IEEE International Conference on Multisensor Fusion and Integration for Intelligent Systems, Taiwan 1999, pp. 99–104.
[18] BIPM, IEC, IFCC, ILAC, ISO, IUPAC, IUPAP and OIML, Evaluation of measurement data – Supplement 1 to the "Guide to the expression of uncertainty in measurement" – Propagation of distributions using a Monte Carlo method, 2008.
[19] ISO 16063-22, *Methods for the calibration of vibration and shock transducers – Part 22: Shock calibration by comparison to a reference transducer*, 2005.
[20] Tomczyk K., *Special signals in the calibration of systems for measuring dynamic quantities*, Measurement 2014, Vol. 49, pp. 148–152.

CONTENTS

TREŚĆ